UNIVERSITY OF NOVA GORICA
GRADUATE SCHOOL

HEAT AND FLUID FLOW SIMULATION OF THE CONTINUOUS CASTING OF STEEL BY A MESHLESS METHOD

DISSERTATION

M.Sc. Robert Vertnik

Mentor: Prof. Dr. Božidar Šarler

Nova Gorica, 2010

Acknowledements

Most of all, I would like to thank my mentor, Professor Božidar Šarler for his support, guidance, patience, and encouragement for finishing the present dissertation. I would also like to thank my dissertation committee members, Professor Andreas Ludwig, Professor Matjaž Hriberšek, and Professor Ching-Shyang Chen, for their remarks, suggestions and comments.

Next, I want to thank Dr. Jonas Bredberg for his suggestions and help about turbulence modelling, especially on Low-Reynolds-Number models.

A special thanks goes to Dr. Dimitrios Sofialidis, Technical Manager at SimTec Ltd., who organized a course in Slovenia for Ansys Fluent CFD software. His guidance and instructions of using Fluent for simulating solidification processes were also very helpful and important.

I would also like to thank my life partner Ana and my son Maks for their support and patience.

Last but not least I would like to thank my parents to guide me through my life and for understanding of my interest in computer science.

Many thanks to Štore Steel, d.o.o., company, especially to B.Sc. Bojan Senčič and B.Sc. Janko Cesar, for supporting my PhD project and for giving me all necessary data, relevant for the developing numerical model of their billet casting machine.

ŠTORE STEEL
PROIZVAJALEC JEKEL OD 1851

I would like to express my gratitude to Slovenian Technology Agency for support in the framework of the project Young Researcher from Economy under contract P-MR-07/15, operation partly financed by the European Union, European Social Fund.

Investing in your future
OPERATION PART FINANCED BY THE EUROPEAN UNION
European Social Fund

Heat and Fluid Flow Simulation of the Continuous Casting of Steel by a Meshless Method

Abstract

A novel two-dimensional (2D) steady-state meshless solution of coupled heat transfer and turbulent fluid flow in continuous casting process of steel is represented in the present dissertation. The meshless method is based on the local collocation with the multiquadric radial basis functions. The local collocation is made over a set of overlapping influence domains, established by five nodes. The Bennon and Incropera mixture continuum model is used to derive the conservation equations of mass, momentum, and energy for the binary solid-liquid phase-change material. The solidification in the mushy zone is treated as a porous media, which is modelled by the Darcy's law. The permeability of the porous media is calculated by the Kozeny-Karman relation, where the morphology of the porous media is modelled by a constant value. The incompressible turbulent flow of the molten steel is described by the Low-Reynolds-Number (LRN) k-ε turbulence model, where two additional transport equations for the turbulent kinetic energy and the dissipation rate are solved. Three different LRN turbulence models are discussed and numerically implemented in the present work: Jones-Launder (JL), Launder-Sharma (LS) and Abe-Kondoh-Nagano (AKN). The velocity-pressure coupling of the incompressible flow is resolved by the explicit Chorin's fractional step method, with the intermediate velocity field, calculated without the pressure term. The transport equations for the energy, the turbulent kinetic energy, and the dissipation rate are solved decoupled from the velocity-pressure algorithm. The governing equations are discretized in their strong formulation. Due to the convection dominated problem, an adaptive upwind technique is used for approximating the convection terms in the transport equations. Various numerical examples are performed in order to validate the developed numerical method. An adaptive upwind technique is tested on a one-dimensional convective-diffusive problem. The natural convection in a square cavity, at Rayleigh numbers 10^6-10^8 and Prandtl (Pr) number 0.71, is used for benchmarking a fully coupled problem of the heat and fluid flow and for testing a velocity-pressure coupling of the fractional step method. A backward-facing step problem is chosen to test the proper implementation of the inflow and outflow boundary conditions, at Reynolds (Re) numbers 300-800 (based on the channel height after the step). The results are also obtained with random node arrangement. The implementation of the LRN turbulence models is tested on a 2D channel flow at $\mathrm{Re}=7890$, $\mathrm{Re}=12300$, and $\mathrm{Re}=30800$ (based on the channel half-height). Due to the similarity of the JL and LS models, only the LS and AKN models are used in further numerical examples. These include the numerical examples considering the turbulent fluid flow in a 2D channel flow at $\mathrm{Re} = 4560$ (based on the channel height) with uncoupled heat transfer at $\mathrm{Pr} = 0.71$, a 2D vertical channel flow at $\mathrm{Re} = 4494$ (based on the channel width), Grashof number $9.6 \cdot 10^5$ and $\mathrm{Pr} = 0.71$ with combined forced and natural convection, and turbulent flow over a backward-facing step at $\mathrm{Re} = 5000$ (based on the step height). In each example, the obtained results are validated and verified by the direct numerical simulation or by the experimental data. Some numerical examples are also simulated and compared with the commercial computational fluid dynamics software package Fluent. The numerical model of the continuous casting of steel is developed. The node arrangement of the real curved billet geometry is generated by the open-source software Gridpak. The initial and the boundary conditions for the velocity, temperature, and turbulence model variables are described in detail. The boundary conditions for the temperature field are assumed from the validated thermal simulation system of the Štore Steel billet continuous caster. The process parameters are assumed directly from the technological program. The material properties of the steel grades are calculated by the JMatPro software and imported into the present numerical model. The developed numerical model is verified with the numerical results, obtained with Fluent. For the verification purpose, the simplified thermo-physical properties of the steel and boundary conditions are used. After successful verification, simulation of the C45 steel grade for a square billet of dimension $0.14\,\mathrm{m}$ is performed at typical casting conditions. The sensitivity study of the morphology constant of a porous media is made. The effects of various process parameters on the velocity and the temperature field inside the billet are analyzed and compared with the reference case. The purpose of the analyses is to test the behaviour of the developed model on variation of process parameters. The developed numerical method is found to be applicable for simulating large spectra of laminar and turbulent fluid flow problems, and it is suitable for solving the solidification phenomena in the continuous casting of steel. The advantages of the novel numerical method are its simplicity, accuracy, similar code for 2D and three-dimensional problems, no integrations are needed, and straightforward applicability in non-uniform node arrangements. Due to its locality and explicit time stepping, the method appears very suitable for parallelization.

Key words

laminar flow, turbulent flow, natural and forced convection, solidification, steel, continuous casting, mixture continuum model, eddy-viscosity models, two-equation turbulence models, local radial basis function collocation method, multiquadrics, explicit time discretization, adaptive upwind scheme, fractional step method, verification and validation, simulation of the continuous casting of steel

Simulacija prenosa toplote in toka kapljevine pri kontinuirnem ulivanju jekla z brezmrežno metodo

Povzetek

V disertaciji je predstavljena nova dvo-dimenzionalno (2D) časovno neodvisna brezmrežna rešitev prenosa toplote in turbulentnega toka kapljevine pri procesu kontinuirnega ulivanja jekla. Brezmrežna metoda temelji na lokalni kolokaciji z mulitkvadričnimi radialnimi baznimi funkcijami. Lokalna kolokacija je izvedena preko prekrivajočih se pod-domen, zgrajenih s petimi točkami. Enačbe za ohranitev mase, gibalne količne in energije za binarni fazno-spremenljivi material so izpeljane na podlagi Bennon in Incroperovega modela kontinumske mešanice. Strjevanje v kašastem področju je obravnavano kot porozni medij, modeliran z Darcyjevim zakonom. Permeabilnost poroznega medija je izračunana z Kozeny-Karmanovo relacijo, pri katerem je morfologija poroznega medija modelirana s konstantno vrednostjo. Turbuletni tok nestisljivega tekočega jekla je opisan z Low-Reynolds-Number (LRN) k-ε turbulentnim modelom, pri katerem sta rešeni dodatni transportni enačbi za turbulentno kinetično energijo in disipacijo. V predstavljenem delu so obravnavani in numerično implementirani trije različni LRN turbulentni modeli: Jones-Launder (JL), Launder-Sharma (LS) in Abe-Kondoh-Nagano (AKN). Hitrostno-tlačna sklopitev nestisljivega toka je rešena z eksplicitno Chorinovo metodo delnih korakov, kjer je vmesna hitrost izračunana brez tlačnega člena. Transportne enačbe za energijo, turbuletno kinetično energijo in disipacijo so rešene ločeno od hitrostno-tlačnega algoritma. Vodilne enačbe so diskretizirane v močni formulaciji. Zaradi konvekcijsko dominatnega problema so konvekcijski členi v transportnih enačbah aproksimirani s pomočjo adaptivne privetrne tehnike. Validacija razvite numerične metode je izvedena na nekaj numeričnih primerih. Adaptivna privetrna tehnika je testirana na eno-dimenzijskem konvekcijsko-difuzijskem problemu. Problem naravne konvekcije v kvadratni kotanji pri Rayleigh-ovih številih 10^6-10^8 in Prandtlovem (Pr) številu 0.71 je uporabljen za testiranje popolnoma sklopljenega problema prenosa toplote in gibalne količine, in za testiranje hitrostno-tlačne sklopitve pri metodi delnih korakov. Problem toka fluida preko stopnice pri Reynolds-ovih (Re) številih 300-800 (glede na višino kanala za stopnico) je izbran za testiranje pravilne implementacije vtočnih in iztočnih robnih pogojev. Rezultati so prav tako izvedeni pri naključni postavitvi točk. Implementacija LRN turbuletnih modelov je testirana na primeru toka v 2D kanalu pri $\mathrm{Re}=7890$, $\mathrm{Re}=12300$ in $\mathrm{Re}=30800$ (glede na polovico višine kanala). Zaradi podobnosti JL in LS modelov, sta v nadaljnih primerih uporabljena samo LS in AKN modela. Izvedeni so sledeči numerični primeri z upoštevanim turbuletnim tokom fluida:

tok v 2D kanalu pri $\mathrm{Re} = 4560$ (glede na višino kanala) s prenosom toplote, kjer je temperatura upoštevana kot pasivni skalar pri $\mathrm{Pr} = 0.71$, tok v vertikalnem 2D kanalu pri $\mathrm{Re} = 4494$ (glede na širino kanala), Grashof-ovem številu $9.6 \cdot 10^5$ in $\mathrm{Pr} = 0.71$ s sklopljeno prisilno in naravno konvekcijo, in turbuletni tok preko stopnice pri $\mathrm{Re} = 5000$ (glede na višino stopnice). V vsakem od naštetih problemov so rezultati verificirani in validirani s podatki iz direktne numerične simulacije ali z eksperimentalnimi podatki. Nekateri izmed naštetih primerov so prav tako simulirani in primerjani s programskim paketom za računalniško dinamiko fluidov Fluent. Razvit je numerični model kontinuiranega ulivanja jekla. Razvrstitev točk realne zvite geometrije gredice je generirana z odprto-kodnim programom Gridpak. Podrobno so opisani začetni in robni pogoji za hitrost, temperaturo in spremenljivke turbuletnega modela. Robni pogoji za temperaturno polje so privzeti iz preverjenega termičnega simulacijskega sistema za kontilivno napravo gredic podjetja Štore Steel. Procesni parametri so neposredno privzeti direktno iz tehnološkega programa. Snovne lasnosti jekel so izračunane s programom JmatPro, in vnesene v razviti numerični model. Numerični model je verificiran z numeričnimi rezultati, dobljenimi s Fluent-om. Za namen verifikacije so uporabljene poenostavljene snovne lasnosti jekla in robni pogoji. Po uspešni verifikaciji je izvedena simulacija jekla C45 za gredico dimenzije $0.14\,\mathrm{m}$ pri tipičnih pogojih ulivanja. Opravljena je občutljivostna študija morfološke konstante poroznega medija. Opravljena je analiza vpliva različnih procesnih parametrov na hitrostno in temperaturno polje v gredici glede na referenčni primer. Namen analize je testirati obnašanje razvitega modela na spremembe procesnih parametrov. Razviti numerični model je uporaben za simulacijo širokega spektra problemov z laminarnim in turbuletnim tokom tekočin in je primeren za reševanje problemov strjevanja pri procesu kontinuirnega ulivanja jekla. Prednosti nove numerične metode so njena enostavnost, natančnost, podobna programska koda za 2D in tri-dimenzionalne probleme, vključenih ni nobenih integracij in enostavna implementacija za neuniformne postavitve točk. Zaradi njene lokalnosti in eksplicitnega časovnega koraka je zelo primerna za paralelizacijo.

Ključne besede

laminarni tok, turbuletni tok, naravna in prisilna konvekcija, strjevanje, jeklo, kontinuirano ulivanje, model kontinumske mešanice, vrtinčno-viskozni modeli, dvo-enačbni turbuletni modeli, lokalna kolokacijska metoda z radialnimi baznimi funkcijami, multikvadriki, eksplicitna časovna diskretizacija, adaptivna privetrna shema, metoda delnih korakov, verifikacija in validacija, simulacija kontinuirnega ulivanja jekla

Contents

List of Figures **v**

List of Tables **xi**

List of Symbols **xiii**

1 Introduction **1**

1.1 Continuous Casting of Steel 1
1.2 Literature Review on Numerical Modelling of the Continuous Casting of Steel 5
1.3 Meshless Numerical Methods 12
1.4 Objectives of the Dissertation 14

2 Physical Model **17**

2.1 Numerical Modelling of Turbulence 17
  2.1.1 Reynolds Time Averaging 20
  2.1.2 Standard k-ε Model 23
  2.1.3 Low-Reynolds-Number Models 26
2.2 Phase-Change Phenomena 30
2.3 Introduction to Modelling of the Solidification Processes 33
2.4 Treatment of Solidification Region from the Fluid Dynamics Perspective 35
2.5 Mixture Continuum Model 37
  2.5.1 Turbulence Modelling in Porous Media 39
  2.5.2 Mass Conservation 41
  2.5.3 Momentum Conservation 41
  2.5.4 Energy Conservation 42
  2.5.5 Transport Equations of the Turbulence Model 44
2.6 The Complete System of the Macroscopic Conservation Equations 45
2.7 Initial Conditions 46
2.8 Boundary Conditions 47

3 Local Radial Basis Function Collocation Method **49**

- 3.1 Radial Basis Functions 49
- 3.2 Radial Basis Function Collocation Method for Interpolating Scattered Data 52
- 3.3 Radial Basis Function Collocation Method (Kansa) for Solving PDEs 55
- 3.4 Local Collocation with RBFs 59
  - 3.4.1 Optimal Free Parameter 61
  - 3.4.2 Finding the Neighbours for Non-Uniform Node Arrangements 64
- 3.5 Solving PDEs with Local Collocation 66

4 Solution Procedure **69**

- 4.1 Time Discretization 69
- 4.2 Treatment of the General Transport Equation 70
- 4.3 Solution of the Incompressible Navier-Stokes Equation 74
- 4.4 Step-by-step Description of the Solution Procedure 75
- 4.5 Boundary Conditions for Pressure 78
- 4.6 Adaptive Upwind Technique 79

5 Numerical Examples **81**

- 5.1 Numerical Implementation 81
- 5.2 Refinement Near the Walls 82
- 5.3 One-dimensional Convective-Diffusive Phase-Change Problem 84
  - 5.3.1 Problem Description 84
  - 5.3.2 Numerical Results 85
- 5.4 Laminar Flow Problems 90
  - 5.4.1 Natural Convection in a Square Cavity 90
    - 5.4.1.1 Problem Description 90
    - 5.4.1.2 Numerical Results 90
  - 5.4.2 Backward-Facing Step 96
    - 5.4.2.1 Problem Description 96
    - 5.4.2.2 Numerical Results 97
- 5.5 Turbulent Flow Problems 105
  - 5.5.1 Two-dimensional Channel Flow 105
    - 5.5.1.1 Problem Description 105
    - 5.5.1.2 Numerical Results at Re=7890 107
    - 5.5.1.3 Numerical Results at Re=12300 and Re=30800 111
  - 5.5.2 Heat Transfer as a Passive Scalar Field 114
    - 5.5.2.1 Problem Description 114
    - 5.5.2.2 Numerical Results 114

5.5.3 Combined Forced and Natural Convection in a 2D Channel Flow 117
5.5.3.1 Problem Description 117
5.5.3.2 Numerical Results 119
5.5.4 Backward Facing Step 126
5.5.4.1 Problem Description 126
5.5.4.2 Boundary Layer Simulation over a Flat Plate 127
5.5.4.3 Numerical Results 128

6 Simulation of the Continuous Casting of Steel 141

6.1 Model Characteristics and Assumptions 141
6.2 Geometry and Node Arrangement 142
6.3 JMatPro Thermo-Physical Properties 146
6.4 Initial Conditions 150
6.5 Boundary Conditions 150
6.6 Numerical Examples 157
6.6.1 Simplified Model and Comparison with Fluent 157
6.6.2 Simulation of the C45 Steel Grade 169
6.6.2.1 Sensitivity of the Darcy's Constant 177
6.6.2.2 Simulation at Different Casting Speed 180
6.6.2.3 Simulation at Different Casting Temperature 185
6.6.2.4 Simulation at Different SEN Depth 190

7 Summary and Conclusions 195

7.1 Summary of the Main Contributions 195
7.2 Technological Relevance 197
7.3 Conclusions and Future Work 198

Appendix A 203

A.1 Analytical Solution of the Convective-Diffusive Phase-Change Problem 203

Bibliography 205

List of Figures

1.1 Scheme of the continuous casting process. 2
1.2 Casting machine for continuous casting of billets in the Štore Steel company. 2
1.3 Physical phenomena in the mould. 4
1.4 Simulation system for temperature field in Štore Steel billet caster. 11
1.5 Input/output GUI programs of the simulation system. 12
1.6 The triangulation of the geometry in FEM and node arrangement in meshless methods. 14
2.1 Typical velocity profile for a turbulent boundary layer flow. 26
2.2 Binary phase-change diagram. 31
2.3 Solidification process in the strand. 37
2.4 Multiphase continuum. 39
3.1 Some of the most commonly used RBFs. 51
3.2 MQ-RBF with different values of the free parameter. 52
3.3 Block diagram of the polynomial interpolation in 1D. 54
3.4 Block diagram of the RBF interpolation in 1D. 55
3.5 Typical node arrangement for the meshless methods. 58
3.6 Node arrangement with typical influence domains. 60
3.7 Local influence domain with the maximum nodal distance. 63
3.8 Local influence domain scaled with the maximum nodal distances. 63
3.9 Non-optimal neighbours in a highly non-uniform node arrangement. 65
3.10 Optimal neighbours in a highly non-uniform node arrangement. 65
3.11 Rotated local coordinate system for $\pi / 4$. 65
4.1 Block diagram of the solution procedure. 78
4.2 The adaptive upwind support. 80
4.3 The upwind function. 80
5.1 Uniform node arrangement. 83
5.2 Normalised uniform node arrangement. 83
5.3 Normalized node arrangement, refined near the wall with $b = 1.75$ 83
5.4 Power function with various exponents. 84
5.5 The final node arrangement, refined near the wall with $b = 1.75$ 84

5.6 Discretization schematics for the quasi 1D convective diffusive problem. 85
5.7 Comparison of the calculated temperatures with the analytical solution in the central nodes at $p_y = 0\,\mathrm{m}$, $\mathrm{Pe} = 2$. 86
5.8 Comparison of the calculated temperatures with the analytical solution in the central nodes at $p_y = 0\,\mathrm{m}$, $\mathrm{Pe} = 10$. 87
5.9 Comparison of the calculated temperatures with the analytical solution in the central nodes at $p_y = 0\,\mathrm{m}$, $\mathrm{Pe} = 50$. 87
5.10 Comparison of the calculated temperatures with the analytical solution in the central nodes at $p_y = 0\,\mathrm{m}$, $\mathrm{Pe} = 100$ 88
5.11 Comparison of the calculated temperatures with the analytical solution in the central nodes at $p_y = 0\,\mathrm{m}$, $\mathrm{Pe} = 200$. 88
5.12 Comparison of the calculated temperatures with the analytical solution in the central nodes at $p_y = 0\,\mathrm{m}$, $\mathrm{Pe} = 500$. 89
5.13 Comparison of the calculated temperatures with the analytical solution in the central nodes at $p_y = 0\,\mathrm{m}$, $\mathrm{Pe} = 1000$ 89
5.14 Problem schematics of the natural convection in a square. 91
5.15 61×61 node arrangement, refined near the walls with $b = 1.2$ 91
5.16 Streamlines and temperature field with isotherms at $\mathrm{Ra} = 10^6$ by using 101×101 node arrangement. 92
5.17 Streamlines and temperature field with isotherms at $\mathrm{Ra} = 10^7$ by using 101×101 node arrangement. 93
5.18 Streamlines and temperature field with isotherms at $\mathrm{Ra} = 10^8$ by using 101×101 node arrangement. 94
5.19 Problem schematics of the backward-facing step. 98
5.20 Levels of the refinement with $b = 1.4$ 99
5.21 A detailed view of the 201×61 node arrangement. 99
5.22 Streamlines for $\mathrm{Re} = 300\text{-}800$ with step 100 by using 301×101 node arrangement. 100
5.23 Wall-shear stress at the lower and upper wall for $\mathrm{Re} = 800$ by using 301×101 node arrangement. 101
5.24 Horizontal velocity profiles across the channel for $\mathrm{Re} = 800$ by using 301×101 node arrangement. 101
5.25 Vertical velocity profiles across the channel for $\mathrm{Re} = 800$ by using 301×101 node arrangement. 102
5.26 Pressure profiles across the channel for $\mathrm{Re} = 800$ by using 301×101 node arrangement. 103
5.27 A detailed view of the 301×101 slightly random node arrangement. 105
5.28 Geometry of the 2D channel flow. 107
5.29 A selected detail of the 151×71 node arrangement. 108

5.30 Non-dimensional velocity profile at the outlet, obtained with the LS model and various node arrangements. 109
5.31 Non-dimensional velocity profile at the outlet, obtained with the JL model and 151×71 node arrangement. 109
5.32 Non-dimensional velocity profile at the outlet, obtained with the LS model and 151×71 node arrangement. 110
5.33 Non-dimensional velocity profile at the outlet, obtained with the AKN model and 151×71 node arrangement. 110
5.34 Non-dimensional kinetic energy profile at the outlet, obtained at the 151×71 node arrangement...111
5.35 Normalized velocity profile at $\mathrm{Re}=12300$ 112
5.36 Absolute difference of the calculated and measured velocity at $\mathrm{Re}=12300$. 112
5.37 Normalized velocity profile at $\mathrm{Re}=30800$ 113
5.38 Absolute difference of the calculated and measured velocity at $\mathrm{Re}=30800$. 113
5.39 Non-dimensional velocity profile obtained with 151×71 node arrangement..116
5.40 Non-dimensional temperature profile obtained with 151×71 node arrangement..116
5.41 Schematics of the mixed convection problem. 118
5.42 A detailed view of the 81×171 node arrangement................................119
5.43 Non-dimensional velocity profile of the aiding flow in wall coordinates. 122
5.44 Non-dimensional velocity profile of the opposing flow in wall coordinates. 122
5.45 Non-dimensional turbulent kinetic energy of the aiding flow in wall coordinates. 123
5.46 Non-dimensional turbulent kinetic energy of the opposing flow in wall coordinates. 123
5.47 Non-dimensional temperature profile of the aiding flow in wall coordinates. 124
5.48 Non-dimensional temperature profile of the opposing flow in wall coordinates. 124
5.49 Non-dimensional velocity profile at the outlet in wall coordinates. 125
5.50 Non-dimensional temperature profile at the outlet in wall coordinates. ..125
5.51 Schematics of the backward-facing step problem.................................126
5.52 Computational domain of the backward-facing step problem. 127
5.53 Schematics of the geometry used for the BLS. 128
5.54 Velocity profile at the inlet. 128

5.55 Node refinement schematics. 129
5.56 A detailed view of the 201×71 node arrangement. 130
5.57 Skin friction at the bottom wall obtained with three different node arrangements. 131
5.58 The normalized velocity u_x at $x/H = 4$. 133
5.59 The normalized velocity u_x at $x/H = 6$. 134
5.60 The normalized velocity u_x at $x/H = 10$ 135
5.61 The normalized velocity u_x at $x/H = 15$ 136
5.62 The normalized velocity u_x at $x/H = 19$ 137
5.63 The streamlines calculated with the LS and AKN model. 138
5.64 The skin friction at the bottom wall with AKN model. 138
5.65 The skin friction at the bottom wall with LS and JL models. 139
6.1 Considered geometry schematics of the continuous casting machine. 143
6.2 Geometry of the SEN with relevant dimensions. 144
6.3 Node arrangement in the mould and around the SEN. 145
6.4 A detailed view of the node arrangement at the end of the mould. 146
6.5 Thermal conductivity of the steel grade C45. 147
6.6 Enthalpy of the steel grade C45. 147
6.7 Liquid fraction of the steel grade C45. 148
6.8 Specific heat of the steel grade C45 obtained by the JMatPro. 149
6.9 Modified specific heat of the steel grade C45 used in the simulations. 149
6.10 Comparison of the measured and simulated temperature in the middle of the cast steel billet surfaces. 153
6.11 Boundary conditions for the velocity field. 153
6.12 Boundary conditions for the temperature field. 154
6.13 Velocity profile u_y at the SEN outlet. 154
6.14 Non-dimensional turbulent kinetic energy at the SEN outlet. 155
6.15 Non-dimensional dissipation rate at the SEN outlet. 155
6.16 Spray systems in the Štore Steel billet caster. 156
6.17 The heat flux at the surface. 156
6.18 Mesh generated with the Gambit. A detail in the mould. 160
6.19 Absolute velocity at the meniscus and in the radial cross-section at the arc length $0.2\,\mathrm{m}$. 161
6.20 Absolute velocity in the radial cross-section at the arc lengths $0.4\,\mathrm{m}$ and $0.6\,\mathrm{m}$. 161
6.21 Absolute velocity in the radial cross-section at the arc lengths $0.8\,\mathrm{m}$ and $1.0\,\mathrm{m}$. 162
6.22 Absolute velocity in the radial cross-section at the arc lengths $1.2\,\mathrm{m}$ and $1.4\,\mathrm{m}$. 162

6.23 Temperature profile at the meniscus and in the radial cross-section at the arc length 0.2 m. 163
6.24 Temperature profile in the radial cross-section at the arc lengths 0.4 m and 0.6 m. 163
6.25 Temperature profile in the radial cross-section at the arc lengths 0.8 m and 1.0 m. 164
6.26 Temperature profile in the radial cross-section at the arc lengths 1.2 m and 1.4 m. 164
6.27 Temperature of the surface along the billet. 165
6.28 Temperature of the surface along the billet with the present method for different billet lengths. 165
6.29 Absolute velocity field in the billet of length 1.8 m. 166
6.30 Absolute velocity field in the billet of lengths 1.8 m and 2.8 m. 167
6.31 Temperature field in the billet. 168
6.32 Absolute velocity field in the billet. 171
6.33 Absolute velocity field in the mould. 172
6.34 Streamlines in the mould. 173
6.35 Temperature field in the billet. 174
6.36 Temperature field in the mould. 175
6.37 Temperature along the surface of the billet. 176
6.38 Liquid fraction profile in the radial cross-section at the end of the mould. 176
6.39 Absolute velocity field in the mould as a function of the Darcy's constant. 178
6.40 Temperature field in the mould as a function of the Darcy's constant. 179
6.41 Surface temperature along the billet as a function of the Darcy's constant. 180
6.42 Absolute velocity field in the mould as a function of the casting speed. 181
6.43 Streamlines in the mould as a function of the casting speed. 182
6.44 Temperature field in the mould as a function of the casting speed. 183
6.45 Surface temperature along the billet as a function of the casting speed. 184
6.46 Liquid fraction profile in the radial cross-section at the end of the mould as a function of the casting speed. 184
6.47 Absolute velocity field in the mould as a function of the casting temperature. 186
6.48 Streamlines in the mould as a function of the casting temperature. 187
6.49 Temperature field in the mould as a function of the casting temperature. 188
6.50 Surface temperature along the billet as a function of the casting temperature. 189

6.51 Liquid fraction profile in the radial cross-section at the end of the mould as a function of the casting temperature. 189
6.52 Absolute velocity field in the mould as a function of the SEN depth...... 190
6.53 Streamlines in the mould as a function of the SEN depth. 191
6.54 Temperature field in the mould as a function of the SEN depth. 192
6.55 Surface temperature along the billet as a function of the SEN depth. 193
6.56 Liquid fraction profile in the radial cross-section at the end of the mould as a function of the SEN depth.. 193

List of Tables

2.1 Closure coefficients of the LRN turbulence models. 28
2.2 Source terms D and E of the LRN turbulence models........................... 28
2.3 Damping functions of the LRN turbulence models................................. 29
5.1 Sensitivity of the results with respect to Pe number at discretization 101×3. 86
5.2 Maximum mid-plane velocities and Nu_{avg} at $\mathrm{Ra}=10^6$........................... 95
5.3 Maximum mid-plane velocities and Nu_{avg} at $\mathrm{Ra}=10^7$........................... 95
5.4 Maximum mid-plane velocities and Nu_{avg} at $\mathrm{Ra}=10^8$........................... 96
5.5 Comparison of results at $\mathrm{Re}=800$. 102
5.6 Grid convergence and comparison at $\mathrm{Re}=600$. 103
5.7 Reattachment positions for various Re numbers by using 301×101 node arrangement. 104
5.8 Reattachment positions for the non-uniform and slightly random node arrangements at $\mathrm{Re}=600$. 104
5.9 Bulk Nusselt number at the outlet...117
5.10 Nusselt number Nu and skin friction C_f at the channel outlet.............121
5.11 Reattachment position. 132
5.12 The normalized velocity u_x at $x/H=4$...133
5.13 The normalized velocity u_x at $x/H=6$...134
5.14 The normalized velocity u_x at $x/H=10$. 135
5.15 The normalized velocity u_x at $x/H=15$. 136
5.16 The normalized velocity u_x at $x/H=19$. 137
6.1 The dimensions of the Štore Steel continuous casting machine. 144
6.2 Simplified material properties...157
6.3 Composition of the C45 steel grade. 170
6.4 Process parameters of the Štore Steel continuous casting machine. 170

List of Symbols

Latin symbols

a_b	billet dimension
A_{lw}	constant
b	refinement level
B_{lw}	dimensionless constant
B_f	buoyancy force term
c	multiquadric free parameter
c_A	solute concentration of species A
c_p	specific heat at constant pressure
$c_{p\wp}$	specific heat at constant pressure of phase $\wp$
c_μ	closure coefficient in μ_t equation
$c_{1\varepsilon}, c_{2\varepsilon}, c_{3\varepsilon}$	closure coefficients in ε equation
c_{rnd}	random number
C	morphology constant of the porous media
d	Euclidian distance
d_1	outer diameter of the SEN
d_2	inner diameter of the SEN
D	source term in k equation
D_S	diffusion coefficient of solute atoms
$\mathbf{D}$	diffusion tensor
E	source term in ε equation
f	function value
$\mathbf{f}$	column vector of solutions
f_1, f_2	damping functions in ε equation
f_μ	damping function in μ_t equation
$f_\wp$	fraction of phase $\wp$
F	function
F_p	Darcy source term (phase interaction force)
F_{pk}	damping source term in k equation
$F_{p\varepsilon}$	damping source term in ε equation
g	gravitational acceleration
G_k	generation of turbulence due to the buoyancy force

Gr	Grashof number
H	height
h	enthalpy
$\bar{h}$	mean part of the enthalpy
h_m	melting enthalpy
$\mathbf{i}_x, \mathbf{i}_y$	base vectors of the x-y coordinate system
$\mathbf{J}_\wp$	surface flux vector of phase $\wp$
k	turbulent kinetic energy
k_{LS}	coefficient in the solidification models
K	permeability
${}_lK$	number of the shape functions in influence domain l
ℓ	characteristic length
L	length
L_{depth}	submerging depth of the SEN
L_{level}	steel level depth
L_m	length of the mould
L_s	length of the secondary cooling system
$m_\wp$	slope of a line of phase $\wp$
$\dot{M}_\wp$	mass production of phase $\wp$
$\mathbf{n}$	normal vector
N	number of points
$N_\wp$	number of phases
Nu	Nusselt number
Nu_{avg}	average Nusselt number
p_{SEN}	position of the SEN
$\mathbf{p}$	position vector of point p
P	pressure
$\bar{P}$	mean part of the pressure
P_k	production term
Pe	Péclet number
r	radial distance between two points
r_0	maximum nodal distance in the influence domain
R	outer radius of the casting machine
Re	Reynolds number
Re_t	turbulent Reynolds number
Re_{tl}	local turbulent Reynolds number
S_ϕ	source term in the transport equation
$\bar{S}_\phi$	mean part of the source term
$\mathbf{S}$	strain-rate tensor
$\bar{\mathbf{S}}$	mean part of the strain-rate tensor

t	time
t_f	local solidification time
T	temperature
$\bar{T}$	mean part of the temperature
T_m	melting temperature
T_{ref}	reference temperature
$T_\wp$	temperature of phase $\wp$
$\mathbf{u}$	velocity
$\mathbf{u}_r$	relative velocity
$\tilde{\mathbf{u}}$	intermediate velocity
$\bar{\mathbf{u}}$	mean part of the velocity
$\mathbf{u}'$	fluctuating part of the velocity
$\bar{u}_\tau$	friction velocity
$\bar{u}_\varepsilon$	Kolmogorov velocity scale
y	normal distance from the wall
V	volume
W	width

Greek symbols

α_i	RBF expansion coefficient
α_t	Brody-Flemings constant
$\boldsymbol{\alpha}$	column vector of variables
β_T	thermal expansion coefficient
δ	Kronecker delta function
δ_b	boundary layer width
δ_{up}	upwind function
$\boldsymbol{\Delta}$	Kronecker delta tensor
ε	dissipation rate
$\tilde{\varepsilon}$	modified dissipation rate
ϕ	transport variable
$\bar{\phi}$	mean part of the transport variable
ϕ'	fluctuating part of the transport variable
Γ	boundary
Γ_t	turbulent diffusivity
φ	velocity potential
κ	von Kármán constant
λ	thermal conductivity
λ_{eff}	effective thermal conductivity
λ_a	dendrite arm spacing

μ	dynamic viscosity
μ_t	turbulent dynamic viscosity
$\mu_{t\wp}$	turbulent dynamic viscosity of phase $\wp$
ν	kinematic viscosity
ν_t	turbulent kinematic viscosity
ρ	density
σ_t	turbulent Prandtl number
σ_k	turbulent Prandtl number for k
σ_ε	turbulent Prandtl number for ε
$\bar{\rho}_\wp$	partial density of phase $\wp$
$\boldsymbol{\tau}_R$	Reynolds stress tensor
τ_w	wall shear stress
Υ	indicator
ω	specific dissipation rate
${}_l\omega$	influence domain l
Ω	domain
ψ_i	radial basis function
$\boldsymbol{\Psi}$	collocation matrix

Subscripts

ana	analytical solution
b	bulk value
i, j, k	counters
l	influence domain
L	liquidus
max	maximum value
min	minimum value
S	solidus
x, y, z	coordinates of the x-y-z coordinate system
$\wp$	phase, $\wp = S, L$

Superscripts

+	non-dimensional variable normalized by the wall variables
*	non-dimensional variable normalized by the u^*
D	Dirichlet boundary conditions
N	Neumann boundary conditions
R	Robin boundary conditions
T	transposed

V	volumetric

Acronyms

1D	One-dimensional
2D	Two-dimensional
3D	Three-dimensional
AKN	Abe-Kondoh-Nagano
BEM	Boundary Element Method
CFD	Computational Fluid Dynamics
CVF	Compaq Visual Fortran
DNS	Direct Numerical Simulation
EMB	Electromagnetic Brake
EVM	Eddy Viscosity Model
FDM	Finite Difference Method
FEM	Finite Element Method
FPM	Finite Point Method
FVM	Finite Volume Method
GA	Gaussian
GUI	Graphical User Interface
IMQ	Inverse Multiquadric
JL	Jones-Launder
LES	Large Eddy Simulation
LRBFCM	Local Radial Basis Function Collocation Method
LRN	Low-Reynolds-Number
LS	Launder-Sharma
MQ	Multiquadric
N-S	Navier-Stokes
PDE	Partial Differential Equation
PIV	Particle Image Velocity
RANS	Reynolds-Averaged Navier-Stokes
RBF	Radial Basis Function
RBFCM	Radial Basis Function Collocation Method
SEN	Submerged Entry Nozzle
SGS	Sub-Grid Scale
TPS	Thin Plate Spline
WLS	Weighted Least Squares

1 Introduction

1.1 Continuous Casting of Steel

Continuous casting [Irwing, 1993] is currently the most common process for production of steel. In the year 2008, the total world production of the crude steel was 1351.289 million tons, where 1243.191 million tons were produced by the continuous casting process [World Steel Committee on Economic Studies, 2009]. Approximately 90 % of all steel grades are produced by this technique. The process is represented in Figure 1.1. The basic principle of the process is based on pouring the liquid steel vertically into a water cooled copper mould which is open at the bottom. Liquid steel solidifies immediately and a solid shell is formed. When the solidified shell is sufficiently thick to contain the molten core at the centre, the strand leaves the mould into the secondary cooling system. The secondary cooling system is composed of the spray cooling systems and rolls. The cooling spray systems further cool the strand surface in order to prevent the re-melting of the solidified shell. Rolls support the steel to minimize bulging due to the ferrostatic pressure, and lead the strand through the casting machine. When the strand is completely solidified, it is cut into required length segments. The cross-section of the strand can be of various shapes: billets, blooms and slabs. Billets are defined as a small square or round cross-sections, blooms are defined as rectangular cross-sections usually with an aspect ratio less than 2, while slabs are anything larger than blooms and usually with an aspect ratio greater than 2. The Figure 1.2 represents the casting machine in Štore Steel company (“http://www.store-steel.si/”) for casting of square billets.

The most important component of the casting machine is the mould, shown in Figure 1.3, where many complex physical phenomena occur. The molten steel is poured with high velocity ($\approx$ 0.3-0.7 m/s) through the Submerged Entry Nozzle (SEN) into the mould. The high velocities in the SEN produce the turbulent fluid flow in the SEN and later in the mould. The turbulent jet, that carries the superheat, flows across the mould and impinges against the solidifying shell. It further separates the flow upward to the top of the free surface and downwards towards the interior of the mould. Several re-circulating zones occur in the mould region, which influence the entrapment of the top surface flux layer of the powder and the motion of the inclusion particles.

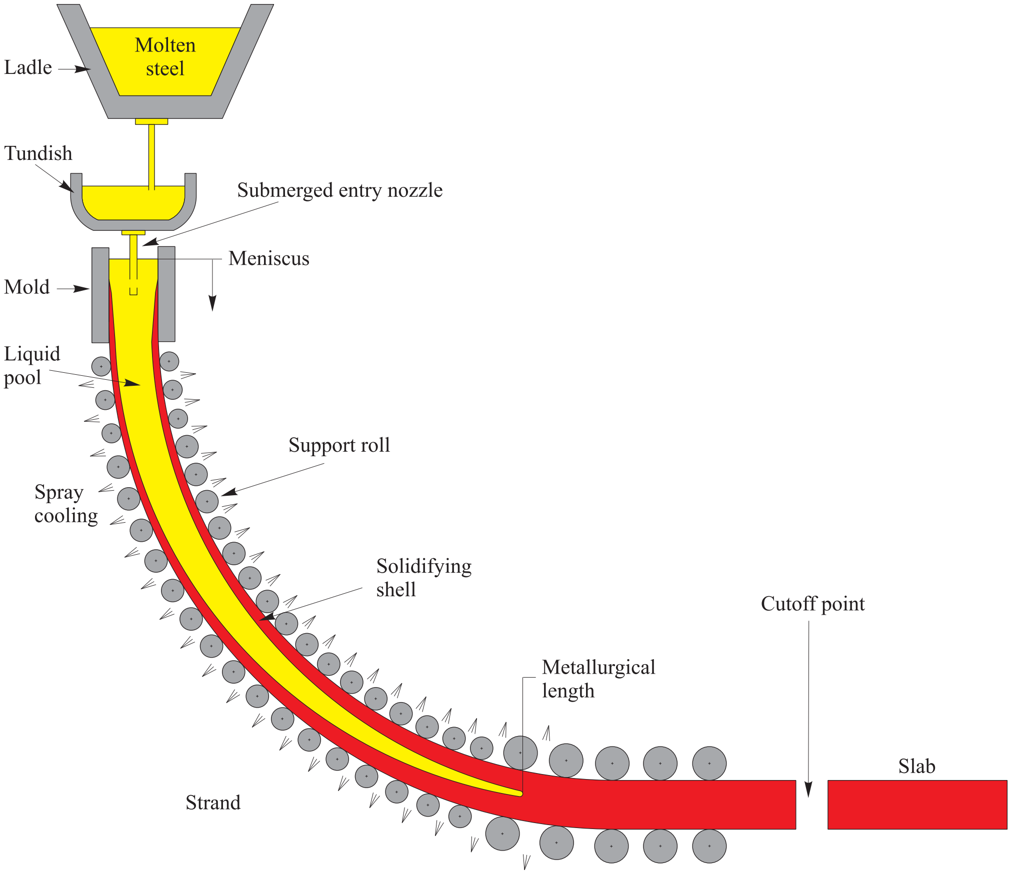

Figure 1.1: Scheme of the continuous casting process.

Figure 1.2: Casting machine for continuous casting of billets in the Štore Steel company.

The mould powder is added on the top surface of the molten steel to prevent heat transfer and chemical reactions between the steel and the surroundings. Due to the high temperatures of the molten steel, the powder melts and forms the surface flux layer, which floats on the top surface of the molten steel. Some liquid flux re-solidifies into a solid flux rim, which prevents the heat transfer at the meniscus. The remaining flux is consumed into the gap between the mould and the solidified strand, which prevents sticking and tries to establish the uniform heat transfer. The important parameters regarding the surface flux layer are the horizontal velocity of the molten steel at the top surface and amount of the powder, which is added on the top surface. If the horizontal velocity is too large, the shear flow and possible vortices can entrain the liquid flux into the steel. The entrapped flux layer than moves with the molten steel in the mould, and can latter be entrapped into the solidified shell, and further produces internal defects of the final product. Also, an improper amount of the mould powder can lead to non-uniform initial solidification and produce various surface defects. Inclusion particles, exiting the SEN, can be described as impurities of the molten steel, having various shape and size. They move with the fluid flow up towards the surface flux layer, or they are entrapped in the solidifying shell. If they are entrapped into the shell, the internal defects can be generated in the final product.

The mould is periodically oscillating to prevent sticking of the solidified strand and the mould. But, the oscillation produces the so called oscillation marks, which affect the heat transfer and produce inclination to surface cracks.

One of the major reasons of internal defects is macrosegregation of solute elements. Macrosegregation refers to variations in composition during the solidification and range in scale from several millimetres to centimetres or even meters. Segregation occurs in the mushy zone due to the difference in solute solubility between the solid and the liquid phase. Normally, the alloying elements have a lower solubility in the solid than in the liquid phase. During solidification, the solutes are therefore rejected into the liquid phase, leading to a continual enrichment of the liquid and lower solute concentrations in the solid. This phenomenon takes place on the scale of the dendrite arms is therefore termed microsegregation. Consider now a small volume element that contains several dendrite arms and the interdendritic liquid between them. The solute-rich liquid or the movement of the solute-poor solid in or out of the volume element changes the average composition of the volume element away from the nominal composition. Since the solute can be advected over large distances, macrosegregation occurs. The described compositional variations in the cast structure result in non-uniformity of mechanical properties of products, which lower the quality of the product.

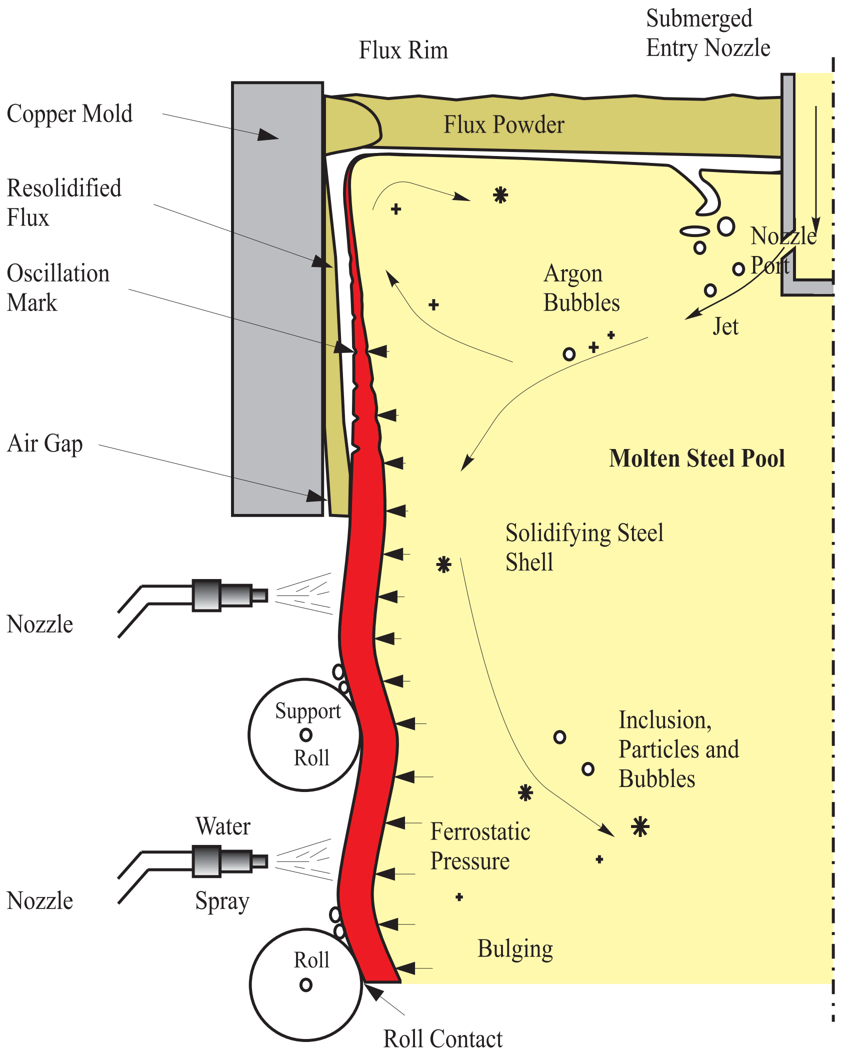

Figure 1.3: Physical phenomena in the mould.

In order to prevent these briefly overviewed defects and to improve the quality of the metal produced, the casting process has to be optimally controlled through the process parameters, such as the casting speed, casting temperature, the SEN depth, spray water flow, etc. Optimal control can be achieved by fully understanding the turbulent fluid flow and other processes inside the mould. The turbulent flow processes are greatly influenced by the geometry (nozzle shape, number of nozzles, etc.) of the SEN, and also its position inside the mould. The analysis of the influence of the process parameters and the geometry parameters of the SEN on the casting process can very hardly or almost impossible be achieved by the measurements inside the mould during the casting process. This fact is due to the very high temperature of the liquid steel and inaccessibility of the interior of the process. An alternative way is to perform measurements in the laboratories via the scaled (usually 1:3) or 1:1 water models [Yuan *et al.*, 2004], where the same geometry of the mould and SEN is used as in the real casting process. These measurements are very expensive especially if we want to change the geometry of the mould or the SEN, and also the solidification effects can not be considered. Beside the experiments, we can use the numerical models, which are these days very popular due to the increasing power of the personal computers and model complexity. There are several advantages of using the numerical models over the experiments: various physical phenomena can be considered at the same time (coupled mass, momentum, energy and turbulent transport processes together with solidification), the changes in the geometry of the casting machine, the steel grade, the process parameters governing the numerical model, the real thermo-physical material properties, etc. can be included.

1.2 Literature Review on Numerical Modelling of the Continuous Casting of Steel

Soon after the first computers arrived, the researchers and the scientists are trying to numerically solve many kinds of physical phenomena in nature and industry. The involved physical processes are prescribed by one or several Partial Differential Equations (PDEs), which are usually non-linear, time dependent, and fully coupled. To numerically evaluate these PDEs, several conventional numerical methods can be used. The Finite Difference Method (FDM) [Özisik, 1994], the Finite Volume Method (FVM) [Versteeg and Malalasekera, 1995], the Finite Element Method (FEM) [Zienkiewicz and Taylor, 2000], and the Boundary Element Method (BEM) [Wrobel, 2001] are the most widely used among them at the present. In the framework of modelling the heat and fluid flow of the continuous casting processes, the FVM is the dominant choice, and still today represents an integral part of the most commercial Computational Fluid Dynamics (CFD) software packages. The numerical models of the continuous casting process can be classified into the following three groups: thermal models, fluid models, and thermo-fluid models.

The thermal models involve only one PDE equation, which describes the heat transfer with solidification. From the numerical point of view, they are very easy to implement, since the velocity is predefined and constant for all phases, i.e. the solid and the liquid phase. If the heat diffusion in the casting direction is neglected, the model can be further simplified into the slice-model, where only the transversal cross-section of the strand (slice) is considered for the computational geometry [Thomas and Storkman, 1988; Thomas *et al.*, 1990; Constales *et al.*, 2002; Gonzalez *et al.*, 2003; Louhenkilpi, 2003; Šarler *et al.*, 2005; Wang *et al.*, 2005; Wang *et al.*, 2007; Zhang *et al.*, 2007]. Transient heat conduction equation is solved by moving the slice from the meniscus to the cutting zone (end of the computational domain) by the prescribed velocity. This technique reduces the computational time significantly and enables to calculate the temperature field up to the cutting zone of the casting machine. The important parameters, such as the shell thickness along the casting direction, the metallurgical length and the temperature of the strand surface before the straightening can be calculated with the satisfactory accuracy. Thomas and co-workers [Thomas *et al.*, 1987] developed slice model with the FEM to predict the temperature field and stress generation in the slab, where only one-quarter of the slice was considered. They calculated the temperature field, air gap formation and the slab shape distortion at various times and as a function of the mould taper amount for AISI 304 stainless steel. In [Thomas *et al.*, 1990], Thomas and co-workers use the same model to optimize the mould taper by calculating the heat flow, shrinkage, and stress generation in the solidifying steel shell. They concluded that the linear taper appears to be a reasonable choice. Constales and co-workers [Constales *et al.*, 2002] developed an inverse numerical model to determine the optimal cooling parameters in the primary and secondary cooling systems under changing the casting speed. Gonzalez with co-workers [Gonzalez *et al.*, 2003] developed computational simulation model with the FEM. The system couples two modules: one for solving the temperature field in the slab and the inverse model for predicting the heat flux between the solidified steel and the mould. The heat flux was obtained by providing the measured temperatures of the thermo-couples installed in the mould plates. An industrial case was also presented. Louhenkilpi [Louhenkilpi, 2003] presents various heat transfer models developed at the Helsinki University of Technology. One of them is called TEMPSIMU-2D, which is a slice model developed by the FVM and implicit time-discretization. Šarler and co-workers [Šarler *et al.*, 2005] have developed a complete simulation system for the billet and slab casting machine, which involves the numerical solver, program for graphic representation of the results (see Figure 1.4), and GUI (Graphical User Interface) programs [Vertnik and Šarler, 2002; Šarler *et al.*, 2005] for easy manipulation of all involved programs (see Figure 1.5). The system is integrated into a real casting facility, and enables an on-line communication between the casting process and the simulation system. They also have developed a real-time program for calculating the metallurgical length, surface temperature at the straightening position, and shell thickness at the end of the mould. Wang and co-workers [Wang *et al.*, 2005] developed a similar model to analyse the temperature field as a function of the main operating parameters including the casting speed, secondary cooling conditions, slab size and steel melt superheat. Zhang and co-workers [Zhang *et al.*, 2007] have used the meshless method, called Finite Point Method (FPM) to calculate the temperature field inside the square billet, where only one symmetric quarter of the billet was considered. The numerical model was verified by the FEM. The growth of the shell-thickness was compared by the measurement data, where very good agreement was found. Another possibility represents the use of a 2D geometry and considers the longitudinal cross-section of the strand [Hardin *et al.*, 2003; Vertnik and Šarler, 2009]. This approach is more suitable for the slab casting, where the ratio between the width and the thickness of the slab is large enough to neglect the heat transfer in the third dimension. This approach needs larger amount of the computer memory and computational time compared to the slice-model. However, the time-dependent solution can be obtained and the process parameters can be included as a function of the casting time. Hardin and co-workers [Hardin *et al.*, 2003] have calculated the two-dimensional heat transfer in the slab by the DYSCOS program, which uses the FVM and implicit time-discretization. For the initial conditions, the model assumes that the caster is in operation under the steady-state conditions, and the slab is present throughout the machine. The numerical results were compared by the measured slab surface temperatures. Vertnik and Šarler [Vertnik and Šarler, 2009] have developed the meshless numerical method based on the local collocation with the radial basis functions (RBFs) to calculate the temperature field inside the square billet. The numerical method is also discussed and used in the present dissertation. The numerical model also considers the growth of the computational domain from the meniscus to the cutting zone of the caster. The results were compared by Fluent at different values of the simulation time. Due to the increasing power of computers, the researchers start to develop three-dimensional (3D) thermo models [Heibi *et al.*, 2006; Louhenkilpi, 2006; Batraeva *et al.*, 2007; Xie *et al.*, 2008]. Heibi and co-workers [Heibi *et al.*, 2006] developed a 3D inverse model to obtain the real thermal behaviour of the mould characteristics in plant production, including the mould heat transfer, the steel solidification, and the slag film distribution, with the objective of understanding the relationship among them. Only the mould was taken into account for the computational geometry. Louhenkilpi [Louhenkilpi, 2006] presented two 3D models: TEMPSIMU-3D for steady-state simulations and DYN for transient simulations. Models are based on FDM, where the upwind scheme was used for convective term and a seven point FDM stencil for the rest of the terms. The IDS software package, developed at the Helsinki University of Technology, was used to include the temperature dependent thermo-physical properties of steel. The IDS and TEMPSIMU packages were coupled together to predict the microstructure evolution in the slab. Batraeva and co-workers [Batraeva *et al.,* 2007] developed a transient numerical model based on an explicit FDM. For the initial condition, the calculated temperature field from the steady-state simulation was used. The model was used for optimization and regulation of the flow rate in the sections of the secondary cooling zone. Xie with co-workers [Xie *et al.*, 2008] also developed a transient model for calculating the temperature field in the mould. They analyzed temperature variation with the consideration of different mould wall thickness and cooling water rates. The model is based on the FEM, developed in the programming language FORTRAN. The experimental data have been used to validate the model.

The fluid models involve the modelling of the turbulent fluid flow on a fixed geometry. Turbulent effects must be included, due to the large melt velocity in the SEN and relatively small dynamic viscosity of the molten steel. Modelling of the turbulent flow problems involves solving additional transport equations, which depend on the turbulence model selected. In engineering practice, the turbulent models based on the eddy-viscosity approach are found to be the most appropriate. The two equation k-ε model is the representative one when modelling the fluid flow of the continuous casting processes. Kubo and co-workers [Kubo *et al.*, 2004] used the numerical simulation of fluid flow under a magnetic field to track the argon gas bubbles in the mould and evaluate the surface velocity at the location between the powder and the molten steel. They use the standard k-ε turbulence model. The computational geometry was assumed to be 2D. Pfeiler and Ludwig [Pfeiler and Ludwig, 2005] used an Eulerian-Lagrangian approach to model 3D turbulent flow with the standard k-ε turbulence model to track the non-metallic inclusions and gas bubbles in continuous casting process. It is a two-phase model, where the melt flow is solved in an Eulerian framework, while the trajectories of the inclusions are tracked in the Lagrangian framework. They performed one-way and two-way coupling between the continuous and dispersed phase. The two-way coupling, which means that the influence of the melt flow on the movement of the inclusions and back influence are considered, was found to be preferable for a proper prediction of the inclusion trajectories. Yuan and co-workers [Yuan *et al.*, 2001] developed two Large Eddy Simulation (LES) models and use CFX computer software (Version 4.2) with a standard k-ε turbulence model for calculating the transient fluid flow inside the mould. The results were compared with the Particle Image Velocity (PIV) measurements, where it was found, that the standard k-ε model is not suitable for predicting the transient flow phenomena. They also perform particle transport simulations to study the distribution of inclusion particles, and the multiphase simulation to study the argon bubbles distribution inside the mould. Comparison of the four different methods to evaluate the fluid velocities in a mould was performed by [Thomas *et al.*, 2001]: the PIV measurements, the standard k-ε model, Direct Numerical Simulation (DNS) with 1.5-milion nodes, and the LES. The PIV measurements were obtained in a water-model with a single-phase to get the time-averaged and transient fluid flow patterns. The same problem was then simulated by the numerical methods. The time-averaged results of all three numerical methods gave very good agreement with the PIV measurements. The transient simulations were not performed very well with the standard k-ε model. The LES model was found to be the most appropriate for simulating transient effects in the mould, but it has to be performed in 3D and it is time-consuming compared to the k-ε model. The paper [Thomas *et al.*, 2001] also incorporated the measurements with the electromagnetic sensors embedded in the mould walls in the plant. The measurements were compared with the time-averaged results of the numerical methods, where a remarkable agreement was found.

The thermo-fluid models involve the solution of the fluid flow with the heat transfer and solidification. Because of the strong coupling between mass, momentum and energy equations, they are much more complex to implement than the thermo- and fluid-models. As regarding the physical models of the binary solid-liquid solidification, a single-phase model was found to be the most representative one. The main reason should be the relatively simple implementation, where each PDE equation is valid in all phases, i.e. solid, liquid and mushy. The fluid flow in the mushy region is usually treated as the porous media, modelled by the Darcy's law, which is a function of the permeability of the porous media. The permeability is calculated by the Kozeny-Carman equation, which is a function of the liquid fraction. Almost all thermo-fluid models, which will be reviewed here, are based on above mentioned assumptions. Those assumptions will not be repeated for each reviewed work, unless stated otherwise. Seyedein and Hasan [Seyedein and Hasan, 1997] developed a 3D numerical model of coupled turbulent flow, heat transfer, and solidification in a continuous slab caster. The LRN-LS turbulence model was used. The governing equations were solved using the FVM on a staggered grid. The effects of the casting speed, superheat of the melt and the immersion depth of the SEN on the velocity and temperature distributions were reported and discussed. Kim and co-workers [Kim *et al.*, 2000] developed a model for analyzing the 3D, steady conservation equations for transport phenomena in a slab caster with electromagnetic brake (EMB) to investigate the effects of EMB on the turbulent melt-flow, temperature fields, and macroscopic solidification of the molten steel. Ha and co-workers [Ha *et al.*, 2003] described a 3D model with involved Maxwell equation to consider the effects of the magnetic field on the turbulent flow field, heat transfer and solidification. They used standard k-ε model. Lan and Khodadadi [Lan and Khodadadi, 2001] developed a 2D transient numerical model for round billets in order to investigate the velocity and temperature fields in the mould during the ladle change. Lam and Bremhorst [Lam and Bremhorst, 1981] LRN turbulence model was used, where the Neumann boundary conditions for the dissipation rate were set at the surface of the billet. They found out that the size of the mushy zone and the shell thickness does not vary during the period of the ladle change. While the volume occupied by the liquid phase expands in the radial direction and its axial extent shrinks during the early stage of the ladle change. Later, those effects were reversed. Also, the surface temperatures vary over the two cycles of the ladle change operation. A fully coupled analysis of fluid flow, heat transfer and stress in a round billet casting was performed by Lee *et al.* [Lee *et al.*, 1999]. The FVM was used to analyse the fluid flow and the heat transfer, while the stress analysis were performed by the FEM. Also, the stress analysis of the mould was included to analyze the deformation of the mould with a mould taper. The velocity-pressure coupling was treated by the SIMPLER algorithm, while the turbulent flow was modelled by the standard k-ε model. The air gap between the mould and the billet was calculated as a function of the solidification shrinkage and thermal contraction of the solidifying shell. They predicted the cracks in the billet based on the calculated yield strength of steel and the crack susceptibility. Further, they analyzed the effects of the casting speed on the velocity and temperature field in the billet. A numerical algorithm, based on the FEM and the enthalpy formulation, was developed by [Wiwatanapataphee *et al.*, 2004]. The turbulent flow was considered by the LS-LRN k-ε model, which was modified to account for the solidification effects in the mushy zone. The developed numerical method was found to be stable and capable of capturing the rapid changes of temperature and velocity near the phase-change boundary. Yang *et al.* [Yang *et al.*, 1998] represent a 3D slab casting model with included governing equation for solute transport. The FVM with the SIMPLER velocity-pressure coupling algorithm were used for solving the system of the governing equations. They represented the temperature and the velocity fields in a slab, and the shell thickness along the mould. The results were also compared with the experimental data, where a very good agreement was found. The profiles of the carbon segregation were given as a function of double diffusive convection and the solidifying process. Aboutalebi and co-workers [Aboutalebi *et al.*, 1995] derived the governing conservation equations on the basis of a continuum mixture model for binary alloys, originally developed by Bennon and Incropera [Bennon and Incropera, 1987]. A 2D geometry was considered for both, round and square billets. The turbulent flow was modelled by the LRN-LS turbulence model, where both transport equations, i.e. k and ε involve additional Darcy's like source terms to account the solidification effects in a mushy zone. Their model also included the transport equation for species in order to predict the solute transport in a billet. The FVM with the SIMPLER velocity-pressure coupling algorithm was used to solve the system of governing equations. They represented the velocity and the temperature field as a function of the casting speed, and the profiles of carbon segregation ratio along the billet. They also predicted the trajectories and density distribution of inclusion particles in a billet as a function of the particle diameter.

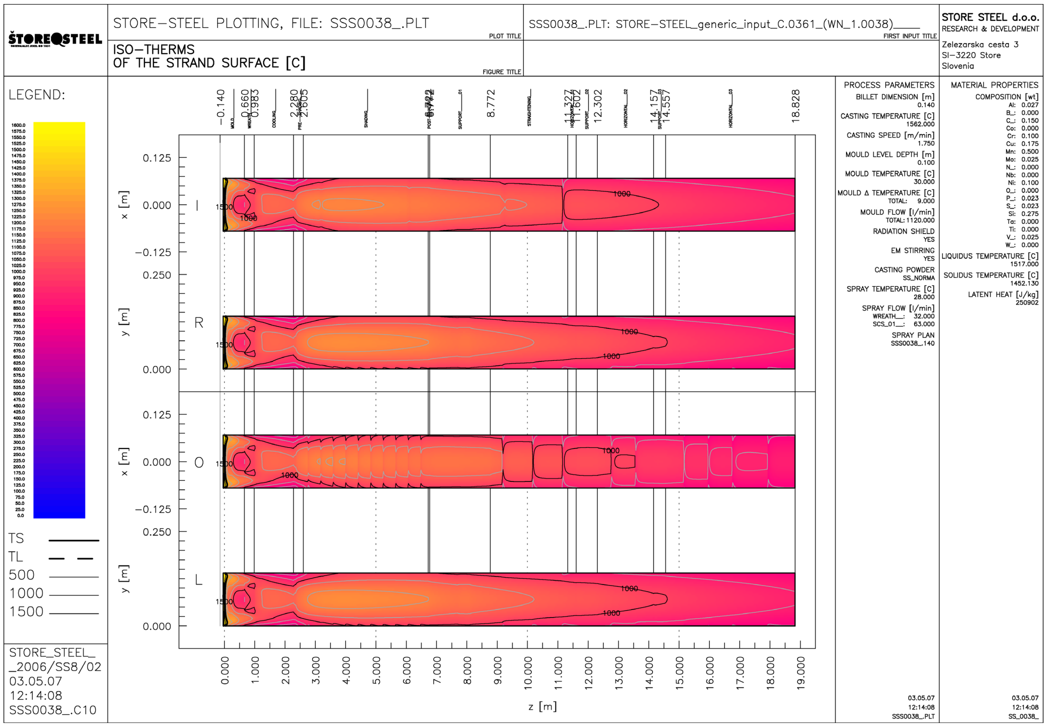

Figure 1.4: Simulation system for temperature field in Štore Steel billet caster [Šarler *et al.*, 2005]. Calculated temperature fields of the billet surface.

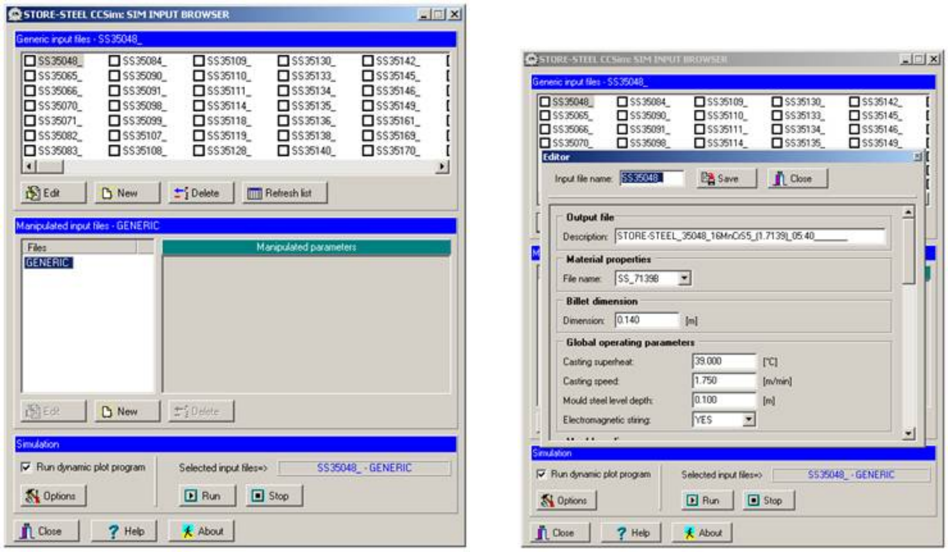

Input file name: SS35048_

Output file
Description: STORE-STEEL_35048_16MnCrS5_(1.7139)_05:40______

Material properties
File name: SS_7139B

Billet dimension
Dimension: 0.140 [m]

Global operating parameters
Casting superheat: 39.000 [°C]
Casting speed: 1.750 [m/min]
Mould steel level depth: 0.100 [m]
Electromagnetic stiring: YES

☑ Run dynamic plot program
Selected input files=> SS35048_ - GENERIC

Figure 1.5: Input/output GUI programs of the simulation system [Vertnik and Šarler, 2002; Šarler *et al.*, 2005].

1.3 Meshless Numerical Methods

To numerically evaluate the physical models in the science and engineering, several different numerical methods can be used, such as FDM, FVM, FEM, BEM, etc. Despite the powerful features of these methods, there are often substantial difficulties in applying them to realistic, geometrically complex two and three dimensional transient situations with moving and/or deforming boundaries.

In recent years, a number of meshless methods [Atluri and Shen, 2002; Atluri, 2004; Liu, 2003; Liu and Gu, 2005] have been developed to circumvent the problem of polygonisation encountered in the classical numerical methods. In meshless methods, approximation is constructed entirely in terms of a set of nodes (see Figure 1.6). There exist a number of different meshless methods such as the element free Galerkin methods, the meshless local Petrov-Galerkin method, the point interpolation method, the point assembly method, the FPM, the FDM with arbitrary irregular grids, smoothed particle hydrodynamics, reproducing kernel particle method, etc. A class of such methods is based on collocation with RBFs [Šarler, 2007]. These functions [Buhmann, 2003] have been first under intensive research in multivariate data and function interpolation [Franke, 1982]. Kansa used them for scattered data approximation [Kansa, 1990a] and than for the solution of partial differential equations [Kansa, 1990b]. The key point of the Radial Basis Function Collocation Method (RBFCM) or Kansa method for solving the PDEs is the approximation of the fields on the boundary and in the domain by a set of global approximation functions. The discretization is, respectively, represented only by grid-points (poles of the global approximation functions) in contrast to FEM method where appropriate polygonisation needs to be generated in addition (see Figure 1.6), or FDM, where points are constrained to the coordinate lines. The main advantage of using the RBFCM for solution of PDEs is its simplicity, applicability to different PDEs, and effectiveness in dealing with arbitrary dimension and complicated domains. The method recently started to be applied in many scientific and engineering disciplines. It has been first used in the heat transport context by [Zerroukat *et al.*, 1998]. The method has been afterwards applied to the classical De Vahl Davis natural convection problem by asymmetric collocation in [Šarler *et al.*, 2001] and additionally by the symmetric and modified collocation in [Šarler, 2005]. The method was used for solution of the Stefan problems [Kovačević *et al.*, 2003], wave equations [Haq *et al.*, 2008] and solid mechanics problems [Mai-Duy *et al.*, 2007a; Le *et al.*, 2008] as well. The method has been formulated instead of deriving the RBFs by integrating the partial derivatives [Mai-Duy and Tran-Cong, 2003] and applied to transient problems [Mai-Cao and Tran-Cong, 2005] fluid flow [Mai-Duy *et al.*, 2007b] and moving boundaries [Mai-Cao and Tran-Cong, 2008]. Several other special developments of the method have been deduced such as the improved treatment of the Neumann boundary conditions [Libre *et al.*, 2008].

The main disadvantage of the mentioned method represent the related full matrices that are very sensitive to the choice of the free parameter in RBFs and are difficult to solve for problems of the order of 3000 unknowns or larger. The solution of related problem has been attempted by domain decomposition [Mai-Duy and Tran-Cong, 2002], multi-grid approach and compactly supported RBFs [Chen *et al.*, 2002] which all represent a substantial complication of the original simple method. The RBFs have been first put into context of porous media flow by [Šarler *et al.*, 2000] where the natural convection problem in Darcy porous media, and later Darcy-Brinkman porous media [Šarler *et al.*, 2004a] have been solved by the dual reciprocity boundary element method. This method belongs to the semi-meshless methods, because the domain fields are approximated by the global interpolation with the RBFs and the boundary fields by the boundary elements (polygons). A truly mesh-less RBFCM has been for the first time used for solution of Darcy porous media in [Šarler *et al.*, 2004b]. A substantial breakthrough in the development of the RBFCM was its local formulation, LRBFCM. This formulation was first developed for diffusion problems [Šarler and Vertnik, 2006], than to convection-diffusion problems with phase-change [Vertnik and Šarler, 2006a], to industrial application of direct chill casting of aluminum alloys [Vertnik *et al.*, 2006], continuous casting of steel [Vertnik and

Šarler, 2008], to solid-solid phase transformations [Kovačević and Šarler, 2005] and to solution of Navier Stokes equations [Divo and Kassab, 2007; Kosec and Šarler, 2008a] and porous media flow [Kosec and Šarler, 2008b]. The method was later used for solving the incompressible turbulent fluid flow problems [Vertnik and Šarler, 2009a], for solving the turbulent fluid flow with solidification in continuous casting of steel [Vertnik and Šarler, 2009c], and multiscale solidification modelling [Šarler *et al.*, 2010]. Several numerical examples from this publication are represented in the present dissertation. A similar, local quadrature based RBF approach, was developed by [Shu *et al.*, 2005]. The main issue of the local version of the RBFCM is the collocation on a sub-set of, in general, overlapping influence domains, which drastically reduces the collocation matrix size on the expense of solving many small matrices instead of a large one. Since the method does not experience significant accuracy drawback in comparison with the global version, it represents a practical choice also for solving very large problems.

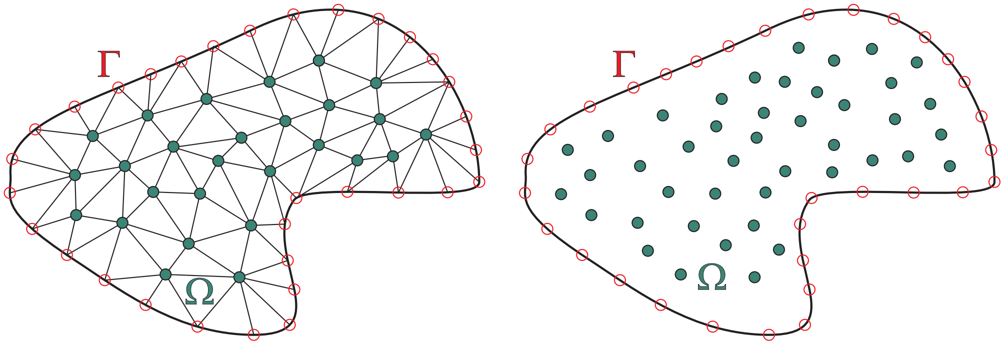

Figure 1.6: Left: the triangulation of the geometry in FEM. Right: the node arrangement in meshless methods.

1.4 Objectives of the Dissertation

The principal goal of the present dissertation is in development of a new numerical method, based on the LRBFCM, to solve the mass, momentum and energy equations which govern the turbulent heat and fluid flow phenomena of the continuous casting process. The objectives of the research performed are

- Extension of the usage of the LRBFCM for solving incompressible laminar flow problems. The involved velocity-pressure coupling algorithm for resolving the fluid incompressibility retained the simplicity, locality and explicitness of the LRBFCM. Validation of the developed numerical method performed on various numerical examples with and without heat transfer.

- Extension of the above developed numerical method for solving incompressible turbulent fluid flow problems, where the turbulence is modelled based on the eddy-viscosity approach. To verify and validate the developed numerical method for various numerical and experimental examples with turbulent fluid flow.
- Development of a numerical model for solving a 2D steady-state heat and fluid flow of the continuous casting of steel. The physical model relies on an existing single-domain mixture continuum model, developed by [Bennon and Incropera, 1987]. The derived turbulence transport equations for modelling the turbulent flow consider the solidification effects, involved in the mushy zone.
- Development of a numerical model of the continuous casting of steel that includes:
  - the temperature dependent thermo-physical properties of the steel grade, calculated by the JMatPro commercial software,
  - the discretization of real curved geometry of the Štore Steel billet caster and
  - the boundary conditions from an already developed thermal numerical model of the Štore Steel billet caster.
- The validation of the numerical model by the numerical results obtained with the software package Fluent.
- The simulation of steel grade C45 with real process parameters used in the Štore Steel billet casting process. Further, the obtained results are used to perform sensitivity study of the Darcy’s constant, and analysis of the effects of the variable process parameters on the solution of the velocity and the temperature fields. Three process parameters are chosen: the casting speed, the casting temperature, and the SEN depth.

2 Physical Model

This chapter describes the basic concepts of mathematical modelling of turbulent flows and solidification processes. First of all, the fundamentals and possibilities of the modelling of turbulence are given. Attention is made on the modelling with the eddy-viscosity turbulence models. The Reynolds-time-averaging procedure is explained, where the averaged transport equation for an arbitrary scalar are derived. Two eddy-viscosity models (EVMs) are discussed: the standard k-ε turbulence model and the LRN k-ε turbulence model. Next, the phase-change phenomena are explained for pure materials and alloys. A simple binary phase-change diagram and some models are presented for evaluating the relationship between the solid fraction and temperature. A brief overview of the mathematical modelling of binary solid-liquid phase-change phenomena is given, with attention to macroscopic transport processes, model simplifications, and connections between the microscopic and the macroscopic scale. From the macroscopic point of view, the mixture continuum model is chosen to be the most appropriate for the numerical modelling of the continuous casting of steel, since it became a representative model in this research area. The basic relationships and principles of the derivation of the mixture continuum conservation equations are presented, while the complete derivation is omitted in the present dissertation. The turbulent effects are modelled by the eddy-viscosity approach, where the Reynolds-time-averaged procedure is performed to obtain the final form of the mass, momentum and energy conservation equation.

2.1 Numerical Modelling of Turbulence

Turbulent flows can be observed in our everyday surroundings. Typical examples are flows around vehicles, buildings, smoke from a chimney, water in a river, flows and combustion in engines, etc. The turbulent flow is known to be irregular, random and chaotic. The flow consists of a spectrum of different eddy sizes. The largest eddies are strongly influenced by the geometry of the flow (i.e., by the boundary conditions), and they control the transport and mixing. The behaviour of the smallest eddies are determined almost entirely by the rate at which they receive energy from the large eddies, and also by the viscosity. They are dissipated into internal energy. Turbulent flow is always 3D and time-dependent, however it can be treated as steady-state and two-dimensional if the equations of motion (i.e. mass and momentum equations) are time averaged. Particular turbulent flows have already been studied experimentally by many researchers, for example two-dimensional channel flow [Laufer, 1948] and the flow through a backward-facing step [Jović and Driver, 1994]. Those experiments are very important, not only for understanding the behaviour of the turbulent flows, but also for developing mathematical models, which are able to accurately predict the properties of the turbulent flows. The modelling of the turbulent flows is known to be very difficult, mainly because there is no prospect of a simple analytic theory. However, with increasing power of computers, several numerical techniques have been established to numerically predict the turbulent flows: DNS, LES, and EVMs. To decide which model is appropriate for a particular flow depends mainly on the available computer power and the desired accuracy [Pope, 2000].

Direct numerical simulation

The classical Navier-Stokes (N-S) equation is directly solved, where all the scales of motion are resolved. It is the simplest one to implement, but the computational cost is very high due to the need for the 3D spatial discretization and the time-dependent solution of the N-S equation. However, the DNS was already successfully used for flow problems with simple geometry with low and moderate Re numbers [Kim *et al.*, 1987; Kasagi *et al.*, 1992; Kasagi *et al.*, 1997; Le *et al.*, 1997]. The results are very important and helpful for developing and estimating other turbulence models, like EVMs.

Eddy-viscosity models

They are still the most popular ones in engineering, especially for simulating complex industrial applications. They are based on the Reynolds-Averaged Navier-Stokes (RANS) equation in which the N-S equation is solved for the mean velocity field. The time-averaging process of the N-S equation generates additional terms, which are called the Reynolds-stresses. These stresses are unknown and have to be determined by a turbulence model, either via the eddy-viscosity hypothesis or from modelled Reynolds-stress transport equations. In the eddy-viscosity approach, the Reynolds-stress tensor is determined by the relationship between the turbulent viscosity and the velocity gradients. The resulting Reynolds-stress tensor is almost identical to the shear-stress tensor of the N-S equation. The turbulent viscosity is calculated by solving the additional one or two transport equations, depending on the turbulence model chosen. In one-equation models, only the transport equation for the turbulent kinetic energy is solved. The turbulent kinetic energy was suggested independently by

Kolmogorov and Prandtl [Pope, 2000] as the base quantity to define the velocity scale for the turbulence. The turbulent length scale in one-equation models is not modelled but rather determined empirically for particular flow types [Wilcox, 1993]. In the two-equation models the turbulent length scale is modelled by solving another transport equation for the dissipation rate ε (the k-ε model) or the specific dissipation rate ω (the k-ω model). Both transport equations, i.e. k and ε (or ω), are derived from the N-S equation [Wilcox, 1993]. After time averaging process, different terms appear in k and ε equations defining various physical phenomena of the turbulent flow, i.e. dissipation, turbulent diffusion, pressure diffusion, productions, etc. Those terms are modelled by introducing damping functions and closure coefficients to describe the behaviour of the typical turbulent flow problem, i.e. turbulent boundary layer, turbulent channel flow, separation, etc. In approximately thirty years of turbulence modelling with the two-equation models, a lot of variations of both k-ε and k-ω models were developed [Wilcox, 1993; Bredberg, 2001; Pope 2000]. Older models [Jones and Launder, 1972; Launder and Sharma, 1974; Chien, 1982; Abe *et al.*, 1994] were mainly developed to represent the turbulent boundary layer in a 2D channel flow. The newer models [Bredberg, 2001] are improved and extended versions of the older ones by introduced additional terms in modelled transport equations. In the present dissertation, the two-equation k-ε models are used to solve various turbulent flows problems, so the next sections are focused strictly on these models.

Large-eddy simulation

In LES simulation, the unsteady motion of the larger scales (large eddies) are represented directly, similar as in DNS. The effects of small scales are modelled. From the point of view of computational cost, the LES is somewhere between DNS and Reynolds stress models, and was developed to overcome the difficulties of both approaches. The LES models are expected to be more accurate as the Reynolds stress models, especially for flows were the large-scale unsteadiness is significant, such as unsteady separation and vortex shading. The simulation must be performed in 3D and time-dependent, however, the number of computational nodes is reduced, because the smaller eddies are modelled (in the simpler way by the EVM). The main part of the LES is the filtering operation, where the velocity is decomposed into the sum of filtered (or resolved) component and a residual (or subgrid-scale, SGS) component. The filtered velocity field, which is 3D and time-depended, represents the motion of the large eddies. Then the filtered form of the N-S equation is derived, which becomes the standard N-S equation, with the momentum equation containing the residual-stress tensor (SGS stress tensor) arising from the residual motions. The

SGS tensor is modelled in a most simple way by EVM. Other details and characteristics about LES can be found in several readings [Pope, 2000; Schiestel, 2008].

2.1.1 Reynolds Time Averaging

Before we introduce the concept of EVM, the Reynolds-time-averaging procedure is presented. This is a statistical approach, where the instantaneous transport variable $\phi(\mathbf{p},t)$ is decomposed into the sum of the mean $\bar{\phi}(\mathbf{p})$ and the fluctuating part $\phi'(\mathbf{p},t)$, i.e.

$$\phi(\mathbf{p},t)=\bar{\phi}(\mathbf{p})+\phi'(\mathbf{p},t), \tag{2.1}$$

where $\mathbf{p}$ and t are position vector and time, respectively. The mean variable $\bar{\phi}(\mathbf{p})$ is defined as

$$\bar{\phi}(\mathbf{p})=\lim_{\Delta t\to\infty}\frac{1}{\Delta t}\int_{t}^{t+\Delta t}\phi(\mathbf{p},t)dt\,. \tag{2.2}$$

The time average of the mean variable produces the mean value, i.e.

$$\overline{\bar{\phi}(\mathbf{p})}=\lim_{\Delta t\to\infty}\frac{1}{\Delta t}\int_{t}^{t+\Delta t}\bar{\phi}(\mathbf{p})dt=\bar{\phi}(\mathbf{p})\,. \tag{2.3}$$

The time average of the fluctuating part is zero. By using the equation (2.3), we get

$$\overline{\phi'}=\lim_{\Delta t\to\infty}\frac{1}{\Delta t}\int_{t}^{t+\Delta t}\left[\phi(\mathbf{p},t)-\bar{\phi}(\mathbf{p})\right]dt=\bar{\phi}(\mathbf{p})-\overline{\bar{\phi}(\mathbf{p})}=\bar{\phi}(\mathbf{p})-\bar{\phi}(\mathbf{p})=0\,. \tag{2.4}$$

Other correlations and principles of time-averaging can be found in [Wilcox, 1993; Bredberg, 1999; Davidson, 2003]. Here, we continue with the time-averaging processes of the mass and momentum equation. The mass and momentum equation of the laminar incompressible flow are defined as

$$\frac{\partial\rho}{\partial t}+\nabla\cdot(\rho\mathbf{u})=0\,, \tag{2.5}$$

$$\frac{\partial}{\partial t}(\rho\mathbf{u})+\nabla\cdot(\rho\mathbf{u}\mathbf{u})=-\nabla P+\nabla\cdot(2\mu\mathbf{S}), \tag{2.6}$$

where ρ, $\mathbf{u}$, P, μ, $\mathbf{S}$ are density, velocity, pressure, dynamic viscosity and strain rate, repectively. A strain-rate tensor is defined as

$$\mathbf{S}=\frac{1}{2}\left[\nabla\mathbf{u}+\left(\nabla\mathbf{u}\right)^{\mathrm{T}}-\frac{2}{3}\nabla\cdot\mathbf{u}\right]. \tag{2.7}$$

Since we are dealing with incompressible flow (i.e. low Mach number), the last term (the dilatation term) in equation (2.7) is zero. Here, it must be noted that we use the term "incompressible" in the sense that the density is independent of pressure ($\partial P/\partial\rho=0$), but it can depend for example on temperature or concentration. In such a case, the strain-rate tensor reduces to

$$\mathbf{S}=\frac{1}{2}\left(\nabla\mathbf{u}+\left(\nabla\mathbf{u}\right)^{\mathrm{T}}\right). \tag{2.8}$$

It is also worth to mention, that the dynamic viscosity μ is variable in general. The time-averaging process of the equations (2.5) and (2.6) gives

$$\frac{\partial\rho}{\partial t}+\nabla\cdot\left(\rho\overline{\mathbf{u}}\right)=0, \tag{2.9}$$

$$\frac{\partial}{\partial t}\left(\rho\overline{\mathbf{u}}\right)+\nabla\cdot\left(\rho\overline{\mathbf{u}}\overline{\mathbf{u}}\right)=-\nabla\overline{P}+\nabla\cdot\left(2\mu\overline{\mathbf{S}}-\rho\overline{\mathbf{u}'\mathbf{u}'}\right), \tag{2.10}$$

where the mean strain rate tensor $\overline{\mathbf{S}}$ is defined as

$$\overline{\mathbf{S}}=\frac{1}{2}\left[\nabla\overline{\mathbf{u}}+\left(\nabla\overline{\mathbf{u}}\right)^{\mathrm{T}}\right]. \tag{2.11}$$

The averaged momentum equation (2.10) is also called the RANS equation. The time-averaged equations (2.9) and (2.10) are almost identical to the instantaneous equations (2.5) and (2.6). The only difference is between the momentum equations, where additional term $\rho\overline{\mathbf{u}'\mathbf{u}'}$ appears in the time-averaged form. This term represents the major problem of the turbulence modelling in the engineering practice. In order to compute the mean-flow variables of the turbulent flow, we also need to compute the $\rho\overline{\mathbf{u}'\mathbf{u}'}$. This term is known as the Reynolds-stress tensor $\boldsymbol{\tau}_R$

$$\boldsymbol{\tau}_R=-\rho\overline{\mathbf{u}'\mathbf{u}'}, \tag{2.12}$$

which has six independent components, which represent correlations between the fluctuating velocities. This additional stress term has to be modelled to close the system of equations (2.10). This is called the *closure problem*, which means that the number of unknowns (ten: three velocity components, pressure, six stresses) is larger than the number of equations (four: the continuity equations and three components of the N-S equation).

In EVMs the Reynolds-stress tensor is a function of turbulent viscosity μ_t and mean rates of deformation

$$\boldsymbol{\tau}_R = -\rho\overline{\mathbf{u}'\mathbf{u}'} = 2\mu_t\overline{\mathbf{S}} = \mu_t\left[\nabla\overline{\mathbf{u}} + \left(\nabla\overline{\mathbf{u}}\right)^{\mathrm{T}}\right] - \frac{2}{3}\rho k\boldsymbol{\Delta}\,. \tag{2.13}$$

This relation is called the Boussinesq assumption. In equation (2.13), μ_t is turbulent dynamic viscosity, and $\boldsymbol{\Delta}$ is a tensor of the Kronecker delta δ, where the components are $\delta_{ij} = 1$ if $i = j$ and $\delta_{ij} = 0$ if $i \neq j$. The last term in equation (2.13) is needed to obtain the proper trace of $\boldsymbol{\tau}_R$ [Wilcox, 1993]. The momentum equation (2.10) is re-written, considering the definition of $\boldsymbol{\tau}_R$, into the following equation

$$\frac{\partial}{\partial t}\left(\rho\overline{\mathbf{u}}\right) + \nabla\cdot\left(\rho\overline{\mathbf{u}}\overline{\mathbf{u}}\right) = -\nabla\overline{P} + \nabla\cdot\left[2\left(\mu + \mu_t\right)\overline{\mathbf{S}} - \frac{2}{3}\rho k\boldsymbol{\Delta}\right]. \tag{2.14}$$

All EVMs are based on this approach. The question is how to calculate μ_t, which has no physical meaning. Because, there is no general prescription to calculate it, there exist many different models. Each model comes with a set of closure coefficients, which were obtained based on the experimental data (older models) or DNS data (newer models). In the next sections we present two of them: the standard k-ε model and the LRN k-ε models. Both of them are the representative models in the numerical modelling of continuous casting processes.

The physical processes in nature or industry can also involve other physical phenomena, for example heat transfer or species transfer. The transport equation for each additional scalar variable has to be also time-averaged. Consider the general transport equation for an arbitrary scalar quantity ϕ represented by the following equation

$$\frac{\partial}{\partial t}\left(\rho\phi\right) + \nabla\cdot\left(\rho\mathbf{u}\phi\right) = \nabla\cdot\left(\mathbf{D}\nabla\phi\right) + S_\phi\,, \tag{2.15}$$

with $\mathbf{D}$ and S_ϕ standing for diffusion tensor and source term, respectively. Using the same principles of the time-averaging of the momentum transport equation, the final time-averaged form of equation (2.15) is

$$\frac{\partial}{\partial t}\left(\rho\overline{\phi}\right) + \nabla\cdot\left(\rho\overline{\mathbf{u}}\overline{\phi}\right) = \nabla\cdot\left(\mathbf{D}\nabla\overline{\phi}\right) + \overline{S}_\phi - \nabla\cdot\left(\rho\overline{\mathbf{u}'\phi'}\right). \tag{2.16}$$

The last term in equation (2.16) represents an extra turbulent transport term, taken to be proportional to the gradient of the mean value of the transported scalar quantity, i.e.

$$-\rho\overline{\mathbf{u}'\phi'} = \Gamma_t \nabla\overline{\phi}\,, \tag{2.17}$$

where Γ_t is the turbulent diffusivity, defined as

$$\Gamma_t = \frac{\mu_t}{\sigma_t}\,. \tag{2.18}$$

In equation (2.18), σ_t is the turbulent Prandtl number. Various experiments show that σ_t is often nearly constant and valued around 1 [Versteeg and Malalasekera, 1995].

2.1.2 Standard *k*-*ε* Model

The standard k-ε turbulence model is the most popular two-equation viscosity model. The turbulent viscosity μ_t is computed by the following expression

$$\mu_t = \rho c_\mu \frac{k^2}{\varepsilon}\,, \tag{2.19}$$

where c_μ is the closure coefficient. In order to compute μ_t, two additional transport equations have to be solved: the first one for the turbulent kinetic energy k and the second one for the dissipation rate ε. The turbulent kinetic energy is defined by taking the trace of the Reynolds-stress tensor, i.e.

$$k = 0.5 \cdot \mathrm{tr}\left(\boldsymbol{\tau}_R\right). \tag{2.20}$$

The transport equation of k is derived from the N-S equation [Davidson, 2003] or by taking the trace of the Reynolds-stress equation [Wilcox, 1993; Bredberg, 1999]. Both leads to the following transport equation

$$\frac{\partial}{\partial t}\left(\rho k\right) + \nabla\cdot\left(\rho\bar{\mathbf{u}}k\right) = \nabla\cdot\left[\left(\mu + \frac{\mu_t}{\sigma_k}\right)\nabla k\right] + P_k - \rho\varepsilon\,, \tag{2.21}$$

where P_k is the production term and σ_k is the turbulent Prandtl number for k. The P_k is defined as

$$P_k = \mu_t \nabla\bar{\mathbf{u}} : \left[\nabla\bar{\mathbf{u}} + \left(\nabla\bar{\mathbf{u}}\right)^{\mathrm{T}}\right]. \tag{2.22}$$

The dissipation rate ε is defined by the following relation

$$\varepsilon = \nu\overline{\frac{\partial u_i'}{\partial x_j}\frac{\partial u_i'}{\partial x_j}}\,, \tag{2.23}$$

where ν is the kinematic viscosity. The transport equation for ε is also derived from the N-S equation [Wilcox, 1993; Bredberg, 1999]. The final equation for ε is given as

$$\frac{\partial}{\partial t}(\rho\varepsilon)+\nabla\cdot(\rho\bar{\mathbf{u}}\varepsilon)=\nabla\cdot\left[\left(\mu+\frac{\mu_t}{\sigma_\varepsilon}\right)\nabla\varepsilon\right]+(c_{1\varepsilon}P_k-c_{2\varepsilon}\rho\varepsilon)\frac{\varepsilon}{k}, \qquad (2.24)$$

where σ_ε is turbulent Prandtl number for ε and $c_{1\varepsilon}, c_{2\varepsilon}$ are the closure coefficients. The closure coefficients c_μ, σ_k, σ_ε, $c_{1\varepsilon}$ and $c_{2\varepsilon}$ are determined and optimized by applying the model to various fundamental flows such as flow in channel, pipes, jets, wakes, etc. They are given the following values

$$c_\mu=0.09\,,\ \sigma_k=1.0\,,\ \sigma_\varepsilon=1.3\,,\ c_{1\varepsilon}=1.44\,,\ c_{2\varepsilon}=1.92\,. \qquad (2.25)$$

There is one serious drawback of modelling the turbulent flows with the standard k-ε model described. It was developed for high Re numbers, so assuming a fully turbulent flow. The problem arises when flow near the boundary is also important, where the Re numbers are very low. Figure 2.1 shows a typical velocity profile for turbulent boundary layer flow. The velocity $\bar{\mathbf{u}}$ and the distance from the wall y are normalized by the friction velocity $\bar{u}_\tau$ to obtain $\bar{\mathbf{u}}^+$ and y^+, i.e.

$$\bar{u}^+=\frac{\bar{u}}{\bar{u}_\tau}, \qquad (2.26)$$

$$y^+=\frac{\rho y\bar{u}_\tau}{\mu}, \qquad (2.27)$$

where $\bar{u}_\tau$ is defined as

$$\bar{u}_\tau=\sqrt{\frac{\tau_w}{\rho}}\ , \qquad (2.28)$$

with τ_w standing for the wall shear stress, calculated by the equation

$$\tau_w=\mu\frac{\partial\bar{u}}{\partial y}\,. \qquad (2.29)$$

The whole domain of the turbulent boundary layer can be divided into three sub-regions: viscous sub-layer, log layer and defect layer (see Figure 2.1). In the viscous sub-layer the fluid is stationary, and also the turbulent eddy motions stop. Close to the surface, the velocity varies approximately linearly with y^+, and gradually asymptotes to the log layer. The log layer typically lies between

$y^+ = 30$ and $y^+ = 0.1\delta_b$ (δ_b is the boundary layer width), where the upper boundary depends upon Re number. In this region the viscous and the turbulent effects are both important. The velocity profile obeys the log-law, i.e.

$$\bar{u}^+ = \frac{1}{\kappa} \ln y^+ + B_{lw}, \tag{2.30}$$

where κ and B_{lw} are von Kármán constant and dimensionless constant, respectively. It was found [Versteeg and Malalasekera, 1995] that for the smooth wall $\kappa = 0.4$ and $B_{lw} = 5.5$. The defect layer is far from the wall, where the inertial forces are dominated and it is free from direct viscous forces. In this region, the log-law of the wake [Versteeg and Malalasekera, 1995] holds

$$\frac{\bar{u}_{\max} - \bar{u}}{u_\tau} = \frac{1}{\kappa} \ln \frac{y}{\delta_b} + A_{lw}, \tag{2.31}$$

where A_{lw} and $\bar{u}_{\max}$ are the constant and the maximal velocity in the boundary layer, respectively. This completes the description of the turbulent flow phenomena near the wall.

The standard k-ε model is not capable of resolving the viscous sub-layer region. If we put more calculation points in this region, the standard k-ε model is not valid, because it was made for fully turbulent flows, so up to the limit between the viscous sub-layer and log layer region. The first calculation point must be located in the log layer, where the wall functions have to be applied. The wall functions obey the log-law, equation (2.30), and they are valid up to the wall. Based on the discussed characteristics of the turbulence modelling with the standard k-ε model, several conclusions can be made:

- The wall functions are valid only in the log layer, and they can not be used in the viscous sub-layer. When the viscous effects are also important, such as separation or reattachment, the model is not appropriate.
- When predicting heat transfer it is in general not a good idea to use wall functions, because the heat transfer near the walls is very important for the temperature field in the whole domain.
- To overcome the represented difficulties, the LRN k-ε was developed [Jones and Launder, 1972].

The derivation of the wall functions and other details about the standard k-ε model, which are not included in the present dissertation, can be found in several classical readings on the subject [Wilcox, 1993; Versteeg and Malalasekera, 1995; Hoffmann and Chiang, 2000].

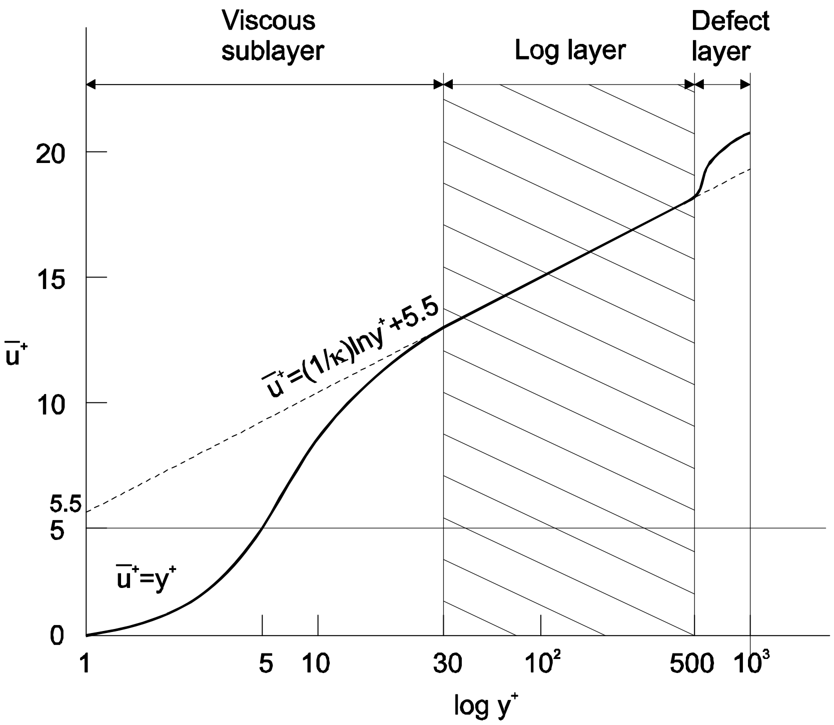

Figure 2.1: Typical velocity profile for a turbulent boundary layer flow.

2.1.3 Low-Reynolds-Number Models

In the previous section we discussed a major problem of using wall functions in the standard k-ε turbulence model. Here, we present the LRN turbulence models, which were developed in order to overcome the weakness of standard model, which cannot predict very well the turbulent boundary layer. The LRN models are on contrary capable of resolving the flow properties up to the wall, where the Re numbers are very low. It must be noted, that the low Re number does not mean the global Re number, but here we are considering the local turbulent Reynolds number Re_{tl}, which varies throughout the computational domain and it is proportional to the ratio of the turbulent and the physical viscosity μ_t / μ, i.e. $\mathrm{Re}_{tl} \propto \mu_t / \mu$. This ratio is very large in the fully turbulent flow and it descends to zero when a wall is approached.

First LRN turbulence model was proposed by [Jones and Launder, 1972]. The transport equations (2.21) and (2.24) of the standard k-ε model were modified into the following form

$$\frac{\partial}{\partial t}(\rho k)+\nabla\cdot(\rho\bar{\mathbf{u}}k)=\nabla\cdot\left[\left(\mu+\frac{\mu_t}{\sigma_k}\right)\nabla k\right]+P_k-\rho\tilde{\varepsilon}+D, \tag{2.32}$$

$$\frac{\partial}{\partial t}(\rho\tilde{\varepsilon})+\nabla\cdot(\rho\mathbf{\bar{u}}\tilde{\varepsilon})=\nabla\cdot\left[\left(\mu+\frac{\mu_t}{\sigma_\varepsilon}\right)\nabla\tilde{\varepsilon}\right]+\left(c_{1\varepsilon}f_1P_k-c_{2\varepsilon}f_2\rho\tilde{\varepsilon}\right)\frac{\tilde{\varepsilon}}{k}+E\,, \quad (2.33)$$

where $\tilde{\varepsilon}$ is a modified dissipation rate, f_1 and f_2 are the damping functions, and D and E are additional source terms. This turbulent model solves $\tilde{\varepsilon}$, which is defined as

$$\tilde{\varepsilon}=\varepsilon-D\,, \quad (2.34)$$

where D is equal to value of ε at the wall, which gives an easy boundary condition $\tilde{\varepsilon}=0$ for transport equation (2.33). Turbulent viscosity in the LRN models is calculated by the following equation

$$\mu_t=\rho c_\mu f_\mu\frac{k^2}{\tilde{\varepsilon}}\,, \quad (2.35)$$

with f_μ standing for the damping function. Many LRN models use $\tilde{\varepsilon}$ for solving the turbulent viscosity, but some of them rather use ε with both D and E equal to zero. In the present dissertation, the following models are used: JL [Jones and Launder, 1972], LS [Launder and Sharma, 1974] and AKN [Abe *et al.*, 1994]. The closure coefficients c_μ, $c_{\varepsilon 1}$, $c_{\varepsilon 2}$, σ_k and σ_ε for each model are given in Table 2.1, the source terms D and E in Table 2.2, and the damping functions f_μ, f_1, f_2 in Table 2.3. In the JL and LS models, the transport equation (2.33) is used to calculate μ_t (equation (2.35)), while the AKN model solves equation (2.33) for ε with the following boundary condition at the wall

$$\varepsilon_w=2\frac{\mu}{\rho}\frac{k}{y^2}\,, \quad (2.36)$$

where y and k are the normal distance and the turbulent kinetic energy at the nearest domain node, respectively.

The damping functions f_μ and f_2 in the AKN model depend on the non-dimensional distance from the wall y^*, defined as

$$y^*=\frac{\rho\bar{u}_\varepsilon y}{\mu}\,. \quad (2.37)$$

In equation (2.37), the $\bar{u}_\varepsilon$ is the Kolmogorov velocity scale, defined as

$$\bar{u}_\varepsilon=(\nu\varepsilon)^{1/4}\,. \quad (2.38)$$

In the damping functions, Re_t is the turbulent Re number, i.e.

$$\mathrm{Re}_t = \frac{k^2}{\nu\varepsilon}. \tag{2.39}$$

The source terms in Table 2.2 are written in tensor index notation. For 2D case with Cartesian x-y coordinate system, the terms are calculated as

$$D = -2\frac{\mu}{\rho}\left[\left(\frac{\partial\sqrt{k}}{\partial p_x}\right)^2 + \left(\frac{\partial\sqrt{k}}{\partial p_y}\right)^2\right], \tag{2.40}$$

$$E = 2\frac{\mu\mu_t}{\rho}\left[\left(\frac{\partial^2 u_x}{\partial p_x^2}\right)^2 + 2\left(\frac{\partial^2 u_x}{\partial p_x \partial p_y}\right)^2 + \left(\frac{\partial^2 u_x}{\partial p_y^2}\right)^2 + \right.$$

$$\left. \left(\frac{\partial^2 u_y}{\partial p_x^2}\right)^2 + 2\left(\frac{\partial^2 u_y}{\partial p_x \partial p_y}\right)^2 + \left(\frac{\partial^2 u_y}{\partial p_y^2}\right)^2\right]. \tag{2.41}$$

Table 2.1: Closure coefficients of the LRN turbulence models.

model	c_μ	$c_{\varepsilon 1}$	$c_{\varepsilon 2}$	σ_k	σ_ε
JL	0.09	1.55	2.00	1.00	1.30
LS	0.09	1.44	1.92	1.00	1.30
AKN	0.09	1.40	1.40	1.50	1.90

Table 2.2: Source terms D and E of the LRN turbulence models.

model	D	E
JL	$-2\frac{\mu}{\rho}\frac{\partial\sqrt{k}}{\partial p_i}\frac{\partial\sqrt{k}}{\partial p_i}$	$2\frac{\mu\mu_t}{\rho}\left(\frac{\partial^2 u_i}{\partial p_j \partial p_k}\right)\left(\frac{\partial^2 u_i}{\partial p_j \partial p_k}\right)$
LS	$-2\frac{\mu}{\rho}\frac{\partial\sqrt{k}}{\partial p_i}\frac{\partial\sqrt{k}}{\partial p_i}$	$2\frac{\mu\mu_t}{\rho}\left(\frac{\partial^2 u_i}{\partial p_j \partial p_k}\right)\left(\frac{\partial^2 u_i}{\partial p_j \partial p_k}\right)$
AKN	0	0

Table 2.3: Damping functions of the LRN turbulence models.

model	f_μ	f_1	f_2
JL	$\exp\left[\dfrac{-2.5}{1+\dfrac{R_t}{50}}\right]$	1.0	$1-0.3\exp\left(-\mathrm{Re}_t^2\right)$
LS	$\exp\left[\dfrac{-3.4}{\left(1+\dfrac{R_t}{50}\right)^2}\right]$	1.0	$1-0.3\exp\left(-\mathrm{Re}_t^2\right)$
AKN	$\left[1-\exp\left(-\dfrac{y^*}{14}\right)\right]^2 \times\left[1+\dfrac{5}{\mathrm{Re}_t^{0.75}}\exp\left(-\left(\dfrac{\mathrm{Re}_t}{200}\right)^2\right)\right]$	1.0	$\left[1-\exp\left(-\dfrac{y^*}{3.1}\right)\right]^2 \times\left[1-0.3\exp\left(-\left(\dfrac{\mathrm{Re}_t}{6.5}\right)^2\right)\right]$

The EVMs are still the most widely used turbulence models in engineering practice. They are the most widely validated models and give very good performance for many industrially relevant flows. However, there exist some flow problems, for which they give poor performance:

- curved boundary layer,
- swirling flows,
- some unconfined flows,
- rotating flows, etc.

When comparing the LRN models, used in the present dissertation, we can conclude the following:

- AKN model is numerically very stable model and gives very good performance for various types of flows, such as the channel flow, and the flow with separation and reattachment. The main disadvantage of using this model is the calculation of the damping functions, which depend on the wall distance. If we are dealing with the pure liquid flows, the calculation of the wall distance is not a hard task. However, when modelling the solidification problems, this could become a problem, since it is almost impossible to define the wall, which is relevant for the turbulence model. The wall is somewhere in the mushy zone, and could not be known in advance. It is a part of the solution, similar as the liquidus and solidus curves in the solidification problem. The CFD commercial software, such as Fluent, calculates the wall distance up to the boundary of the fixed geometry, even for the solidification problems, which is definitely not correct.

- LS and JL models are very old turbulence models and very similar to each other. The JL model was the first LRN and is practically not in use any more today. While, the LS model is an extended version of the JL model, and very well established model with overall average prediction. It is repeatedly used as a comparative model in science and it is implemented in the various CFD commercial packages. They are both numerically unstable, due to extra source terms D and E in the k and ε equations, respectively. However, the LS model is the most popular in modelling of the continuous casting process. The reason is in its damping functions, which are simpler then in the AKN model and depend only on the Re_t. The numerical stability can be improved in LS model by removing an extra source terms and using the Neumann boundary condition for ε equation [Prescott and Incropera, 1995].

2.2 Phase-Change Phenomena

Heat transfer problems involving dissolution or solidification are generally referred to as solid-liquid phase-change problems or moving boundary problems, and also as Stefan problems [Šarler, 1995]. They involve free or moving boundaries between the phases that need to be determined as a part of the solution. Dissolution is the phenomena, where the solid phase, of in general multi-component material, is changed into a liquid, by absorbing heat. Solidification is the inverse phenomena of dissolution, where the liquid phase is changed to solid, by releasing heat. Absorbed or released heat energy is often termed as latent heat, which influences the phase-change velocity.

For pure substances or eutectic alloys, the phase-change phenomena occur at a fixed temperature, called the melting point temperature T_m. When the temperature of a substance is equal to a melting temperature, the phase-change process commences. At this stage, the latent heat is absorbed to a material or released from a material to change its phase. During the melting or freezing, the liquid and the solid are assumed to be in thermodynamic equilibrium, and the temperature of the substance does not change. The solid and the liquid phases are separated by a single moving interface which determines the boundary between the phases.

In the case of alloys, dissolution or solidification takes place over an extended range of temperature, where the solid and the liquid phases are separated by a two-phase moving region, the 'mushy zone'. This is a region only from the macroscopic point of view. When observing microscopically, it shows a highly complex solid-liquid inter-phase morphology. The upper limit of this temperature range at which the mixture becomes completely liquid is termed as liquidus temperature T_L and the lower limit at which solidification is complete and the mixture is entirely solid is termed as the solidus temperature T_S. The mass fraction of the solid phase (solid fraction) in the mixture, f_S, is zero at T_L and unity at T_S, and in the mushy zone has values between zero and unity. The relation between the solid fraction and the temperature may be evaluated from the phase-change diagrams, shown in Figure 2.2, where the temperature is presented as a function of the solute concentration c_A. For any given solute concentration, there exists an equilibrium liquidus and solidus temperature. Likewise, for any given temperature, there is an equilibrium solidus solute concentration $c_{A,S}$ and liquidus solute concentration $c_{A,L}$. The liquidus or solidus temperature can be approximated (linearly) by the following equation

$$T_{\wp} = T_m + m_{\wp} c_{A,\wp} \; ; \; \wp = L, S \, , \tag{2.42}$$

where $m_{\wp}$ is the slope of the liquidus or the solidus line at $c_{A,\xi}$.

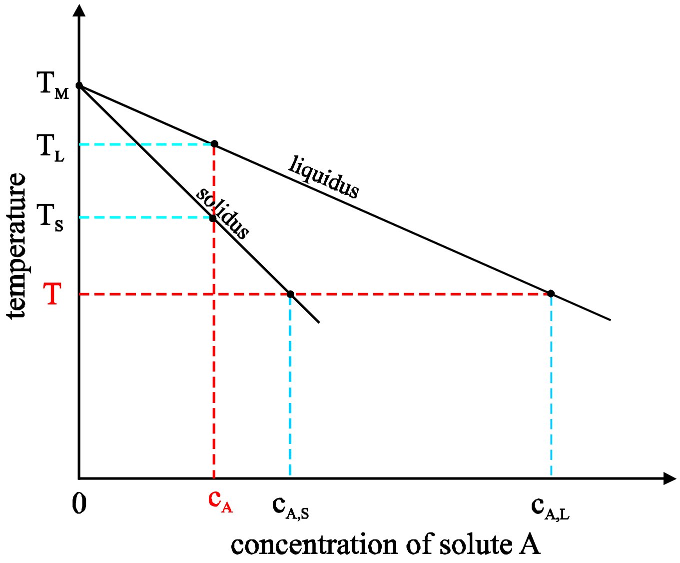

Figure 2.2: Binary phase-change diagram.

A more detailed description of the discussed physical phenomena can be found in the following literature [Crank, 1984; Dantzig, 2001; Šarler, 1995; Šarler, 2009].

The relation between the solid fraction and the temperature in practical solidification analysis can be evaluated through several models [Hong, 2004]:

a) Linear distribution of latent heat

The latent heat is linearly distributed over the solidification range between T_L and T_S.

$$f_S = \frac{T_L - T}{T_L - T_S};\ T_S \le T \le T_L. \tag{2.43}$$

b) Level rule (equilibrium solidification model)

Complete mixing of solute in liquid and solid is assumed. The solid fraction as a function of temperature (see Figure 2.2) is given by

$$f_S = \frac{T_L - T}{(1-k_{LS})(T_m - T)};\ T_S \le T \le T_L, \tag{2.44}$$

where k_{LS} is defined as

$$k_{LS} = \frac{c_{A,S}}{c_{A,L}}. \tag{2.45}$$

c) Scheil model

Complete mixing of solute in liquid and no mixing of solute in solid is assumed. In this case the solid fraction as a function of temperature is given by

$$f_S = 1 - \left(\frac{T_m - T}{T_m - T_L}\right)^{\frac{1}{(k_{LS}-1)}};\ T_S \le T \le T_L. \tag{2.46}$$

d) Brody-Flemings model

Complete mixing in liquid and partial mixing in solid are assumed. Here, the solid fraction as a function of temperature is given by

$$f_S = (1+\alpha_t k_{LS})\left[1 - \left(\frac{T_m - T_L}{T_m - T}\right)^{\frac{1}{(k_{LS}-1)}}\right];\ T_S \le T \le T_L, \tag{2.47}$$

where α_t is the Brody-Flemings constant and it is defined as

$$\alpha_t = \frac{4D_S t_f}{\lambda_a^2}, \tag{2.48}$$

with D_S, t_f and λ_a are the diffusion coefficient of solute atoms in solid, the local solidification time, and the dendrite arm spacing, respectively.

Beside above models, there exist several commercial software packages, which are able to calculate material properties as a function of temperature. They are based on thermodynamic calculations and experimentally obtained databases, which cover a wide range of steel grades. One of them is JmatPro by Sente Software, which was developed for general and stainless steel grades. It has several different calculation modules, such as: thermodynamic properties, solidification, thermo-physical properties, mechanical properties, phase transformation, and others. The calculated data are exported into text files, which can be further used in different numerical models.

In the present dissertation, two different approaches are used: model based on linear distribution of latent heat, and calculated with the JmatPro (Version 5.0, Sente Software, “http://www.sentesoftware.co.uk/jmatpro.aspx”).

The first approach is used in the simplified numerical example, where the validation of the numerical model is performed. The thermo-physical properties are considered as a linear function of temperature between the liquidus and the solidus temperature.

The second approach uses the JMatPro calculations to obtain a realistic temperature-depended liquid fraction and thermo-physical properties of a relevant multi-component steel. The following thermo-physical properties, calculated by the JMatPro, are considered: solidus temperature, liquidus temperature, enthalpy, thermal conductivity, and specific heat. The density in our numerical model is assumed to be constant and equals the density at the solidus temperature.

2.3 Introduction to Modelling of the Solidification Processes

Mathematical modelling of transport phenomena in the solidification processes of metal alloys is increasingly becoming an important tool for predicting the state of the final product. In such systems, the phase transformation takes place over a range of temperatures, also called the mushy zone. Due to the complicated nature and morphology of the dendritic solidification in the mushy zone, are the detailed microscopic models which account for transport phenomena in the whole system on a microscopic level still beyond the capabilities of today’s computing facilities. Therefore, the models are usually based on the general macroscopic conservation principles and semi-empirical laws that describe the interactions between the solid and liquid phases on a microscopic level [Viskanta, 1990; Ni and Incropera, 1994]. The general conservation principles are applied to an arbitrary fixed control volume, which is larger than a phase element but smaller than the characteristic domain dimension of the system. To derive the governing equations, the following models have been established: Mixture model by Flemings, Mixture continuum model, and Two-phase averaged model.

Mixture model by Flemings

In this approach, the mushy region is treated by volume elements, which contain both liquid and solid phase. Equations, describing the solidification process, heat flow, and species redistribution in the mushy region, are obtained by performing the heat and mass balances over each control volume. The basic model was first derived by Flemings and co-workers [Mahrebian *et al.*, 1970]. They derived an equation to predict the liquid fraction distribution by knowing the velocity and the temperature distribution in the mushy region. The interdendritic flow in the mushy region can be obtained by the Darcy’s law, which approximates the mushy region as a porous medium. Further, the temperature distribution in the mushy region is obtained through the solution of an energy balance in the mushy zone. In the solid and liquid regions, the velocity and temperature distributions are calculated by the single-phase conservation equations. The model equations, describing transport processes in each region, are normally solved by the complicated multi-domain numerical algorithms, which are capable of explicitly tracking the interface boundaries between all three regions. The macro-segregation is then obtained from the equilibrium phase diagram (see Figure 2.2), which accounts that the liquid and the solid phases are in equilibrium.

Mixture continuum model

The mixture continuum model was derived based on the macroscopic conservation principles for dendritic solidification, without considering microscopic equations, by utilizing the continuum theory of mixtures. The solid, the liquid and the mushy regions are not treated separately, but rather one set of equations are derived, which are valid for the entire system. This is the main advantage over the previously described mixture theory, but in order to make the problem solvable, several simplifications and assumptions are introduced [Bennon and Incropera, 1987; Voller *et al.*, 1989]. The complete mixture continuum model was first proposed and derived by [Bennon and Incropera, 1987]. In their model, the following assumptions were used to close the problem: the solid and the liquid phases in the mixture continuum are in equilibrium state, and the velocity of the solid phase is prescribed. Almost all numerical solutions of the heat and fluid flow in the continuous casting of steel process are based on this model and assumptions [Aboutalebi, 1993; Seyedein and Hasan, 1997; Ha *et al.*, 2003]. Our equations are derived by the same mixture continuum approach and a detail description of the basic principles and derivation are shown in Section 2.5.

Two-phase averaged model

The main disadvantage of all mixture formulations is that they do not explicitly provide any relationships between the macroscopic and the microscopic parameters, such as the phase interactions. Usually, they assume a complete thermal, chemical and mechanical equilibrium between the solid and liquid phases in the averaging volume of mixture. However, this assumption is not valid for solidification of multi-component mixtures, where strong gradients and discontinuities can occur on a microscopic scale. Also mixture models assume that the velocity of the solid phase is equal to zero, or it is equal to the prescribed value, i.e. casting velocity in the continuous casting of steel. An alternative approach to the mixture models involves the use of the volume averaging procedure which can be strongly linked to the microscopic conditions. This technique was first introduced for the solidification problem by [Beckermann and Viskanta, 1988], and was later used to develop a more general two-phase averaged model for transport phenomena during solidification [Ni and Beckermann, 1991]. In this approach, each phase is treated separately and the interactions between the phases are considered explicitly. The macroscopic equations for each phase are averaged over an averaging volume, containing both liquid and solid. The averaged equations are valid in every region of the multi-phase system, including the pure solid and the pure liquid regions. A constitutive linkage between the macroscopic and the microscopic transport processes is established by constitutive relations for the surface tension, pressure, interfacial transfers due to phase-change, interfacial stress, heat and species transfer, etc. A detailed explanation and derivation of the model are given in [Ni and Beckermann, 1991; Beckermann and Viskanta, 1993]. A drawback of this formulation is that it includes two times more conservative equations than the mixture model.

2.4 Treatment of Solidification Region from the Fluid Dynamics Perspective

The solidification process of the steel in the strand is characterized by the following three regions: pure liquid, mushy and pure solid. The mushy region is further divided into the slurry region and the porous media (see Figure 2.3). The question arises, how the solidification affects the convection in each region, and further, how to treat those effects in the physical model.

The pure liquid region contains the molten steel and various inclusions, i.e. impurities, non-metallic inclusions and powder, which are floating in the liquid. In this region, the solidification does not occur, and only the body forces (buoyancy and solute forces) are acting on the convection in the physical model. Due to the strong forced convection, the inclusions are moving along with the flow of the molten steel, and can be assumed since their concentration is low to have no effects on the flow pattern.

The slurry region consists of freely floating equiaxed dendrites and the liquid phase. Most of the equiaxed dendrites are created by solidification process at the liquidus inter-phase, while some of them are resulting from the break-off of the columnar dendrites. They can flow back into the pure liquid region and re-melt again, while some of them stick onto the columnar dendrites. The fluid flow modelling in this region is far more complex than in a pure liquid region. In almost all cases of the numerical models of the continuous casting process, the slurry region is not considered. However, it could be modelled by assuming that the solid phase is moving with the same velocity as the liquid phase [Voller *et al.*, 1998]. By using the given velocity assumption, the two-fluid equations can be combined into a one-phase equation. The effective diffusion coefficients, such as the effective dynamic viscosity and the effective thermal conductivity, are calculated as the average of the single phase coefficients [Voller *et al.*, 1998]. The effects of the solidification are considered by specifying a large solid viscosity μ_S, which forces the velocity to be equal to the system velocity. In this case, the slurry region is the only region considered in the mushy zone, the system velocity is the velocity of a pure solid. While, in the case with considered slurry region and the porous media region, the problem arises, how to treat the coupling of both regions. Here, it is worth to mention the extension of the mixture continuum model [Ni and Incropera, 1994], which involves the modelling of the solid movement in the form of floating or settling crystals.

The porous media involves a solid matrix consisting of the columnar dendrites and the interdendritic liquid phase, filled between the dendrites. Between the dendrites, the interdendritic liquid is flowing or it is captured, depending on the size of the pores. The size of the pores between the dendrites is defined by the primary and secondary arm spacing. In the early stage of formation this region, the pores are large enough to allow flow of the liquid phase through the porous matrix. While in the later stages, the pores are so small that they could capture the liquid between the dendrites. The captured liquid is therefore moving along with the porous matrix with the prescribed casting velocity. From the numerical point of view, the flow in the porous matrix is treated by the Darcy law, explained in the continuation of this chapter.

In a pure solid region, the material is completely solidified, and forms the solid shell. The solid shell is moving in the casting direction with the withdrawal speed, determined by the dummy-bar and powered rolls motion.

The physical model in the present dissertation involves only three regions: pure liquid, porous media, and pure solid.

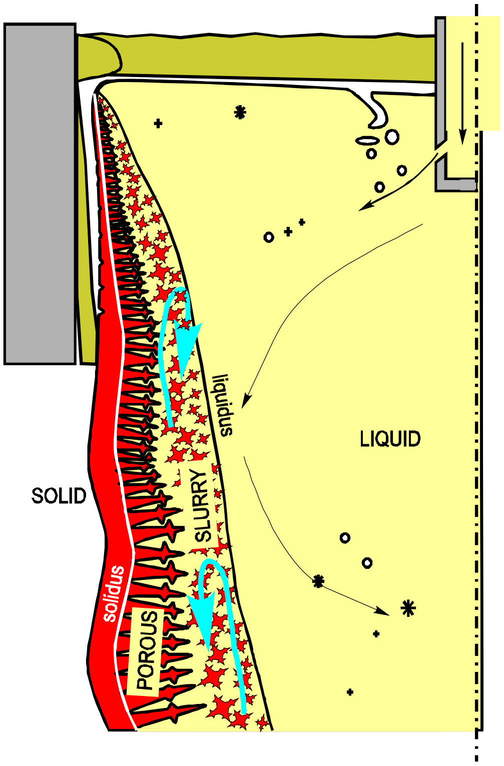

Figure 2.3: Solidification process in the strand.

2.5 Mixture Continuum Model

In the mixture continuum approach, mass, momentum and energy continuum equations are obtained by summing-up the general phase conservation equation over each phase, where the interactions of one phase with the other phases are considered by including the source terms in the individual phase conservation equations. The derived system of continuum equations is valid throughout the physical domain, which comprises solid, liquid and mushy zone. The model is easily implemented by single-phase numerical procedures but has several limitations, such as:

- the thermal and the species non-equilibrium is not treated,

- the interfacial species transfer is neglected,
- the specific interfacial geometry and the solid structures have not been incorporated into the model, and
- the linkage between the physical phenomena occurring on the macroscopic and the microscopic scales are weak in general.

A continuum (see Figure 2.4) is composed of $N_\wp$ distinct separable phases $\wp$. Any location $\mathbf{p}$ can be occupied by all phases. The mean velocity of the phase $\wp$, relative to a fixed reference frame, is termed as the phase velocity $\mathbf{u}_\wp$. The partial density $\bar{\rho}_\wp$ of the phase $\wp$, which describes the relationship between the phase density $\rho_\wp$ and the phase volume fraction $f_\wp$, can be expressed as

$$\bar{\rho}_\wp = f_\wp \rho_\wp, \tag{2.49}$$

where $f_\wp$ is the volume fraction of the phase $\wp$, i.e.

$$f_\wp = \frac{V_\wp}{V}, \tag{2.50}$$

with $V_\wp$ and V standing for volume of phase $\wp$ and the volume of continuum, respectively. Then the mixture density and the averaged mixture velocity of the mixture continuum are defined as

$$\rho = \sum_{N_\wp} \bar{\rho}_\wp, \tag{2.51}$$

$$\mathbf{u} = \frac{1}{\rho} \sum_{N_\wp} f_\wp \rho_\wp \mathbf{u}_\wp. \tag{2.52}$$

The relationship between the phase volume fractions is explicitly given by the following statement, i.e. no porosity is assumed

$$\sum_{N_\wp} f_\wp = 1. \tag{2.53}$$

A general transport equation of a scalar $\phi_\wp$ of the phase $\wp$ in a multiphase mixture can be expressed in a differential form as

$$\frac{\partial}{\partial t}\left(\bar{\rho}_\wp \phi_\wp\right) + \nabla \cdot \left(\bar{\rho}_\wp \mathbf{u}_\wp \phi_\wp\right) = -\nabla \cdot \left(f_\wp \mathbf{J}_\wp\right) + f_\wp S_\wp, \tag{2.54}$$

where $\mathbf{J}_\wp$ and $S_\wp$ are the diffusion flux vector and the volumetric source terms, respectively. The conservation equations of the mixture are then obtained by the summation of the individual equations of phases.

The complete derivation of the conservation equations for binary alloy solidification has been explained in detail in [Bennon and Incropera, 1987]. In the present dissertation, only the final form of each equation is represented.

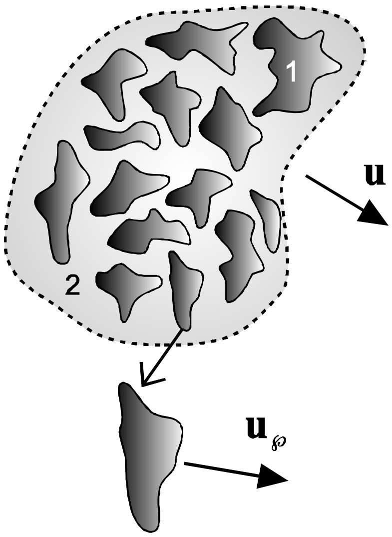

Figure 2.4: Multiphase continuum. $\mathbf{u}$: mass averaged mixture velocity. $\mathbf{u}_\wp$: velocity of phase $\wp$.

2.5.1 Turbulence Modelling in Porous Media

Turbulence modelling in porous media remains an open issue in engineering and science. There is a little attention given to this topic [Antohe and Lage, 1997], especially in the modelling of the solid-liquid alloy solidification. The complete derivation of the macroscopic transport equations for mass, momentum, energy, turbulent kinetic energy, and the dissipation rate was for the first time made in great detail by Antohe and Lage [Antohe and Lage, 1997]. They assumed the incompressible turbulent flow of the fluid in porous media where the solid phase is assumed to be rigid, isotropic and fixed. The derivation starts by writing the instantaneous form of the momentum equation for the liquid velocity in porous media. Then the same equation was time-averaged by the Reynolds approach. The transport equation for the turbulent kinetic energy is obtained by subtracting the time-averaged momentum equation from the instantaneous momentum equation, and multiplying it by the fluctuating velocity. The derived equation is then time-averaged to obtain the time-averaged transport equation for the turbulent kinetic energy. The transport equation for the dissipation rate is obtained by a similar procedure. Additional terms, such as the Darcy's (microscopic viscous drag) term, Forcheimmer (microscopic form drag) term, Brinkman (viscous diffusion) term, and Bousinesq-Oberbeck (buoyancy) term, which are included in the momentum equation as the source term, describing the physical phenomena in porous media, remains also in the derived equation for the turbulent kinetic energy and the dissipation rate.

In modelling of the continuous casting of steel, the majority of the researchers are using a single-phase formulation of all involved equations, i.e. mass, momentum, energy, the turbulent kinetic energy, and the dissipation rate, to describe the solidification process in the mushy region, which is treated as a porous medium. In the single-phase formulation, the mushy region is treated as a single-phase, where the solidification effects on the convection are considered by the Darcy's source term. The Darcy's source term in the momentum equation damps the velocity in the mushy zone to the prescribed velocity of the solid phase. How fast the Darcy's term damps the velocity field, greatly depends on the permeability of the porous media. In the solidification of alloys, the permeability is usually described by the Kozeny-Karman relation, in which the permeability is a function of a liquid fraction and the morphology constant of the porous matrix. The morphology constant is a free parameter, and defines how fast the Darcy's term damps the velocity field. Some researches [Shyy *et al.*, 1992; Lan and Khodadadi, 2001; Wiwatanapataphee *et al.*, 2004] set the value around 10^6 ($\mathrm{N{\cdot}s{\cdot}m^{-4}}$) as the mushy zone constant, but some others [Aboutalebi *et al.*, 1995; Seyedein and Hasan, 1997; Kim *et al.*, 2000] use the relation by [Minakawa *et al.*, 1985] as the permeability constant, which yields the value around $10^{10}\,\mathrm{m^{-2}}$. The transport equations of the turbulence model are also described in a single-phase form without additional terms describing the turbulent effects. This yields the same equations as defined for the turbulent flow of a pure liquid. Prescott and Incropera [Prescott and Incropera, 1995] used the mixture continuum formulation [Bennon and Incropera, 1987] to describe the turbulent effects to a binary alloy solidification. The transport equations for the turbulent kinetic energy and the dissipation rate are written in a single-phase formulation, where the turbulent viscosity is treated as the liquid one. In their work, the Darcy's term is added to the transport equation for the turbulent kinetic energy, but the transport equation for the dissipation rate is defined without Darcy's term. A similar approach was used by [Aboutalebi *et al.*, 1995], however the Darcy's term was added in both equations, i.e. for the turbulent kinetic energy and the dissipation rate.

In the present dissertation, we use the approach by [Antohe and Lage, 1997] to derive the macroscopic mixture transport equations for the turbulent kinetic energy and the dissipation rate.

The mass, momentum and energy time-averaged equations are obtained in the following way. First, each transport equation for an arbitrary scalar quantity ϕ

for each phase is summed together to obtain the mixture form. Then, the derived equations are time-averaged to get the final equations.

2.5.2 Mass Conservation

The mass conservation equation is derived from equation (2.54) with $\phi_{\wp}=1$, $\mathbf{J}_{\wp}=0$ and $S_{\wp}=\dot{M}_{\wp}$, where $\dot{M}_{\wp}$ is production of phase $\wp$. Because $\sum_{N_{\wp}} f_{\wp}\dot{M}_{\wp}=0$, the final time-averaged form is written as

$$\frac{\partial\rho}{\partial t}+\nabla\cdot\left(\rho\bar{\mathbf{u}}\right)=0. \tag{2.55}$$

2.5.3 Momentum Conservation

The momentum equation is derived from the equation (2.54) with $\phi_{\wp}=\mathbf{u}_{\wp}$, $\mathbf{J}_{\wp}=-p_{\wp}\mathbf{I}+\left(2\mu\mathbf{S}\right)_{\wp}$ and $\mathbf{S}_{\wp}=\mathbf{F}_{p\wp}+\rho_{\wp}\mathbf{B}_{f\wp}$, i.e.

$$\frac{\partial}{\partial t}\left(\rho\mathbf{u}\right)+\nabla\cdot\left(\rho\mathbf{uu}\right)=-\nabla P+\nabla\cdot\left[2\mu_L\frac{\rho}{\rho_L}\mathbf{S}\right]+\mathbf{F}_p+\mathbf{B}_f, \tag{2.56}$$

where $\mathbf{F}_p$ and $\mathbf{B}_f$ are the phase interaction force in the multiphase region and the buoyancy force, respectively.

In the present dissertation, the multiphase region (mushy region) is characterized by a permeable solid matrix, which can be stationary or its motion is prescribed by the predefined constant velocity, as in continuous casting processes. For such systems, the fluid flow in the mushy region can be modelled as flow through porous media, where the Darcy law can be used. By the Darcy's law, the phase interaction force is proportional to the superficial liquid velocity relative to the velocity of the porous solid, i.e.

$$\mathbf{F}_p=\frac{\mu_L}{K}f_L\mathbf{u}_r, \tag{2.57}$$

where K is the permeability and $\mathbf{u}_r=\mathbf{u}_L-\mathbf{u}_S$ is the relative velocity. The permeability can be described as a function of the porosity or a function of the liquid fraction. In the process of continuous casting of steel, the velocity of the solid phase is constant and prescribed in advance, and assuming that the phase densities are constant, the final equation of the phase interaction force [Bennon and Incropera, 1987] is defined as

$$\mathbf{F}_p=-\frac{\mu_L}{K}\frac{\rho}{\rho_L}\left(\mathbf{u}-\mathbf{u}_S\right). \tag{2.58}$$

The permeability in equation (2.58) is defined as a function of liquid fraction in such a way, that when the liquid fraction decreases, permeability also decreases, and forces all the velocities to value zero in the case of stationary solid phase, or to the prescribed constant velocity in the case of continuously moving solid phase (rigid body), such as in the continuous casting. A well known expression for obtaining the permeability is the Kozeny-Carman equation

$$K = \frac{f_L^3}{C\left(1 - f_L\right)^2}, \tag{2.59}$$

where C is a morphology constant of the porous media. The buoyancy body force $\mathbf{B}_f$ in equation (2.56) is defined by the following relation

$$\mathbf{B}_f = \rho_L \beta_T \mathbf{g}\left(T - T_{ref}\right), \tag{2.60}$$

where β_T, $\mathbf{g}$ and T_{ref} are the thermal expansion coefficient of the fluid, the gravitational acceleration, and the reference temperature, respectively.
The time-averaged momentum conservation equation (2.56) of the mixture is obtained as

$$\frac{\partial\left(\rho\bar{\mathbf{u}}\right)}{\partial t} + \nabla\cdot\left(\rho\bar{\mathbf{u}}\bar{\mathbf{u}}\right) = -\nabla\bar{P} + \nabla\cdot\left(2\mu_L\frac{\rho}{\rho_L}\bar{\mathbf{S}}\right) + \mathbf{F}_p + \mathbf{B}_f - \nabla\cdot\left(\overline{\rho\mathbf{u}'\mathbf{u}'}\right). \tag{2.61}$$

In the equation (2.61), the last term is the Reynolds-stress tensor, which is defined by the equation (2.13). After substituting the equation (2.13) into the equation (2.61), we get the final time-averaged momentum equation

$$\frac{\partial}{\partial t}\left(\rho\bar{\mathbf{u}}\right) + \nabla\cdot\left(\rho\bar{\mathbf{u}}\bar{\mathbf{u}}\right) = -\nabla\bar{P} + \nabla\cdot\left[2\left(\mu_L\frac{\rho}{\rho_L} + \mu_t\right)\bar{\mathbf{S}}\right] - \frac{2}{3}\rho\nabla k +$$

$$\mathbf{F}_p + \mathbf{B}_f\,. \tag{2.62}$$

2.5.4 Energy Conservation

A mixture continuum energy conservation equation for binary solid-liquid phase-change is derived from the equation (2.54) with $\phi_\wp = h_\wp$, $\mathbf{J}_\wp = \lambda_\wp\nabla T$ and $S_\wp = \dot{E}_\wp$, i.e.

$$\frac{\partial}{\partial t}\left(\rho h\right) + \nabla\cdot\left(\rho_S f_S \mathbf{u}_S h_S + \rho_L f_L \mathbf{u}_L h_L\right) = \nabla\cdot\left(\lambda\nabla T\right). \tag{2.63}$$

In equation (2.63) h is defined as the mixture enthalpy, i.e.

$$h = \frac{\left(f_S \rho_S h_S + f_L \rho_L h_L \right)}{\rho}, \tag{2.64}$$

where the constitutive temperature-enthalpy relationship h_S and h_L are

$$h_S = \int_{T_{ref}}^{T} c_{pS} dT, \tag{2.65}$$

$$h_L = \int_{T_{ref}}^{T_S} c_{pS} dT + \int_{T_S}^{T} c_{pL} dT + h_m = h_S\left(T\right) + \int_{T_S}^{T} \left(c_{pL} - c_{pS} \right) dT + h_m, \tag{2.66}$$

respectively [Šarler and Kuhn, 1998a]. The mixture thermal conductivity λ is defined through the mixture rule, i.e.

$$\lambda = f_S \lambda_S + f_L \lambda_L. \tag{2.67}$$

The time-averaging procedure of the equation (2.63) gives the following time-averaged energy equation

$$\frac{\partial}{\partial t}\left(\rho \bar{h}\right) + \nabla \cdot \left(\rho_S f_S \bar{\mathbf{u}}_S \bar{h}_S + \rho_L f_L \bar{\mathbf{u}}_L \bar{h}_L \right) = \nabla \cdot \left(\lambda \nabla \bar{T} \right) - \nabla \cdot \overline{\rho_S f_S \mathbf{u}'_S h'_S} - \nabla \cdot \overline{\rho_L f_L \mathbf{u}'_L h'_L}. \tag{2.68}$$

The last two terms in the equation (2.68) are known to be the turbulent heat fluxes. They are modelled by the Boussinesq formula. The modelled turbulent heat flux is prescribed as

$$\overline{\rho_\wp \mathbf{u}'_\wp h'_\wp} = -\frac{\mu_{t\wp}}{\sigma_t} \nabla \bar{h}_\wp, \tag{2.69}$$

where σ_t is the turbulent Prandtl number, which depends on the selected EVM. As already discussed, its value is around 1 [Launder and Sharma, 1974; Willcox, 1993]. Because we are dealing with the systems where the velocity of solid phase is zero or constant, the fluctuating part of the velocity of solid phase $\mathbf{u}'_S$ is equal to zero, i.e.

$$\overline{f_S \rho_S \mathbf{u}'_S h'_S} = 0, \tag{2.70}$$

while the second turbulent heat flux has a non-zero value, and it is defined by the following equation

$$\overline{f_L \rho_L \mathbf{u}'_L h'_L} = -f_L \frac{\rho_L \nu_t}{\sigma_t} \nabla \bar{h}_L, \tag{2.71}$$

where ν_t is the turbulent kinematic viscosity, i.e.

$$\nu_t = c_\mu f_\mu \frac{k^2}{\varepsilon}. \tag{2.72}$$

2.5.5 Transport Equations of the Turbulence Model

Turbulence modelling by the LRN turbulent models requires solving two additional mixture transport equations for k and ε. Their derivation is tedious and complex to understand, but explained in great details in various works [Antohe and Lage, 1997; Bredberg, 1999; Davidson, 2003]. By considering these works, the derivation of the mixture form of the momentum equation is the same as for the single-phase [Bredberg, 1999; Davidson, 2003], except an additional source term is involved due to the Darcy's term is the mixture momentum equation [Antohe and Lage, 1997]. Also the density ratio in the diffusive term of the mixture momentum equation remains in both equations of the turbulence model. The final form of the two transport equations are

$$\frac{\partial}{\partial t}(\rho k) + \nabla \cdot (\rho \bar{\mathbf{u}} k) = \nabla \cdot \left[\frac{\rho}{\rho_L}\left(\mu_L + \frac{\mu_t}{\sigma_k} \right) \nabla k \right] + P_k + G_k - \rho\varepsilon + \rho D + F_{pk}, \tag{2.73}$$

$$\frac{\partial}{\partial t}(\rho \varepsilon) + \nabla \cdot (\rho \bar{\mathbf{u}} \varepsilon) = \nabla \cdot \left[\frac{\rho}{\rho_L}\left(\mu_L + \frac{\mu_t}{\sigma_\varepsilon} \right) \nabla \varepsilon \right] + \left[c_{1\varepsilon} f_1 (P_k + c_{3\varepsilon} G_k) - c_{2\varepsilon} f_2 \rho\varepsilon \right] \frac{\varepsilon}{k} + \rho E + F_{p\varepsilon}, \tag{2.74}$$

where F_{pk} and $F_{p\varepsilon}$ represent additional damping source terms for k and ε, respectively. They both have a similar form and meaning as the Darcy's term, equation (2.58), in the momentum equation (2.62), i.e.

$$F_{pk} = -\frac{\mu_L}{K}\frac{\rho}{\rho_L} k, \tag{2.75}$$

$$F_{p\varepsilon} = -\frac{\mu_L}{K}\frac{\rho}{\rho_L} \varepsilon. \tag{2.76}$$

In both equations (2.73) and (2.74), the G_k is the generation of turbulence due to the buoyancy force, defined as

$$G_k = -g\beta_T \frac{\nu_t}{\sigma_t}\frac{\partial T}{\partial p_y}. \tag{2.77}$$

G_k is multiplied in the equation (2.74) by the closure coefficient $c_{3\varepsilon}$, which is in the present dissertation calculated by the following relation [Henkes *et al.*, 1991]

$$c_{3\varepsilon} = \tanh\left|\frac{\overline{u}_{\parallel}}{\overline{u}_{\perp}}\right|. \tag{2.78}$$

In the above equation, $\overline{u}_{\parallel}$ and $\overline{u}_{\perp}$ are the velocity components, parallel and perpendicular to the gravitational vector, respectively.

Also other approaches, without Darcy's terms, can be used to account for the solidification effects to the turbulent flow in a porous media, such as modifying the damping function f_μ in the turbulence model. In [Shyy *et al.*, 1992], the authors suggested the following relation

$$f_\mu = f_\mu\sqrt{f_L}\,. \tag{2.79}$$

This technique was also used in modelling of the heat and fluid flow with solidification in the continuous casting processes [Lan and Khodadadi, 2000].

2.6 The Complete System of the Macroscopic Conservation Equations

In this section, the complete set of previously described governing equations for solving the incompressible turbulent flow with solidification is given. The derived system of macroscopic transport equations describes the physical model of the metal solidification in the continuous casting process of steel. All other numerical examples in the present dissertation rely on this system of equations, where some terms (Darcy's terms, body-force terms, etc.) are neglected or modified based on the physical nature of the treated such problem. From this point on, an over-bar of the time-averaged variables is omitted.

The conservation equations for the mass, momentum, energy, turbulent kinetic energy, and dissipation rate are, respectively, given as

$$\nabla\cdot\mathbf{u} = 0, \tag{2.80}$$

$$\begin{aligned}\rho\frac{\partial\mathbf{u}}{\partial t} + \rho\nabla\cdot(\mathbf{u}\mathbf{u}) = -\nabla P + \nabla\cdot\left\{(\mu_L+\mu_t)\left[\nabla\mathbf{u}+(\nabla\mathbf{u})^{\mathrm{T}}\right]\right\} - \frac{2}{3}\rho\nabla k - \\ \mu_L\frac{C(1-f_L)^2}{f_L^3}(\mathbf{u}-\mathbf{u}_S) + \rho\beta_T\mathbf{g}(T-T_{ref}),\end{aligned} \tag{2.81}$$

$$\rho\frac{\partial h}{\partial t}+\rho\nabla\cdot(\mathbf{u}h)=\nabla\cdot(\lambda\nabla T)+\rho\nabla\cdot\left(\mathbf{u}h-f_S\mathbf{u}_S h_S-f_L\mathbf{u}_L h_L\right)+ \nabla\cdot\left(f_L\frac{\rho_L\nu_t}{\sigma_t}\nabla h_L\right), \tag{2.82}$$

$$\rho\frac{\partial k}{\partial t}+\rho\nabla\cdot(\mathbf{u}k)=\nabla\cdot\left[\left(\mu_L+\frac{\mu_t}{\sigma_k}\right)\nabla k\right]+P_k+G_k-\rho\varepsilon+\rho D- \mu_L\frac{C\left(1-f_L^2\right)}{f_L^3}k, \tag{2.83}$$

$$\rho\frac{\partial \varepsilon}{\partial t}+\rho\nabla\cdot(\mathbf{u}\varepsilon)=\nabla\cdot\left[\left(\mu_L+\frac{\mu_t}{\sigma_\varepsilon}\right)\nabla \varepsilon\right]+ \left[c_{1\varepsilon}f_1\left(P_k+c_{3\varepsilon}G_k\right)-c_{2\varepsilon}f_2\rho\varepsilon\right]\frac{\varepsilon}{k}+\rho E-\mu_L\frac{C\left(1-f_L^2\right)}{f_L^3}\varepsilon. \tag{2.84}$$

2.7 Initial Conditions

It is well known that all five transport equations (2.80), (2.81), (2.82), (2.83) and (2.84) are strongly coupled. So it is very important how we choose the initial conditions for each transport variable. The initial condition for velocity field is obtained by solving the potential field

$$\nabla^2\varphi=0, \tag{2.85}$$

where φ stands for velocity potential. Laplace equation (2.85) is solved by the sparse-matrix approach [Lee *et al.*, 2003], presented in Section 3.5. The following boundary conditions are used:

- At the inlet boundaries and solid walls, the Neumann boundary conditions for velocity potential are prescribed

  $$\frac{\partial\varphi}{\partial\mathbf{n}_\Gamma}=-\mathbf{u}\cdot\mathbf{n}_\Gamma, \tag{2.86}$$

  where $\mathbf{n}_\Gamma$ is a normal vector on boundary Γ.
- At the outlet boundaries, the Dirichlet boundary conditions for velocity potential are set to

  $$\varphi=0. \tag{2.87}$$

After solving the potential flow field, the velocity field in the domain is obtained by the following relation

$$\mathbf{u} = \nabla \varphi . \tag{2.88}$$

This procedure guarantees the solenoidality of the initial velocity field, which helps to improve the convergence of the solution during the early stages of such simulation.

The initial temperature field is set to a constant value for all computations in the present dissertation.

In order to prescribe the proper initial conditions for k and ε, two different techniques might be employed:

- Use of the uniform profile for both k and ε. A few thousand time steps have to be usually performed with smaller time step to achieve the consistency between the velocity, pressure, k and ε. When a large mismatch of the transport variables at the initial times is reduced, larger time steps can be used.
- Use of the assumption of the turbulent equilibrium [Yoder and Georgiadis, 1999], where the production of the k equals the rate of dissipation. In order to use this technique, another turbulence model, usually algebraic model, is first run to get initial values of the turbulent viscosity.

In the present dissertation, the turbulence transport variables are initialized by the first approach.

2.8 Boundary Conditions

Four different types of boundaries are considered in the present dissertation: inlet, outlet, symmetry, and wall. The following boundary conditions are used at these boundaries:

- At the inlet boundary, the Dirichlet boundary conditions for velocity components, temperature, k and ε are prescribed.
- At the outlet boundary, the Neumann boundary conditions for velocity components, temperature, k and ε are prescribed and set to zero, i.e.

$$\frac{\partial \mathbf{u}}{\partial \mathbf{n}_\Gamma} = 0 , \ \frac{\partial T}{\partial \mathbf{n}_\Gamma} = 0 , \ \frac{\partial k}{\partial \mathbf{n}_\Gamma} = 0 , \ \frac{\partial \varepsilon}{\partial \mathbf{n}_\Gamma} = 0 . \tag{2.89}$$

- At the symmetry line, the same Neumann boundary conditions as for the outlet boundary are used, except for the velocity component, perpendicular to the symmetry line, where the Dirichlet boundary conditions are prescribed and set to zero.

- At the wall, the Dirichlet no-slip boundary conditions are set, which implies that the velocity components, k and ε are all set to zero. When using AKN turbulence model, ε is set by the equation (2.36). Regarding the temperature, Dirichlet, Neumann, or Robin boundary conditions can be prescribed.

3 Local Radial Basis Function Collocation Method

RBF approximations have been demonstrated to be most useful in many scientific and technological fields. Applications of such approximations in the context of interpolation are manifold. This chapter represents the LRBFCM for interpolating scattered data and for solving the PDEs. Some of the most important types of RBFs are presented. The RBFCM for interpolating scattered data and solving the PDE [Kansa, 1990a; Kansa, 1990b] is introduced. Its local version, i.e. LRBFCM [Šarler and Vertnik, 2006], is derived and explained in details.

3.1 Radial Basis Functions

RBFs can be expressed in the following form

$$\psi_i(r) = \psi(\mathbf{p} - \mathbf{p}_i)\,;\ \psi_i : \mathbb{R}^d \to \mathbb{R}\,, \tag{3.1}$$

and depend only on the distance between the position vector $\mathbf{p} \in \mathbb{R}^d$ and the reference position vector $\mathbf{p}_i \in \mathbb{R}^d$ ($\mathbf{p}_i$ is usually called the centre) and are radially symmetric. This means that any rotation makes no difference to the function value. This explains the term *radial*. In equation (3.1), $\mathbb{R}$ represents real number, d spatial dimension, and r radial distance.
For two-dimensional Cartesian system, the position vector $\mathbf{p}$ is represented by

$$\mathbf{p} = p_x \mathbf{i}_x + p_y \mathbf{j}_y\,, \tag{3.2}$$

where p_x, p_y are the Cartesian coordinates and $\mathbf{i}_x$, $\mathbf{j}_y$ Cartesian base vectors of the position vector $\mathbf{p}$. The radial distance between two vectors is defined by the Euclidean norm

$$r = \left\| \mathbf{p} - \mathbf{p}_i \right\| = \sqrt{(p_x - p_{xi})^2 + (p_y - p_{yi})^2}\,. \tag{3.3}$$

To explain *basis function* part, let's suppose we have fixed certain reference vector points (called centres) $\mathbf{p}_1, \ldots, \mathbf{p}_N \in \mathbb{R}^d$ and the following function $F(\mathbf{p})$

which is represented as a linear combination of the function ψ centred at the points $\mathbf{p}_i$

$$F(\mathbf{p}) \approx \sum_{i=1}^{N} \alpha_i \psi_i(\mathbf{p}); \; \psi_i(\mathbf{p}) = \psi(\mathbf{p} - \mathbf{p}_i), \tag{3.4}$$

where N and α_i stands for a number of points and expansion coefficients, respectively. So we have approximated a function $F(\mathbf{p})$ which is in the function space spanned by the basis functions $\psi_i(\mathbf{p})$. Some commonly used forms of the RBF are:

- Gaussian (GA) (Figure 3.1a)

$$\psi(r) = e^{-(cr)^2}, \tag{3.5}$$

- multiquadric (MQ) (Figure 3.1b)

$$\psi(r) = \sqrt{r^2 + c^2}, \tag{3.6}$$

- inverse multiquadric (IMQ) (Figure 3.1c)

$$\psi(r) = \frac{1}{\sqrt{r^2 + c^2}}, \tag{3.7}$$

- thin plate spline (TPS) (Figure 3.1d)

$$\psi(r) = \left(\frac{r}{c}\right)^2 \log\left(\frac{r}{c}\right). \tag{3.8}$$

In all numerical examples in the present dissertation, only the MQ-RBF are used. The choice is made on the basis of multivariate interpolation tests [Franke, 1982], where the best accuracy was found with MQ-RBFs. This function include the free parameter c, which has to be predetermined or set as a part of the solution. Since there is still no rigorous mathematical background for its determination, the parameter is chosen based on the numerical experiments. The MQ-RBF is plotted in Figure 3.2 as a function of the free parameter.

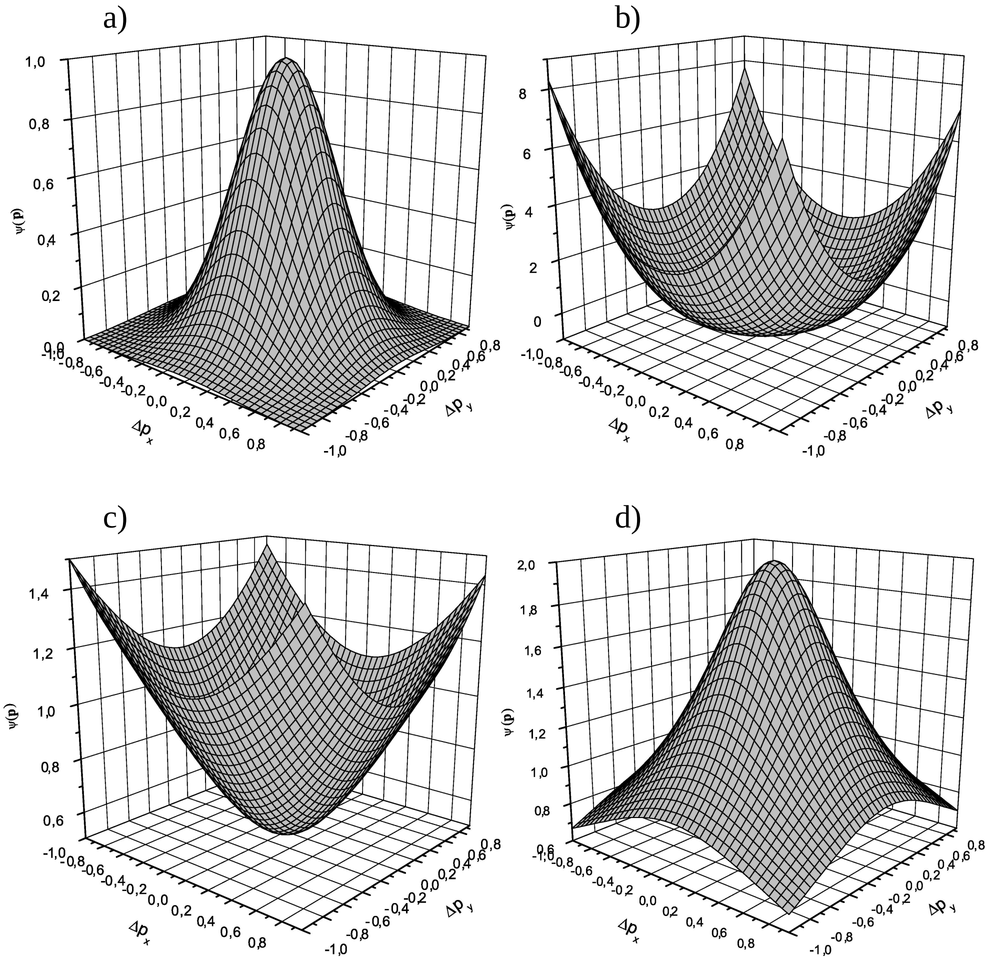

Figure 3.1: Some of the most commonly used RBFs. a) GA-RBF, b) TPS-RBF, c) MQ-RBF, and d) IMQ-RBF. All functions are calculated with the free parameter $c = 0.5$.

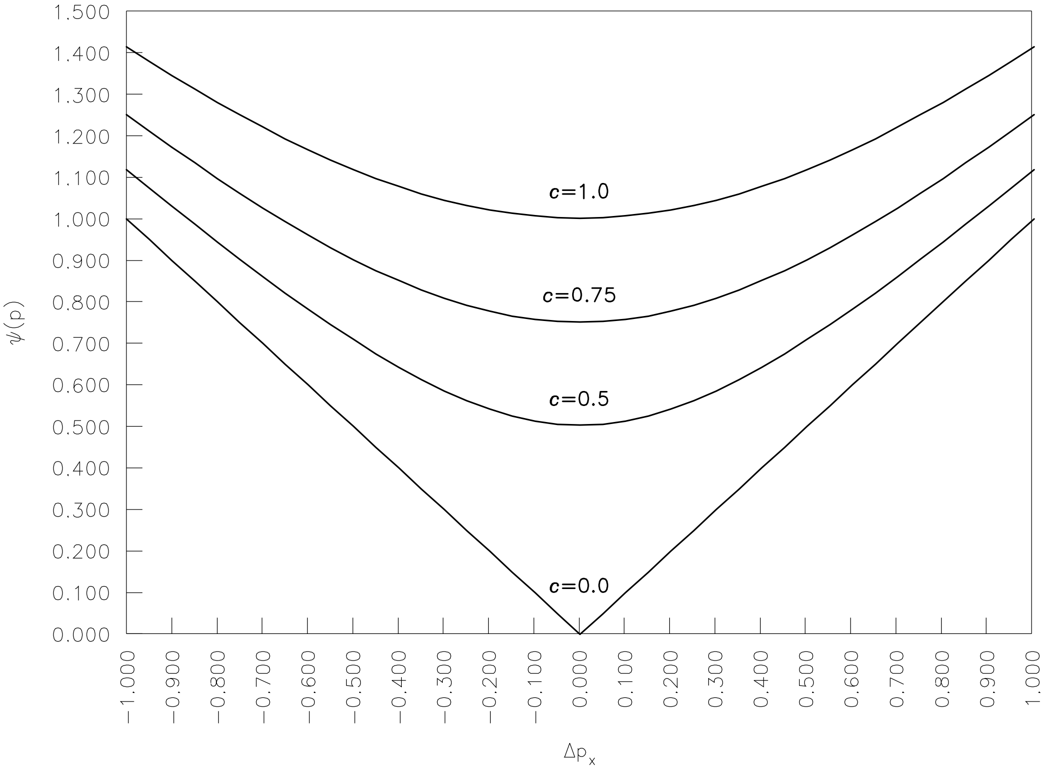

Figure 3.2: MQ-RBF with different values of the free parameter.

3.2 Radial Basis Function Collocation Method for Interpolating Scattered Data

A problem frequently occurring in science and engineering is the approximation of a function F, the value of which is known only on a set of points. One way to obtain such an approximation is by interpolation. For one-dimensional (1D) problems, many methods exist for solving this problem. Most of them (e.g. polynomial and piecewise polynomial splines) involve the same general idea: for a given set of N data points $p_{x_1},\dots,p_{x_N}\in\mathbb{R}$ and corresponding data values $f_1,\dots,f_N\in\mathbb{R}$, a set of basis functions $\psi_1(p_x),\dots,\psi_N(p_x)\in\mathbb{R}$ is chosen such that a linear combination of these functions satisfies the interpolation conditions. To be more specific, a function $F(p_x)$ is sought of the form

$$F(p_x)\approx\sum_{i=1}^{N}\alpha_i\psi_i(p_x), \tag{3.9}$$

such that $F\left(p_{x_i}\right)=f_i$ for $i=1,\dots,N$. The interpolation conditions lead to a linear system of equations which determines the expansion coefficients α_i as

$$\sum_{i=1}^{N} \alpha_i \psi_i \left(p_{x\,j} \right) = f_j \;,\; j = 1,\dots,N \;. \tag{3.10}$$

The procedure is also depicted as a block diagram in Figure 3.3. For many choices of the basis functions $\psi_i \left(p_x \right)$, this linear system is guaranteed to be non-singular, whenever the data points $p_{x_1},\dots,p_{x_N} \in \mathbb{R}$ are distinct.

For data sets in more than one-dimension, the prescribed approach with polynomial basis (independent of the data points) no longer works. It can be shown that there exist distinct data sets, for which linear system of equation for determining the expansion coefficients becomes singular (i.e. there does not exist an interpolation in the form of equation (3.9)). However, with piecewise polynomial splines, it is possible to interpolate data in two and three dimensions. This technique works very well for gridded or otherwise highly regularly distributed data sets. For scattered data sets, we usually need a triangulation, which is not a trivial task for complex two and especially for three dimensional problems. The reason for this is that it has to be decided where the piecewise polynomials lie and where they are joined smoothly together.

Instead of taking a linear combination of a set of basis functions that are independent of the data points, one takes a linear combination of translates of a single basis function that is radial symmetric about its centre. This approach, pioneered by Hardy [Hardy, 1971], is referred to as the MQ method. Hardy used MQ-RBF as the basis function to solve a problem from cartography. Namely, given a set of sparse, scattered measurements from some source points on a topographic surface, construct a "satisfactory" continuous function that represents the surface.

The RBFCM is a generalized version of the Hardy's MQ method, and is defined as follows: Given a set of N distinct data points $\mathbf{p}_1,\dots,\mathbf{p}_N \in \mathbb{R}^d$ and corresponding data values $f_1,\dots,f_N \in \mathbb{R}$, the RBF interpolation is given by

$$F\left(\mathbf{p}\right) \approx \sum_{i=1}^{N} \alpha_i \psi_i \left(\mathbf{p}\right) \;;\; r_i = \left\| \mathbf{p} - \mathbf{p}_i \right\| , \tag{3.11}$$

where $\psi\left(r_i\right)$ is some radial function and $\|\cdot\|$ is the Euclidean norm (3.3). The expansion coefficients α_i are determined from the interpolation conditions

$$F\left(\mathbf{p}_i\right) = f_i \;;\; i = 1,\dots,N \;, \tag{3.12}$$

which leads to the following linear system of equations

$$\mathbf{\Psi} \boldsymbol{\alpha} = \mathbf{f} \;, \tag{3.13}$$

where the components of $\mathbf{\Psi}$ are given by $\Psi_{ij} = \psi\left(\left\| \mathbf{p}_i - \mathbf{p}_j \right\| \right)$. The whole procedure is also represented in 1D as a block diagram in Figure 3.4. The method has the ability to handle arbitrarily scattered data, to be easily generalized to several space dimensions, and to provide spectral convergence. Respectively, the method became very popular in several different types of applications. Some of these applications include cartography, neural networks, medical imaging [Carr *et al.*, 1997], surface fitting [Carr *et al.*, 2001; Carr *et al.*, 2003], surface reconstruction [Carr *et al.*, 2001], and the numerical solution of PDEs [Kansa, 1990a; Kansa, 1990b].

More detailed description of the RBF methods can be found in recent monographs [Buhmann, 2003; Liu, 2003; Liu ang Gu, 2005].

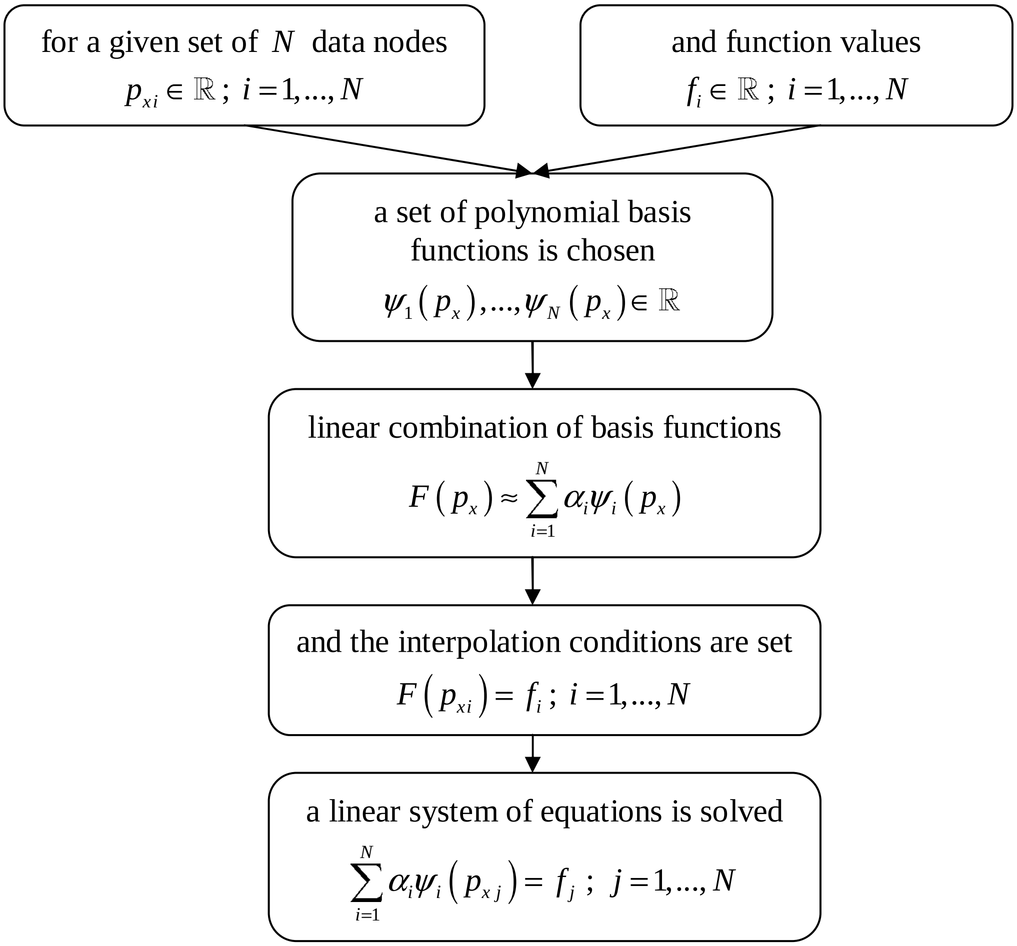

Figure 3.3: Block diagram of the polynomial interpolation in 1D.

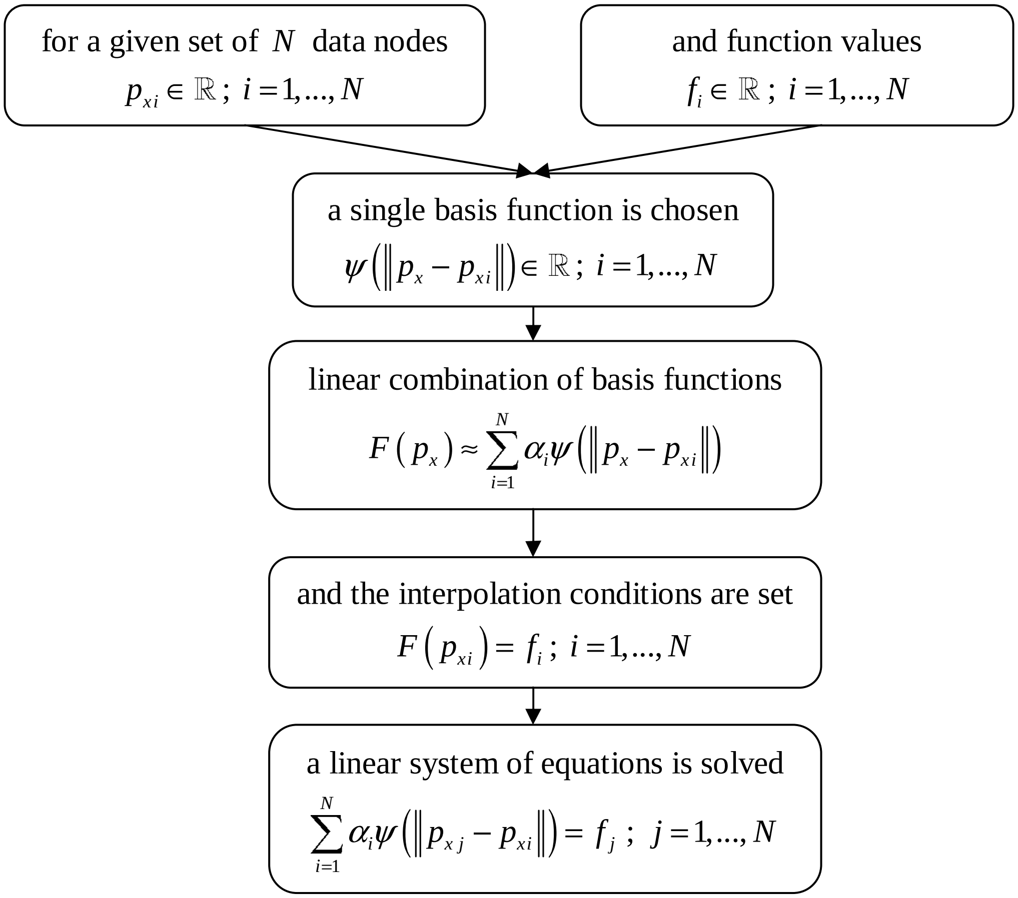

Figure 3.4: Block diagram of the RBF interpolation in 1D.

3.3 Radial Basis Function Collocation Method (Kansa) for Solving PDEs

In recent decade the RBFCM became a useful alternative to FDM and FEM for solving partial differential equations. We are focusing on pure collocation method for this purpose which was first introduced by Kansa [Kansa, 1990a; Kansa, 1990b]. In this method, the PDE and the boundary conditions are satisfied by collocation. We are giving an example for solving a Poisson boundary value problem.

Consider a domain Ω with boundary Γ, shown in Figure 3.5. We have to solve the following Poisson equation

$$\nabla^2 \phi(\mathbf{p}) = S_{\Omega}\left(\mathbf{p}\right); \ \mathbf{p} \in \Omega \tag{3.14}$$

defined in the domain Ω, subject to the Dirichlet boundary conditions on the part of the boundary Γ^D and Neumann boundary conditions on the part of the boundary Γ^N, where $\Gamma = \Gamma^D \cup \Gamma^N$.

$$\phi(\mathbf{p}) = S_\Gamma^D(\mathbf{p})\,;\ \mathbf{p} \in \Gamma^D, \tag{3.15}$$

$$\nabla\phi(\mathbf{p})\cdot\mathbf{n}_\Gamma = \frac{\partial\phi(\mathbf{p})}{\partial\mathbf{n}_\Gamma} = S_\Gamma^N(\mathbf{p})\,;\ \mathbf{p} \in \Gamma^N, \tag{3.16}$$

where $\mathbf{p}$ stands for the position vector, and $\mathbf{n}_\Gamma$ for the normal on the boundary. We discretize the domain with N_Ω domain points and the boundary with N_Γ boundary points, of which N_Γ^D coincide with the Dirichlet part of the boundary and N_Γ^N with the Neumann part of the boundary. The total number of the discretization points is

$$N = N_\Omega + N_\Gamma = N_\Omega + N_\Gamma^D + N_\Gamma^N\,. \tag{3.17}$$

The points are denoted $\mathbf{p}_i; i = 1, 2, ..., N$. In Kansa's method, the approximate solution for the problem (3.14)-(3.16) can be expressed as

$$\phi(\mathbf{p}) = \sum_{i=1}^{N} \psi_i(\mathbf{p})\,\alpha_i\,, \tag{3.18}$$

where α_i is an expansion coefficient to be determined from collocation (i.e. interpolation) and $\psi_i(\mathbf{p}) = \psi(\mathbf{p} - \mathbf{p}_i)$ is a RBF. The coefficients $\boldsymbol{\alpha}$ are computed by solving the following linear system of equations

$$\boldsymbol{\alpha} = \boldsymbol{\Psi}^{-1}\boldsymbol{\phi}\,;\ \psi_{ij} = \psi_j(\mathbf{p}_i)\,;\ \phi_i = \phi(\mathbf{p}_i)\,. \tag{3.19}$$

By using the solution of the system (3.19), the equations (3.14)-(3.16) can be written as

$$\sum_{j=1}^{N} \nabla^2\psi_j(\mathbf{p}_i) \sum_{k=1}^{N} \underline{\psi}_{jk}^{-1}\phi_k = S_\Omega(\mathbf{p}_i)\,;\ i = 1, 2, ..., N_\Omega\,, \tag{3.20}$$

$$\sum_{j=1}^{N} \psi_j(\mathbf{p}_i) \sum_{k=1}^{N} \underline{\psi}_{jk}^{-1}\phi_k = S_\Gamma^D(\mathbf{p}_i)\,;\ i = N_\Omega + 1, N_\Omega + 2, ..., N_\Omega + N_\Gamma^D\,, \tag{3.21}$$

$$\sum_{j=1}^{N} \left(\nabla\psi_j(\mathbf{p}_i)\cdot\mathbf{n}_\Gamma\right) \sum_{k=1}^{N} \underline{\psi}_{jk}^{-1}\phi_k = S_\Gamma^N(\mathbf{p}_i)\,;$$
$$i = N_\Omega + N_\Gamma^D + 1, N_\Omega + N_\Gamma^D + 2, ..., N\,. \tag{3.22}$$

The equations (3.20)-(3.22) can be written in a compact form as the following system of equations for each point $\mathbf{p}_i$

$$\Upsilon_{\Omega i}\sum_{j=1}^{N}\nabla^2\psi_j\left(\mathbf{p}_i\right)\sum_{k=1}^{N}{}_{l}\Psi_{jk}^{-1}\phi_k+\Upsilon_{\Gamma i}^{D}\sum_{j=1}^{N}\psi_j\left(\mathbf{p}_i\right)\sum_{k=1}^{N}{}_{l}\Psi_{jk}^{-1}\phi_k+$$

$$\Upsilon_{\Gamma i}^{N}\sum_{j=1}^{N}\nabla\psi_j\left(\mathbf{p}_i\right)\cdot\mathbf{n}_{\Gamma}\sum_{k=1}^{N}{}_{l}\Psi_{jk}^{-1}\phi_k=\Upsilon_{\Omega i}S_{\Omega i}+\Upsilon_{\Gamma i}^{D}S_{\Gamma i}^{D}+\Upsilon_{\Gamma i}^{N}S_{\Gamma i}^{N};\ i=1,2,...,N, \tag{3.23}$$

where we introduced the domain and the boundary indicators

$$\Upsilon_{\Omega}\left(\mathbf{p}\right)=\begin{cases}0;\,\mathbf{p}\notin\Omega\\ 1;\,\mathbf{p}\in\Omega\end{cases}, \tag{3.24}$$

$$\Upsilon_{\Gamma}^{D}\left(\mathbf{p}\right)=\begin{cases}0;\,\mathbf{p}\notin\Gamma^{D}\\ 1;\,\mathbf{p}\in\Gamma^{D}\end{cases}, \tag{3.25}$$

$$\Upsilon_{\Gamma}^{N}\left(\mathbf{p}\right)=\begin{cases}0;\,\mathbf{p}\notin\Gamma^{N}\\ 1;\,\mathbf{p}\in\Gamma^{N}\end{cases}. \tag{3.26}$$

The system of equations (3.23) can be written in a compact form

$$\sum_{i=1}^{N}\Psi_{ij}\phi_i=S_i;\ j=1,2,...,N, \tag{3.27}$$

with matrix elements Ψ_{ij}

$$\Psi_{ij}=\Upsilon_{\Omega i}\sum_{j=1}^{N}\nabla^2\psi_j\left(\mathbf{p}_i\right)\sum_{k=1}^{N}\Psi_{jk}^{-1}+\Upsilon_{\Gamma i}^{D}\sum_{j=1}^{N}\psi_j\left(\mathbf{p}_i\right)\sum_{k=1}^{N}\Psi_{jk}^{-1}+$$

$$\Upsilon_{\Gamma i}^{N}\sum_{j=1}^{N}\nabla\psi_j\left(\mathbf{p}_i\right)\cdot\mathbf{n}_{\Gamma}\sum_{k=1}^{N}\Psi_{jk}^{-1}, \tag{3.28}$$

$$S_i=\Upsilon_{\Omega i}S_{\Omega i}+\Upsilon_{\Gamma i}^{D}S_{\Gamma i}^{D}+\Upsilon_{\Gamma i}^{N}S_{\Gamma i}^{N}. \tag{3.29}$$

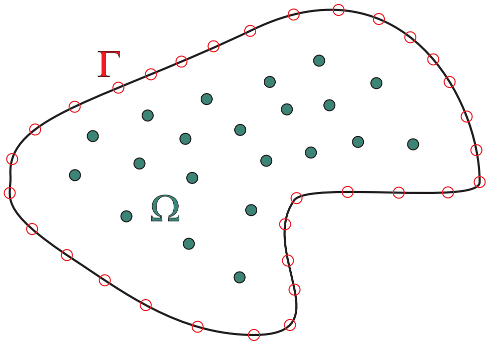

Figure 3.5: Typical node arrangement for the meshless methods. Red empty circles: boundary nodes. Green full circles: domain nodes.

We can easily see that the implementation of Kansa's method is quite simple and straightforward. These are the main reasons that this technique is getting popular and has been applied to many areas such as the solution of N-S equation [Mai-Duy and Tran-Cong, 2001; Šarler, 2005] or the solution of solid-liquid phase-change problems [Kovačević *et al.*, 2003] and porous media flow [Šarler *et al.*, 2004]. In contrast to formulation advantages of this method, collocation systems are often very badly conditioned, especially for larger problems (more than approximately thousand centers). The free parameter c has to be very carefully chosen in order to achieve sufficient conditioning of the matrix. The method has been further upgraded to symmetric collocation [Fasshauer, 1997; Power and Barraco, 2002], to modified collocation [Chen, 2002] and to indirect collocation [Mai-Duy and Tran-Cong, 2003]. In contrast to advantages over mesh generation, all the listed methods unfortunately fail to perform for large problems, because they produce fully populated matrices, sensitive to the choice of the free parameters in RBFs. One of the possibilities for mitigating this problem is to employ the domain decomposition [Mai-Duy and Tran-Cong, 2002]. However, the domain decomposition re-introduces some sort of meshing which is not attractive. The concept of local collocation in the context of RBF-based solution of Poisson equation has been introduced by [Lee *et al.*, 2003; Tolstykh and Shirobokov, 2003]. For interpolation of the function value in a certain node the authors use only data in the (neighbor) nodes that fall into the influence domain of this node. The procedure results in a matrix that is of the same size as the matrix in the original Kansa method, however it is sparse. The circular influence domains have been used in [Lee *et al.*, 2003] where 1D and 2D Poisson equation has been solved by using MQ-RBFs and IMQ-RBFs with a detailed analysis of the influence of the free parameter on the results. In [Tolstykh and Shirobokov, 2003] the stencil-shaped domains have been used where a class of linear and non-linear elasticity problems have been solved with a fixed free parameter. The differential quadrature method, that calculates the derivatives of a function by a weighted linear sum of functional values at its neighbor nodes has been structured with the RBFs in [Shu *et al.*, 2003]. Despite the local properties, the matrix still has a similar form as in [Lee *et al.*, 2003; Tolstykh and Shirobokov, 2003]. Mathematically it represents the same method as [Šarler and Vertnik, 2006].

3.4 Local Collocation with RBFs

The local collocation method with RBF's, i.e. LRBFCM, was developed in order to circumvent the ill-conditioning problem in solving large PDE problems with global Kansa method. The idea comes from diffuse approximate method (DAM) [Nayroles *et al.*, 1988; Sadat and Couturier, 2000; Vertnik *et al.*, 2004], which approximates a function locally over a set of neighbour nodes. The neighbour nodes are usually situated around the vicinity of the observed node. The polynomial functions are used as a basis functions, and a function is approximated by the Weighted Least Squares (WLS) method. The same technique is used in the LRBFCM, but instead of the polynomial functions we use the MQ-RBFs, and the function is approximated by the collocation (i.e. interpolation).

We start with the representation of the function over a set of ${}_lN$ scattered nodes ${}_l\mathbf{p}_j;\ j=1,2,...,{}_lN$ in the following way

$$F(\mathbf{p}) \approx \sum_{k=1}^{{}_lK} {}_l\psi_k(\mathbf{p})\, {}_l\alpha_k\,, \tag{3.30}$$

where ${}_l\psi_k$ stands for the shape functions, ${}_l\alpha_k$ for the expansion coefficients of the shape functions, and ${}_lK$ represents the number of the shape functions. The left lower index on entries of equation (3.30) represents the influence domain ${}_l\omega$ on which the coefficients ${}_l\alpha_k$ are determined. The influence domain ${}_l\omega$ can in general be contiguous (overlapping) or non-contiguous (non-overlapping). Each of the influence domains ${}_l\omega$ includes ${}_lN$ nodes of which ${}_lN_\Omega$ can in general be in the domain and ${}_lN_\Gamma$ on the boundary, i.e. ${}_lN = {}_lN_\Omega + {}_lN_\Gamma$. The influence domain of the node ${}_l\mathbf{p}$ is defined with the nodes having the nearest ${}_lN-1$ distances to the node ${}_l\mathbf{p}$. The five noded ${}_lN=5$ influence domains are used in the present dissertation. Typically chosen influence domains are shown in Figure 3.6. For the domain node, the influence domain contains the domain and boundary nodes in general. While for the boundary node, the influence domain usually contains this boundary node and all the remaining nodes.

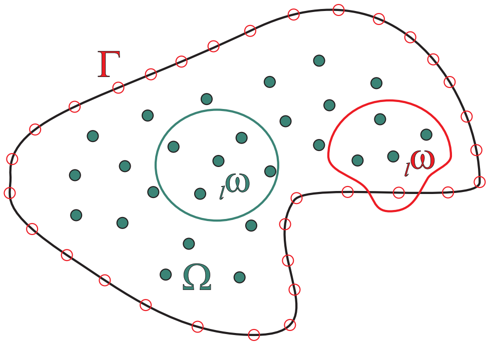

Figure 3.6: Node arrangement with typical influence domains. Green full circle: internal influence domain. Red empty circle: boundary influence domain.

Let us assume the known function values ${}_l f_j$ in the nodes ${}_l\mathbf{p}_j$ of the influence domain ${}_l\omega$. The collocation implies

$$F\left({}_l\mathbf{p}_j\right) = \sum_{k=1}^{{}_l N} {}_l\psi_k\left({}_l\mathbf{p}_j\right) {}_l\alpha_k \,. \tag{3.31}$$

For the coefficients to be computable, the number of the shape functions has to match the number of the collocation nodes ${}_l K = {}_l N$, and the collocation matrix has to be non-singular. The system of equations (3.31) can be written in a matrix-vector notation

$$ {}_l\underline{\boldsymbol{\psi}}\,{}_l\boldsymbol{\alpha} = {}_l\mathbf{f}\,;\ {}_l\underline{\psi}_{kj} = {}_l\psi_k\left({}_l\mathbf{p}_j\right);\ {}_l f_j = F\left({}_l\mathbf{p}_j\right). \tag{3.32}$$

The coefficients ${}_l\boldsymbol{\alpha}$ can be computed by inverting the system (3.32)

$$ {}_l\boldsymbol{\alpha} = {}_l\underline{\boldsymbol{\psi}}^{-1}\,{}_l\mathbf{f}\,. \tag{3.33}$$

By taking into account the expressions for the calculation of the coefficients ${}_l\boldsymbol{\alpha}$, the collocation representation of function $u(\mathbf{p})$ on influence domain ${}_l\omega$ can be expressed as

$$F(\mathbf{p}) \approx \sum_{k=1}^{{}_l N} {}_l\psi_k(\mathbf{p}) \sum_{j=1}^{{}_l N} {}_l\underline{\psi}_{kj}^{-1}\, {}_l f_j \,. \tag{3.34}$$

Let us introduce a two dimensional Cartesian coordinate system with base vectors $\mathbf{i}_\varsigma; \varsigma = x, y$ and coordinates $p_\varsigma; \varsigma = x, y$, i.e. $\mathbf{p} = \mathbf{i}_x p_x + \mathbf{i}_y p_y$. The first partial spatial derivatives of $F(\mathbf{p})$ on influence domain ${}_l\omega$ can be expressed as

$$\frac{\partial}{\partial p_\varsigma} F(\mathbf{p}) \approx \sum_{k=1}^{{}_l N} \frac{\partial}{\partial p_\varsigma} {}_l\psi_k(\mathbf{p}) \sum_{j=1}^{{}_l N} {}_l\underline{\psi}_{kj}^{-1}\, {}_l f_j \ ;\ \varsigma = x, y \,. \tag{3.35}$$

The second partial spatial derivatives of $F(\mathbf{p})$ on influence domain ${}_l\omega$ can be expressed as

$$\frac{\partial^2}{\partial p_\varsigma p_\zeta} F(\mathbf{p}) \approx \sum_{k=1}^{{}_lN} \frac{\partial^2}{\partial p_\varsigma p_\zeta} {}_l\psi_k(\mathbf{p}) \sum_{j=1}^{{}_lN} {}_l\underline{\Psi}^{-1}_{kj}\, {}_lf_j \; ; \; \varsigma, \zeta = x, y \, . \tag{3.36}$$

The MQ-RBF is used for the shape functions

$${}_l\psi_k(\mathbf{p}) = \left[{}_lr_k^2(\mathbf{p}) + c^2 \right]^{1/2}; \; {}_lr_k^2 = (\mathbf{p} - {}_l\mathbf{p}_k) \cdot (\mathbf{p} - {}_l\mathbf{p}_k), \tag{3.37}$$

where c represents the free parameter. The explicit values of the involved first and second derivatives of $\psi_k(\mathbf{p})$ are

$$\frac{\partial}{\partial p_\varsigma} {}_l\psi_k(\mathbf{p}) = \frac{p_\varsigma - {}_lp_{k\varsigma}}{\left({}_lr_k^2 + c^2 \right)^{1/2}}; \; \varsigma = x, y \, , \tag{3.38}$$

$$\frac{\partial^2}{\partial p_\varsigma^2} {}_l\psi_k(\mathbf{p}) = \frac{\left(p_y - {}_lp_{k\varsigma} \right)^2 + c^2}{\left({}_lr_k^2 + c^2 \right)^{3/2}}; \; \varsigma = x, y \, , \tag{3.39}$$

$$\frac{\partial^2}{\partial p_\varsigma p_\zeta} {}_l\psi_k(\mathbf{p}) = \frac{\partial^2}{\partial p_\xi p_\zeta} {}_l\psi_k(\mathbf{p}) = -\frac{\left(p_\varsigma - {}_lp_{k\varsigma} \right)\left(p_\zeta - {}_lp_{k\zeta} \right)}{\left({}_lr_k^2 + c^2 \right)^{3/2}}; \quad \varsigma, \zeta = x, y \, . \tag{3.40}$$

The calculated partial derivatives are then used to solve general transport equation in Section 4.2, which represents the solution of the initial value problem. While, the solution of the boundary value problem by the local approach is presented in Section 3.5.

3.4.1 Optimal Free Parameter

Selecting the value of optimal free parameter in RBFs is one of the important tasks in the discussed meshless method. The choice of the optimum value of this parameter is still an unresolved problem, and the optimum value is usually at the present state-of-the-art found by using numerical experiments. Some authors [Mai-Dui and Tran-Cong, 2001] claim that the free parameter is related to the typical grid distance. Other researchers [Zhang *et al.*, 2000] did not find any relation, and claim simply that the optimum free parameter is problem dependent. Wang and Liu [Wang and Liu, 2002] analyzed the extended MQ, i.e.

$$ {}_l\psi_k(\mathbf{p}) = \left[{}_l r_k^2(\mathbf{p}) + c^2 \right]^{\beta}, \tag{3.41} $$

where the exponent β is a free parameter as well. The authors concluded that by proper fixing of both parameters the solution becomes independent on the node density, node distribution and problem. [Lee *et al.*, 2003] found that the results are less sensitive to the choice of the free parameter in the local collocation methods as in the global ones. The optimal value depends on the number of the nodes, the position of the nodes and the function value in the nodes in the influence domain. The number of nodes is usually fixed for all influence domains for an application, so the influence of the number of nodes is not considered. Since the nodes in the influence domain are usually scattered, the scale of the influence domain region for each reference node could be different, and the optimal free parameter for accurate numerical results may also be different. To assign different values of the free parameter for each node is very difficult. This difficulty can be handled at least in the following two ways:

a) By using the dimensionless free parameter c

The MQ-RBF (equation (3.37)) is changed into the following form

$$ {}_l\psi_k(\mathbf{p}) = \left[{}_l r_k^2(\mathbf{p}) + (c\,{}_l r_0)^2 \right]^{1/2}, \tag{3.42} $$

where ${}_l r_0$ represents the scaling parameter (see Figure 3.7). The scaling parameter ${}_l r_0$ is set to the maximum nodal distance in the influence domain

$$ {}_l r_0 = \max {}_l r_i \left({}_l\mathbf{p}_j \right);\ i,j = 1,2,...,{}_l N. \tag{3.43} $$

The derivatives are calculated by the equations (3.38)-(3.40), where the free parameter c is replaced by the dimensionless free parameter $c\,{}_l r_0$.

b) By using the normalized influence domain region

The normalization of the influence domain is performed by scaling the distance in x and y direction (see Figure 3.8). In equation (3.37) the scaled radial distance ${}_l r_k$ between the two nodes is calculated as

$$ {}_l r_k^2 = \left(\frac{p_x - {}_l p_{kx}}{{}_l p_{x_{max}}} \right)^2 + \left(\frac{p_y - {}_l p_{ky}}{{}_l p_{y_{max}}} \right)^2, \tag{3.44} $$

where the scaling parameters ${}_l p_{x_{max}}$ and ${}_l p_{y_{max}}$ are set to the maximum nodal distance in both directions of the influence domain

$$ {}_l p_{\varsigma_{max}} = \max\left({}_l p_{\varsigma i} - {}_l p_{\varsigma j} \right);\ i,j = 1,2,...,{}_l N;\ \varsigma = x,y. \tag{3.45} $$

The derivatives are calculated by the following equations

$$\frac{\partial}{\partial p_\varsigma}\,{}_l\psi_k(\mathbf{p}) = \frac{1}{{}_l p_{\varsigma_{max}}}\frac{p_\varsigma - {}_l p_{k\varsigma}}{\left({}_l r_k^2 + c^2\right)^{1/2}}\,;\ \varsigma = x, y\,, \tag{3.46}$$

$$\frac{\partial^2}{\partial p_\varsigma^2}\,{}_l\psi_k(\mathbf{p}) = \frac{1}{{}_l p_{\varsigma_{max}}^2}\frac{\left(p_\varsigma - {}_l p_{k\varsigma}\right)^2 + c^2}{\left({}_l r_k^2 + c^2\right)^{3/2}}\,;\ \varsigma = x, y\,, \tag{3.47}$$

$$\frac{\partial^2}{\partial p_\varsigma p_\zeta}\,{}_l\psi_k(\mathbf{p}) = \frac{\partial^2}{\partial p_\zeta p_\varsigma}\,{}_l\psi_k(\mathbf{p}) = -\frac{1}{{}_l p_{\varsigma_{max}}\,{}_l p_{\zeta_{max}}}\frac{\left(p_\varsigma - {}_l p_{k\varsigma}\right)\left(p_\zeta - {}_l p_{k\zeta}\right)}{\left({}_l r_k^2 + c^2\right)^{3/2}}\,;$$

$$\varsigma, \zeta = x, y\,. \tag{3.48}$$

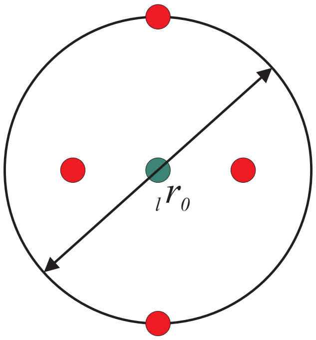

Figure 3.7: Local influence domain with the maximum nodal distance. Green node: reference node. Red nodes: neighbor nodes.

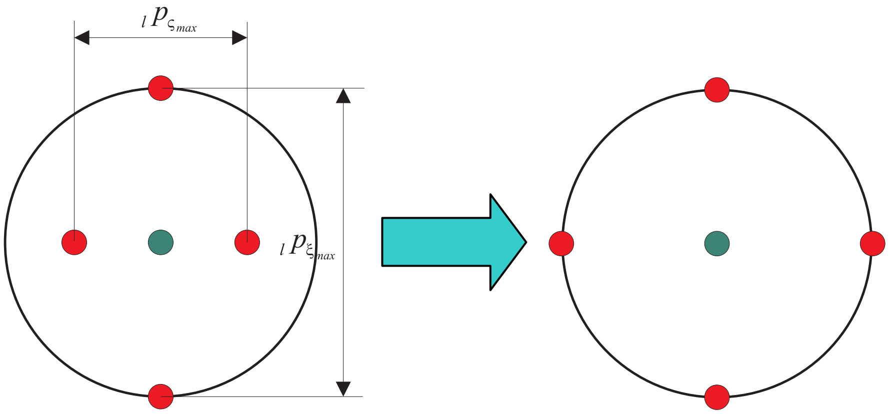

Figure 3.8: Local influence domain scaled with the maximum nodal distance in ς and ξ direction. Left: influence domain before scaling. Right: after scaling.

3.4.2 Finding the Neighbours for Non-Uniform Node Arrangements

One of the important tasks in using the local collocation is the selection of the optimal neighbours for the considered node. The optimal neighbours are nodes which are closest to the considered node and their spatial position assures the calculation of all derivatives, which are needed for solving the PDE. Finding the closest nodes for uniform node arrangements is a trivial task, since the closest nodes are already the optimum neighbours. The problem arises when dealing with non-uniform node arrangements. Than the closest nodes are not the optimal neighbours (see Figure 3.9). The problem with this influence domain is in calculation of the derivatives in vertical direction, where we do not have enough information. So, we must include at least two nodes in the y-direction, even if they are not the closest to the considered node. This could be achieved by searching the nodes in different quadrants. The following step-by-step procedure can be used:

Step1

The origin of the local Cartesian coordinate system is set at the considered node. The coordinate system is then divided into four quadrants, as shown in Figure 3.10 (left picture).

Step2

The Euclidian distances are calculated between each of the nodes and the considered node. For each node, we also calculate an angle based on the local coordinate system.

Step3

The optimal neighbours are those with the closest distance to the considered node, and at least one node must lie in each quadrant (see Figure 3.10, right picture).

We can also rotate the local coordinate system by $\pi / 4$, as shown in Figure 3.11, where also the quadrants are rotated. Searching the closest nodes in such a rotated local systems is used for finding the optimal neighbours in curved node arrangements of the discretized continuous casting machine.

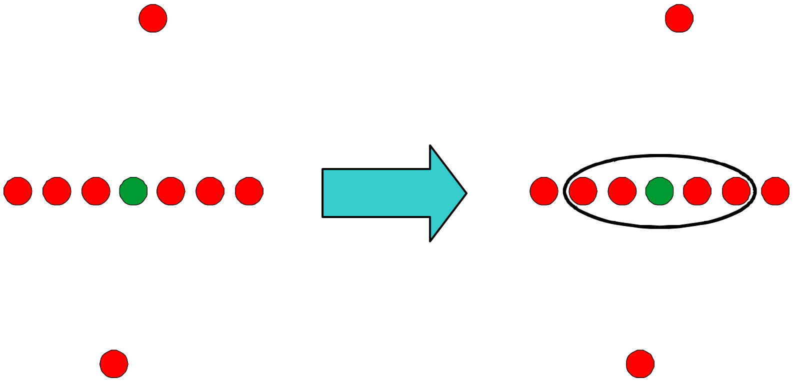

Figure 3.9: Non-optimal neighbours in a highly non-uniform node arrangement. Left: considered node with surrounding nodes. Right: closest non-optimal neighbours.

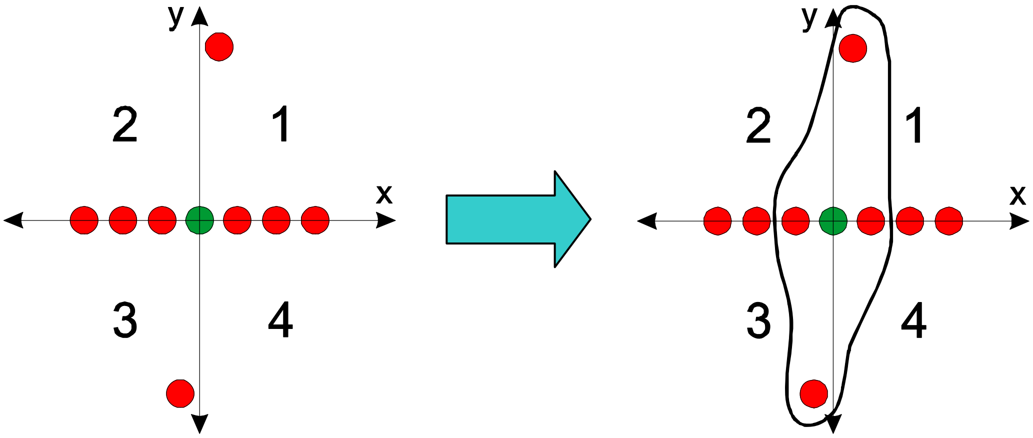

Figure 3.10: Optimal neighbours in a highly non-uniform node arrangement. Left: considered node with surrounding nodes and four quadrants. Right: closest optimal neighbours.

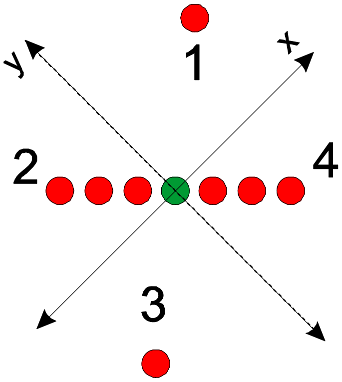

Figure 3.11: Rotated local coordinate system for $\pi / 4$.

3.5 Solving PDEs with Local Collocation

We present the solution of the same boundary value problem as in Section 3.3, but using the LRBFCM. Such a solution was first represented by [Lee *et al.*, 2003], where the global sparse matrix is constructed and solved. In this approach, the ill-conditioning problem of the global Kansa's method is mitigated, since the sparse global matrix is much easier to solve than a fully global matrix.

We start with the same problem definition as in Section 3.3. The region $\Omega \cup \Gamma$ is further divided into N overlapping influence domains ${}_l\omega; l = 1, 2, ..., N$. Each of the influence domains consists of ${}_lN$ points ${}_l\mathbf{p}_j; j = 1, 2, ..., {}_lN$ that coincide with some of the global points $\mathbf{p}_i; i = 1, 2, ..., N$. There is a relation between the global and the local points indices on each of the influence domains. This relation is $i = i(l, j)$. $i(l, j)$ is a function of the local influence domain index l and local index j. The following is defined $i(i,1) = i$. The following is valid $p_{i(l,j)} = {}_l p_j; l = 1, 2, ..., N$, $j = 1, 2, ..., {}_lN$. The transport variable is represented on each of the influence domains by ${}_lN$ RBF's ${}_l\psi_j(\mathbf{p}); j = 1, 2, ..., {}_lN$, and their coefficients ${}_l\alpha_j; j = 1, 2, ..., {}_lN$, i.e.

$$\phi(\mathbf{p}) = \sum_{j=1}^{{}_lN} \psi_{i(l,j)}(\mathbf{p})\, {}_l\alpha_j; \mathbf{p} \in {}_l\Omega. \tag{3.49}$$

The action of the Laplace operator on a transport variable can be calculated as

$$\nabla^2\phi(\mathbf{p}) = \sum_{j=1}^{{}_lN} \left[\nabla^2\psi_{i(l,j)}(\mathbf{p})\right] {}_l\alpha_j; \mathbf{p} \in {}_l\Omega. \tag{3.50}$$

The coefficients ${}_l\alpha_j$ are determined by collocation

$$\phi\left(\mathbf{p}_{i(l,k)}\right) = \sum_{j=1}^{{}_lN} {}_l\psi_{i(l,j)}\left(\mathbf{p}_{i(l,k)}\right) {}_l\alpha_n; \mathbf{p} \in {}_l\Omega; k = 1, 2, ..., {}_lN, \tag{3.51}$$

$$\phi_{i(l,k)} = \sum_{j=1}^{{}_lN} {}_l\mathbf{\Psi}_{jk}\, {}_l\alpha_j;\ j, k = 1, 2, ..., {}_lN, \tag{3.52}$$

with the matrix element ${}_l\mathbf{\Psi}_{jk}$ of the matrix ${}_l\mathbf{\Psi}$ defined as

$${}_l\mathbf{\Psi}_{jk} = {}_l\psi_{i(l,j)}\left(\mathbf{p}_{i(l,k)}\right). \tag{3.53}$$

We determine the coefficients ${}_l\alpha_j$ by inverting the matrix ${}_l\mathbf{\Psi}$ (i,e. ${}_l\mathbf{\Psi}^{-1}\, {}_l\mathbf{\Psi} = {}_l\mathbf{I}$)

$$ {}_l\alpha_j = \sum_{k=1}^{{}_lN} {}_l\Psi^{-1}_{jk}\phi_{i(l,k)} \,. \tag{3.54}$$

The RBF representation (3.49) of $\phi(\mathbf{p})$ on each of the influence domains thus reads

$$\phi(\mathbf{p}) = \sum_{j=1}^{{}_lN}\sum_{k=1}^{{}_lN} {}_l\psi_{i(l,j)}(\mathbf{p})\, {}_l\Psi^{-1}_{jk}\phi_{i(l,k)} \,. \tag{3.55}$$

The collocation in global point $\mathbf{p}_l ; l = 1,2,...,N$ reads

$$\phi_l = \sum_{j=1}^{{}_lN}\sum_{k=1}^{{}_lN} {}_l\psi_{lj}\, {}_l\Psi^{-1}_{jk}\phi_{i(l,k)} \,. \tag{3.56}$$

By using the Laplace equation and the boundary conditions we can write the following system of equations for each point $\mathbf{p}_l ; l = 1,2,...,N$

$$\Upsilon_{\Omega l}\sum_{j=1}^{{}_lN}\sum_{k=1}^{{}_lN}\left[\nabla^2\, {}_l\psi_{lj}\right] {}_l\Psi^{-1}_{jk}\phi_{i(l,k)} + \Upsilon^D_{\Gamma l}\sum_{j=1}^{{}_lN}\sum_{k=1}^{{}_lN} {}_l\psi_{lj}\, {}_l\Psi^{-1}_{jk}\phi_{i(l,k)} +$$

$$\Upsilon^N_{\Gamma l}\sum_{j=1}^{{}_lN}\sum_{k=1}^{{}_lN}\left[\nabla\, {}_l\psi_{lj}\cdot\mathbf{n}_l\right] {}_l\Psi^{-1}_{jk}\phi_{i(l,k)} = \Upsilon_{\Omega l}S_{\Omega l} + \Upsilon^D_{\Gamma l}S^D_{\Gamma l} + \Upsilon^N_{\Gamma l}S^N_{\Gamma l} \,;\ i,l = 1,2,...,N \,, \tag{3.57}$$

where the domain (equation (3.24)) and the boundary indicators (equation (3.25) and (3.26)) are used. The sparse system of equations (3.57) can be written in a compact form

$$\sum_{m=1}^{N}\Psi_{lm}\phi_m = S_l \,;\ l = 1,2,...,N \,, \tag{3.58}$$

with matrix elements Ψ_{li}

$$\Psi_{lm} = \Upsilon_{\Omega l}\sum_{j=1}^{{}_lN}\sum_{k=1}^{{}_lN}\left[\nabla^2\, {}_l\psi_{lj}\right] {}_l\Psi^{-1}_{jk}\delta_{i(l,k)m} + \Upsilon^D_{\Gamma l}\sum_{j=1}^{{}_lN}\sum_{k=1}^{{}_lN} {}_l\psi_{lj}\, {}_l\Psi^{-1}_{jk}\delta_{i(l,k)m} +$$

$$\Upsilon^N_{\Gamma l}\sum_{j=1}^{{}_lN}\sum_{k=1}^{{}_lN}\left[\nabla\, {}_l\psi_{lj}\cdot\mathbf{n}_l\right] {}_l\Psi^{-1}_{jk}\delta_{i(l,k)m} \,, \tag{3.59}$$

$$S_l = \Upsilon_{\Omega l}S_{\Omega l} + \Upsilon^D_{\Gamma l}S^D_{\Gamma l} + \Upsilon^N_{\Gamma l}S^N_{\Gamma l} \,. \tag{3.60}$$

and Kronecker delta

$$\delta_{im} = \begin{cases} 1; i = m \\ 0; i \neq m \end{cases}. \tag{3.61}$$

4 Solution Procedure

In this chapter the solution procedure for the numerical solution of the incompressible turbulent flow with solidification is presented. First, the solution procedure of the general transport equation is given. The derived procedure stands as a base for solution of all other transport equations, such as: momentum, energy, the turbulent kinetic energy and the dissipation rate. Next, we present the fractional step method to solve the velocity field, satisfying the flow incompressibility. This velocity-pressure coupling algorithm is chosen in order to develop a simple time-advancement scheme of the proposed solution procedure. The solution of the involved transport equations, described in Section 2.6, is given through the step-by-step description. Then, the initial and the boundary conditions, which are required to solve the system of transport equations, are fully described. To overcome the instabilities due to the convection dominated situations, an adaptive-upwind technique is introduced.

4.1 Time Discretization

The transient problems have numerous important applications in science and engineering. Almost all industrial processes experience transients during various stages of the operation. For example, the start-up phase of the continuous casting of steel billets, where the billet moves out of the mould to the secondary cooling zone and is therefore exposed to different boundary conditions which result in transient variations of boundary solid-liquid interface position and temperature field [Vertnik *et al.*, 2007; Vertnik and Šarler, 2009].

In time-dependent problems, the transport variable $\phi(\mathbf{p})$ besides the space, also depends on time, i.e. $\phi(\mathbf{p},t)$, which is additional variable to be discretized. The time discretization defines the direction for information transfer, namely from the past into the future. The common types of the time discretization procedures are explicit, implicit and Crank-Nicolson. In all numerical examples in the present dissertation, only the simple explicit time discretization is used to derive the solution procedure of various conservative equations. The explicit scheme simultaneously involves only one unknown variable for the future time, which can be directly calculated from known variables from current time, i.e.

$$\frac{\partial \phi(\mathbf{p},t)}{\partial t} \approx \frac{\phi(\mathbf{p},t_0+\Delta t)-\phi(\mathbf{p},t_0)}{\Delta t} = \mathrm{F}\left(\phi(\mathbf{p},t_0)\right)+\mathrm{O}(\Delta t)\,. \tag{4.1}$$

The reasons for using explicit time discretizaton are:

- For domain nodes the matrix of the system of equations (3.32) is constant. For this purpose the LU (lower/upper) factorization of the matrix is performed for domain nodes before the start-up of calculation. The system of linear equations (3.32) is then solved with pre-calculated coefficient matrix of the LU factorization. This procedure strongly increases the calculation speed of the system (3.32).
- The matrix is very small, only 5×5 in the present dissertation.
- To deal with nonlinear thermo-physical properties and nonlinear boundary conditions of the convective-diffusive phase-change problems, the time step is often restricted to small values, similar that would be used in the implicit scheme. The stability issue is of less importance, respectively.

The explicit time-stepping strategy is only conditionally stable, which means that the time step value is restricted by the stability criteria, usually derived by the von-Neumann stability analysis [Kunz and Lakshminarayana, 1992]. The stability criteria for a system of the governing equations described in the Section 2.6, is impossible to define. The actual time step should be determined manually with numerical experiments. Usually, the momentum equations and the transport equations of the turbulent model require smaller time step for a stable solution as the energy equation.

4.2 Treatment of the General Transport Equation

Consider the general transport equation, defined on a connected fixed domain Ω with boundary Γ, standing for a reasonably broad spectra of mass, energy, momentum, and species transfer problems

$$\frac{\partial}{\partial t}\left[\rho \mathrm{C}(\phi)\right]+\nabla\cdot\left[\rho \mathbf{u} \mathrm{C}(\phi)\right]=\nabla\cdot\left(\mathbf{D}\nabla\phi\right)+S \tag{4.2}$$

with ρ, ϕ, t, $\mathbf{u}$, $\mathbf{D}$, and S standing for density, transport variable, time, velocity, diffusion tensor

$$\mathbf{D}=\begin{bmatrix} D_{11} & D_{12} & D_{13} \\ D_{21} & D_{22} & D_{23} \\ D_{31} & D_{32} & D_{33} \end{bmatrix} \tag{4.3}$$

and source, respectively. The scalar function C stands for a constitutive relation between the conserved $\mathrm{C}(\phi)$ and the diffused ϕ quantities. We seek the solution of the governing equation for the transport variable at the final time $t_0+\Delta t$, where t_0 represents initial time and Δt the positive time increment. The solution is constructed by the initial and boundary conditions that follow. The initial value of the transport variable $\phi(\mathbf{p},t)$ at a node with position vector $\mathbf{p}$ and time t_0 is defined through the known function ϕ_0

$$\phi(\mathbf{p},t)=\phi_0(\mathbf{p})\,;\ \mathbf{p}\in\Omega+\Gamma\,. \tag{4.4}$$

The boundary Γ is divided into not necessarily connected parts $\Gamma=\Gamma^D\cup\Gamma^N\cup\Gamma^R$ with Dirichlet, Neumann and Robin type boundary conditions, respectively. At the boundary node $\mathbf{p}$ with normal $\mathbf{n}_\Gamma$ and time $t_0\le t\le t_0+\Delta t$, these boundary conditions are defined through known functions ϕ_Γ^D, ϕ_Γ^N, ϕ_Γ^R, $\phi_{\Gamma ref}^R$

$$\phi=\phi_\Gamma^D\,;\ \mathbf{p}\in\Gamma^D\,, \tag{4.5}$$

$$\frac{\partial}{\partial\mathbf{n}_\Gamma}\phi=\phi_\Gamma^N\,;\ \mathbf{p}\in\Gamma^N\,, \tag{4.6}$$

$$\frac{\partial}{\partial\mathbf{n}_\Gamma}\phi=\phi_\Gamma^R\left(\phi-\phi_{\Gamma ref}^R\right);\ \mathbf{p}\in\Gamma^R\,. \tag{4.7}$$

The numerical discretization of equation (4.2), using explicit (Euler) time discretization has the form

$$\frac{\partial\left[\rho\mathrm{C}(\phi)\right]}{\partial t}\approx\frac{\rho_0\mathrm{C}(\phi)-\rho_0\mathrm{C}(\phi_0)}{\Delta t}=-\nabla\cdot\left[\mathbf{u}_0\rho_0\mathrm{C}(\phi_0)\right]+\nabla\cdot(\mathbf{D}\nabla\phi_0)\,. \tag{4.8}$$

From equation (4.8) the unknown function value $\mathrm{C}(\phi)_l$ in domain node $\mathbf{p}_l$ can be calculated as

$$\mathrm{C}(\phi)_l=\mathrm{C}(\phi)_{0l}+\frac{\Delta t}{\rho_0}\left(-\nabla\cdot\left[\mathbf{u}_0\rho_0\mathrm{C}(\phi)_{0l}\right]+\nabla\mathbf{D}_{0l}\cdot\nabla\phi_{0l}+\mathbf{D}_{0l}\cdot\nabla^2\phi_{0l}\right). \tag{4.9}$$

In continuation, the following assumption regarding the form of the diffusion tensor $\mathbf{D}$ is made

$$\mathbf{D}=D\begin{bmatrix}1&0&0\\0&1&0\\0&0&1\end{bmatrix}. \tag{4.10}$$

The explicit calculation of expression (4.9) in 2D Cartesian coordinates is

$$\begin{aligned}
\mathrm{C}(\phi)\,{}_l = \mathrm{C}(\phi)_{0l} + \frac{\Delta t}{\rho_0}\Bigg(& \sum_{k=1}^{{}_lN} \frac{\partial}{\partial p_x}\,{}_l\psi_k(\mathbf{p}_l) \sum_{j=1}^{{}_lN} {}_l\underline{\Psi}^{-1}_{kj}\,{}_l\left(u_{0x}\rho_0 \mathrm{C}(\phi)_0\right)_j + \\
& \sum_{k=1}^{{}_lN} \frac{\partial}{\partial p_y}\,{}_l\psi_k(\mathbf{p}_l) \sum_{j=1}^{{}_lN} {}_l\underline{\Psi}^{-1}_{kj}\,{}_l\left(u_{0y}\rho_0 \mathrm{C}(\phi)_0\right)_j + \\
& \left(\sum_{k=1}^{{}_lN} \frac{\partial}{\partial p_x}\,{}_l\psi_k(\mathbf{p}_l) \sum_{j=1}^{{}_lN} {}_l\underline{\Psi}^{-1}_{kj}\,{}_lD_{0j}\right)\cdot\left(\sum_{k=1}^{{}_lN} \frac{\partial}{\partial p_x}\,{}_l\psi_k(\mathbf{p}_l) \sum_{j=1}^{{}_lN} {}_l\underline{\Psi}^{-1}_{kj}\,{}_l\phi_{0j}\right) + \\
& \left(\sum_{k=1}^{{}_lN} \frac{\partial}{\partial p_y}\,{}_l\psi_k(\mathbf{p}_l) \sum_{j=1}^{{}_lN} {}_l\underline{\Psi}^{-1}_{kj}\,{}_lD_{0j}\right)\cdot\left(\sum_{k=1}^{{}_lN} \frac{\partial}{\partial p_y}\,{}_l\psi_k(\mathbf{p}_l) \sum_{j=1}^{{}_lN} {}_l\underline{\Psi}^{-1}_{kj}\,{}_l\phi_{0j}\right) + \\
& \sum_{n=1}^{{}_lN} \frac{\partial^2}{\partial p_x^2}\,{}_l\psi_k(\mathbf{p}_l) \sum_{j=1}^{{}_lN} {}_l\underline{\Psi}^{-1}_{kj}\,{}_l\phi_{0j} + \sum_{j=1}^{{}_lN} \frac{\partial^2}{\partial p_y^2}\,{}_l\psi_k(\mathbf{p}_l) \sum_{j=1}^{{}_lN} {}_l\underline{\Psi}^{-1}_{kj}\,{}_l\phi_{0j}\Bigg),
\end{aligned} \tag{4.11}$$

where the equations (3.35) and (3.36) have been employed.

The complete solution procedure follows the below defined steps 1-5.

Step 1

First, the initial conditions are set in the domain and boundary nodes and the required derivatives are calculated from the known nodal values.

Step 2

The equation (4.11) is used to calculate the new values of the variable $\mathrm{C}(\phi)_l$ at time $t_0 + \Delta t$ in the domain nodes.

Step 3

The transport variable ϕ_l is calculated from the constitutive relation $\mathrm{C}(\phi)$ in the domain nodes.

$$\phi_l = C(\phi). \tag{4.12}$$

Step 4

The unknown transport variable ϕ_l at time $t_0 + \Delta t$ in the Dirichlet, Neumann, and Robin boundary nodes is calculated. The coefficients ${}_l\boldsymbol{\alpha}$ have to be determined from the new values in the domain, calculated in *Step 3*, and from the information on the boundary conditions. Let us introduce domain, Dirichlet, Neumann, and Robin boundary indicators for this purpose. These indicators are defined as

$$\Upsilon_{\Omega j} = \begin{cases} 1; \mathbf{p}_j \in \Omega \\ 0; \mathbf{p}_j \notin \Omega \end{cases}, \quad \Upsilon_{\Gamma j}^{D} = \begin{cases} 1; \mathbf{p}_j \in \Gamma^D \\ 0; \mathbf{p}_j \notin \Gamma^D \end{cases}, \quad \Upsilon_{\Gamma j}^{N} = \begin{cases} 1; \mathbf{p}_j \in \Gamma^N \\ 0; \mathbf{p}_j \notin \Gamma^N \end{cases},$$

$$\Upsilon_{\Gamma j}^{R} = \begin{cases} 1; \mathbf{p}_j \in \Gamma^R \\ 0; \mathbf{p}_j \notin \Gamma^R \end{cases}. \tag{4.13}$$

The coefficients ${}_l\boldsymbol{\alpha}$ are calculated from the system of linear equations

$$\begin{aligned} &\sum_{k=1}^{{}_lN} {}_l\Upsilon_{\Omega j}\, {}_l\psi_k\left({}_l\mathbf{p}_j\right) {}_l\alpha_k + \sum_{k=1}^{{}_lN} {}_l\Upsilon_{\Gamma j}^{D}\, {}_l\psi_k\left({}_l\mathbf{p}_j\right) {}_l\alpha_k \\ &+ \sum_{k=1}^{{}_lN} {}_l\Upsilon_{\Gamma j}^{N} \frac{\partial}{\partial n_\Gamma} {}_l\psi_k\left({}_l\mathbf{p}_j\right) {}_l\alpha_k + \sum_{k=1}^{{}_lN} {}_l\Upsilon_{\Gamma j}^{R} \frac{\partial}{\partial n_\Gamma} {}_l\psi_k\left({}_l\mathbf{p}_j\right) {}_l\alpha_k = \\ &= {}_l\Upsilon_{\Omega j}\, {}_l\phi_j + {}_l\Upsilon_{\Gamma j}^{D}\, {}_l\phi_j^{D} + {}_l\Upsilon_{\Gamma j}^{N}\, {}_l\phi_j^{N} + \\ &\qquad {}_l\Upsilon_{\Gamma j}^{R}\, {}_l\phi_{\Gamma j}^{R} \left(\sum_{k=1}^{{}_lN} {}_l\psi_k\left({}_l\mathbf{p}_j\right) {}_l\alpha_k - {}_l\phi_{\Gamma ref\, j}^{R} \right). \end{aligned} \tag{4.14}$$

The system (4.14) can be written in a compact form

$${}_l\underline{\boldsymbol{\Psi}}\, {}_l\boldsymbol{\alpha} = {}_l\mathbf{b} \tag{4.15}$$

with the following system matrix entries

$$\begin{aligned} {}_l\underline{\Psi}_{jk} = {}&{}_l\Upsilon_{\Omega j}\, {}_l\psi_k\left({}_l\mathbf{p}_j\right) + {}_l\Upsilon_{\Gamma j}^{D}\, {}_l\psi_k\left({}_l\mathbf{p}_j\right) + {}_l\Upsilon_{\Gamma j}^{N} \frac{\partial}{\partial n_\Gamma} {}_l\psi_k\left({}_l\mathbf{p}_j\right) + \\ &{}_l\Upsilon_{\Gamma j}^{R} \left[\frac{\partial}{\partial n_\Gamma} {}_l\psi_k\left({}_l\mathbf{p}_j\right) - {}_l\phi_{\Gamma j}^{R} \sum_{k=1}^{{}_lN} {}_l\psi_k\left({}_l\mathbf{p}_j\right) \right] \end{aligned} \tag{4.16}$$

and with the following explicit form of the augmented right hand side vector

$${}_lb_j = {}_l\Upsilon_{\Omega j}\phi_j + {}_l\Upsilon_{\Gamma j}^{D}\phi_{\Gamma j}^{D} + {}_l\Upsilon_{\Gamma j}^{N}\phi_{\Gamma j}^{N} - {}_l\Upsilon_{\Gamma j}^{R}\, {}_l\phi_{\Gamma j}^{R}\, {}_l\phi_{\Gamma ref\, j}^{R}\,. \tag{4.17}$$

Step 5

The unknown boundary values are set from equation (3.34).

When searching the steady-state solution, the following criterion

$$\max\left|\phi_l - \phi_{0l}\right| \le \phi_{\mathrm{ste}} \tag{4.18}$$

has to be met. The parameter ϕ_{ste} is defined as the steady-state convergence margin. In case the steady-state criterion is fulfilled or the time of calculation exceeds the foreseen time of interest, the calculation is stopped.

4.3 Solution of the Incompressible Navier-Stokes Equation

The fluid flow is in all numerical examples of the present dissertation treated as incompressible. From the computational point of view, these flows are very difficult to handle, because the continuity equation (2.80) does not have a dominant variable. It contains only the velocity components, and there is no obvious link with the pressure as in the case for compressible flow, where the continuity equation (2.55) can be used to determine the density, and the pressure is calculated from an equation of state. One way to overcome this difficulty is to construct a pressure field by satisfying the continuity equation. The pressure equation is constructed by taking the divergence of the momentum equation. The resulting equation is then simplified by knowing the continuity equation, which leads to the final form of the pressure Poisson equation. This approach is used to calculate the pressure in explicit and implicit based methods. A large collection of CFD books exist [Patankar, 1980; Fletcher, 1988; Versteeg and Malalasekera, 1995; Ferziger and Perić, 2002], which represent and describe these methods in detail. The most popular, also found in the CFD commercial packages, are SIMPLE, SIMPLER, SIMPLEC and PISO, which were developed in a strong connection with the FVM.

Beside the pressure-velocity coupling algorithms, there exist several other techniques for solving incompressible flows, such as streamfunction-vorticity method [Ferziger and Perić, 2002], fractional step method [Chorin, 1968], and artificial-compressibility method [Chorin, 1967].

The coupling between the continuity and the momentum equation is in the present dissertation based on Chorin's fractional step method. It belongs to the so called "projection methods", where the computations of the velocity and the pressure fields are decoupled. The main idea is to calculate the intermediate velocity field without the pressure gradient. The pressure is rather calculated separately with considering the continuity equation. The final velocity field is then updated (corrected to satisfy the incompressibility constraint) with the pressure gradient. The Chorin's original method is developed based on the explicit time discretization, but the whole procedure can be treated also implicitly [Kim and Moin, 1984].

An step-by-step elaboration of the explicit fractional step method is as follows:

Step 1

Solve the momentum equations without pressure term to get the intermediate velocity $\tilde{\mathbf{u}}$, which does not satisfy the incompressibility constraint, i.e.

$$\tilde{\mathbf{u}} = \mathbf{u}_0 + \frac{\Delta t}{\rho}\left[-\rho\nabla\cdot(\mathbf{u}\mathbf{u}) + \nabla\cdot(2\mu\mathbf{S})\right]_0, \tag{4.19}$$

and $\nabla\cdot\tilde{\mathbf{u}} \neq 0$ in general.

Step 2

Solve the Poisson's equation for pressure

$$\nabla^2 P = \frac{\rho}{\Delta t}\nabla\cdot\tilde{\mathbf{u}} \quad . \tag{4.20}$$

The related boundary conditions to the equation (4.20) can be found in Section 4.5.

Step 3

The velocity field is updated

$$\mathbf{u} = \tilde{\mathbf{u}} - \frac{\Delta t}{\rho}\nabla P, \tag{4.21}$$

and ready for the next time step, starting with the equation (4.19).

The fractional step approach was already used for solving incompressible fluid flow with the meshless methods. In [Oñate *et al.*, 2000], the finite point method was used to solve the various laminar flow problems: driven cavity at $\mathrm{Re} = 1000$ and backward facing step at $\mathrm{Re} = 389$. The results were obtained by the three-step semi-implicit fractional step scheme. The local version of the RBF based meshless scheme was developed by [Sanyasiraju and Chandhini, 2008] for solving the unsteady incompressible flows. The local scheme was derived by considering the Lagrange representation of the RBF interpolation vector. An explicit fractional step method was used, where the following examples were performed: Couette flow at $\mathrm{Re} = 1$, plain Poiseuille flow at $\mathrm{Re} = 1$, flow in a lid-driven cavity at $\mathrm{Re} = 100, 1000, 3200$, flow over a backward-facing step at $\mathrm{Re} = 800$, and flow through vascular stenosis at various Re numbers.

4.4 Step-by-step Description of the Solution Procedure

We seek the solution of the velocity field, temperature field, and k and ε fields at time $t + t_0$ by assuming known fields $\mathbf{u}$, T, k and ε at time t_0 and known initial and boundary conditions. At every time step, the following explicit numerical algorithm is employed:

Step 1

The intermediate velocity field is calculated first, without considering the pressure gradient

$$\tilde{\mathbf{u}} = \mathbf{u}_0 + \frac{\Delta t}{\rho}\Bigg[-\rho\nabla\cdot(\mathbf{uu}) + \nabla\cdot\Big[(\mu_L+\mu_t)\big[\nabla\mathbf{u}+(\nabla\mathbf{u})^{\mathrm{T}}\big]\Big] - \frac{2}{3}\rho\nabla k - \mu_L \frac{C(1-f_L)^2}{f_L^3}(\mathbf{u}-\mathbf{u}_S) + \rho\beta_T \mathbf{g}\left(T-T_{ref}\right)\Bigg]_0, \qquad (4.22)$$

where the index 0 represents the initial conditions at time $t = t_0$.

Step 2

The pressure Poisson equation (4.20) is solved, which can be solved by converting it into a diffusion equation [Divo and Kassab, 2007] or by solving the sparse matrix [Lee *et al.*, 2003]. An additional possibility represents the use of the local pressure correction [Kosec and Šarler, 2008] which seems to be most efficient. However the last correction has not been yet successfully tested for inflow and outflow situations. In the present dissertation, the approach by Lee *et al.* is used, where the solution of the sparse matrix is solved by the direct method. The construction of the sparse matrix is presented in Section 3.5. In case of the fixed node arrangement, the left-hand side of the sparse matrix can be LU decomposed before the first time step. This numerical approach significantly improves the performance, since only the back substitution is used to solve the pressure field at each time step. The boundary conditions for the pressure equation are explicitly given in the Section 4.5.

Step 3

The intermediate velocity components are corrected through the calculated pressure gradient by the equation (4.21).

Step 4

The energy equation is solved to obtain the enthalpy field

$$h = h_0 + \frac{\Delta t}{\rho}\Bigg[\nabla\cdot(\lambda\nabla T) - \rho\nabla\cdot(\mathbf{u}h) + \rho\nabla\cdot\left(\mathbf{u}h - f_S\,\mathbf{u}_S h_S - f_L\,\mathbf{u}_L h_L\right) + \nabla\cdot\left(f_L \frac{\rho_L \nu_t}{\sigma_t}\nabla h_L\right)\Bigg]_0 . \qquad (4.23)$$

Step 5

The temperature field is calculated from the enthalpy field, calculated in step 4, using the inverse of the constitutive temperature-enthalpy relationship (equations (2.65) and (2.66)), i.e.

$$T = T(h) \tag{4.24}$$

Step 6

After the solution of the temperature field, the transport equations (3.6) and (3.7) of the turbulence model are solved

$$k = k_0 + \frac{\Delta t}{\rho}\left[-\rho\nabla\cdot(\mathbf{u}k) + \nabla\cdot\left[\left(\mu_L + \frac{\mu_t}{\sigma_k}\right)\nabla k\right] + P_k + G_k - \rho\varepsilon + \rho D - \mu_L \frac{C\left(1-f_L^2\right)}{f_L^3} k \right]_0 , \tag{4.25}$$

$$\varepsilon = \varepsilon_0 + \frac{\Delta t}{\rho}\left[-\rho\nabla\cdot(\mathbf{u}\varepsilon) + \nabla\cdot\left[\left(\mu_L + \frac{\mu_t}{\sigma_\varepsilon}\right)\nabla\varepsilon\right] + \left[c_{1\varepsilon} f_1 \left(P_k + c_{3\varepsilon} G_k\right) - c_{2\varepsilon} f_2 \rho\varepsilon\right]\frac{\varepsilon}{k} + \rho E - \mu_L \frac{C\left(1-f_L^2\right)}{f_L^3}\varepsilon \right]_0 . \tag{4.26}$$

Step 7

The turbulent viscosity is updated, using the equation (2.35), and the solution is ready for the next time step.

The block diagram of the described algorithm is schematically represented in Figure 4.1.

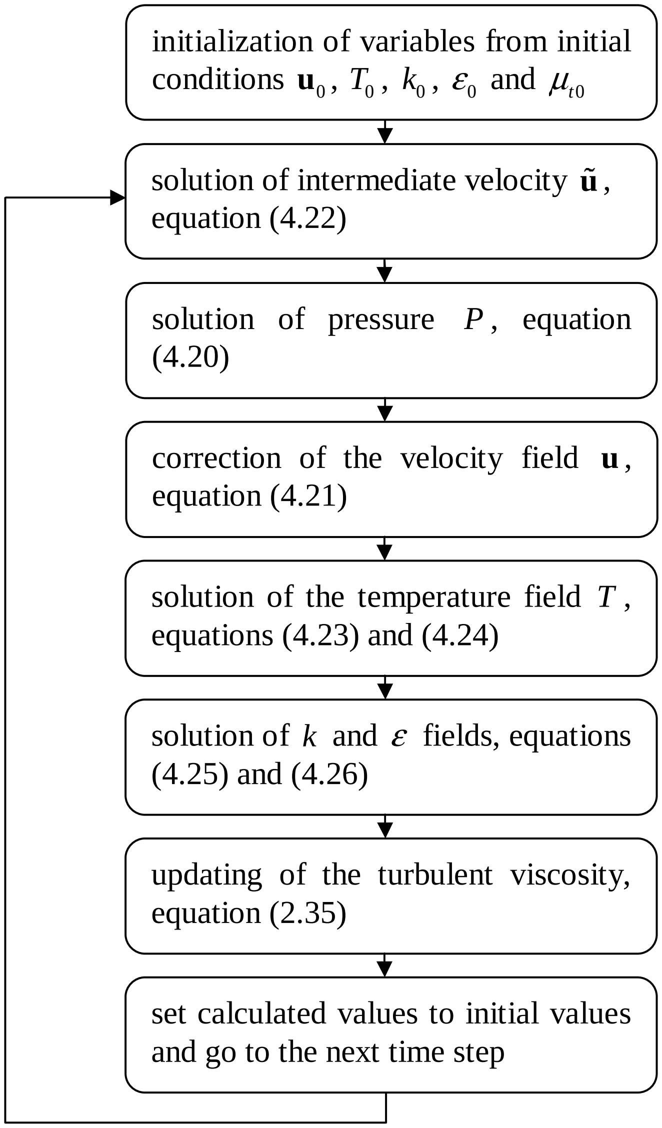

Figure 4.1: Block diagram of the solution procedure.

4.5 Boundary Conditions for Pressure

Boundary condition for pressure equation (4.20) at inlet, symmetry and wall are of the Neumann type. They are constructed by using the normal component of the momentum equation (2.6) with explicit time discretization, i.e.

$$\rho \frac{\mathbf{n}_\Gamma \cdot \left(\mathbf{u}_w - \mathbf{u}_0\right)}{\Delta t} = -\mathbf{n}_\Gamma \cdot \nabla P + \mathbf{n}_\Gamma \cdot \left[-\rho \nabla \cdot \left(\mathbf{u}\mathbf{u}\right) + \nabla \cdot \left(2\mu \mathbf{S}\right)\right]_0 . \tag{4.27}$$

By using the equation (4.19) for derivation of $\mathbf{u}_0$, and substituting the resulting equation into equation (4.27), we get the following boundary condition for pressure

$$\mathbf{n}_\Gamma \cdot \nabla P = \frac{\rho}{\Delta t}\mathbf{n}_\Gamma \cdot \left(\tilde{\mathbf{u}} - \mathbf{u}_w\right), \tag{4.28}$$

where $\tilde{\mathbf{u}}$ is solved by the equation (4.19) at the wall. In equation (4.28), the $\mathbf{u}_w$ represent the wall velocities at t_0.

At the outlet boundary the Direchlet boundary condition for pressure is used, equal to the prescribed ambient pressure. The ambient pressure is in all discussed cases set to zero.

4.6 Adaptive Upwind Technique

The turbulent flows belong to the convection dominated problems. If the spatial discretization is not fine enough, the solution becomes instable or oscillatory. Without any special numerical technique, the five nodded LRBFCM gives similar results as the central scheme in FDM, where the solution exhibits oscillatory behaviour for Péclet (Pe) number is greater than two. To stabilize the numerical solution, the adaptive upwind technique [Lin and Atluri, 2000; Gu and Liu, 2005] is used, where the adaptive upwind support domain is constructed based on the local Pe number. This technique was already found to be very successful in the numerical modelling of the heat transfer in the continuous casting process [Vertnik *et al.*, 2007].

In the adaptive upwind support technique, the expansion coefficients are first calculated by the LRBFCM. The derivatives of the convection terms are then calculated in the point $p_{\Delta\varsigma}$, shifted by the central offset distance Δp_ς in the opposite direction of the velocity (see Figure 4.2). The position of the shifted point is defined as

$$p_{\Delta\varsigma} = p_\varsigma - \Delta p_\varsigma;\ \varsigma = x, y\,. \tag{4.29}$$

The central offset distance is calculated by

$$\Delta p_\varsigma = \mathrm{sign}(u_\varsigma)\,\delta_{up}\frac{d}{2};\ \varsigma = x, y\,, \tag{4.30}$$

where δ_{up} is the upwind function, presented in Figure 4.3, and d is the distance between the central point and the neighbour points in the opposite direction of the velocity, as shown in Figure 4.2. The upwind function is defined as

$$\delta_{up} = \coth\left|\mathrm{Pe}_{\varsigma}\right| - \frac{1}{\left|\mathrm{Pe}_{\varsigma}\right|};\ \varsigma = x, y \tag{4.31}$$

and the Pe number for the energy and the momentum equation, respectively as

$$\mathrm{Pe} = \frac{\rho c_p u_x \left(p_x^+ - p_x^-\right)}{\lambda + \lambda_t};\ \lambda_t = \frac{\rho c_p \nu_t}{\sigma_t}, \tag{4.32}$$

$$\mathrm{Pe} = \frac{\rho u_x \left(p_x^+ - p_x^-\right)}{\mu + \mu_t} \equiv \mathrm{Re}. \tag{4.33}$$

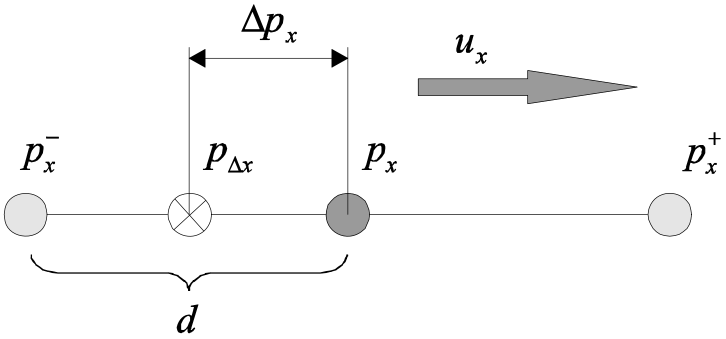

Figure 4.2: The adaptive upwind support.

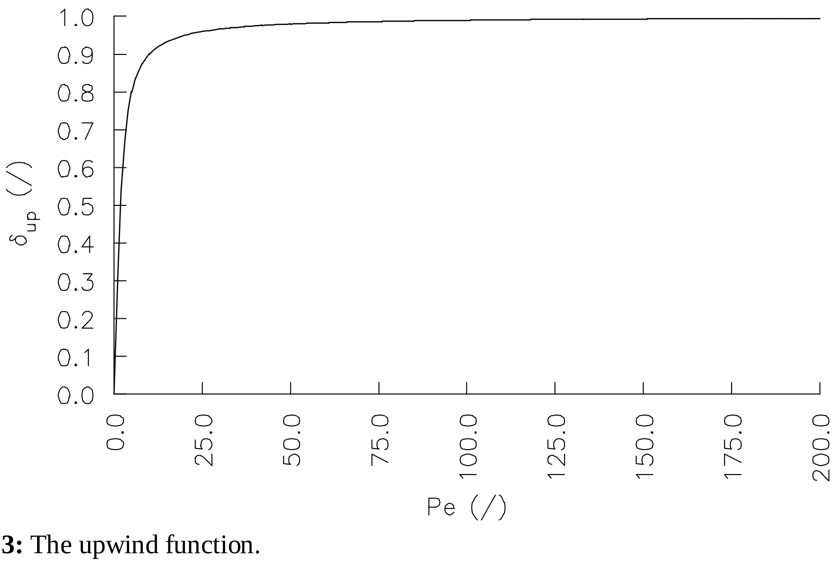

Figure 4.3: The upwind function.

The accuracy and stability of the adaptive upwind technique is demonstrated by the numerical example in Section 5.3.

5 Numerical Examples

In this chapter, the numerical examples for validation of the developed numerical algorithm are presented. First, a detailed explanation of the refinement procedure of the node generation near the walls is given. Next, the adaptive-upwind technique is tested on a 1D convective-diffusive phase-change problem. The obtained results are compared with the analytical solution at various Pe numbers. This technique is further used in all examples, where the turbulent flow is involved. The fluid flow examples are arranged into two separable groups, i.e. laminar and turbulent flow problems.

The laminar flow problems contain two numerical examples: the natural convection in a square cavity and the flow over a backward-facing step. The natural convection in a square cavity is performed to test the implementation of the fractional step method and the fully coupled problem between the momentum and the energy equations. The laminar flow over a backward-facing step is chosen in order to test the implementation of the inlet and the outlet boundary conditions, and the separation and reattachment phenomena.

The turbulent flow problems contain four examples: 2D channel flow, 2D channel flow with temperature as a passive scalar, 2D channel flow with combined forced and natural convection, and flow over a backward-facing step. The first two examples are mainly chosen to test the implementation of a LRN turbulence models, i.e. JL, LS and AKN model. The third example is found to be very important, since similar physical phenomena are involved in the continuous casting of steel. It involves the forced convection, the free-stream flow through a 2D channel, and natural convection due to the differentially heated walls. The last example is a standard test problem for evaluating the turbulence models. The results are compared with the results obtained by the DNS data, experimental data, and with the numerical results obtained by the commercial software Fluent (Version 6.3.26, ANSYS, Inc., “http://www.fluent.com/”).

5.1 Numerical Implementation

The presented numerical method is written in Compaq Visual Fortran (CVF) (Version 6.6a).

The linear system of equations for local collocation is solved by LAPACK library (Version 3.0). The left side of a matrix is inverted by calling the following two routines in a sequence: DGETRF for computing an LU factorization of a matrix, and DGETRI for computing an inverse of a matrix using the LU factorization computed by DGETRF routine. The final solution is obtained by using the multiplication of the inverted left side and right side of the matrix with the Fortran function MATMUL. The first two routines, i.e. DGETRF and DGETRI, are called only once before the simulation starts, due to the fixed node arrangements.

The sparse matrix is solved by the HSL 2007 library, package MA48 (Version 2.1.0, “http://www.hsl.rl.ac.uk/”). The MA48 package has ability to solve unsymmetric sparse system with the conventional direct method using the Gaussian elimination. First, the routine MA48AD is called to prepare data structures for factorization, optionally permuting the left side matrix to block upper triangular form. Next, the MA48BD routine is used to factorize the left side matrix with the given data provided by routine MA48AD. A sparse system is then solved by the routine MA48CD, which uses the factors produced by MA48BD routine. The routines MA48AD and MA48BD are called only once, before the simulation starts. This is allowed when using the fixed node arrangements, since the left side of the matrix depends only on the node position and thus it is unchanged during the simulation. So, in each time step, only the MA48CD routine is called.

All graphics outputs (simple graphs, contours, streamlines, fields, etc.) are generated in CVF with the PGPlot graphic library (Version 5.2.2, “http://www.astro.caltech.edu/~tjp/pgplot/”). The streamlines are constructed by integrating the calculated velocity field with the fourth-order Range-Kutta integrator [Press *et al.*, 1992].

The simulations are performed on the following computers:

- Compaq 8710w, Mobile Workstation, Intel Core Duo 2.4 GHz processor and
- HP xw9300 Workstation, 2x AMD Opteron 2.6 GHz processor.

5.2 Refinement Near the Walls

The node arrangements in the numerical examples with the fluid flow calculations are generated with the refinement near the walls in order to achieve a better accuracy in the boundary layers. Here, we present a detailed procedure of the refinement through an example of node generation of a horizontal edge:

- First, the uniform node arrangement (see Figure 5.1), is created by the following equation

$$p_{xn}^{uniform} = x_{\min} + \left(n-1\right)\frac{(x_{\max} - x_{\min})}{N_\Omega + N_\Gamma - 1};\; n = 1, 2, ..., N_\Omega + N_\Gamma. \tag{5.1}$$

Figure 5.1: Uniform node arrangement.

- The node arrangement is then normalised (see Figure 5.2), respectively. In the normalised arrangement the position of each node $p_{xn}^{uniform}$ lies between 0 and 1, i.e.

$$p_{xn}^{uniform} = \frac{p_{xn}^{uniform} - x_{\min}}{x_{\max} - x_{\min}}. \tag{5.2}$$

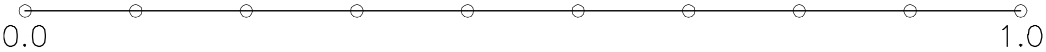

Figure 5.2: Normalised uniform node arrangement.

- The uniform node position $p_{xn}^{uniform}$ is then recalculated by the power function to obtain its refinement position

$$p_{xn}^{refined} = 1.0 - (1.0 - p_{xn}^{uniform})^b, \tag{5.3}$$

where $p_{xn}^{refined}$ and b are standing for refined node position and exponent of the power function, respectively. Figure 5.4 represents the effect of the exponent b, which defines the level of the refinement. The refined node position in the normalized arrangement is shown in Figure 5.3.

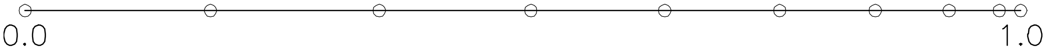

Figure 5.3: Normalized node arrangement, refined near the wall with $b = 1.75$.

- After refinement, the node positions are scaled back (de-normalized) to get the final discretization (see Figure 5.5), in physical coordinates

$$p_{xn}^{refined} = x_{\min} + p_{xn}^{refined}\left(x_{\max} - x_{\min}\right). \tag{5.4}$$

This procedure also allows to use other refinement functions, i.e. tanh or parabolic, but they are not used in the present dissertation. The same technique is applied for vertical edges. In each numerical example, where the refinement is used, the level of the refinement b is given.

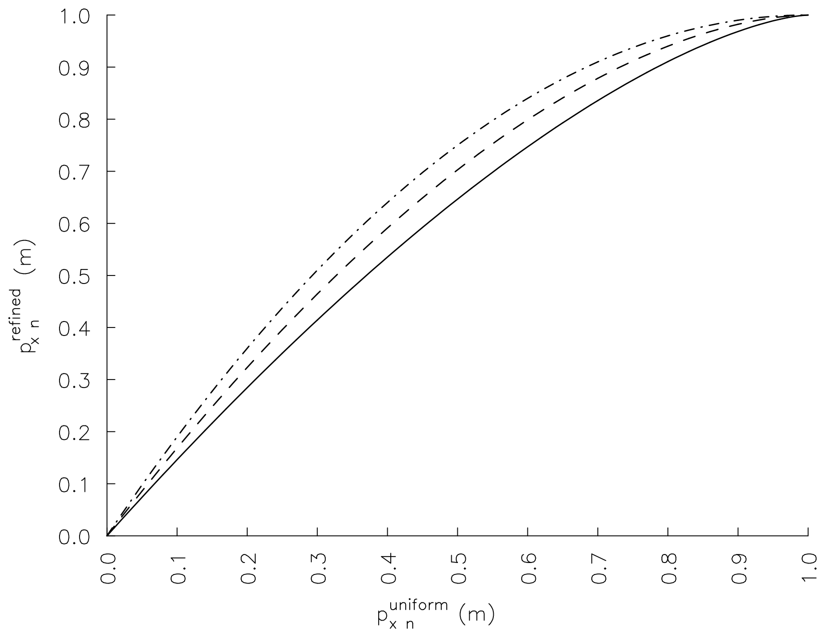

Figure 5.4: Power function with various exponents. Solid line: $b = 1.5$. Dashed line: $b = 1.75$. Dashed-dot line: $b = 2.0$.

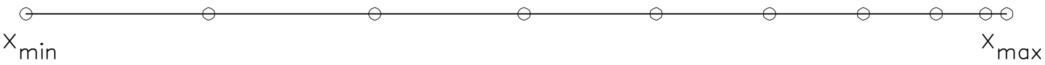

Figure 5.5: The final node arrangement, refined near the wall with $b = 1.75$.

5.3 One-dimensional Convective-Diffusive Phase-Change Problem

5.3.1 Problem Description

This example was already analyzed in detail in the master thesis [Vertnik, 2007] and in the publication [Vertnik and Šarler, 2006a]. It is chosen in the present dissertation, in order to assess the adaptive-upwind technique, described in Section 4.6.

The computations are done with uniform domain discretizations of the type $N \times 3$ (see Figure 5.6), with $N = N_\Gamma + N_\Omega$, $N_\Gamma = 2 \times (N-2) + 2$ and $N_\Omega = N - 2$, defined on strip-shaped domains with longitudinal coordinates $p_x^- = 0\,\mathrm{m}$, $p_x^+ = 1\,\mathrm{m}$, and transversal coordinates $p_y^\pm = \pm 0.5$. An example of the schematic of 21×3 discretization is shown in Figure 5.6. The steady-state solution is reached through a transient from the initial uniform temperature $T_0 = T_\Gamma^-$ and a jump of the boundary conditions at p_x^- from $T_\Gamma^- = 0\,\mathrm{K}$ to $T_\Gamma^+ = 1\,\mathrm{K}$ for $t > t_0$ and stopped through the steady state criterion, defined by the equation

(4.18). The steady-state criterion used in all calculations in this test is $T_{\mathrm{ste}} = 10^{-8}\,\mathrm{K}$. The time-step used is $\Delta t = 10^{-6}\,\mathrm{s}$.

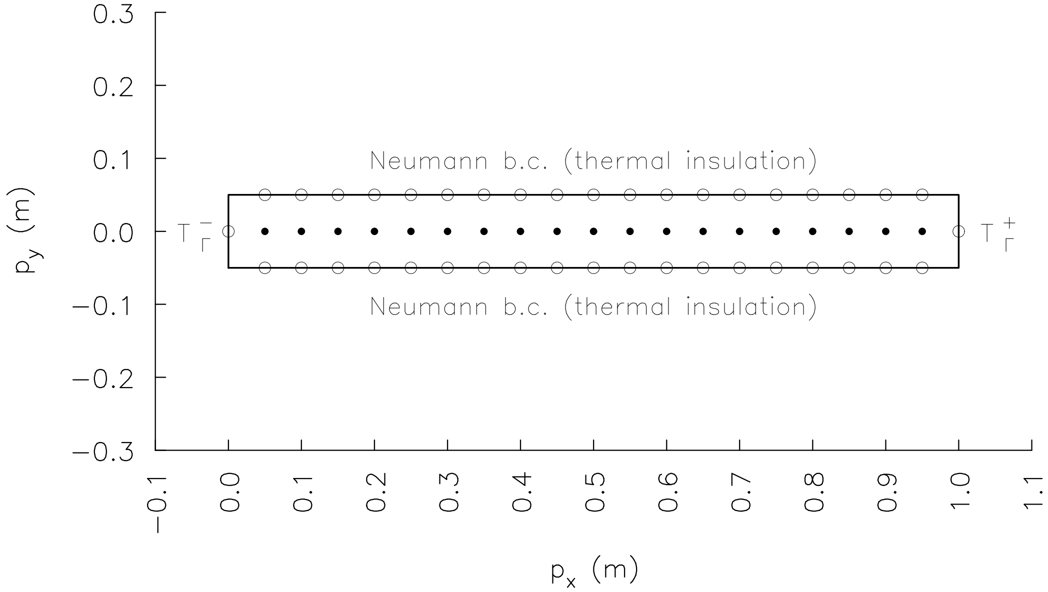

Figure 5.6: Discretization schematics $N \times 3$; $N' = 21$, with boundary conditions for solving the quasi-1D convective diffusive problem.

5.3.2 Numerical Results

The calculations are performed with constant unit thermal properties and single phase material, with 201×3 discretization. The results are compared with the analytical solution, presented in Appendix A.1. A comparison is performed through the following error measures

$$T_{\max} = \max \left| T(\mathbf{p}_n, t) - T_{\mathrm{ana}}(\mathbf{p}_n, t) \right|; \; n = 1, 2, ..., N, \tag{5.5}$$

$$T_{\mathrm{avg}} = \frac{1}{N} \sum_{n=1}^{N} \left| T(\mathbf{p}_n, t) - T_{\mathrm{ana}}(\mathbf{p}_n, t) \right|; \; n = 1, 2, ..., N, \tag{5.6}$$

where $T_{\max}$ and T_{avg} are the maximum absolute temperature error and the average absolute temperature error, respectively. In both equations (5.5) and (5.6), T_{ana} stands for analytical solution and N represents the total number of the domain nodes.

The influence of adaptive-upwind technique on the accuracy and stability of the numerical results is made by the sensitivity study with respect to Pe number. The accuracy of the results, based on the $T_{\max}$ and T_{avg} errors, are given in Table 5.1. The results, obtained with and without upwind, are represented for various

Pe numbers in Figures 5.7-5.13. Without upwind, the solution is stable up to the $\mathrm{Pe}=100$. At higher Pe values, the solution becomes unstable, as we can see from Figures 5.11, 5.12 and 5.13. The adaptive-upwind technique completely eliminates those instabilities and also gives very good results at low Pe numbers, which is its main advantage over the classical upwind technique.

Table 5.1: Sensitivity of the results with respect to Pe number at 101×3 node arrangement.

Pe	T_{avg} (K)		$T_{\max}$ (K)	
	no upwind	upwind	no upwind	upwind
2	9.609E–4	9.779E–4	1.557E–3	1.585E–3
10	2.412E–4	5.502E–4	5.364E–4	1.525E–3
50	3.999E–4	1.168E–3	7.743E–3	2.109E–2
100	8.103E–4	1.861E–3	3.447E–2	6.680E–2
200	1.550E–3	2.172E–3	0.135E+0	0.138E+0
500	7.423E–3	1.421E–3	0.435E+0	0.124E+0
1000	1.981E–2	7.440E–4	0.666E+0	6.978E–2

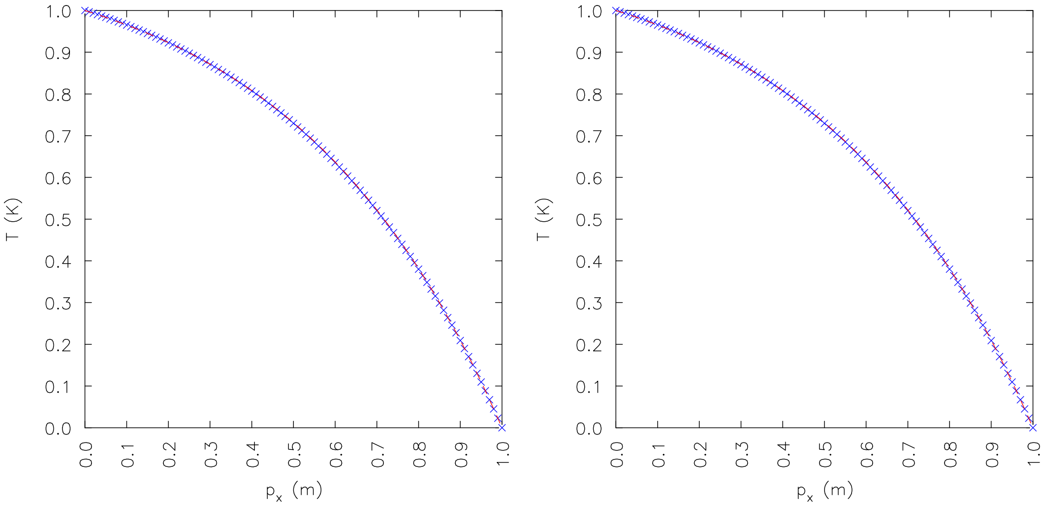

Figure 5.7: Comparison of the calculated temperatures with the analytical solution in the central nodes at $p_y = 0$ m, $\mathrm{Pe} = 2$. Red dashed line: analytical solution. Blue crosses: present method. Left: no upwind. Right: upwind.

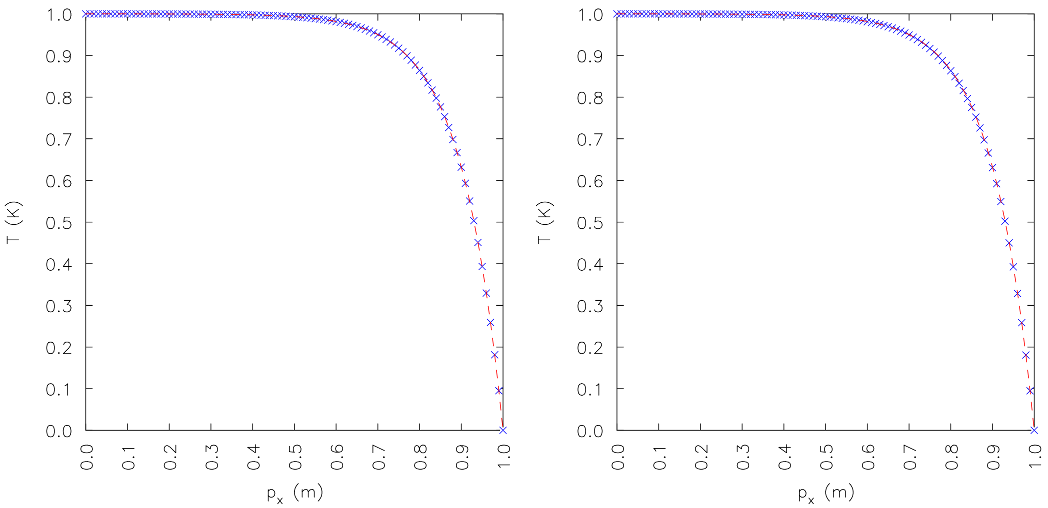

Figure 5.8: Comparison of the calculated temperatures with the analytical solution in the central nodes at $p_y = 0$ m, $\mathrm{Pe} = 10$. Red dashed line: analytical solution. Blue crosses: present method. Left: no upwind. Right: upwind.

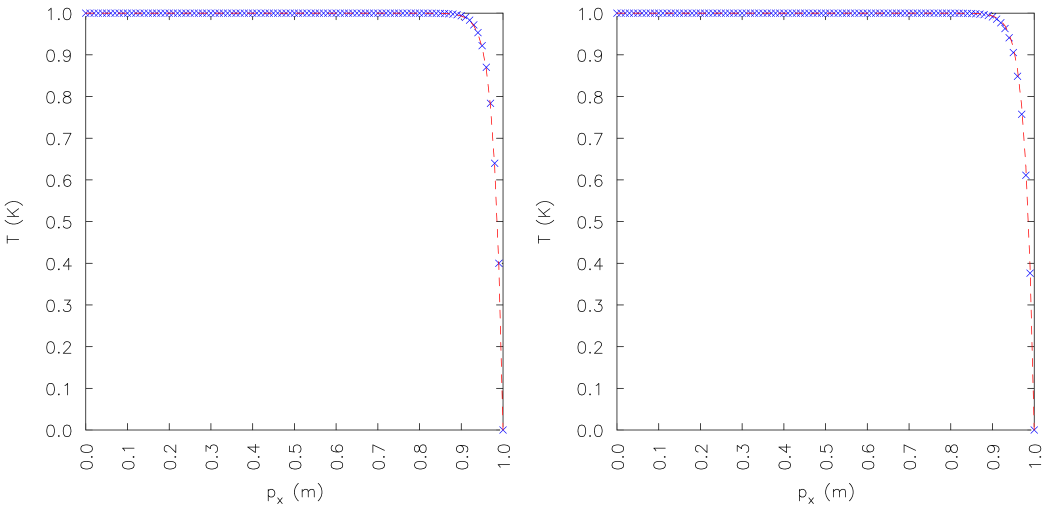

Figure 5.9: Comparison of the calculated temperatures with the analytical solution in the central nodes at $p_y = 0$ m, $\mathrm{Pe} = 50$. Red dashed line: analytical solution. Blue crosses: present method. Left: no upwind. Right: upwind.

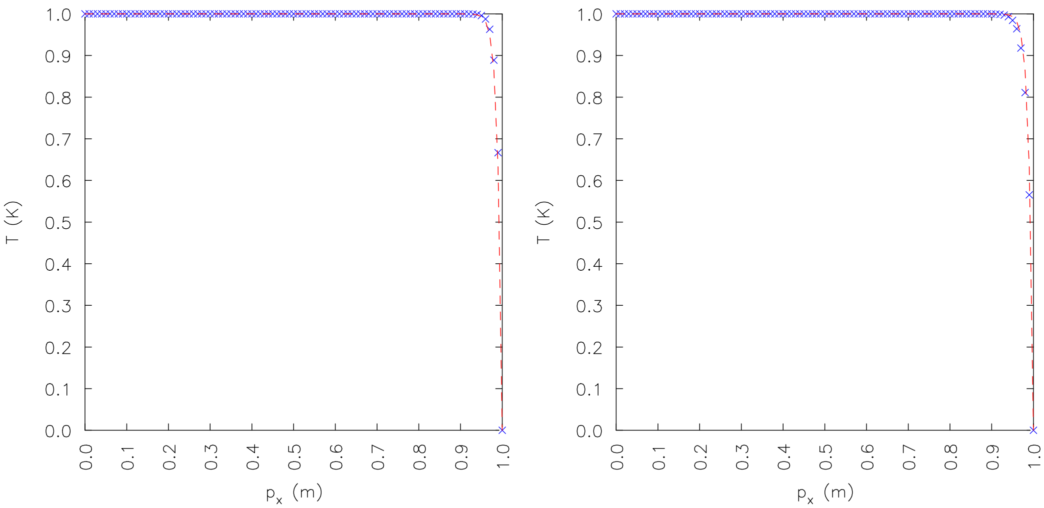

Figure 5.10: Comparison of the calculated temperatures with the analytical solution in the central nodes at $p_y = 0$ m, $\mathrm{Pe} = 100$. Red dashed line: analytical solution. Blue crosses: present method. Left: no upwind. Right: upwind.

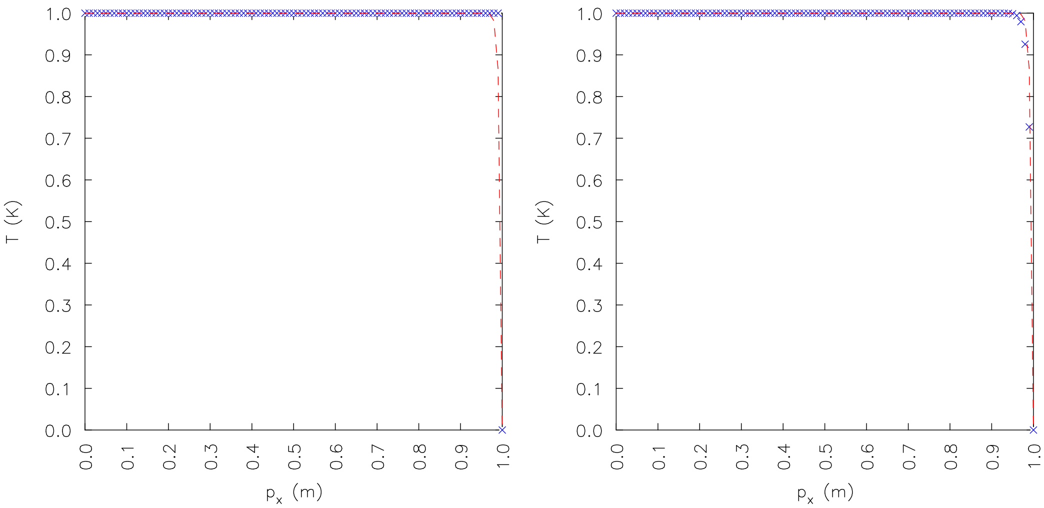

Figure 5.11: Comparison of the calculated temperatures with the analytical solution in the central nodes at $p_y = 0$ m, $\mathrm{Pe} = 200$. Red dashed line: analytical solution. Blue crosses: present method. Left: no upwind. Right: upwind.

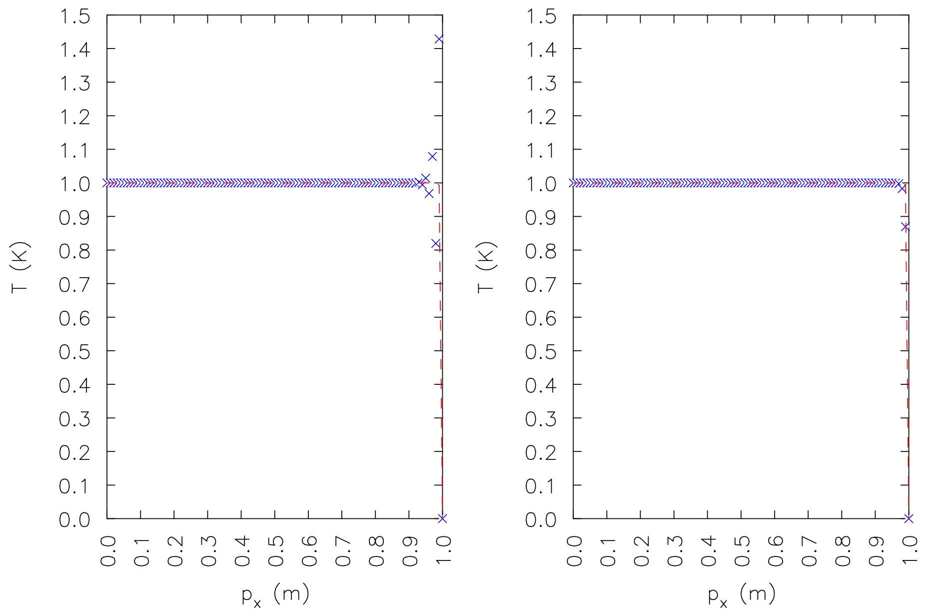

Figure 5.12: Comparison of the calculated temperatures with the analytical solution in the central nodes at $p_y = 0$ m, $\mathrm{Pe} = 500$. Red dashed line: analytical solution. Blue crosses: present method. Left: no upwind. Right: upwind.

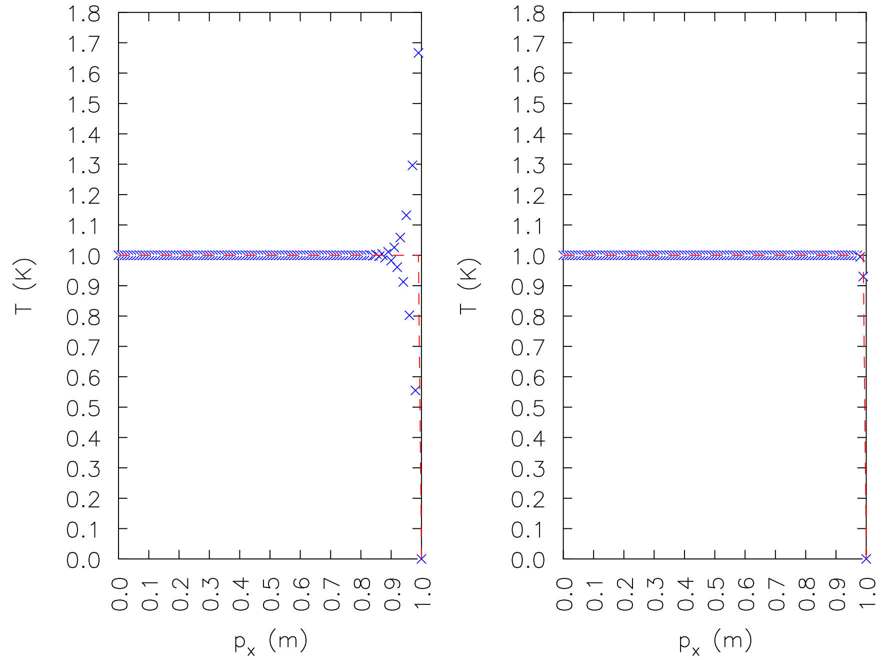

Figure 5.13: Comparison of the calculated temperatures with the analytical solution in the central nodes at $p_y = 0$ m, $\mathrm{Pe} = 1000$. Red dashed line: analytical solution. Blue crosses: present method. Left: no upwind. Right: upwind.

5.4 Laminar Flow Problems

5.4.1 Natural Convection in a Square Cavity

5.4.1.1 Problem Description

This example is very well established in science for developing and testing various numerical algorithms, capable of solving thermal fluid flow problems [Davis, 1983; Sadat and Couturier, 2000; Wan *et al.*, 2001; Šarler, 2005; Kosec and Šarler, 2007]. Natural convection is an important physical phenomenon, which can be found in nature and industrial applications, such as furnaces, electronics cooling, materials processing, etc.

Computational domain is a closed square cavity with height $H = 1$ and width $L = 1$. The cavity is differentially heated on vertical walls and isolated on horizontal walls, shown in Figure 5.14. No slip boundary condition for the velocity $\mathbf{u} = 0$ is applied at the walls. Calculations are performed with three different node arrangements: 61×61, 81×81 and 101×101 (without 4 corner nodes). To enhance the accuracy in the boundary layer, the arrangements are refined near the walls with a refinement level $b = 1.2$ from the centre to the walls. A schematic of 61×61 node arrangement is presented in Figure 5.15. Square cavity is filled with air having Prandtl number $\mathrm{Pr} = 0.71$ and experiencing the uniform initial temperature field $T_0 = (T_h + T_c)/2$.

5.4.1.2 Numerical Results

The steady-state solution of the velocity and temperature field is searched, approached by the transient calculation with the fixed time step. The streamlines and the temperature fields are presented for 101×101 node arrangement and various Rayleigh numbers: $\mathrm{Ra} = 10^6$, $\mathrm{Ra} = 10^7$ and $\mathrm{Ra} = 10^8$ in Figures 5.16, 5.17 and 5.18, respectively. The Rayleigh number is defined as

$$\mathrm{Ra} = \frac{g \beta \Delta T L^3 \rho^2 c_p}{\lambda \mu}. \tag{5.7}$$

The numerical results are compared with the [Davis, 1983; Sadat and Couturier, 2000; Wan *et al.*, 2001; Šarler, 2005; Kosec and Šarler, 2007] in terms of maximum mid-plane velocities and averaged Nusselt number Nu_{avg} at the hot wall, presented in Table 5.2, Table 5.3 and Table 5.4 for $\mathrm{Ra} = 10^6$, $\mathrm{Ra} = 10^7$ and $\mathrm{Ra} = 10^8$, respectively. Nu_{avg} is calculated by the following relation

$$\mathrm{Nu}_{avg} = -\frac{\int_0^H \mathrm{Nu}\,\mathrm{d}y}{H}, \tag{5.8}$$

where Nu is a local Nusselt number, defined as

$$\mathrm{Nu} = -\frac{L}{T_h - T_c}\frac{\partial T}{\partial n}. \tag{5.9}$$

We can conclude from the comparison, that the accuracy of the calculated velocity and temperature field of the developed method is very good. Also the implementation of the fractional step method for solving the incompressible fluid flow problems is successfully approved.

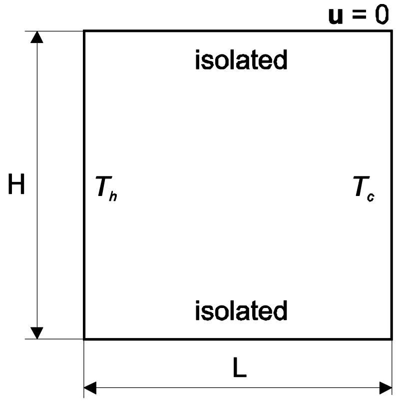

Figure 5.14: Problem schematics of the natural convection in a square.

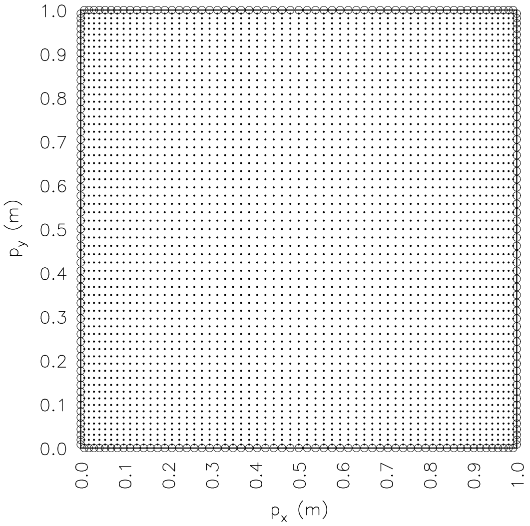

Figure 5.15: 61×61 node arrangement, refined near the walls with a refinement level $b = 1.2$.

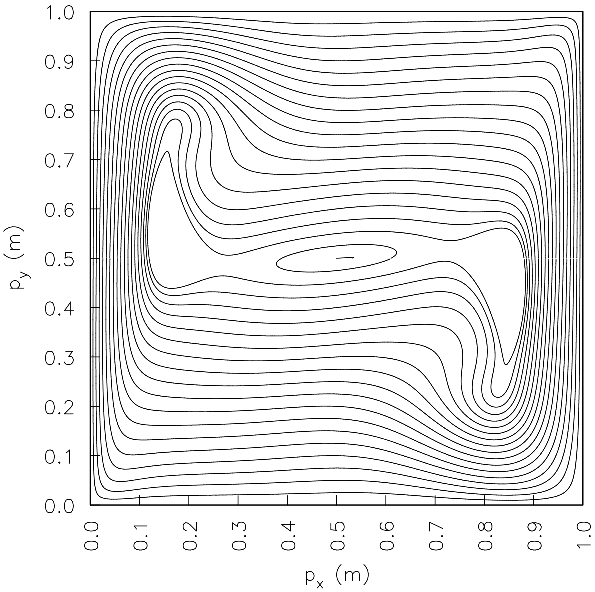

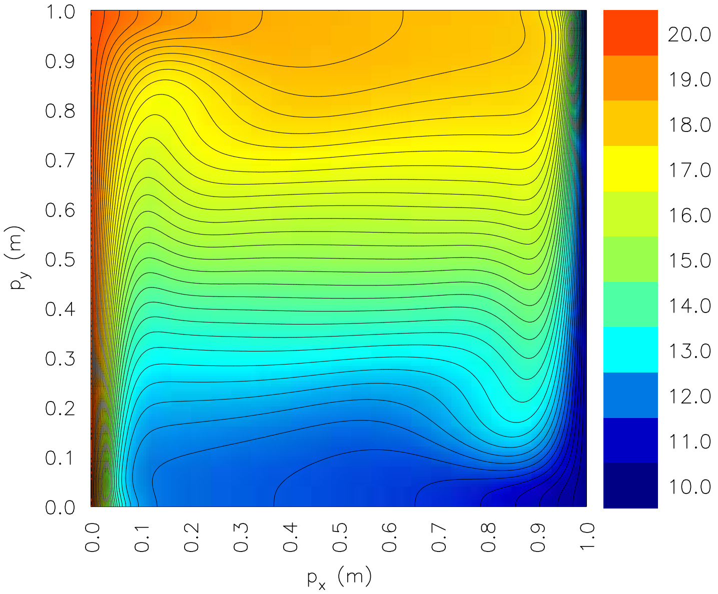

Figure 5.16: Streamlines (top) and temperature field with isotherms (bottom) at $\mathrm{Ra} = 10^6$ by using 101×101 node arrangement.

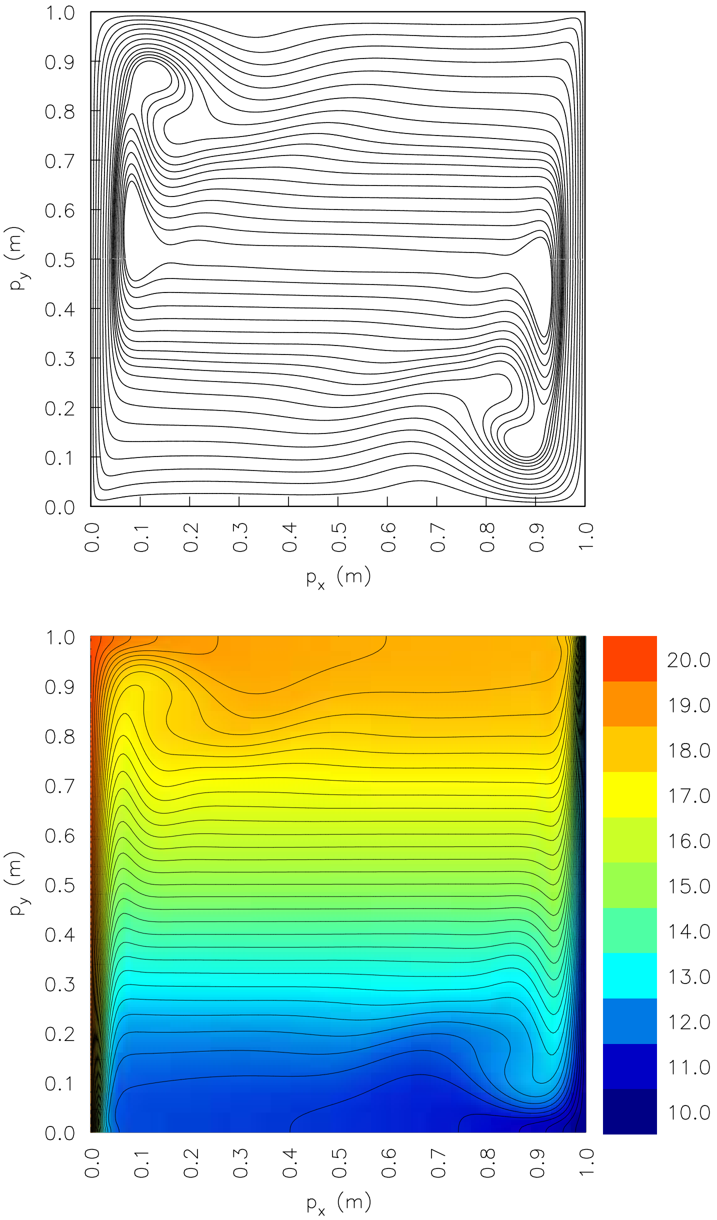

Figure 5.17: Streamlines (top) and temperature field with isotherms (bottom) at $\mathrm{Ra} = 10^7$ by using 101×101 node arrangement.

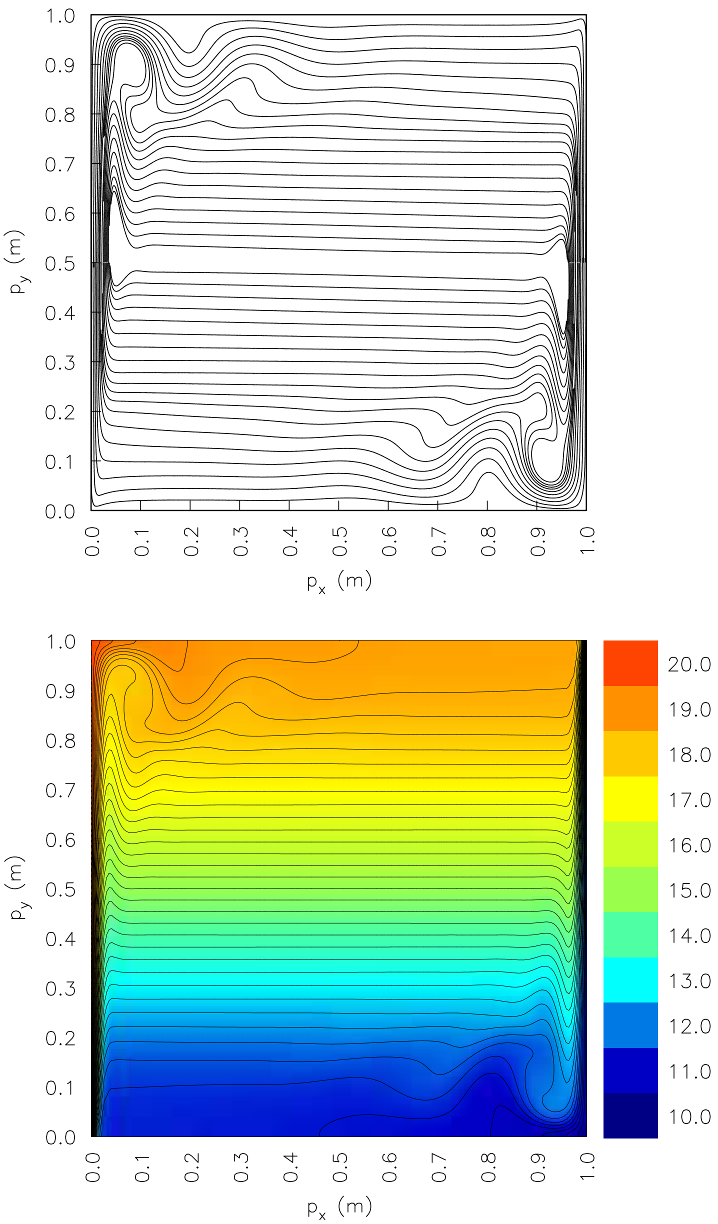

Figure 5.18: Streamlines (top) and temperature field with isotherms (bottom) at $\mathrm{Ra}=10^8$ by using 101×101 node arrangement.

Table 5.2: Maximum mid-plane velocities and Nu_{avg} at $\mathrm{Ra} = 10^6$.

$\mathrm{Ra} = 10^6$		$u_{x,\max}$	$u_{y,\max}$	Nu_{avg}
[Davis, 1983]		65.33	216.75	8.798
[Sadat and Couturier, 2000]		64,33	219,41	8.832
[Wan *et al.*, 2001]		65.40	227.11	8.800
[Šarler, 2005]		61.55	211.67	/
[Kosec and Šarler, 2007]		65.91	221.37	8.970
present method	$61 \times 61; \Delta t = 10^{-5}\,\mathrm{s}$	63.38	214.69	8.860
	$81 \times 81; \Delta t = 10^{-5}\,\mathrm{s}$	64.01	218.26	8.850
	$101 \times 101; \Delta t = 5 \cdot 10^{-6}\,\mathrm{s}$	64.26	219.43	8.840

Table 5.3: Maximum mid-plane velocities and Nu_{avg} at $\mathrm{Ra} = 10^7$.

$\mathrm{Ra} = 10^7$		$u_{x,\max}$	$u_{y,\max}$	Nu_{avg}
[Sadat and Couturier, 2000]		145.68	687.43	16.59
[Wan *et al.*, 2001]		143.56	714.48	16.65
[Kosec and Šarler, 2007]		149.61	687.20	16.92
present method	$61 \times 61; \Delta t = 10^{-5}\,\mathrm{s}$	134.11	671.58	16.72
	$81 \times 81; \Delta t = 10^{-5}\,\mathrm{s}$	139.76	686.24	16.64
	$101 \times 101; \Delta t = 10^{-6}\,\mathrm{s}$	142.62	685.09	16.61

Table 5.4: Maximum mid-plane velocities and Nu_{avg} at $\mathrm{Ra} = 10^8$.

$\mathrm{Ra} = 10^8$		$u_{x,\max}$	$u_{y,\max}$	Nu_{avq}
[Sadat and Couturier, 2000]		319.19	2180.10	30.94
[Wan *et al.*, 2001]		296.71	2259.08	31.48
[Kosec and Šarler, 2007]		278.49	2095.23	32.12
present method	$61\times61; \Delta t = 10^{-5}$ s	/	/	/
	$81\times81; \Delta t = 10^{-6}$ s	244.31	2069.66	30.87
	$101\times101; \Delta t = 10^{-6}$ s	260.79	2133.17	30.78

5.4.2 Backward-Facing Step

5.4.2.1 Problem Description

The problem of the laminar incompressible flow over a backward-facing step is a standard test for investigating the flow separation and reattachment. It was used by numerous researchers as a benchmark test for various numerical methods [Gartling, 1990; Gresho, 1993; Chiang *et al.*, 1999; Keskar and Lyn, 1999; Barton, 1995; Barton and Kirby, 2000]. The geometry of the problem (see Figure 5.19) is characterized by a planar channel with sudden change of the geometry, which creates the process of flow separation and generation of several re-circulating zones downward the step. A similar phenomena can be observed in engineering practice, such as the continuous casting process of metal alloys.

The computational domain considers only the physical domain after the step, where the step has height $H = 0.5$ and the channel length after the step is $L = 30H$. A node arrangement is generated with a refinement near the top and the bottom walls, around the centreline, and near the step in the horizontal direction with the refinement level $b = 1.4$ (see Figure 5.20). An example of the detailed view of the generated node arrangement is shown in Figure 5.21. The flow conditions are defined by the Re number based on the characteristic length $\Delta\ell$, i.e.

$$\mathrm{Re} = \frac{\rho u_0 \Delta\ell}{\mu}. \tag{5.10}$$

In this example, $\Delta\ell$ is equal to $2H$ and the velocity u_0 is equal to the inlet velocity of fluid u_{x0}, entering into the channel before the step. u_{x0} is uniform and equal to unity.

The accuracy of the numerical method is evaluated based on the velocity profiles at different horizontal positions, wall shear stresses, pressure, and reattachment positions of the re-circulating zones. The reattachment is defined as the horizontal position, measured from the step, where the wall-shear stress is equal to zero.

The following boundary conditions are used:

- At the inlet the fully-developed velocity profile is set, which is a parabolic function in the horizontal direction [Gartling, 1990], i.e.

$$u_x\left(p_y\right) = 24 p_y \left(0.5 - p_y\right); 0.0 \le p_y \le 0.5 . \tag{5.11}$$

- At the outlet boundary, the Neumann boundary conditions for velocity components are prescribed and are all set equal to zero.
- At the wall, the Dirichlet no-slip boundary conditions are set, which implies that the velocity components are all set to zero.

The time step $\Delta t = 10^{-3}$ s is set for all calculations.

5.4.2.2 Numerical Results

The calculations are first performed at $\text{Re} = 600$ and three different node arrangements, i.e. 201×61, 251×81 and 301×101 (without 4 corner nodes), to achieve the grid independent solution. The results are presented in Table 5.6, where the calculated reattachment positions of the re-circulating zones are given and compared by [Barton, 1995]. The position p_{x1} defines the reattachment of the lower re-circulating zone, and the positions p_{x2}, p_{x3} the upper re-circulating zone (see Figure 5.22). The 301×101 node arrangement is chosen in further calculations.

The effect of the Re number on the flow development is shown in Figure 5.22, where the streamlines are plotted. The Re numbers are ranging from 300-800 with step $\Delta\text{Re} = 100$. At the $\text{Re} = 300$, only the lover re-circulating zone exists, while with the $\text{Re} \ge 400$, another re-circulating zone at the top wall starts to develop. With enhancing of the Re number, both re-circulating zones become larger. The calculated reattachment positions at various Re numbers are presented in Table 5.7, compared with the results obtained by Barton [Barton, 1995].

Figures 5.23 to 5.26 represent detailed results of the wall shear stress along the upper and the lower wall, horizontal velocity profiles, vertical velocity profiles, and pressure profiles across the channel at $p_x = 7$ and $p_x = 15$, respectively. The wall shear stress is calculated by the following equation

$$\tau_w = \mu \frac{\partial u_x}{\partial p_y}. \tag{5.12}$$

The profiles are obtained for the case with $\mathrm{Re} = 800$ and 301×101 node arrangement. The results are compared with the results by Gartling [Gartling, 1990], where excellent agreement is found. The only visual difference is found in the vertical velocity profile at $x = 7$ (see Figure 5.25). The plotted value of the pressure by Gartling is modified, because he used different boundary conditions (the convective ones) at the outlet boundary as in our calculations.

The calculated reattachment positions at $\mathrm{Re} = 800$ are compared with other authors [Gartling, 1990; Gresho *et al.*, 1993; Chiang *et al.*, 1999; Keskar and Lyn, 1999; Barton and Kirby, 2000] in Table 5.5, where a very good agreement is observed.

The present method is also tested on a slightly random 301×101 node arrangement by repositioning the non-uniform node arrangement with the following relation

$$p_{\varsigma(random)} = p_{\varsigma(non-uniform)} + c_{rnd} \delta r_{\min} \,;\; \varsigma = x, y\,, \tag{5.13}$$

with c_{rnd}, δ and $r_{\min}$ standing for a random number $-1 \le c_{rnd} \le +1$, a displacement factor, and the minimum distance between the nodes in the influence domain of the non-uniform node arrangement, respectively. In this example, a displacement factor is $\delta = 0.5$. A detailed view of the generated slightly random node arrangement is shown in Figure 5.27. The calculation is performed at $\mathrm{Re} = 600$ and with the same time step as for the non-uniform node arrangement. Table 5.8 represents the calculated reattachment positions, compared by the results obtained with the non-uniform node arrangement. On the basis of this comparison, we can conclude, that the present meshless numerical method is capable of solving such kind of problems on a slightly random node arrangements.

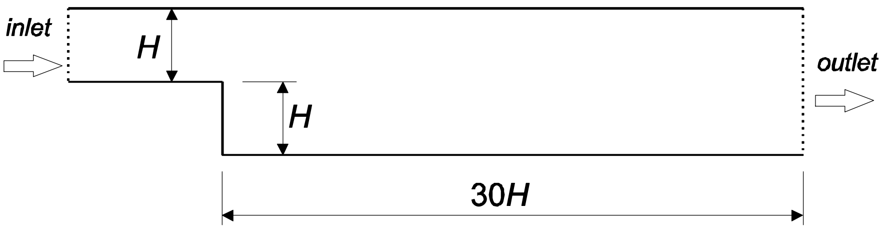

Figure 5.19: Problem schematics of the backward-facing step.

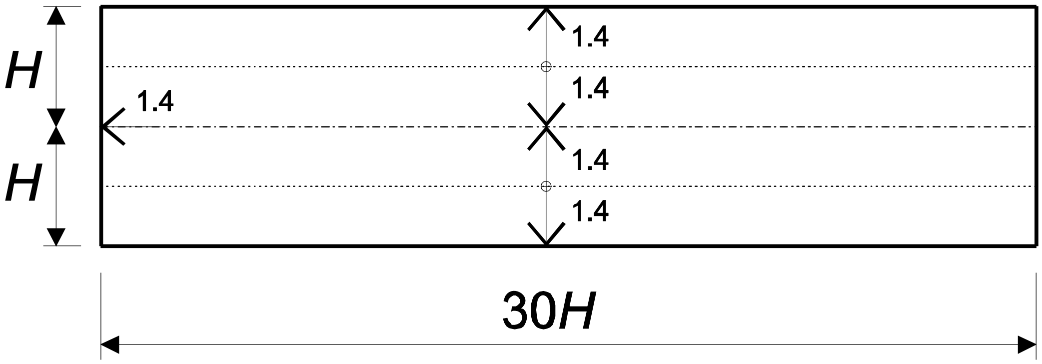

Figure 5.20: Levels of the refinement with $b = 1.4$.

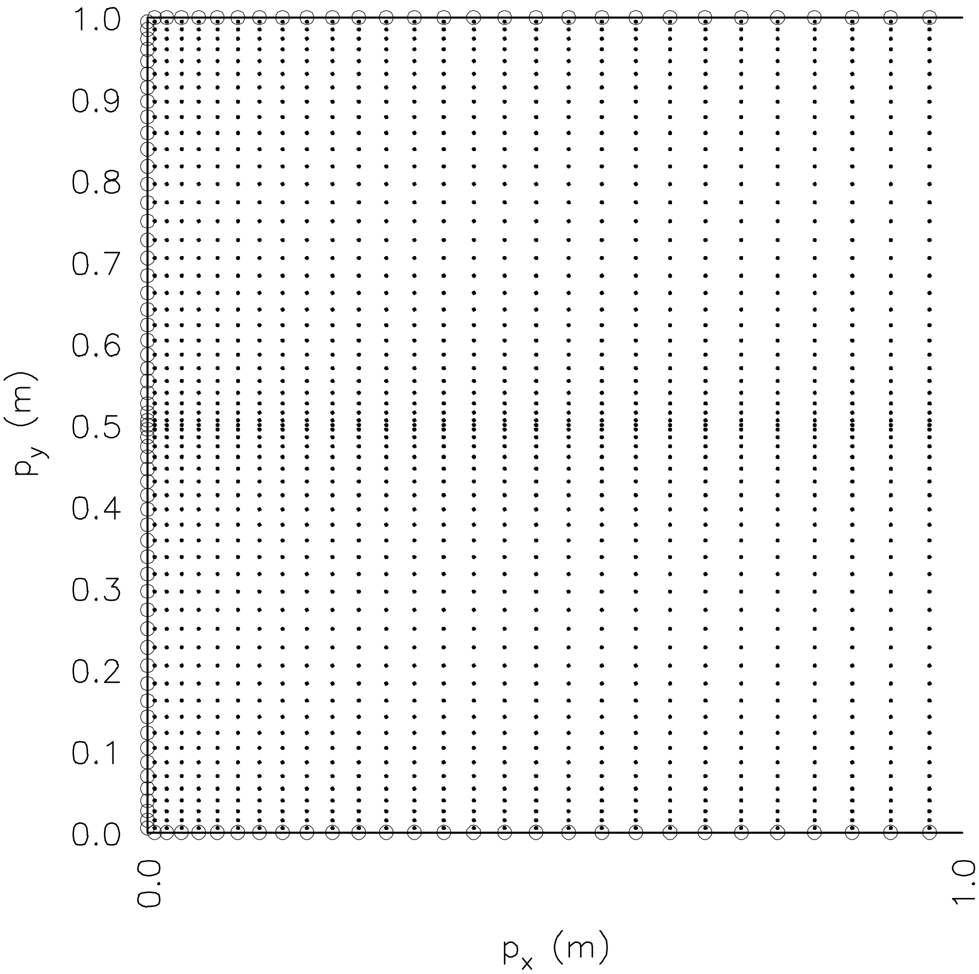

Figure 5.21: A detailed view of the 201×61 node arrangement. o: boundary nodes. •: domain nodes.

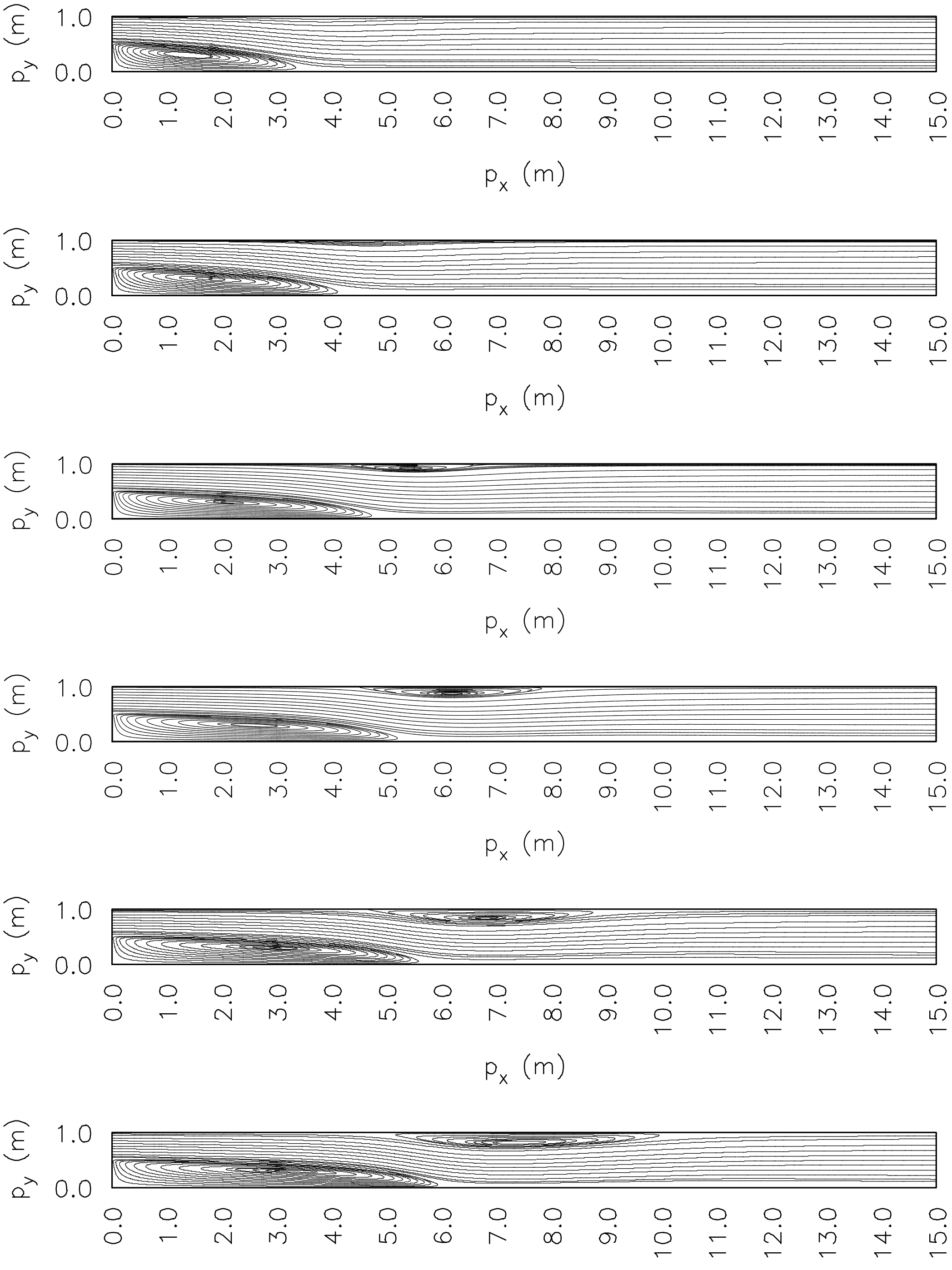

Figure 5.22: Streamlines for $\mathrm{Re} = 300\text{-}800$ with step 100 (from top to bottom) by using 301×101 node arrangement.

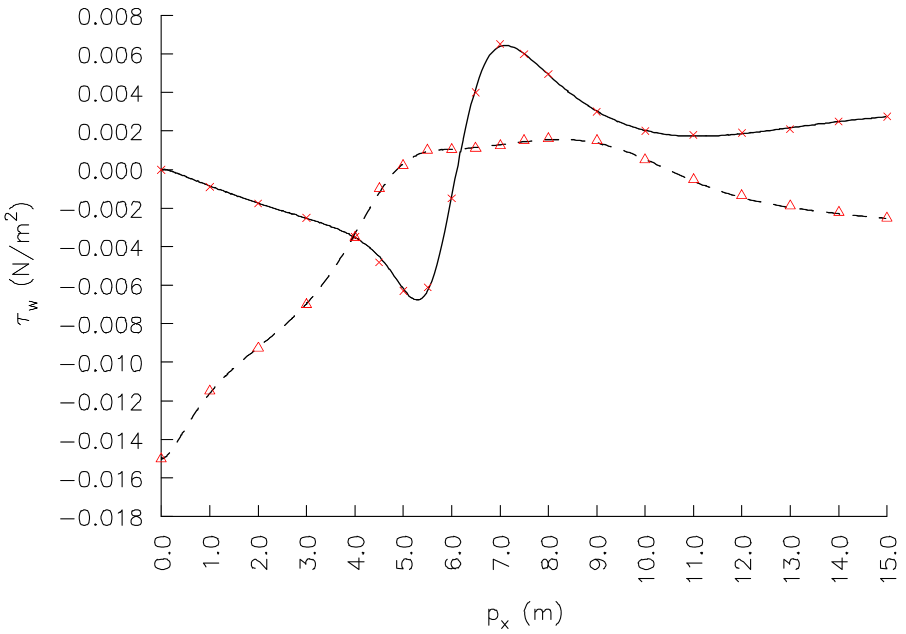

Figure 5.23: Wall-shear stress at the lower and upper wall for $\mathrm{Re} = 800$ by using 301×101 node arrangement. Lines: present method. Red symbols: [Gartling, 1990]. Solid line and ×: lower wall. Dashed line and Δ: upper wall.

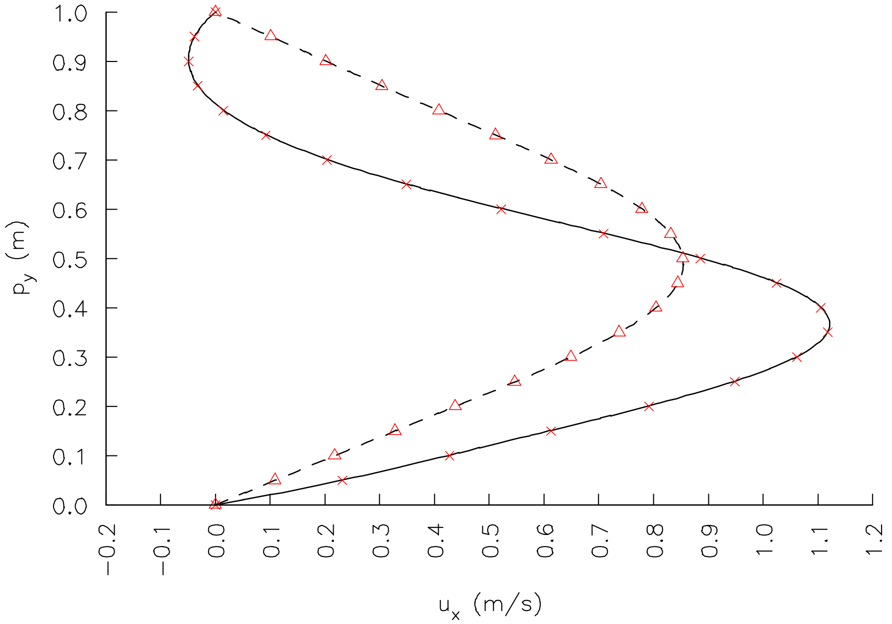

Figure 5.24: Horizontal velocity profiles across the channel for $\mathrm{Re} = 800$ by using 301×101 node arrangement. Lines: present method. Red symbols: [Gartling, 1990]. Solid line and ×: at $p_x = 7$. Dashed line and Δ: $p_x = 15$.

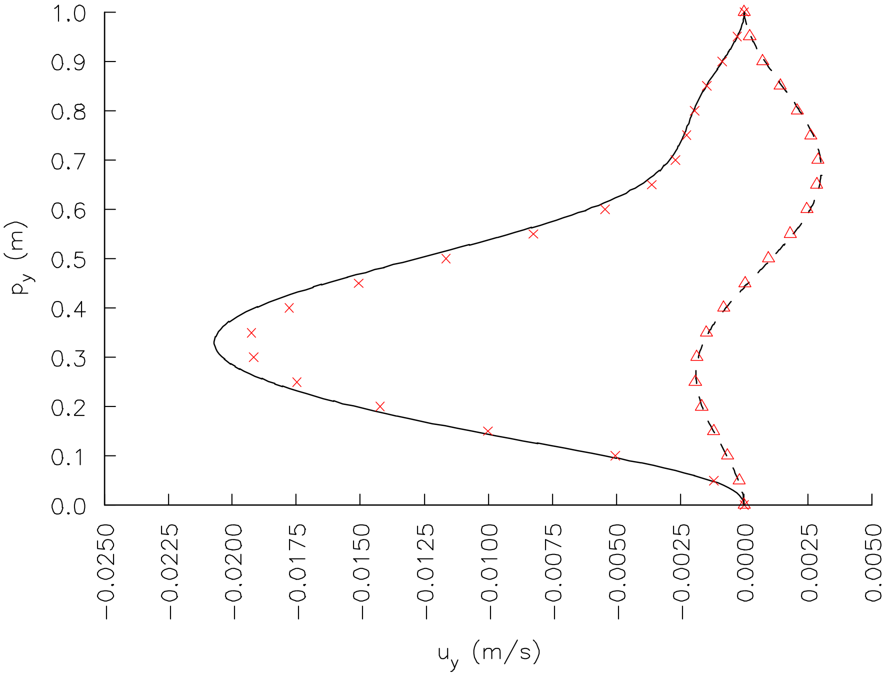

Figure 5.25: Vertical velocity profiles across the channel for $\mathrm{Re}=800$ by using 301×101 node arrangement. Lines: present method. Red symbols: [Gartling, 1990]. Solid line and ×: at $p_x=7$. Dashed line and Δ: $p_x=15$.

Table 5.5: Comparison of results at $\mathrm{Re}=800$.

	p_{x1}	p_{x2}	p_{x3}
[Gartling, 1990]	6.10	4.85	10.48
[Gresho *et al.*, 1993]	6.10	4.86	10.48
[Chiang *et al.*, 1999]	6.16	4.82	10.63
[Barton, 1995]	6.08	4.81	11.03
[Keskar and Lyn, 1999]	6.09	4.85	10.48
[Barton and Kirby, 2000]	6.01	5.02	9.90
present method	6.11	4.87	10.47

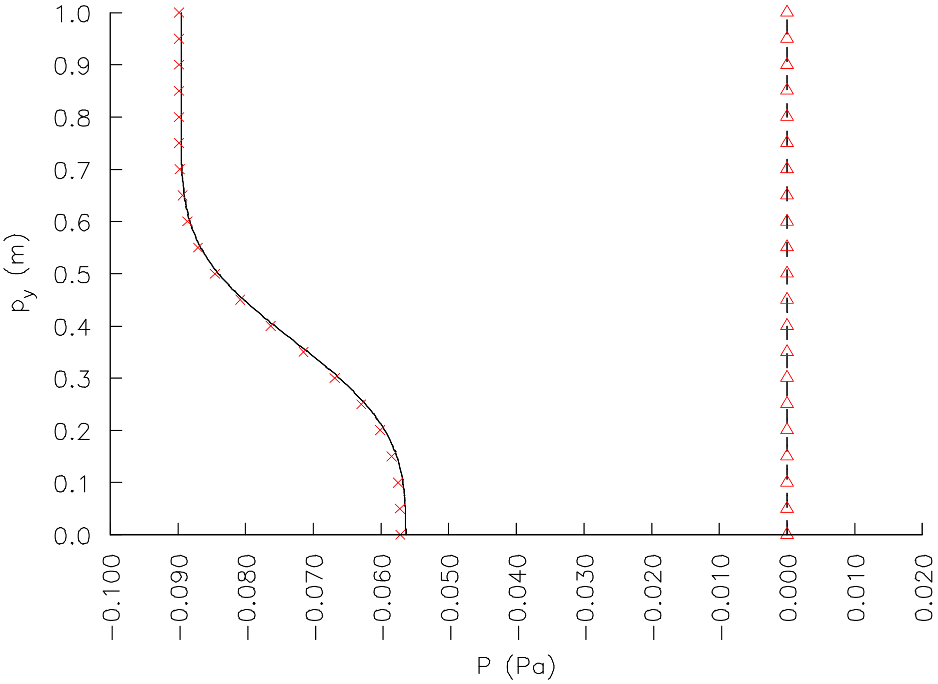

Figure 5.26: Pressure profiles across the channel for $\text{Re} = 800$ by using 301×101 node arrangement. Lines: present method. Red symbols: [Gartling, 1990]. Solid line and ×: at $p_x = 7$. Dashed line and Δ: $p_x = 15$.

Table 5.6: Grid convergence and comparison at $\text{Re} = 600$.

		p_{x1}	p_{x2}	p_{x3}
[Barton, 1995]		5.36	4.36	8.12
present method	200×60	5.43	4.44	8.09
	250×80	5.41	4.41	8.10
	300×100	5.39	4.39	8.10

Table 5.7: Reattachment positions for various Re numbers by using 301×101 node arrangement.

Re		p_{x1}	p_{x2}	p_{x3}
300	[Barton, 1995]	3.55	/	/
	present method	3.57	/	/
400	[Barton, 1995]	4.30	4.10	5.15
	present method	4.33	4.03	5.17
500	[Barton, 1995]	4.95	4.22	6.68
	present method	4.98	4.23	6.72
600	[Barton, 1995]	5.36	4.36	8.12
	present method	5.39	4.39	8.10
700	[Barton, 1995]	/	/	/
	present method	5.81	4.67	9.31
800	[Barton, 1995]	6.08	4.81	11.03
	present method	6.11	4.87	10.47

Table 5.8: Reattachment positions for the non-uniform and slightly random node arrangements at $\mathrm{Re} = 600$.

	p_{x1}	p_{x2}	p_{x3}
non-uniform	5.39	4.39	8.10
slightly random	5.40	4.40	8.13

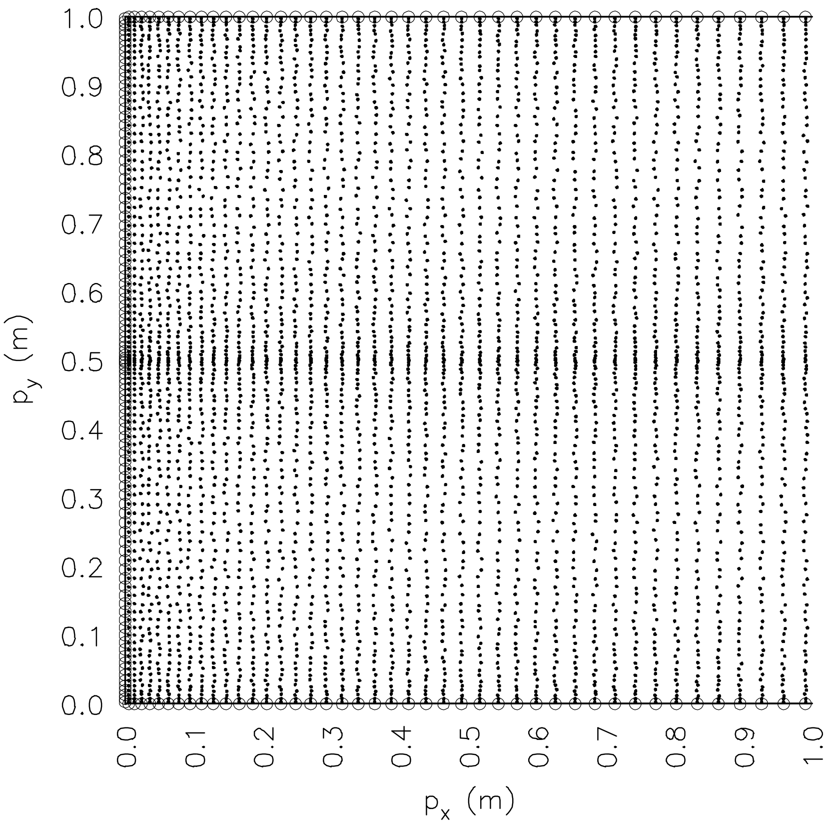

Figure 5.27: A detailed view of the 301×101 slightly random node arrangement. o: boundary nodes. •: domain nodes.

5.5 Turbulent Flow Problems

5.5.1 Two-dimensional Channel Flow

5.5.1.1 Problem Description

Turbulent flow in a channel is a standard benchmark test for turbulence models [Jones and Launder, 1972; Lam and Bremhorst, 1981; Chien, 1982; Abe *et al.*, 1995]. Before availability of the first DNS calculations [Kim *et al.*, 1987], the turbulence models were evaluated and developed based on the experimental data [Laufer, 1948]. In this numerical example, we used both data in order to check the proper implementation of all three turbulence models, i.e. JL, LS and AKN.

The physical domain is a 2D channel with length L and height H. In our computations, only one half of a channel height $H/2=1.0\,\mathrm{m}$ is considered, as shown in Figure 5.28. The length of the channel is large enough to achieve the fully developed flow at the channel outlet. The density and the inlet velocity are both equal to unity, while the dynamic viscosity μ is calculated from the Re number, based on the half channel width.

The following boundary conditions are used:

- At the inlet, Dirichlet boundary condition is set for the velocity field, the turbulent kinetic energy, and the dissipation rate. The horizontal velocity u_{x0} is uniform and equal to unity, while vertical velocity u_{y0} is zero. The turbulent kinetic energy and the dissipation rate profiles are also uniform and defined by the following empirical relations [Versteeg and Malalasekera, 1995]

$$k_0 = \frac{3}{2}\left(I \cdot u_{x0}\right)^2, \tag{5.14}$$

$$\varepsilon_0 = C_\mu^{3/4}\frac{k_0^{3/2}}{0.07D}, \tag{5.15}$$

  where I is the turbulent intensity, calculated from an empirical correlation for the pipe flows [Versteeg and Malalasekera, 1995]

$$I = 0.16\,\mathrm{Re}^{-1/8}. \tag{5.16}$$

- At the outlet boundary, the Neumann boundary conditions in the normal direction for velocity components, the turbulent kinetic energy, and the dissipation rate are prescribed and set to zero.
- At the wall, the Dirichlet no-slip boundary conditions are set, which implies that the velocity components, the turbulent kinetic energy, and the dissipation rate are all set to zero.
- At the symmetry line, the Neumann boundary conditions in the normal direction for the horizontal velocity component, the turbulent kinetic energy, and the dissipation rate are prescribed and set to zero. For the vertical velocity component, the Dirichlet boundary condition is prescribed and equal to zero.

The numerical results are compared with the DNS data [Kim *et al.*, 1987] at low $\mathrm{Re} = 7890$ number ($\Delta\ell = H/2$, see equation (5.10)), and with the experimental data [Laufer, 1948] at higher $\mathrm{Re} = 12300$ and $\mathrm{Re} = 30800$ numbers ($\Delta\ell = H/2$). Previous results at $\mathrm{Re} = 12300$ have already been published in [Vertnik and Šarler, 2009], where the JL model with closure coefficient $C_{\varepsilon 1} = 1.45$ is used.

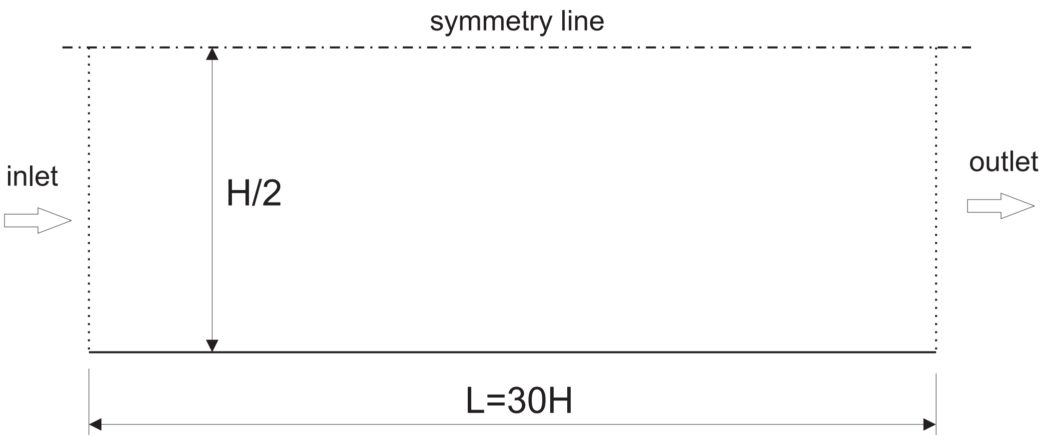

Figure 5.28: Geometry of the 2D channel flow.

5.5.1.2 Numerical Results at Re=7890

This example is first evaluated with LS model and three different node arrangements: 151×31, 151×51 and 151×71 (without four corner nodes). The node arrangements are refined near the walls to achieve $y^+ \leq 1$ of the first node near the wall (see Figure 5.29). A refinement level $b = 2.0$, 1.8 and 1.6 is used for each node arrangement, respectively, with the time step $\Delta t = 10^{-3}$ s. Figure 5.30 represents the calculated non-dimensional velocity at the outlet of the channel, where it is evident, that with the finer 151×71 node arrangement we obtain almost grid-independent solution. From this figure, we can also see, that the LS model over-predicts the velocity profile away from the viscous sub-layer region. This is a normal behaviour of the LS model, found also by other authors [Wilcox, 1993; Bredberg, 2001].

Next, we run the simulations with 151×71 node arrangements and various levels of refinement near the wall, i.e. $b=1.2$, 1.4 and 1.6. Figures 5.31 to 5.33 represent the results by the JL, LS and AKN models, respectively. The JL model under-predicts the velocity already in the viscous sub-layer, and over-predicts it in the log layer [Bredberg, 2001]. The LS model is an extended version of the JL model, and better predicts the velocity profile in the viscous sub-layer, while similarly as JL model, over-predicts the profile in the log layer [Wilcox, 1993; Bredberg, 2001]. The AKN model slightly under-predicts the velocity profile in the range between the viscous sub-layer and the log layer [Abe *et al.*, 1994; Bredberg, 2001]. The AKN model excellently predicts the viscous sub-layer region and region away from the log layer.

The profile of the non-dimensional turbulent kinetic energy is shown in Figure 5.34, where the 151×71 node arrangement is used. It is dimensionalised by the friction velocity as

$$k^{+} = \frac{k}{u_{\tau}^{2}}. \tag{5.17}$$

The best prediction is obtained with the AKN model. A similar comparison was made by Bredberg [Bredberg, 2001], who reached the same conclusions.

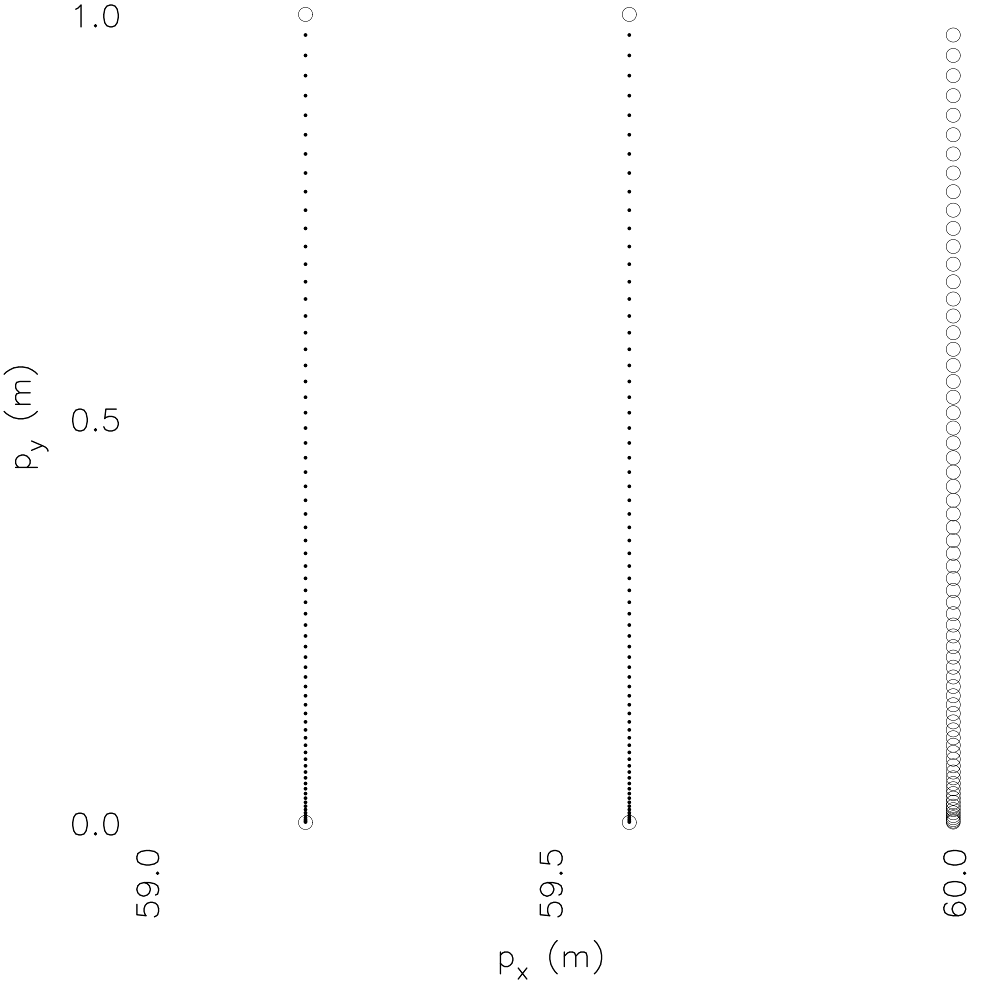

Figure 5.29: A selected detail of the 151×71 node arrangement. o: boundary nodes. •: domain nodes.

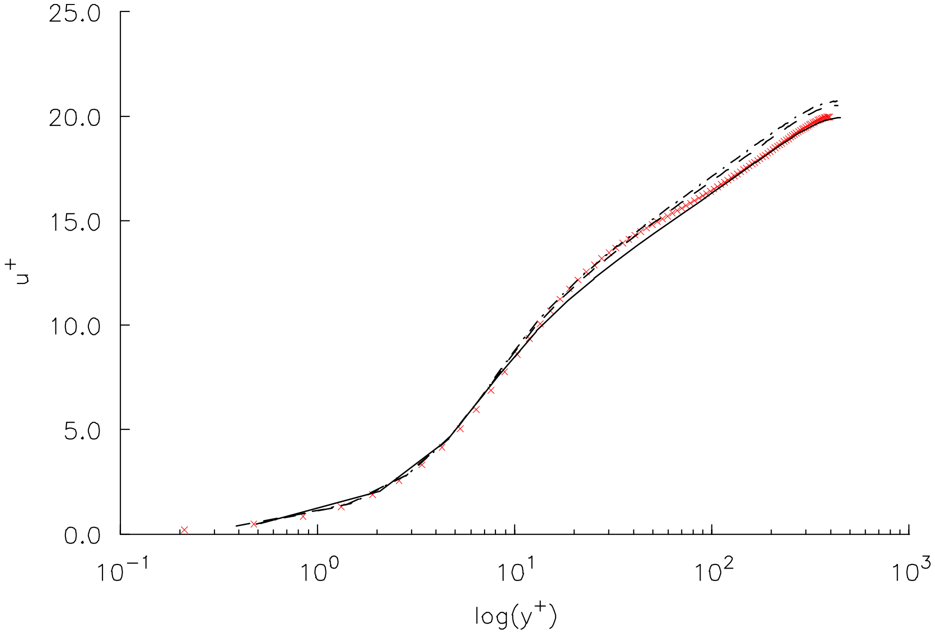

Figure 5.30: Non-dimensional velocity profile at the outlet, obtained with the LS model. Red symbols ×: DNS by [Kim *et al.*, 1987]. Solid line: 151×31. Dashed line: 151×51. Dash-doted line: 151×71 node arrangement.

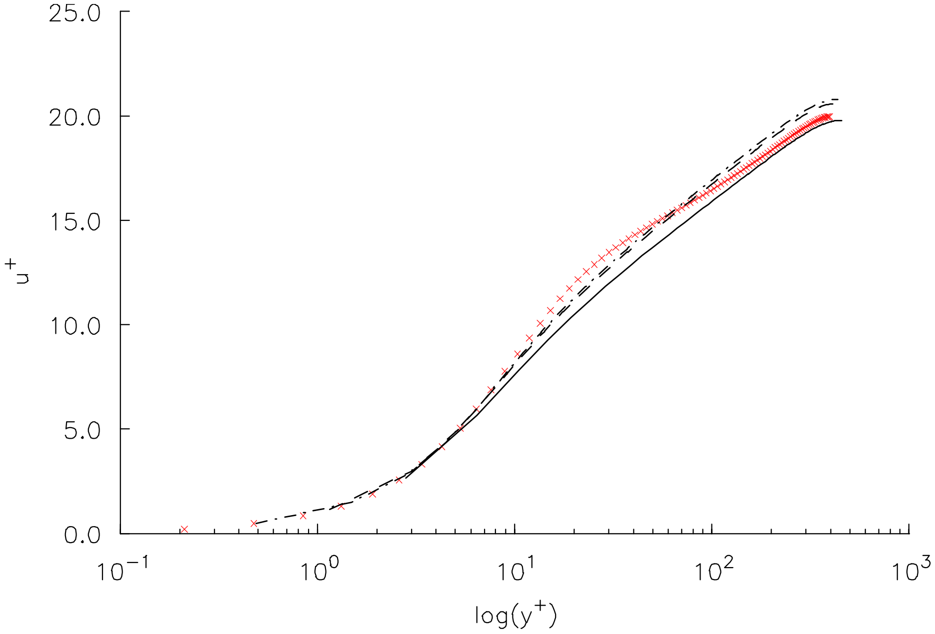

Figure 5.31: Non-dimensional velocity profile at the outlet, obtained with the JL model and 151×71 node arrangement. Red symbols ×: DNS by [Kim *et al.*, 1987]. Solid line: $y^+ = 2.80$. Dashed line: $y^+ = 1.15$. Dash-doted line: $y^+ = 0.49$.

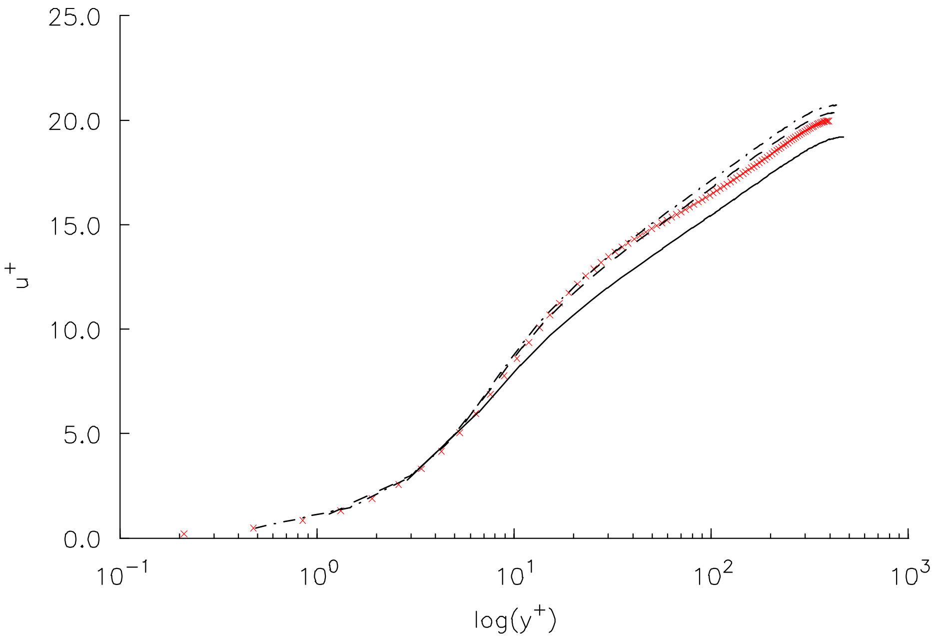

Figure 5.32: Non-dimensional velocity profile at the outlet, obtained with the LS model and 151×71 node arrangement. Red symbols ×: DNS by [Kim *et al.*, 1987]. Solid line: $y^+ = 2.87$. Dashed line: $y^+ = 1.15$. Dash-doted line: $y^+ = 0.49$.

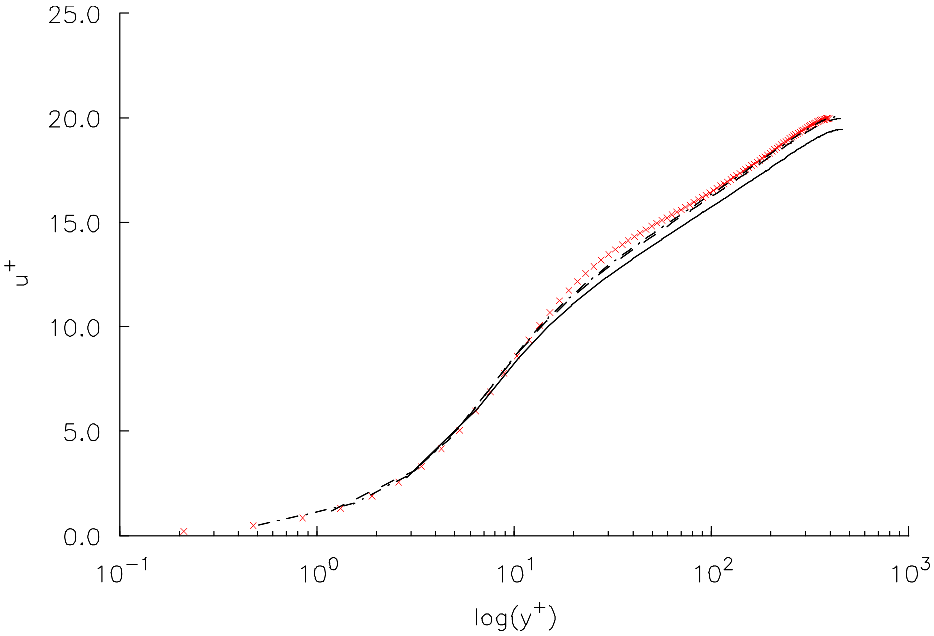

Figure 5.33: Non-dimensional velocity profile at the outlet, obtained with the AKN model and 151×71 node arrangement. Red symbols ×: DNS by [Kim *et al.*, 1987]. Solid line: $y^+ = 2.84$. Dashed line: $y^+ = 1.19$. Dash-doted line: $y^+ = 0.50$.

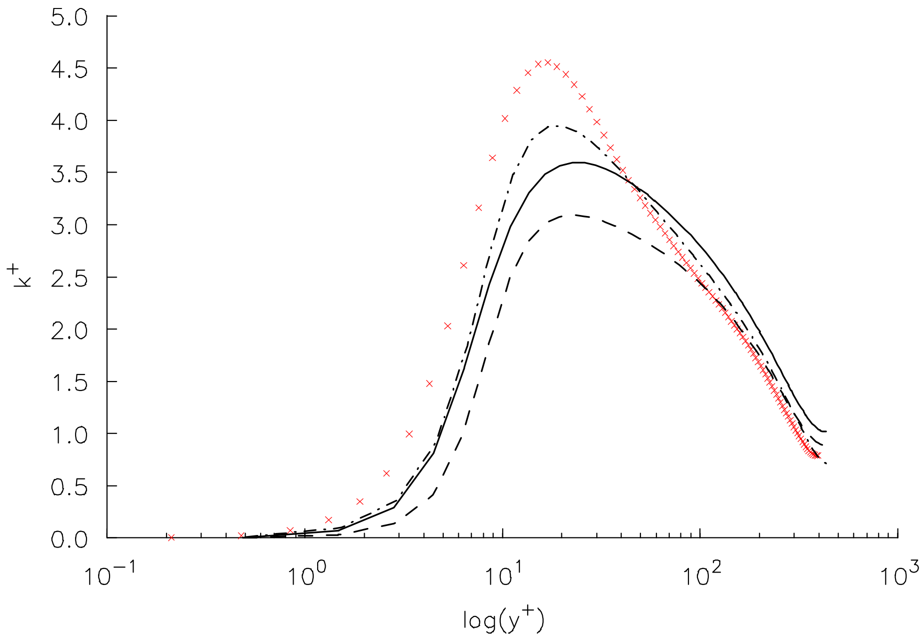

Figure 5.34: Non-dimensional kinetic energy profile at the outlet, obtained at the 151×71 node arrangement. Red symbols ×: DNS by [Kim *et al.*, 1987]. Solid line: JL model. Dashed line: LS model. Dash-doted line: AKN model.

5.5.1.3 Numerical Results at Re=12300 and Re=30800

This example tackles the solution at higher values of the Re number. The 151×71 node arrangement with node refinement level $b=1.8$. This level of refinement is suitable for $\mathrm{Re}=12300$, while for $\mathrm{Re}=30800$, the level of refinement is enhanced to $b=2.1$. The time step is equal to $\Delta t=5\cdot10^{-4}\,\mathrm{s}$ at $\mathrm{Re}=12300$ and $\Delta t=5\cdot10^{-5}\,\mathrm{s}$ at $\mathrm{Re}=30800$. The numerical results are also obtained by Fluent, where AKN model is set as the turbulence model, and the mesh is generated with a 100000 (1000×100) quadrilateral finite volume cells. The mesh is refined near the wall. We obtain $y^+=0.1$ for $\mathrm{Re}=12300$, and $y^+=0.25$ for $\mathrm{Re}=30800$ with Fluent.

Figures 5.35 and 5.37 represent the calculated velocity profile at the $\mathrm{Re}=12300$ and $\mathrm{Re}=30800$, obtained with different turbulent models and with Fluent. A comparison shows very small differences between the numerical results and the experiment. For better insight, the absolute differences between the calculated velocity profile of the various turbulence models and the measurements are plotted in Figures 5.36 and 5.38 for $\mathrm{Re}=12300$ and $\mathrm{Re}=30800$, respectively.

It is difficult to conclude which turbulence model performs the best. On the basis of presented absolute differences between the numerical results and the experiment, the best agreement is given by the LS model, and the worse with the

AKN model. However, we are confident that all LRN models are properly implemented. This is the main aim of this numerical example.

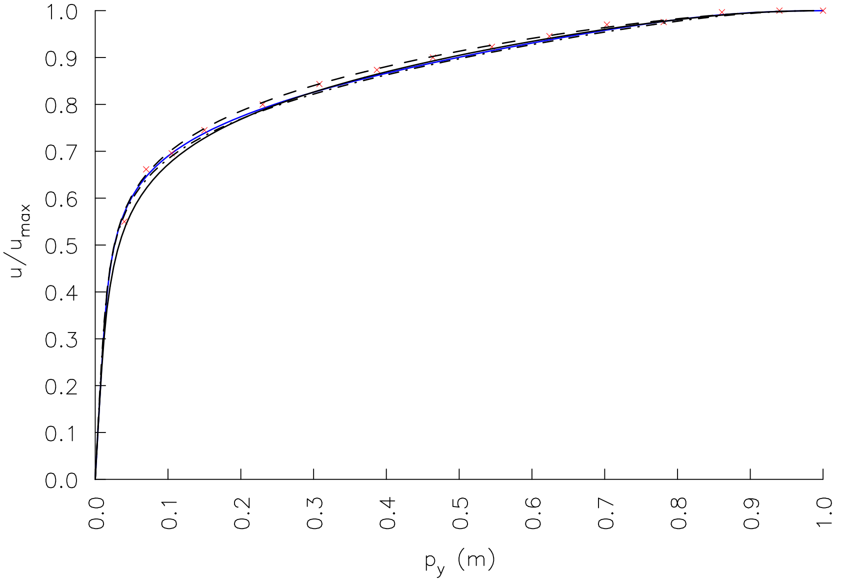

Figure 5.35: Normalized velocity profile at $\mathrm{Re}=12300$. 151×71 node arrangement. Solid line: JL model. Dashed line: LS model. Dash-doted line: AKN model. Solid blue line: Fluent with the AKN model.

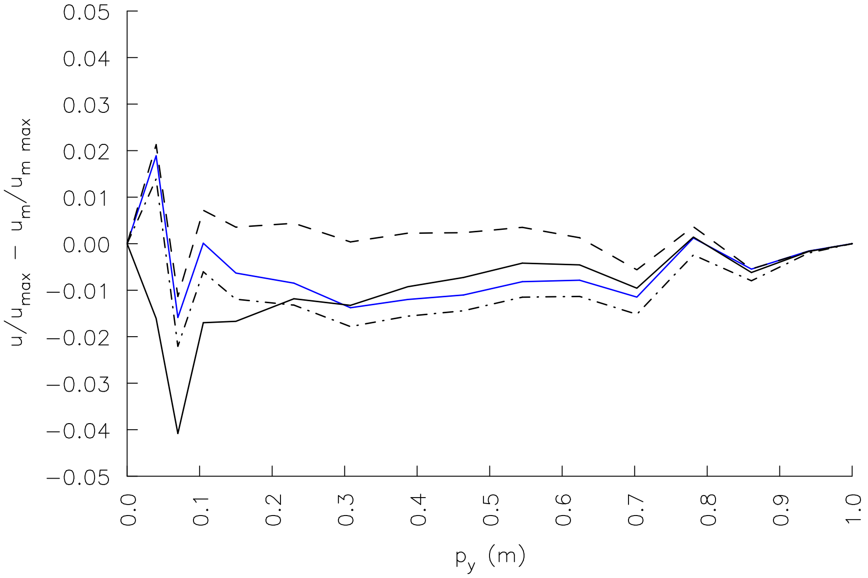

Figure 5.36: Absolute difference of the calculated u and measured velocity u_m at $\mathrm{Re}=12300$. 151×71 node arrangement. Solid line: JL model. Dashed line: LS model. Dash-doted line: AKN model. Solid blue line: Fluent with the AKN model.

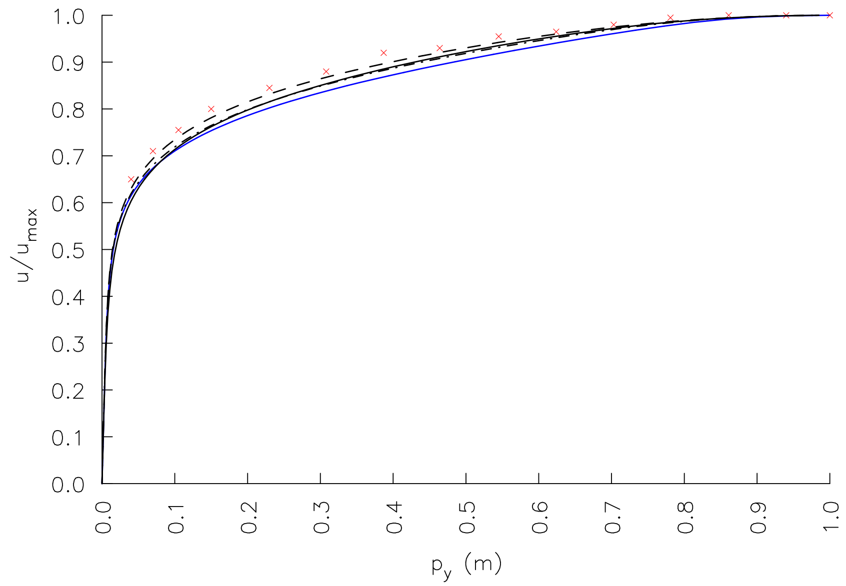

Figure 5.37: Normalized velocity profile at $\mathrm{Re} = 30800$. 151×71 node arrangement. Solid line: JL model. Dashed line: LS model. Dash-doted line: AKN model. Solid blue line: Fluent with the AKN model.

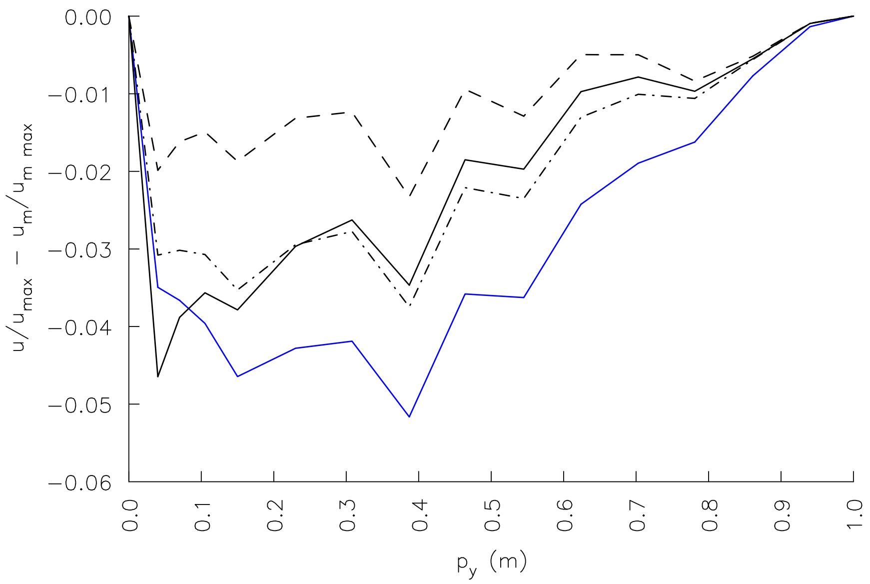

Figure 5.38: Absolute difference of the calculated u and measured velocity u_m at $\mathrm{Re} = 30800$. 151×71 node arrangement. Solid line: JL model. Dashed line: LS model. Dash-doted line: AKN model. Solid blue line: Fluent with the AKN model.

5.5.2 Heat Transfer as a Passive Scalar Field

5.5.2.1 Problem Description

We simulate the fully developed thermal field in a 2D channel at $\mathrm{Re} = 4560$ ($\Delta\ell$ is equal to the channel height, see equation (5.10)) and $\mathrm{Pr} = 0.71$ on which the walls are heated with a constant heat flux. With bouyancy effects neglected, temperature is considered as a passive scalar, which means, that the energy equation is un-coupled from the momentum and the turbulent transport equations. An example is taken from the database “DNS Database of Turbulence and Heat Transfer”, http://www.thtlab.t.u-tokyo.ac.jp/DNS/dns_database.html, example CH122_PG.WL1, and also published [Kasagi *et al.*, 1992]. The same problem was also solved by the EVM [Chen *et al.*, 2007]. They used the AKN model for the velocity field and two-equation model for the thermal field [Abe *et al.*, 1995]. This model will be denoted as AKNT.

The geometry of a 2D channel is the same as in the previous example (see Figure 5.28). The boundary conditions for the velocity components, the turbulent kinetic energy and the dissipation rate are also the same. For the temperature field, we used the following boundary conditions:

- At the inlet, the Dirichlet boundary condition is set, where temperature is uniform and equal to 288.15 K (15 °C).
- At the outlet, the Neumann boundary condition in the normal direction is prescribed and set to zero.
- At the wall, the Neumann boundary condition with a constant heat flux, equal to 500 W/m^2.
- At the symmetry line: the same boundary condition is used as for the outlet boundary.

The 151×71 node arrangement is used, with the same refinement level as in the previous example. The LS and AKN models are used, while the JL is omitted, since the LS is extended (improved) version of the JL model. Turbulent Prandtl number is used as constant and equal to 0.9. The time step is equal to $\Delta t = 10^{-3}$ s.

5.5.2.2 Numerical Results

In Figure 5.39, the calculated non-dimensional velocity profile is presented. Comparing with the DNS data, we got a very good prediction with the AKN model. The LS model over-predicts it out from the log-layer, similar as in the previous example.

Figure 5.40 represents the non-dimensional temperature field, obtained by the following relation

$$T^{+}=\frac{T_w-T}{T_\tau}\ , \tag{5.18}$$

where T_w and T_τ are standing for the wall and the friction temperature, respectively. The friction temperature is defined as

$$T_\tau=\frac{q_w}{\rho c_p u_\tau}\ . \tag{5.19}$$

In equation (5.19), q_w is the wall heat flux (equal to 500 W/m^2) and u_τ is the friction velocity. Both models (LS and AKN) predict very well the viscous sub-layer. In the log layer, the AKN model under-predicts, and the LS model over-predicts the temperature profile.

The results are also analyzed on the basis of the bulk Nusselt number Nu_b at the outlet. It is calculated as

$$Nu_b=\frac{q_w D}{\lambda\left(T_w-T_b\right)}, \tag{5.20}$$

with D and T_b standing for the half channel height and the bulk temperature, respectively. T_b is calculated by the following equation

$$T_b=\frac{\int_0^{H/2}\rho u_x c_p T\,dy}{\int_0^{H/2}\rho u_x c_p\,dy}\ . \tag{5.21}$$

The calculated Nu_b with various turbulence models are presented in Table 5.9. An excellent agreement is obtained with the AKNT model, which is expected, due to use of the two-equation model for the thermal field. With the present method, where the simplest Bousinesq model for the turbulent diffusivity of heat and constant Prandtl number are used, the AKN predicts the Nu number better than the LS model. The LS model gives 6.5% under-prediction and the AKN gives $4.5\,\%$ over-prediction.

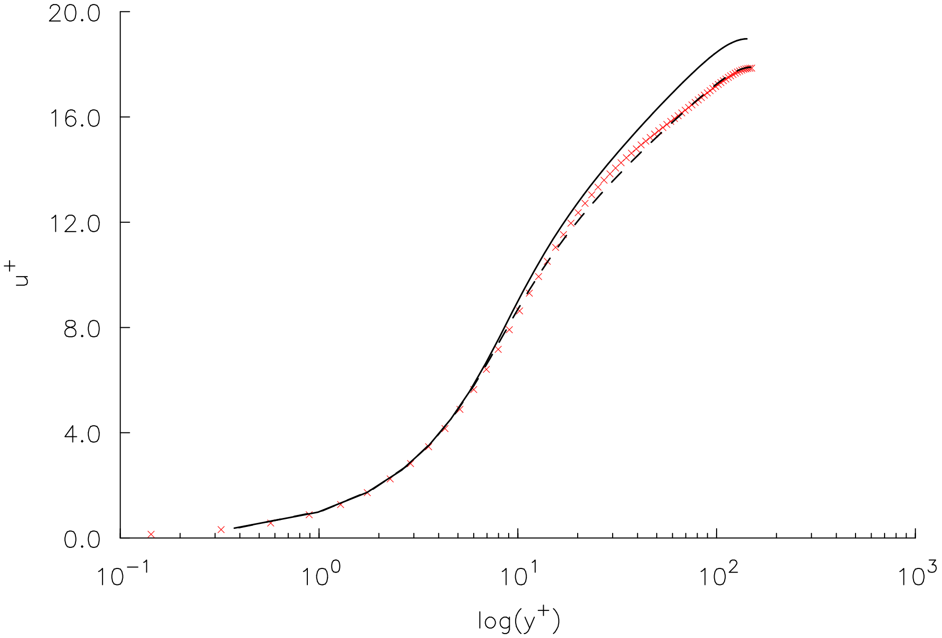

Figure 5.39: Non-dimensional velocity profile obtained with 151×71 node arrangement. Red symbols ×: DNS data. Solid line: LS model. Dashed line: AKN model.

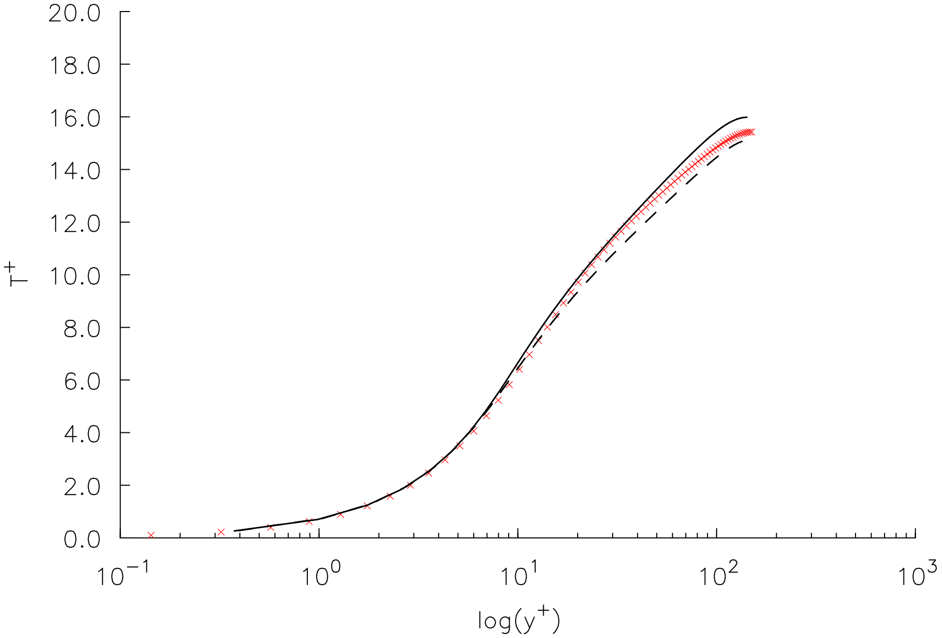

Figure 5.40: Non-dimensional temperature profile obtained with 151×71 node arrangement. Red symbols ×: DNS data. Solid line: LS model. Dashed line: AKN model.

Table 5.9: Bulk Nusselt number at the outlet.

	turbulence model	Nu_b	error (%)
[Kasagi *et al.*,1992]	DNS	15.4	0
[Chen *et al.*, 2007]	AKNT	15.5	<1
present method	LS	14.4	6.5
	AKN	16.1	4.5

5.5.3 Combined Forced and Natural Convection in a 2D Channel Flow

5.5.3.1 Problem Description

The fluid flow in the continuous casting process is driven by the combined turbulent forced and natural convection. The presented method was already tested for natural convection in a square cavity, where the flow was treated as laminar. The same case with turbulent natural convection was already investigated experimentally and numerically by many authors [Markatos and Pericelous, 1984; Henkes *et al.*, 1991; Ampofo and Karayiannis, 2003; Hsieh and Lien, 2004]. However, we rather chose the DNS test by Kasagi [Kasagi and Nishimura, 1997] with combined forced and natural convection turbulent flow in a 2D vertical channel. The forced convection drives the fluid upward, while the buoyancy force acts upward at the hot wall and downward at the cold wall. The results are also presented on the website ("DNS Database of Turbulence and Heat Transfer", http://www.thtlab.t.u-tokyo.ac.jp/DNS/dns_database.html, example CH1221BU.WL1). Those results were used by many researchers to evaluate various turbulence models, such as the LES [Yin and Bergstrom, 2004; Wang *et al.*, 2007] and EVMs [Billard *et al.*, 2008].

The geometry of the problem is a vertical channel of width W and height H, $H/W = 120$ (see Figure 5.41). The flow with constant uniform velocity and temperature is entering into the channel at the bottom and leaving the channel at the top. Vertical walls are kept at different (left wall hot, right wall cold), but constant temperatures. At the outlet, the flow is assumed to be fully developed. The forced flow and the buoyancy force drive the flow upward near the hot wall (adding flow at the left wall), and downward near the cold wall (opposing flow at the right wall). The Re number is set to 4494 ($\Delta\ell = W$, see equation (5.10)), and the Grashof number based on the temperature difference between the vertical walls and the channel width is 9.6×10^5, i.e.

$$\mathrm{Gr}=\frac{g\beta_T\left(T_h-T_c\right)W^3}{\nu^2}. \tag{5.22}$$

The fluid is assumed to be air with $\mathrm{Pr}=0.71$. The case is elaborated in [Vertnik and Šarler, 2010].

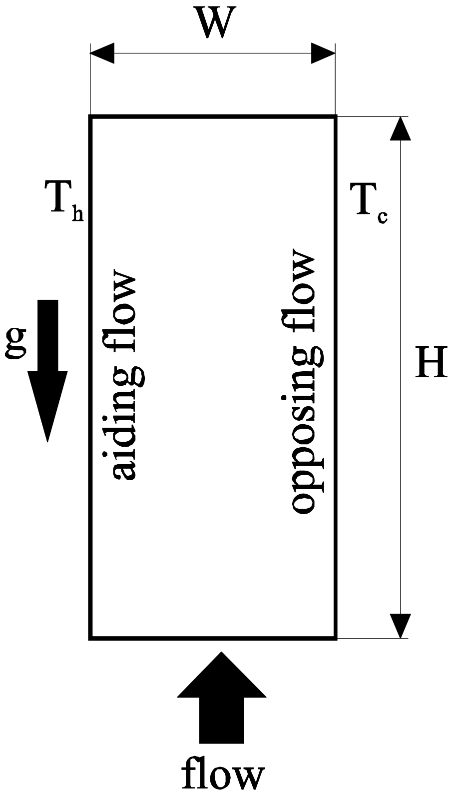

Figure 5.41: Schematics of the mixed convection problem.

Calculations are performed on 81×171 node arrangement with (without 4 corner nodes), which is found sufficiently fine to obtain a reasonably grid-independent solution. We also used 61×171 and 71×171 node arrangements, where negligible difference is found between the 71×171 and 81×171 arrangements. The same conclusions can be drawn, when more nodes are used in the vertical direction. The discretization in the vertical direction p_y is uniform and in the horizontal p_x direction is non-uniform, sufficiently refined near the walls to achieve the position of the first point to be in the range $y^+\leq1$ at each of the vertical walls (see Figure 5.42). The time step is set to $\Delta t=0.001\mathrm{s}$ for all calculations.

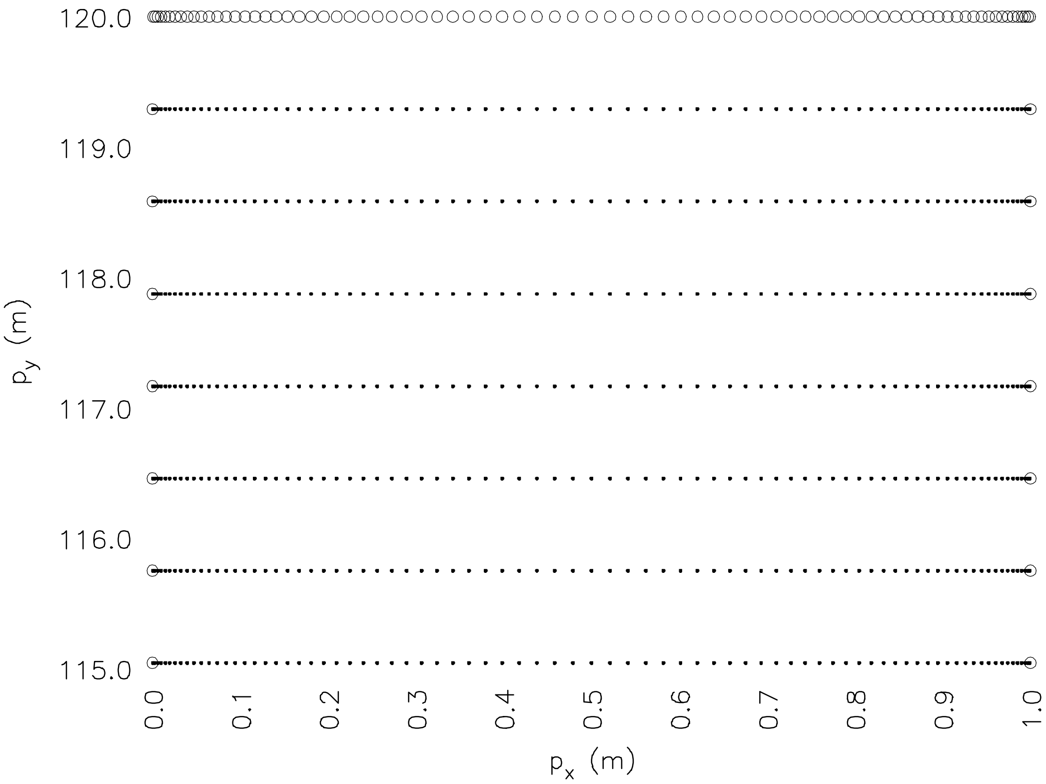

Figure 5.42: A detailed view of the 81×171 node arrangement. o: boundary nodes. •: domain nodes.

5.5.3.2 Numerical Results

The results are presented in form of non-dimensional variables, i.e. u^+ (see equation (2.26)), T^+ (see equation (5.18)) and k^+ (see equation (5.17)) for velocity, temperature and the turbulent kinetic energy, respectively.

Figures 5.43 and 5.44 are representing the non-dimensional velocity profile of the aiding and opposing flow at the outlet. The prediction of the velocity profile in the region near the walls (viscous sub-layer) agrees very well with the DNS data. In the outer layer, the LS model over-predicts the DNS data, which is a normal behaviour of the LS model [Billard *et al.*, 2008; Bredberg, 2001; Wilcox, 1993]. See all of the previous examples. A better agreement with the DNS data is obtained by the AKN model, which predicts the velocity profile very well in both regions.

The non-dimensional turbulent kinetic energy is represented in Figures 5.45 and 5.46 for the aiding and opposing flows, respectively. On the aiding flow side, the k is under-predicted, also out of the viscous sub-layer region. The reason could be in the anisotropy of the Reynolds-stresses, which were found by the DNS solution to be enhanced in the aiding flow. However, it seems that the anisotropy does not affect the prediction of the velocity field, especially when the AKN model is used (see Figures 5.43 and 5.44). The turbulent kinetic energy of the opposing flow agrees very well, since it was reported by the DNS data, that the anisotropy of the Reynolds-stresses in this region is weakened.

The temperature profile is shown in Figures 5.47 and 5.48 for the hot (aiding flow) and cold (opposing flow) walls, respectively. For the opposing flow, the calculated results are in good agreement with the DNS. However, on the aiding side, we observe larger differences between the LRN models and DNS. The reason could be in modelling the turbulent diffusivity and turbulent viscosity with a constant turbulent Prandtl number (set to 0.9 in the present dissertation). This assumption holds only for simple boundary layer flows, where the velocity and the temperature fields develop simultaneously [Abe *et al.*, 1995]. In our case, the similarity between the temperature and the velocity fields does not hold, since the boundary layer is affected by the buoyancy force. It is observed from the DNS [Kasagi and Nishimura, 1997] and LES [Wang *et al.*, 2007], that the buoyancy force effects the velocity fluctuations differently as the temperature fluctuations. The velocity fluctuations are enhanced in the opposing flow and reduced in the aiding flow, while the opposite effects are observed for the temperature fluctuations. For better prediction of such behaviour, the turbulent diffusivity should be modelled by the two-equation models for thermal field [Abe *et al.*, 1995].

Due to the buoyancy effects, the velocity and the temperature profiles at the outlet become un-symmetric. This behaviour is shown in Figures 5.49 and 5.50 for the velocity and temperature, respectively. The results are presented in the following non-dimensional relations

$$u^* = \frac{u_y}{u_\tau^*}, \tag{5.23}$$

$$\Theta^* = \frac{T^* - T_c^*}{T_h^* - T_c^*}, \tag{5.24}$$

where Θ^* stands for the normalized mean temperature. u_τ^* is the friction velocity, calculated from the wall shear stress, averaged on the two walls, i.e. cold and hot walls. T^* stands for friction temperature, calculated by the following equation

$$T^* = \frac{T}{T_\tau^*}, \tag{5.25}$$

where T_τ^* is calculated from the averaged wall heat flux, i.e.

$$T_\tau^* = \frac{q_h + q_c}{2\rho c_p u_\tau^*} . \tag{5.26}$$

The equation (5.25) is used for calculating the T_h^* and T_c^* on the hot and cold walls, respectively. We can conclude, that the AKN model predicts the velocity profile with a very good accuracy, while the LS model over-predicts the velocity profile. The temperature profile is over-predicted by both models for the aiding flow, and agrees very good with the DNS data for the opposing wall.

The accuracy of the represented method is evaluated also as a function of the Nusselt number and the skin friction at the top of the channel (at the outlet), which are calculated by the following equations

$$\mathrm{Nu} = \frac{2 \cdot q_w \cdot d \cdot \lambda}{T_b - T_w} , \tag{5.27}$$

$$C_f = \frac{2 \cdot \tau_w}{\rho \cdot u_b^2} , \tag{5.28}$$

respectively. In equations (5.27) and (5.28), T_b and u_b are a bulk-averaged quantities over d, which is the interval from the wall to the maximum velocity location. A bulk-averaged temperature is calculated by equation (5.21), while a bulk-averaged velocity is calculated as

$$u_b = \frac{1}{d} \int_0^d u_y dy . \tag{5.29}$$

The results are presented in Table 5.10, where an excellent agreement is achieved with both turbulence models.

Table 5.10: Nusselt number Nu and skin friction C_f at the channel outlet.

	turbulence model	aiding flow		opposing flow	
		Nu	C_f	Nu	C_f
DNS	/	7.42	9.90E-3	20.94	7.90E-3
present method	LS	5.92	9.96E-3	21.97	7.30E-3
	AKN	7.18	1.05E-2	22.71	7.87E-3

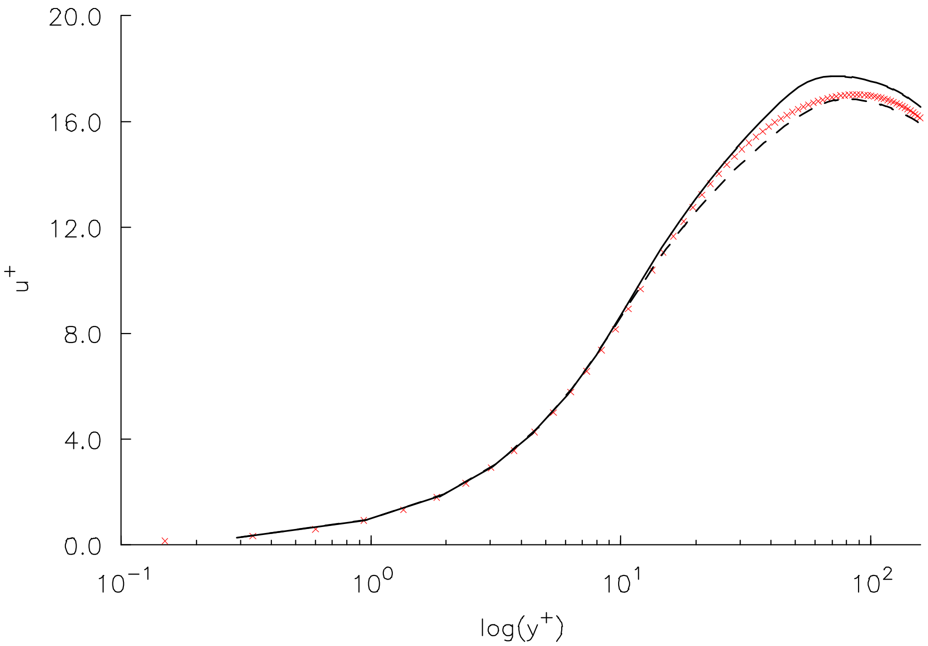

Figure 5.43: Non-dimensional velocity profile of the aiding flow in wall coordinates. Red ×: DNS solution [Kasagi an Nishimura, 1997]. Solid line: present method with LS model. Dashed line: present method with AKN model.

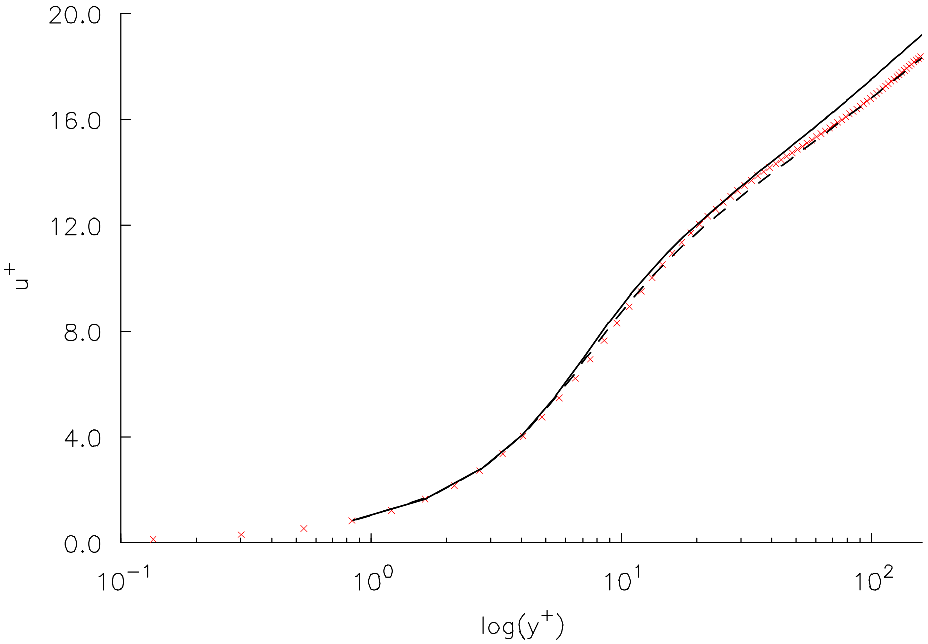

Figure 5.44: Non-dimensional velocity profile of the opposing flow in wall coordinates. Red ×: DNS solution [Kasagi an Nishimura, 1997]. Solid line: present method with LS model. Dashed line: present method with AKN model.

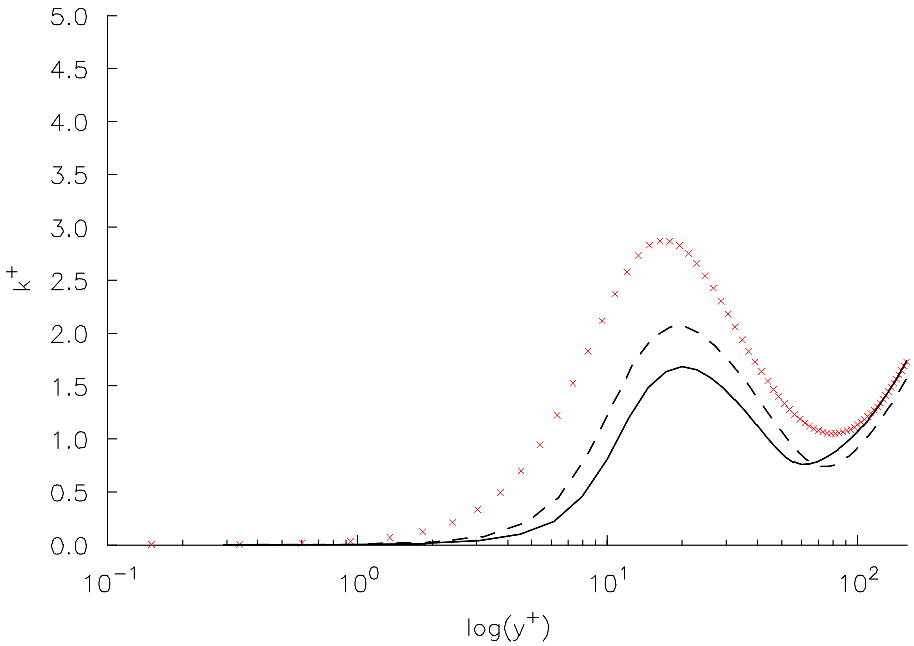

Figure 5.45: Non-dimensional turbulent kinetic energy of the aiding flow in wall coordinates. Red ×: DNS solution [Kasagi an Nishimura, 1997]. Solid line: present method with LS model. Dashed line: present method with AKN model.

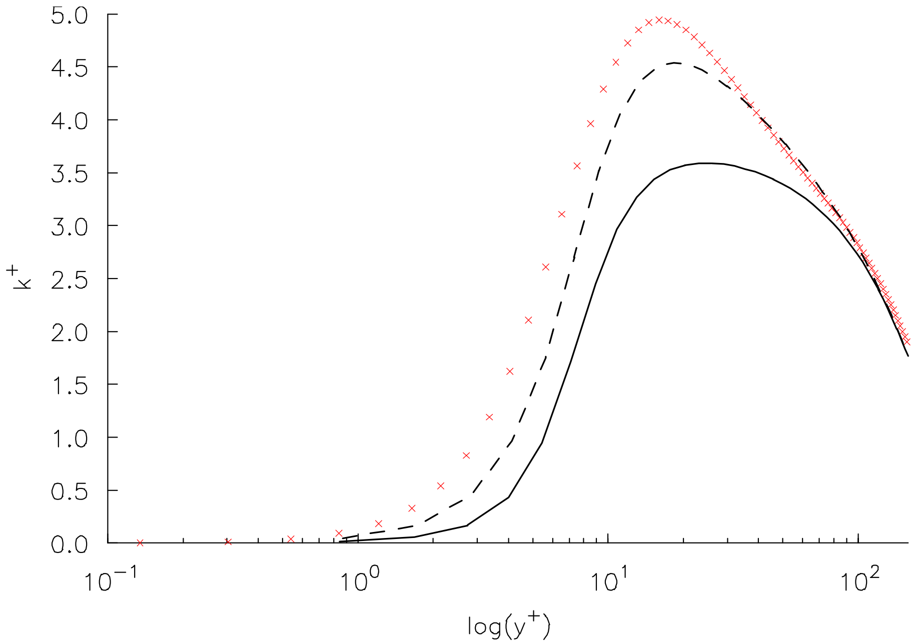

Figure 5.46: Non-dimensional turbulent kinetic energy of the opposing flow in wall coordinates. Red ×: DNS solution [Kasagi an Nishimura, 1997]. Solid line: present method with LS model. Dashed line: present method with AKN model.

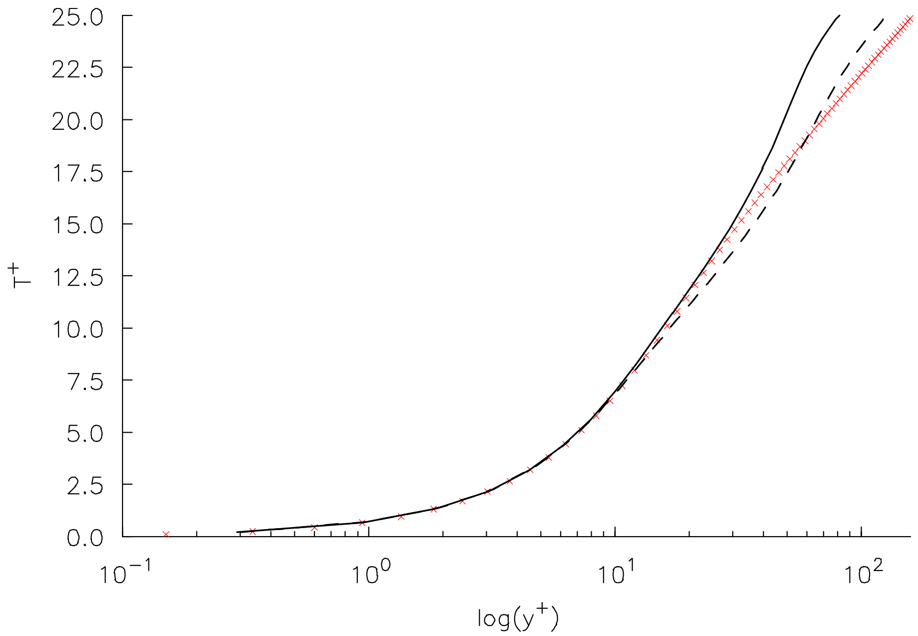

Figure 5.47: Non-dimensional temperature profile of the aiding flow in wall coordinates. Red ×: DNS solution [Kasagi an Nishimura, 1997]. Solid line: present method with LS model. Dashed line: present method with AKN model.

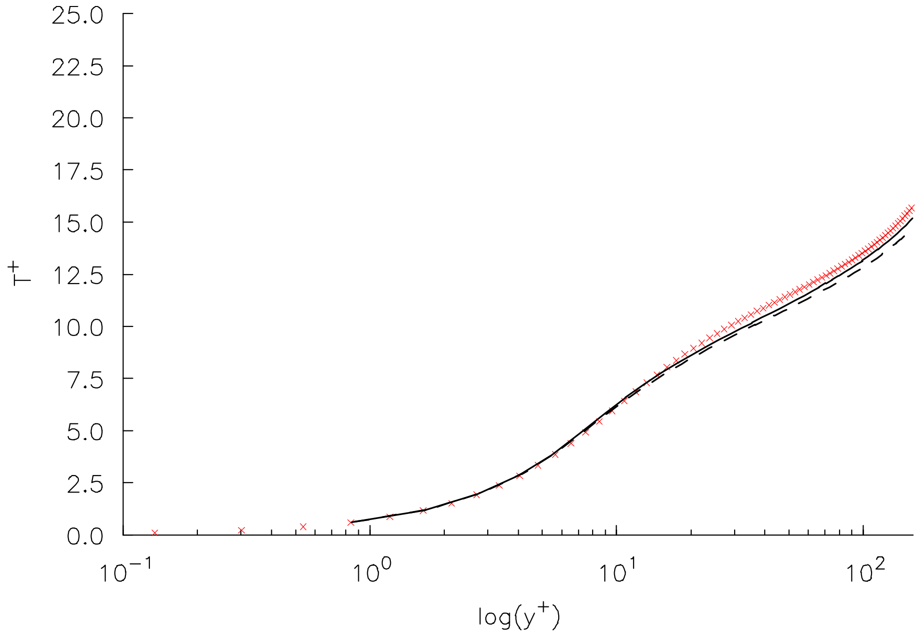

Figure 5.48: Non-dimensional temperature profile of the opposing flow in wall coordinates. Red ×: DNS solution [Kasagi an Nishimura, 1997]. Solid line: present method with LS model. Dashed line: present method with AKN model.

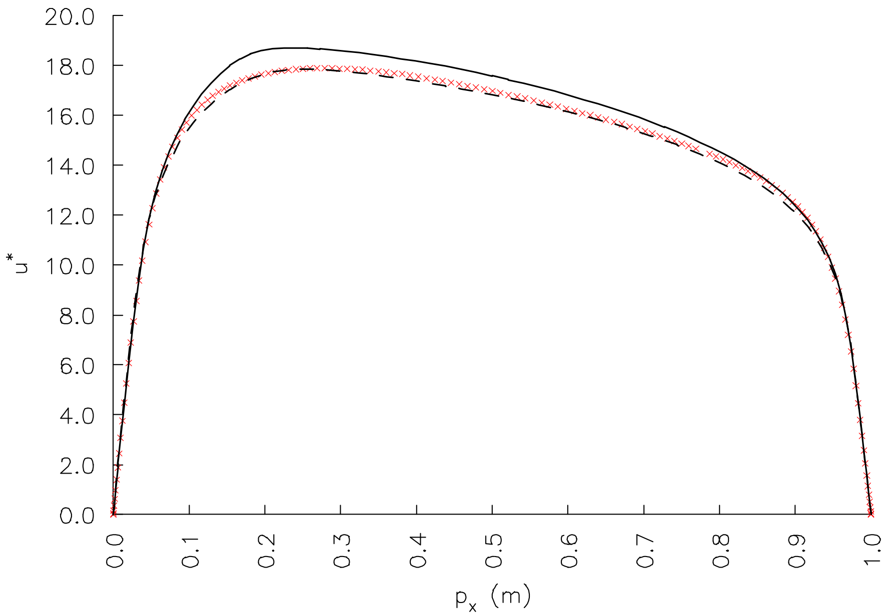

Figure 5.49: Non-dimensional velocity profile at the outlet in wall coordinates. Red ×: DNS solution [Kasagi an Nishimura, 1997]. Solid line: present method with LS model. Dashed line: present method with AKN model.

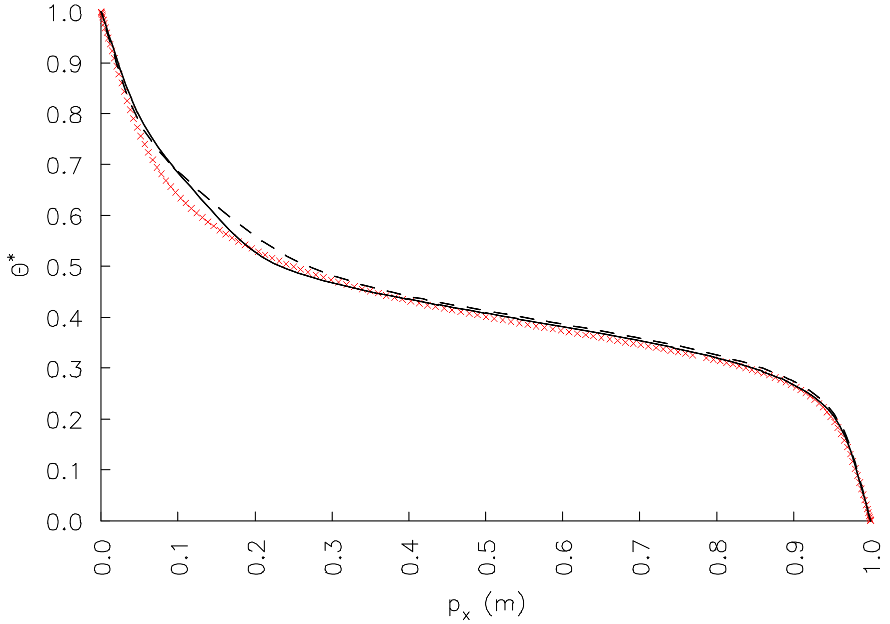

Figure 5.50: Non-dimensional temperature profile at the outlet in wall coordinates. Red ×: DNS solution [Kasagi an Nishimura, 1997]. Solid line: present method with LS model. Dashed line: present method with AKN model.

5.5.4 Backward Facing Step

5.5.4.1 Problem Description

The backward facing step problem is probably the most important example for evaluating the turbulence models [Bredberg, 2001; Seo, 2001; Chen *et al.*, 2006; Ghotbi *et al.*, 2008]. This problem was arranged experimentally and evaluated by many authors [Adams, 1984; Vogel, 1984; Jović and Driver, 1994]. Despite the simple geometry, complex physical phenomena occur, such as the flow separation and reattachment.

The geometry of the physical domain is taken from the experiment by [Jović and Driver, 1994], shown in Figure 5.51. The experiment is characterized by the step height $H = 1.0\,\mathrm{m}$, the channel length after the step $L = 30H$ and by the $\mathrm{Re}_H = 5000$ ($\Delta\ell$ is equal to the step height, see equation (5.10)), which determines the inlet conditions at the step. In the experiment, the flow conditions in the channel upstream was achieved at the distance $p_x / H = -3.05$ before the step with the Re number based on the momentum thickness $\mathrm{Re}_\theta = 610$. The Re_θ is defined as

$$\mathrm{Re}_\theta = \frac{\rho \theta u_0}{\mu}, \tag{5.30}$$

where θ is the momentum thickness and u_0 is the free stream velocity of the air. Both quantities are taken directly from the experiment and have values $\theta = 0.12\,\mathrm{cm}$ and $u_0 = 7.72\,\mathrm{m/s}$. The numerical results of the described problem have already been published in [Vertnik and Šarler, 2009], where the JL model with closure coefficient $C_{\varepsilon 1} = 1.45$ was used.

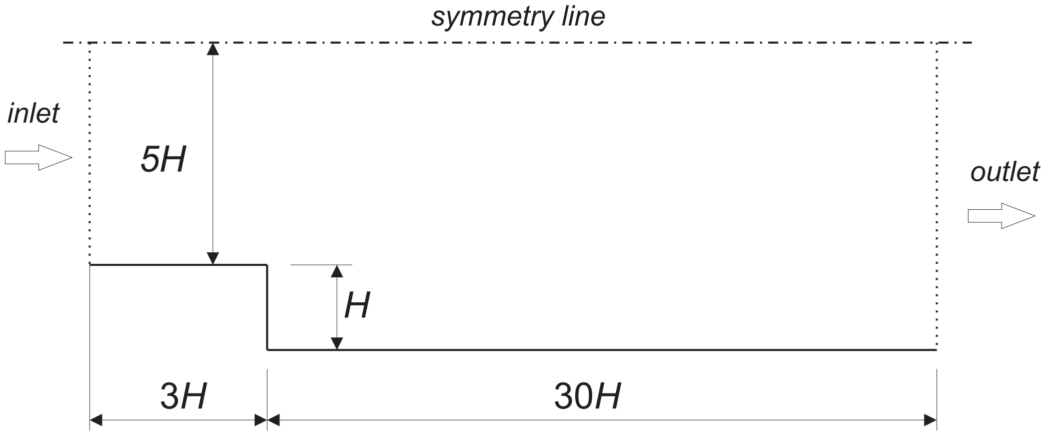

Figure 5.51: Schematics of the backward-facing step problem.

The computational domain of the backward facing step considers only the physical domain after the step, shown in Figure 5.52. At the initial state, the following uniform conditions are set: $u_{x0} = u_{y0} = 0\,\text{m/s}$, and $k_0 = \varepsilon_0 = 0.001$.
The following boundary conditions are used:

- At the inlet, the calculated profiles of u_x, k, ε and μ_t from the boundary layer simulation (BLS) over a flat plate are used, described in the next section. Velocity in the vertical direction u_y is equal to zero.
- At the outlet and at the symmetry line: the same boundary conditions are used as in the 2D channel flow (see section 5.5.1).

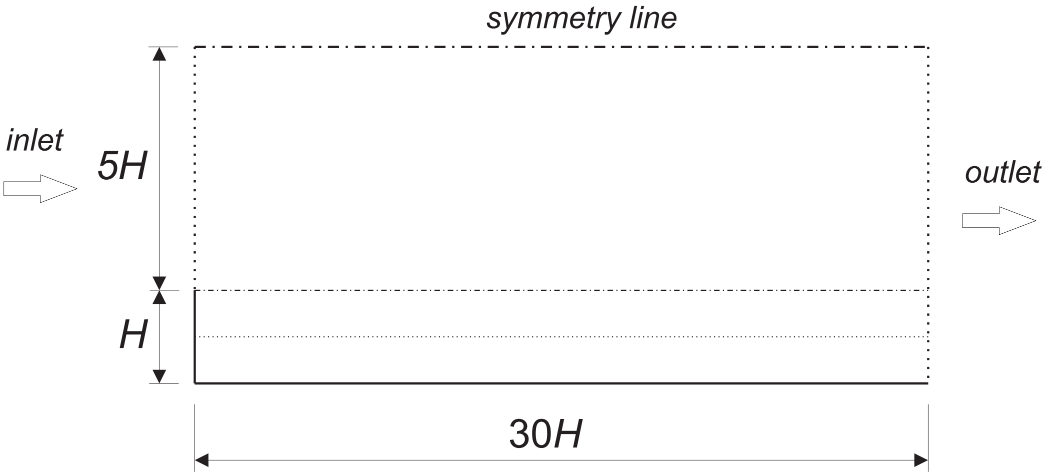

Figure 5.52: Computational domain of the backward-facing step problem.

5.5.4.2 Boundary Layer Simulation over a Flat Plate

In order to achieve the same inlet conditions as in the experiment, the BLS over a flat plate is performed with the present method. The geometry for the BLS is shown in Figure 5.53, where the following boundary conditions are used:

- At the inlet, the same boundary conditions are used as in the 2D channel flow example (see Section 5.5.1).
- At the bottom, $10H$ before the leading edge of the plate, the symmetry boundary condition is set to provide a uniform profile at the leading edge. At the remaining $50H$ of the bottom edge, the no-slip boundary conditions are set.
- At the left and the top boundaries, the outlet boundary conditions are set.

The desired Re_θ and the velocity profile of the Jović and Driver measurements are achieved with the simulation length of the flat plate $L = 50H$. The 101×81 node arrangement is used, with the refinement near the bottom edge. The results of the BLS, obtained with the LS and the AKN model, are presented in Figure 5.54, where the velocity profile is plotted.

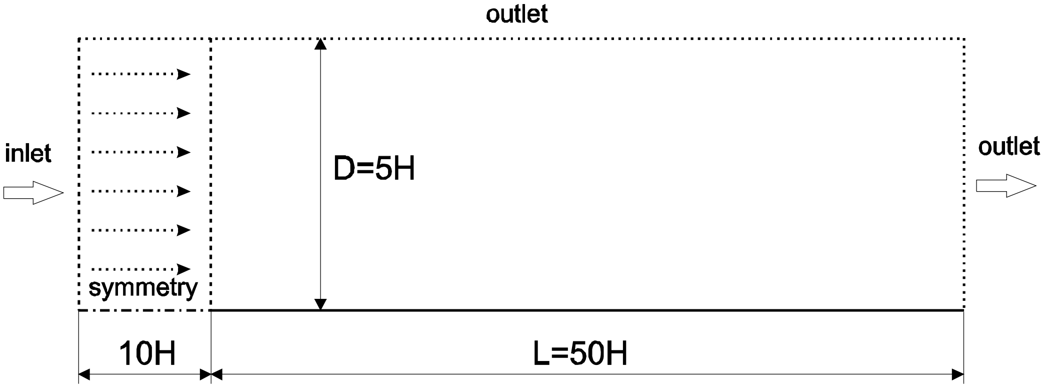

Figure 5.53: Schematics of the geometry used for the BLS.

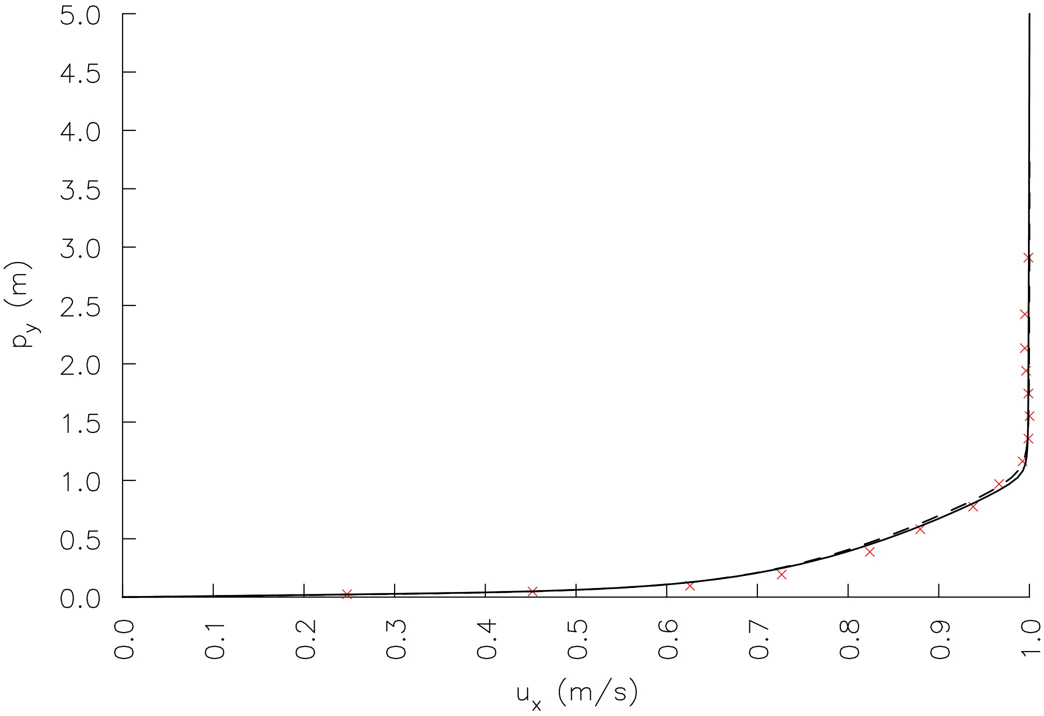

Figure 5.54: Velocity profile at the inlet. Symbol ×: measurements [Jović and Driver, 1994]. Solid line: present method with LS model. Dashed line: present method with AKN model.

5.5.4.3 Numerical Results

The calculations are performed first with the AKN model and at three different node arrangements: 201×71, 201×91, and 201×111 (without 4 corner nodes).

The node arrangements in the domain are generated in such a way, that the number of nodes in the vertical direction in the free stream region ($p_y \geq 1.0$) is constant for all three arrangements and equal to 40. While the number of nodes in the step region ($p_y < 1.0$) is changing, i.e. 29 for 201×71, 49 for 201×91 and 69 for 201×111. The node arrangement is generated with a refinement near the walls as presented in Figure 5.55. When using the AKN model, the refinement level b_1 is equal to 1.8 in all three arrangements, while b_2 is different in each arrangement: 1.6 for 201×71, 1.4 for 201×91 and 1.2 for 201×111. The levels are different in order to keep the time step value equal to 10^{-3} s. A detailed view of the 201×71 node arrangement is shown in Figure 5.56. The obtained grid convergence is presented in Figure 5.57, where the skin friction at the bottom wall is plotted. We also try to use denser discretization in the horizontal direction with 251 and 301 nodes, but we obtained the results without any improvements. When using the LS model, the refinement of the node arrangement near the bottom wall is enhanced to get the stable profile of the skin friction. For the 201×111 node arrangement, the refinement level $b_1 = 2.2$ is acceptable. With this refinement level, the time step is reduced to $2.5 \cdot 10^{-4}$ s.

The results are compared with the measurements [Jović and Driver, 1994] (JD), with the results obtained by the DNS of turbulent flow [Le *et al.*, 1997], and with the results obtained by Fluent. Calculations with the present method are performed with LS and AKN turbulence models.

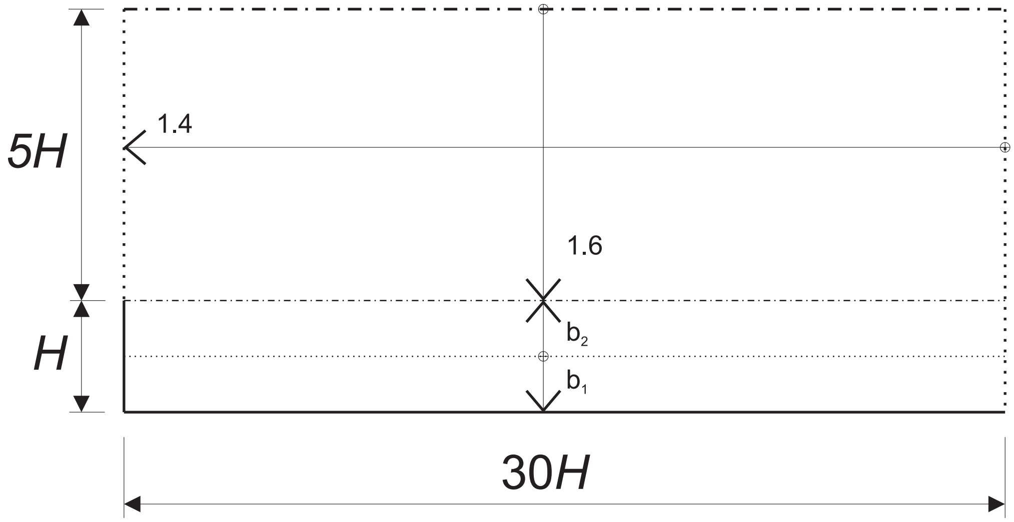

Figure 5.55: Node refinement schematics.

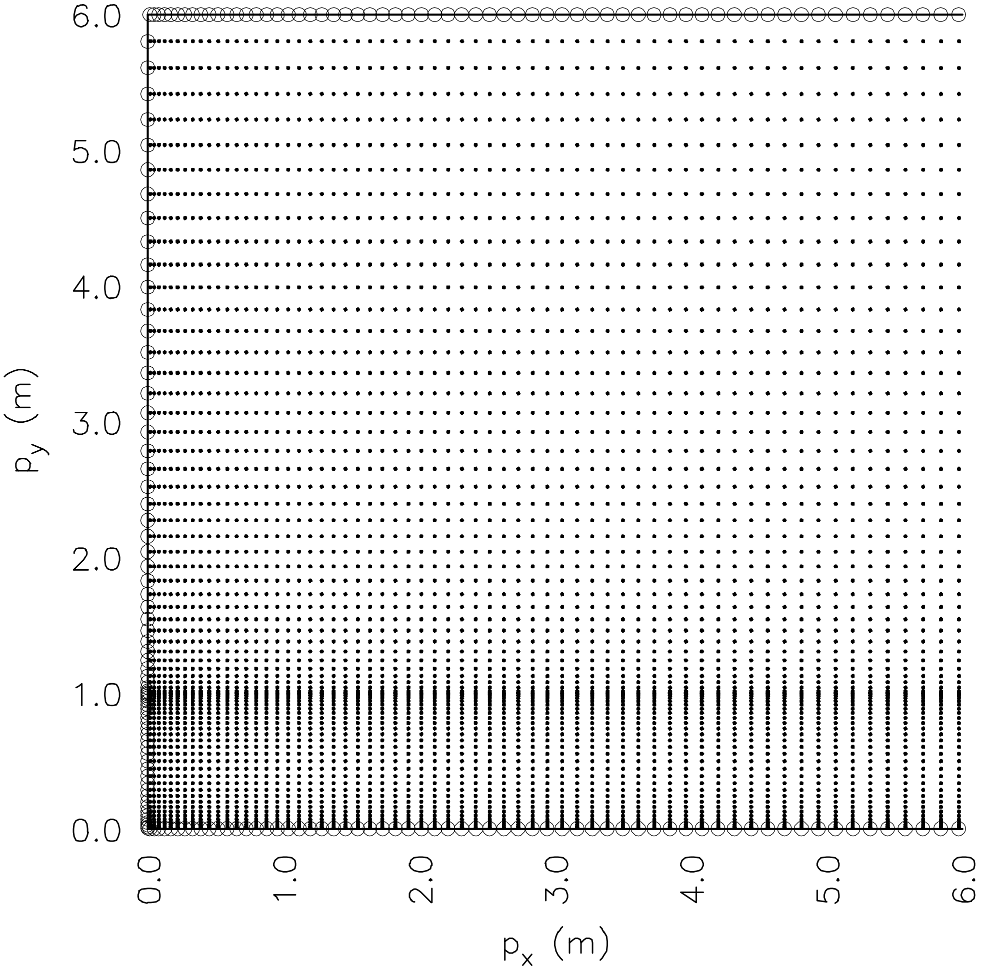

Figure 5.56: A detailed view of the 201×71 node arrangement. Points: interior nodes. Circles: boundary nodes.

In Fluent, the calculations are performed with the non-uniform mesh with 80000 finite volumes (400×200 quadrilateral finite volumes) with a similar refinement near the walls as in our model. With this very fine discretization, a reasonable mesh-independence of the results has been achieved. Only the AKN turbulence model is used. However, Fluent has the ability to use the LS model, but it has implemented its modified version, without D and E source terms in the transport equations for k and ε, respectively (see equations (2.83) and (2.84)). Because of these modifications, this is not the original model by Launder and Sharma [Launder and Sharma, 1974], and thus we did not use it in the present dissertation. The same boundary conditions and material properties are set as in the LRBFCM calculations.

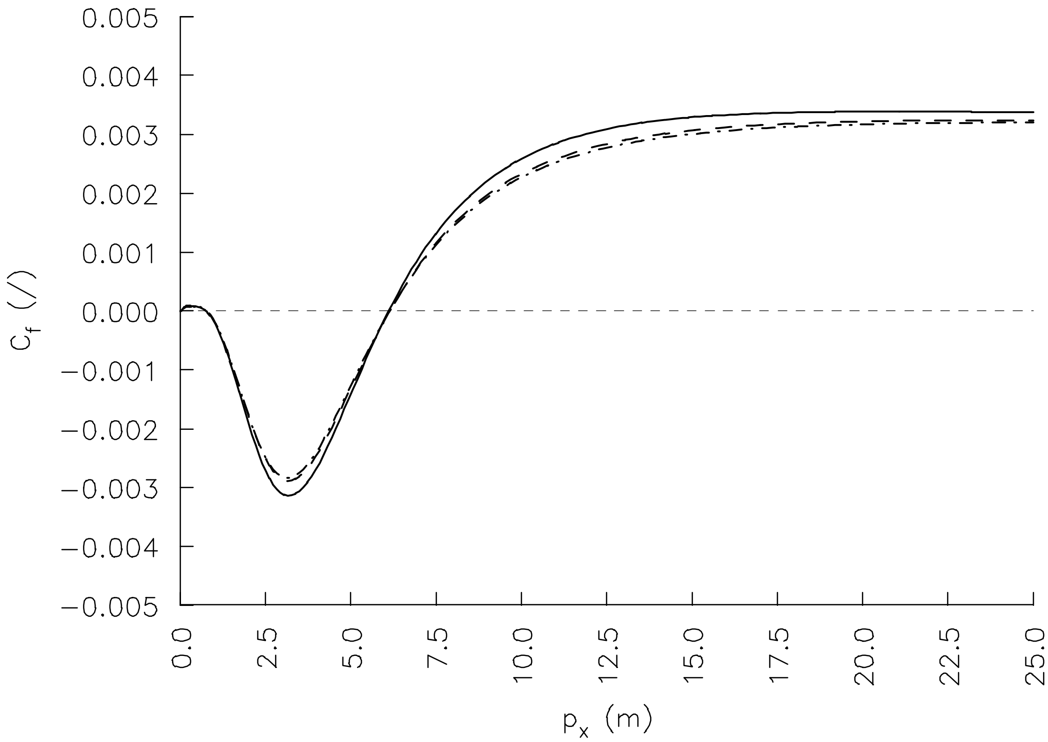

Figure 5.57: Skin friction at the bottom wall obtained with three different node arrangements: Solid line: 201×71. Dashed line: 201×91. Dash-doted line: 201×111.

The calculated velocity profile u_x, normalized by the inlet velocity in the upstream channel u_{x0}, is compared with the results obtained by other methods at different x/H positions. For better insight into the obtained results, the normalized velocity profile u_x at each x/H position is plotted as a separate figure: at $x/H=4$ in Figure 5.58, at $x/H=6$ in Figure 5.59, at $x/H=10$ in Figure 5.60, at $x/H=15$ in Figure 5.61 and at $x/H=19$ in Figure 5.62. Below each figure, the normalized numerical and experimental velocity values u_x are also tabulated in Tables 5.12, 5.13, 5.14, 5.15 and 5.16. The differences between all methods and experiment are more clearly visible from the tabulated values. There are several reasons to explain these differences. The prevailing one is because of the use of different turbulence models, where each model has its own advantages and disadvantages. The DNS results are most accurate, since the N-S equation is directly solved. The prediction with the LS model is very good in the range between the position of the step and at $x/H=4$. Around the fluid separation downward the step, especially around the reattachment position, the LS model is losing its accuracy. The reasons are in the D and E source terms in the transport equations for k and ε, respectively. They both include second order derivatives, which are very sensitive in the separation regions. This is the reason why Fluent does not use these terms. With the AKN model, we obtained over-prediction in the range before the reattachment position and an under-prediction in the remaining region (after the reattachment position). However, the results with the AKN model of the present method and Fluent are in excellent agreement. The calculated velocity field of the whole computational domain is presented with the generated streamlines, plotted in Figure 5.63.

The important quantity in the backward-facing step simulations is the reattachment position. The reattachment position is obtained based on the horizontal velocity u_x at the first inner point, closest to the bottom wall. The reattachment is at the position, where the velocity u_x is equal to zero. The second approach is based on the skin friction, defined by the following equation

$$C_f = \frac{2\tau_w}{\rho u_{x0}^2}, \tag{5.31}$$

where τ_w and u_{x0} are the wall shear stress at the bottom wall and the inlet velocity in the upstream channel, respectively. The reattachment is at the position, where the skin friction is equal to zero. The later approach is used in the present dissertation. With the LS model we got the position at $x/H = 6.64$, while with the AKN model at $x/H = 6.14$. The related reattachment positions obtained by experiment and other authors are represented in Table 5.11. The skin friction, calculated by equation (5.31), is also presented in Figure 5.64 for the AKN model and in Figure 5.65 for the LS and JL models. In both figures, the skin friction from the DNS results and the experimental measurements are plotted as well.

Table 5.11: Reattachment position.

	turbulence model	reattachment position- x/H
experiment JD	/	6.00±0.15
present method	LS	6.64
present method	AKN	6.14
DNS	/	6.28
Fluent	AKN	6.20
[Bredberg, 2001]	JL	6.17
[Bredberg, 2001]	LS+YAP	6.83
[Bredberg, 2001]	AKN	5.65

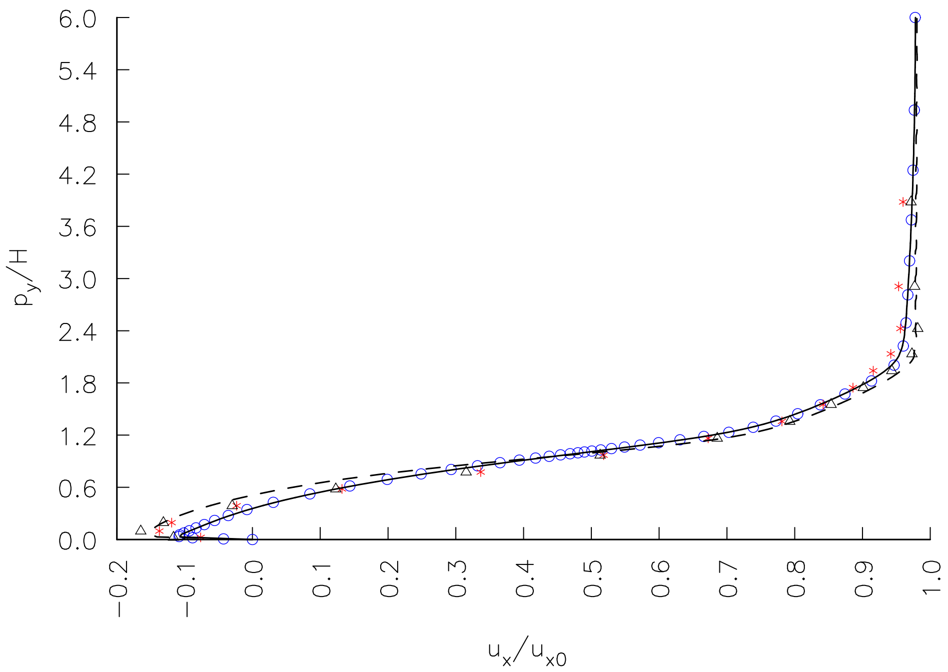

Figure 5.58: The normalized velocity u_x at $x/H = 4$. Solid line: present with AKN model. Dashed line: present with LS model. Blue o: Fluent with AKN model. Δ: DNS. Red ∗: JD.

Table 5.12: The normalized velocity u_x at $x/H = 4$.

	experiment JD	DNS	Fluent AKN	present AKN	present LS
0.025	-0.0764	-0.1164	-0.0983	-0.0861	-0.1167
0.097	-0.1373	-0.1647	-0.0944	-0.0921	-0.1498
0.194	-0.1192	-0.1314	-0.0641	-0.0613	-0.1319
0.388	-0.0233	-0.0299	0.0163	-0.0148	-0.0631
0.582	0.1321	0.1230	0.1206	0.1244	0.0464
0.776	0.3368	0.3153	0.2675	0.2730	0.2164
0.970	0.5181	0.5129	0.4519	0.4586	0.4648
1.164	0.6723	0.6857	0.6476	0.6487	0.6945
1.358	0.7811	0.7928	0.7709	0.7682	0.7994
1.552	0.8420	0.8537	0.8389	0.8369	0.8637
1.746	0.8860	0.9012	0.8940	0.8914	0.9158
1.940	0.9158	0.9433	0.9371	0.9332	0.9567
2.134	0.9417	0.9730	0.9568	0.9545	0.9760
2.425	0.9559	0.9816	0.9637	0.9627	0.9782
2.910	0.9534	0.9770	0.9676	0.9672	0.9780
3.880	0.9598	0.9716	0.9730	0.9730	0.9783

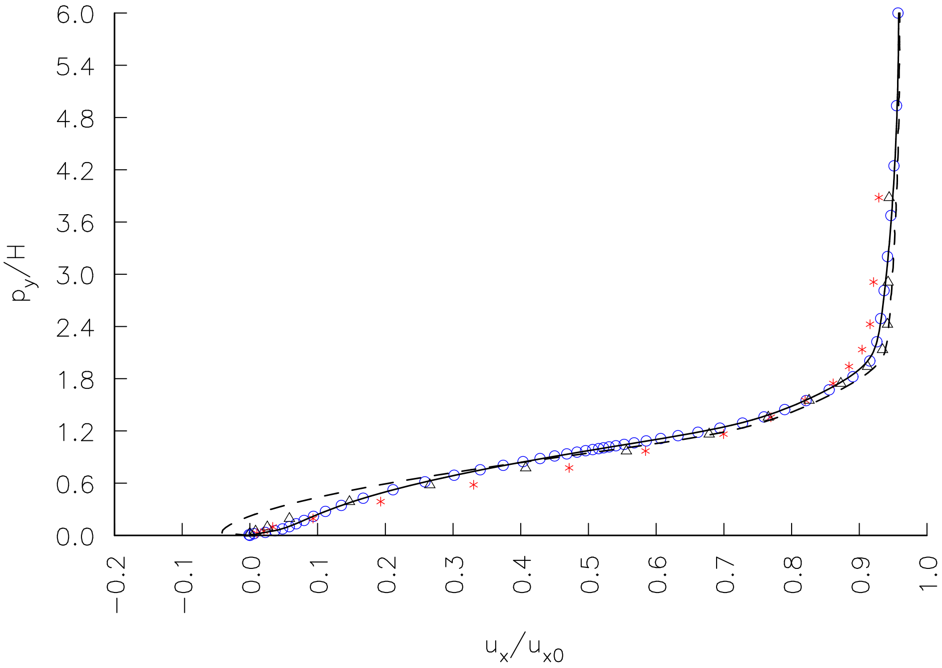

Figure 5.59: The normalized velocity u_x at $x/H = 6$. Solid line: present with AKN model. Dashed line: present with LS model. Blue o: Fluent with AKN model. Δ: DNS. Red ∗: JD.

Table 5.13: The normalized velocity u_x at $x/H = 6$.

	experiment JD	DNS	Fluent AKN	present AKN	present LS
0.025	0.0104	-0.0002	0.0114	0.0158	-0.0343
0.049	0.0207	0.0083	0.0343	0.0330	-0.0406
0.097	0.0337	0.0257	0.0565	0.0565	-0.0345
0.194	0.0933	0.0583	0.0865	0.0868	-0.0093
0.388	0.1930	0.1471	0.1515	0.1524	0.0734
0.582	0.3303	0.2657	0.2400	0.2416	0.1929
0.776	0.4715	0.4073	0.3544	0.3569	0.3457
0.970	0.5842	0.5560	0.4936	0.4964	0.5225
1.164	0.6995	0.6783	0.6462	0.6457	0.6844
1.358	0.7694	0.7656	0.7580	0.7551	0.7802
1.552	0.8199	0.8258	0.8223	0.8202	0.8407
1.746	0.8614	0.8727	0.8738	0.8696	0.8888
1.940	0.8847	0.9122	0.9090	0.9046	0.9236
2.134	0.9041	0.9343	0.9228	0.9218	0.9385
2.425	0.9158	0.9416	0.9304	0.9309	0.9436
2.910	0.9210	0.9426	0.9379	0.9387	0.9479

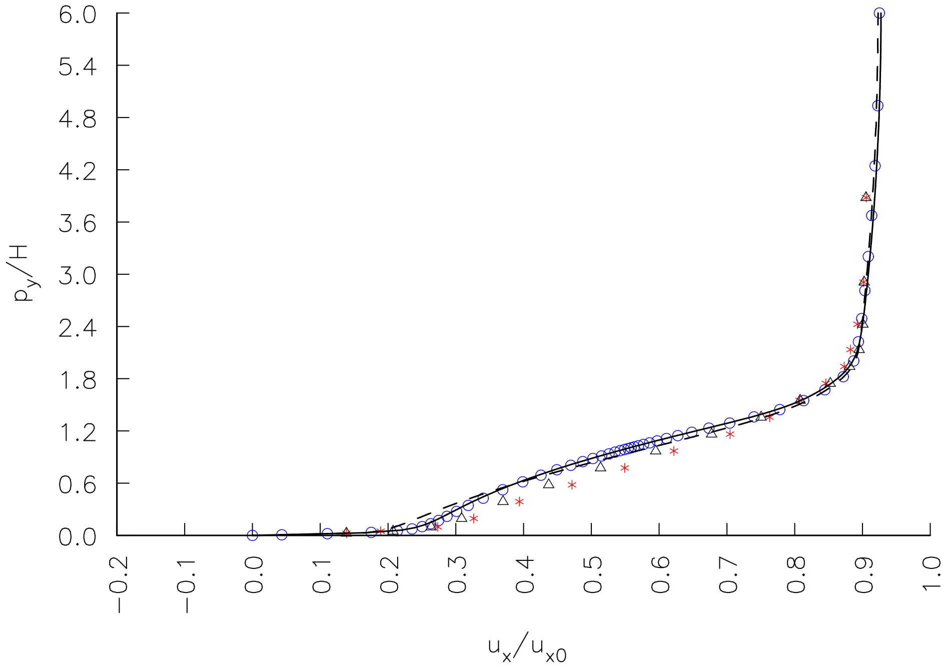

Figure 5.60: The normalized velocity u_x at $x/H=10$. Solid line: present with AKN model. Dashed line: present with LS model. Blue o: Fluent with AKN model. Δ: DNS. Red ∗: JD.

Table 5.14: The normalized velocity u_x at $x/H=10$.

	experiment JD	DNS	Fluent AKN	present AKN	present LS
0.025	0.1386	0.1386	0.1344	0.1325	0.1395
0.049	0.1891	0.2073	0.2073	0.1965	0.1839
0.097	0.2733	0.2636	0.2482	0.2427	0.2098
0.194	0.3264	0.3086	0.2805	0.2752	0.2429
0.388	0.3938	0.3697	0.3298	0.3250	0.3075
0.582	0.4715	0.4370	0.3874	0.3832	0.3829
0.776	0.5492	0.5135	0.4577	0.4544	0.4705
0.970	0.6218	05949	0.5412	0.5386	0.5670
1.164	0.7047	0.6774	0.6371	0.6347	0.6661
1.358	0.7629	0.7505	0.7383	0.7348	0.7552
1.552	0.8070	0.8079	0.8141	0.8093	0.8193
1.746	0.8458	0.8524	0.8593	0.8537	0.8606
1.940	0.8730	0.8811	0.8832	0.8805	0.8847
2.134	0.8821	0.8951	0.8916	0.8928	0.8941
2.425	0.8925	0.9006	0.8977	0.9002	0.8993
2.910	0.9015	0.9024	0.9048	0.9075	0.9053

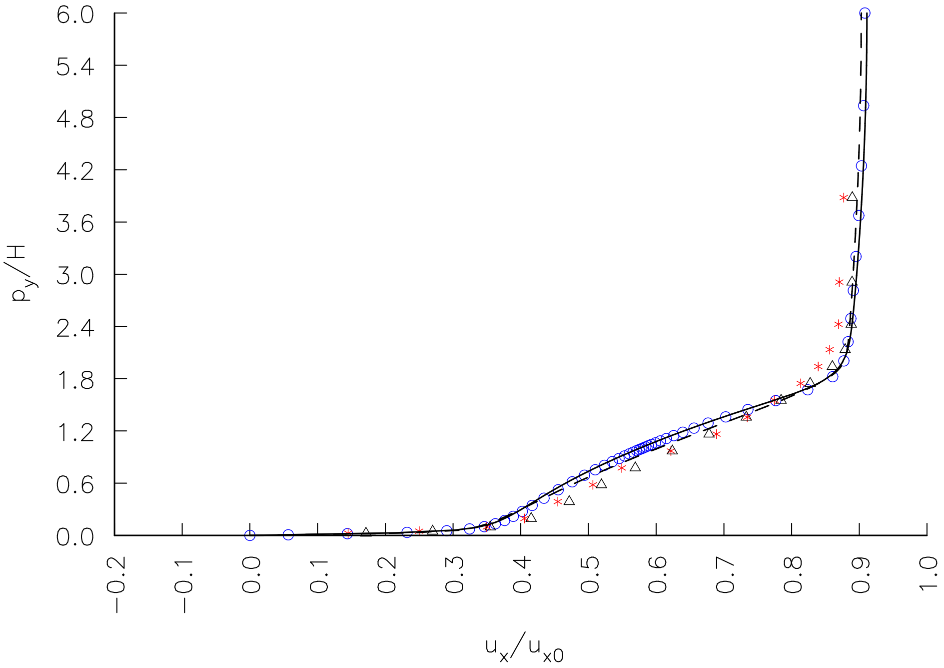

Figure 5.61: The normalized velocity u_x at $x/H = 15$. Solid line: present with AKN model. Dashed line: present with LS model. Blue o: Fluent with AKN model. Δ: DNS. Red ∗: JD.

Table 5.15: The normalized velocity u_x at $x/H = 15$.

	experiment JD	DNS	Fluent AKN	present AKN	present LS
0.025	0.1451	0.1714	0.1756	0.1756	0.1982
0.049	0.2500	0.2698	0.2806	0.2671	0.2826
0.097	0.3497	0.3549	0.3432	0.3358	0.3344
0.194	0.4054	0.4154	0.3825	0.3750	0.3709
0.388	0.4547	0.4717	0.4261	0.4192	0.4232
0.582	0.5065	0.5192	0.4681	0.4618	0.4751
0.776	0.5492	0.5692	0.5157	0.5101	0.5314
0.970	0.6218	0.6239	0.5703	0.5654	0.5923
1.164	0.6891	0.6782	0.6320	0.6279	0.6566
1.358	0.7344	0.7332	0.7015	0.6979	0.7222
1.552	0.7746	0.7845	0.7780	0.7736	0.7852
1.746	0.8135	0.8275	0.8453	0.8389	0.8397
1.940	0.8394	0.8602	0.8733	0.8708	0.8729
2.134	0.8562	0.8792	0.8815	0.8828	0.8819
2.425	0.8692	0.8882	0.8866	0.8895	0.8859
2.910	0.8705	0.8894	0.8922	0.8954	0.8902

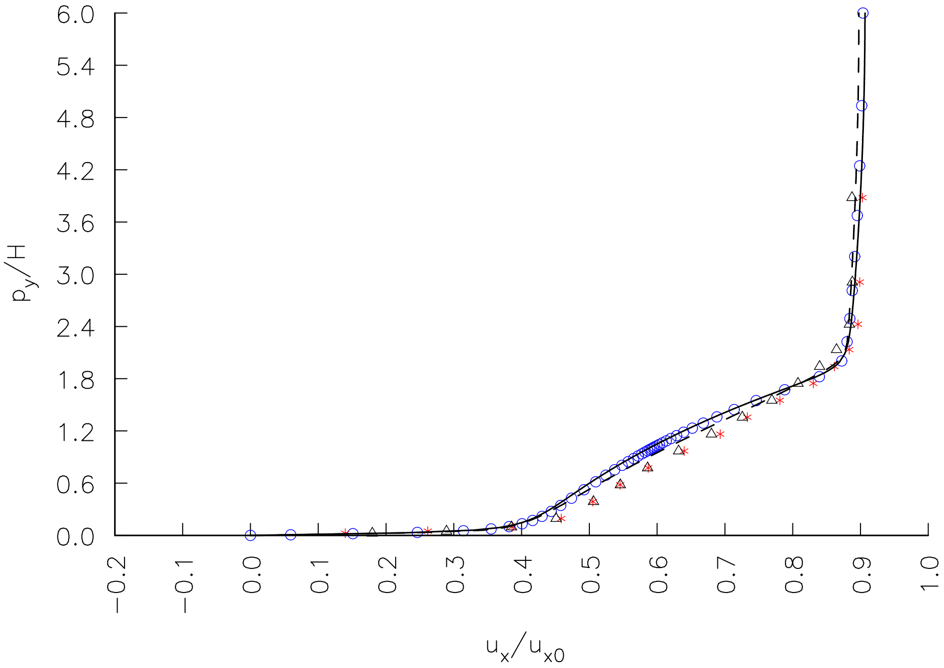

Figure 5.62: The normalized velocity u_x at $x/H=19$. Solid line: present with AKN model. Dashed line: present with LS model. Blue o: Fluent with AKN model. Δ: DNS. Red ∗: JD.

Table 5.16: The normalized velocity u_x at $x/H=19$.

	experiment JD	DNS	Fluent AKN	present AKN	present LS
0.025	0.1399	0.1798	0.1846	0.1859	0.1994
0.049	0.2616	0.2892	0.3021	0.2885	0.3051
0.097	0.3860	0.3852	0.3779	0.3704	0.3786
0.194	0.4585	0.4509	0.4233	0.4156	0.4192
0.388	0.5052	0.5061	0.4663	0.4591	0.4680
0.582	0.5453	0.5457	0.5028	0.4962	0.5117
0.776	0.5868	0.5859	0.5419	0.5358	0.5569
0.970	0.6399	0.6316	0.5852	0.5799	0.6049
1.164	0.6930	0.6801	0.6335	0.6289	0.6554
1.358	0.7332	0.7256	0.6873	0.6834	0.7076
1.552	0.7811	0.7693	0.7473	0.7438	0.7602
1.746	0.8303	0.8078	0.8137	0.8094	0.8111
1.940	0.8614	0.8397	0.8654	0.8617	0.8565
2.134	0.8834	0.8646	0.8780	0.8789	0.8779
2.425	0.8964	0.8836	0.8834	0.8863	0.8826
2.910	0.8990	0.8879	0.8887	0.8919	0.8865

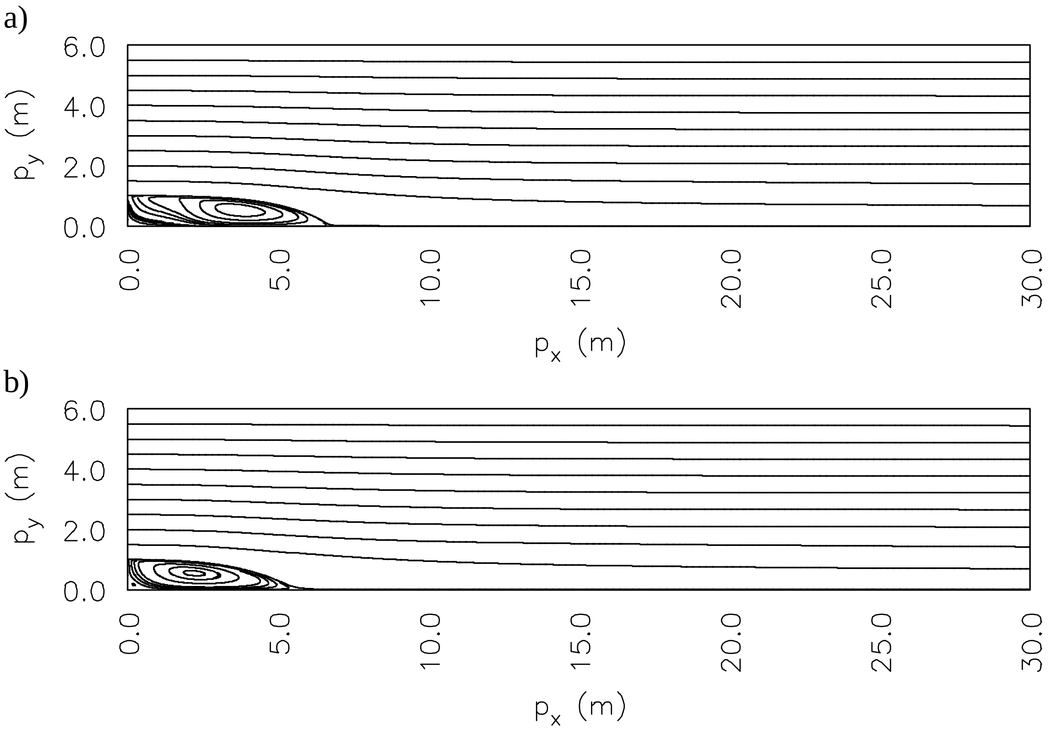

Figure 5.63: The streamlines calculated with the LS (a) and AKN (b) model.

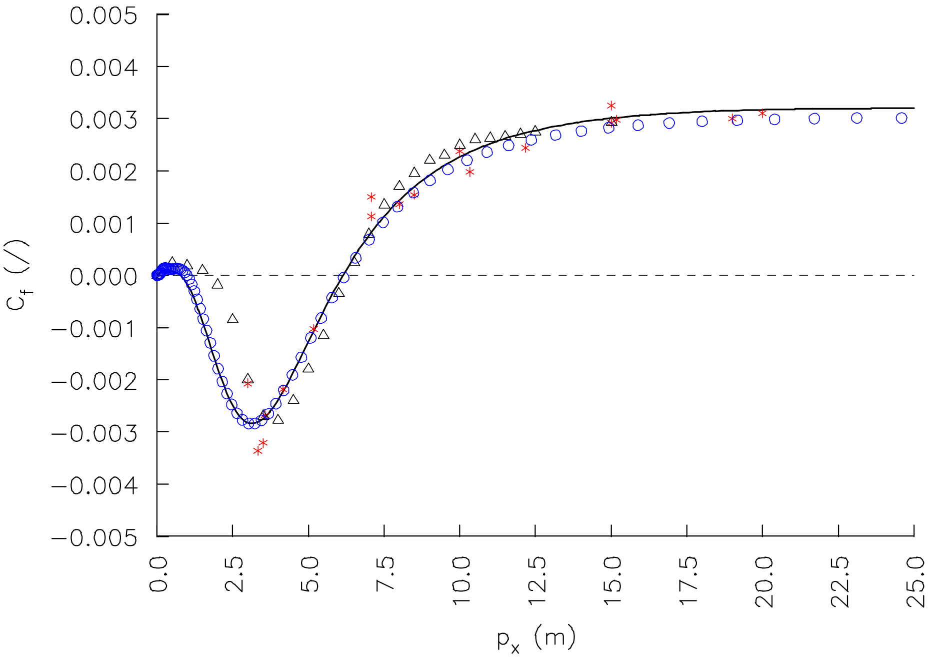

Figure 5.64: The skin friction at the bottom wall with AKN model. Solid line: present method. Blue o: Fluent. Δ: DNS. Red ∗: JD.

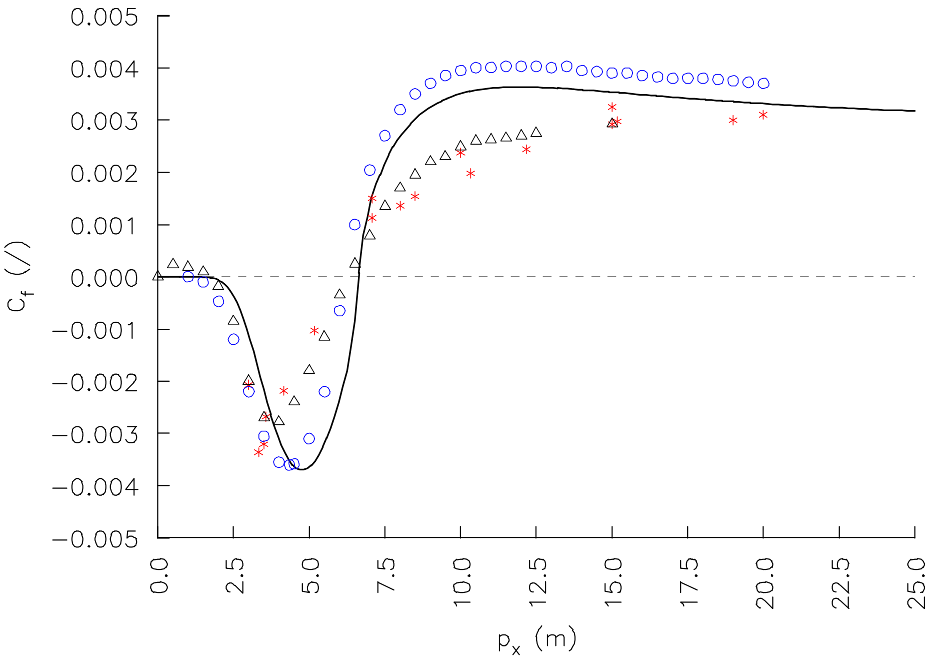

Figure 5.65: The skin friction at the bottom wall with LS and JL models. Solid line: present method with LS model. Blue o: [Bredberg, 2001] with JL model. Δ: DNS. Red ∗: JD.

6 Simulation of the Continuous Casting of Steel

The last chapter is dedicated to the numerical model of the continuous casting of steel. The model characteristics and assumptions are first explained in details. Next, the geometry of the casting machine is presented, with the procedure of the node arrangement generation. The boundary conditions are elaborated. The numerical model is validated by the results obtained with Fluent, where the simplified geometry and material properties are used. The comparison is analyzed on the basis of selected velocity and temperature profiles, and velocity and temperature fields. In the last section, various simulations with thermo-physical properties obtained by the JMatPro, and with the real process parameters, taken from the casting machine are performed. The effects of various process parameters on the velocity and temperature field are analyzed.

6.1 Model Characteristics and Assumptions

The following characteristics and assumptions are considered in the present model:

- The continuous casting operates at steady state.
- A real curved 2D geometry of the casting machine in Štore Steel company is considered. This assumption is not a good realistic approximation for a billet caster since 3D simulations should be used. But the discretization of the 3D geometry leads to a node arrangement with a very large number of nodes. In order to get the solution with such a node arrangements in a reasonable computational time, the numerical model should be modified to run on a parallel network of computers.
- The molten steel behaves as an incompressible Newtonian fluid.
- The thermo-physical properties of the steel are considered as a function of temperature, calculated by the JMatPro. The density is assumed to be constant and equal for both phases, i.e. the solid and the liquid phase. Its value is taken from that at the solidus temperature, also obtained by the JMatPro. The dynamic viscosity and the thermal expansion coefficient of the molten steel are fixed to 0.006 (Pa s) and $10^{-4}\,\mathrm{K}^{-1}$, respectively.

- The boundary conditions for the temperature field are taken from the already developed simulation system for Štore Steel casting machine [Šarler *et al.*, 2005].
- The heat release due to the solid-solid transformation is not taken into account.
- The solidification in a mushy zone is assumed to be as columnar-dendritic, and acts as a porous media. The velocity of the solid phase is constant, equal to the casting speed (speed of the rigid body). No equiaxed grains are assumed to float in the melt.
- The mixture-continuum model is used for deriving the conservation equations for mass, momentum, energy, and for equations of the turbulence model. This means that at each location in the mushy zone, the material is treated as a mixture, occupied simultaneously by all phases and all constituents. A detailed explanation and the derivation of the mixture model is presented in Chapter 2.

6.2 Geometry and Node Arrangement

The casting machine is composed of the mould, the secondary cooling system and the rolls. The present numerical model of the continuous casting process involves only the first two parts, as shown in Figure 6.1. The shape of the casted billet in the casting direction is an arc of a circle with radius $r_0 = 6\,\mathrm{m}$, measured from the centre of a circle to the outer side of the mould. The position of the centre point of a circle, according to the origin of the selected coordinate system (see Figure 6.1), is at $x = 6.0\,\mathrm{m}$ and $y = 0.0\,\mathrm{m}$. The geometry of the SEN is presented in Figure 6.2. Its geometrical shape is a hollow cylinder (tube). The meaning of each dimension and its value of the casting machine and the SEN is represented in Table 6.1. The same values are used for generating node arrangements in the present numerical model. Note that the tubular SEN is a 2D model, whereas the billet is modelled as an infinitely broad slab.

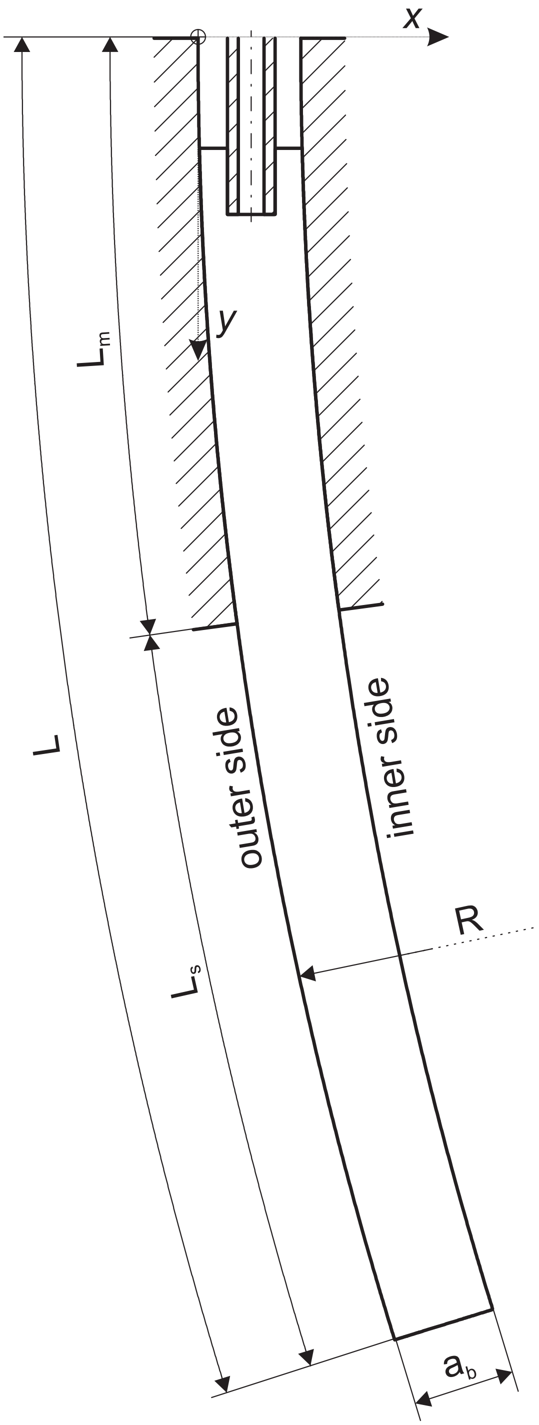

Figure 6.1: Considered geometry schematics of the continuous casting machine.

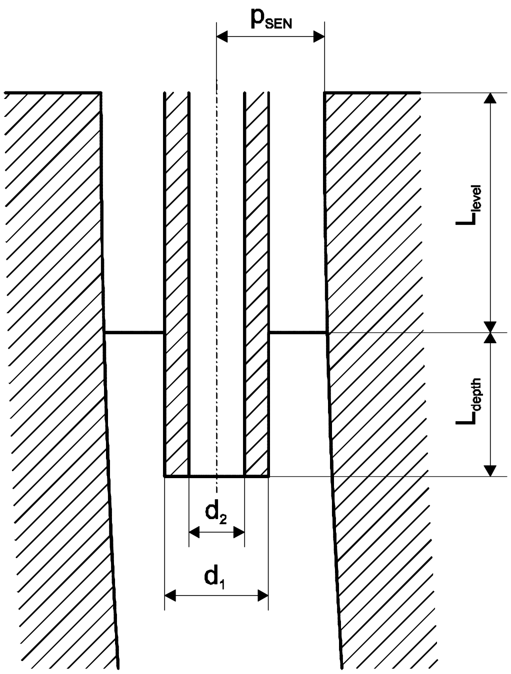

Figure 6.2: Geometry of the SEN with relevant dimensions.

Table 6.1: The dimensions of the Štore Steel continuous casting machine.

dimension	description	value (m)
L_m	length of the mould	0.8000
L_s	length of the secondary cooling system	1.0000
a_b	billet dimension	0.1400
d_1	outer diameter of the SEN	0.0650
d_2	inner diameter of the SEN	0.0350
p_{SEN}	position of the SEN	0.0725
L_{level}	steel level depth	0.1500
L_{depth}	submerging depth of the SEN	0.0900
R	outer radius of the casting machine	6.0000

The node generation for a non-curved geometry is easy to handle, while special care should be considered in curved geometry. Theoretically, the meshless methods allow the solution of the PDE on a scattered node arrangement. This was already analysed by many authors on a relatively very simple examples, i.e. heat transfer in a square cavity [Lee *et al.*, 2003]. However, for such a complex geometry and also physical problem of the casting process, we did not generate a random node arrangement, but rather use an automatic orthogonal grid generator with the open-source software package Gridpak (Version 5.3, “http://marine.rutgers.edu/po/gridpak.html”). Gridpak is a package written in Fortran language, and creates an orthogonal grid based on the available boundary information. First, we generate a node arrangement for each boundary, and then pass the coordinates of the generated boundary node arrangements into the Gridpak solver, which returns the coordinates of the interior nodes. An example of the generated node arrangement used in the present dissertation, is shown in Figures 6.3 and 6.4. It is refined near the walls, around the SEN and near the end of the mould. More nodes are generated in the regions between the SEN and walls along the whole billet, where also the mushy zone exists. Based on the comparison with Fluent and experience from the numerical results in the previous chapter, we came up with the node arrangement with 57637 nodes. The arrangement is optimized in such a way that the time step value is kept large as much as possible without jeopardizing the stability and accuracy of the solution.

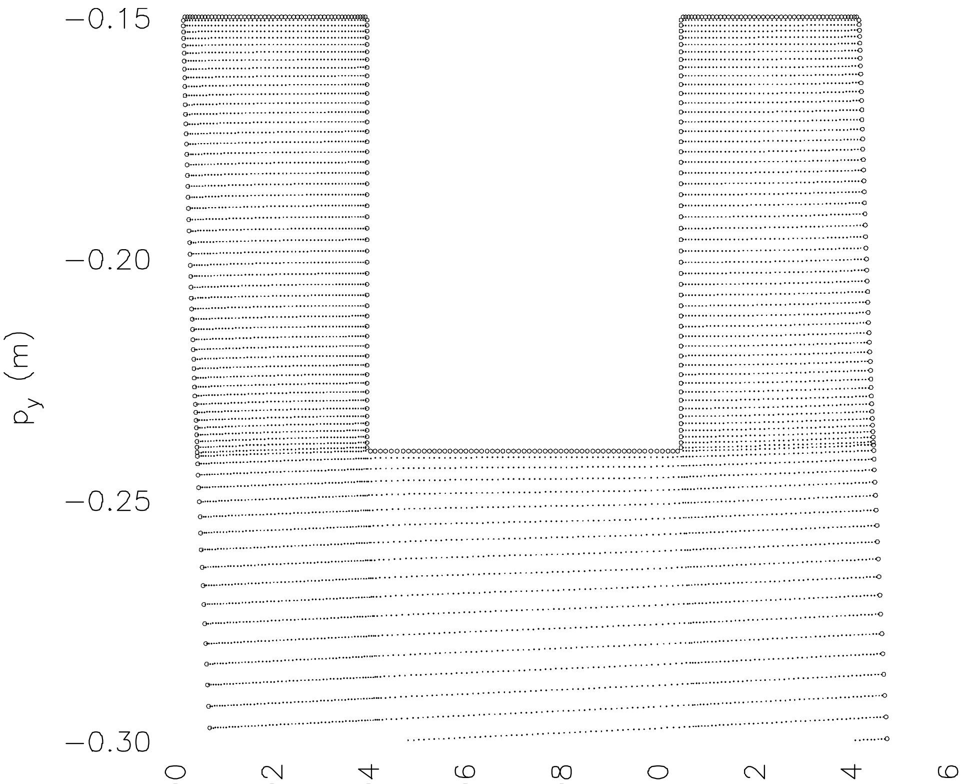

Figure 6.3: Node arrangement in the mould and around the SEN.

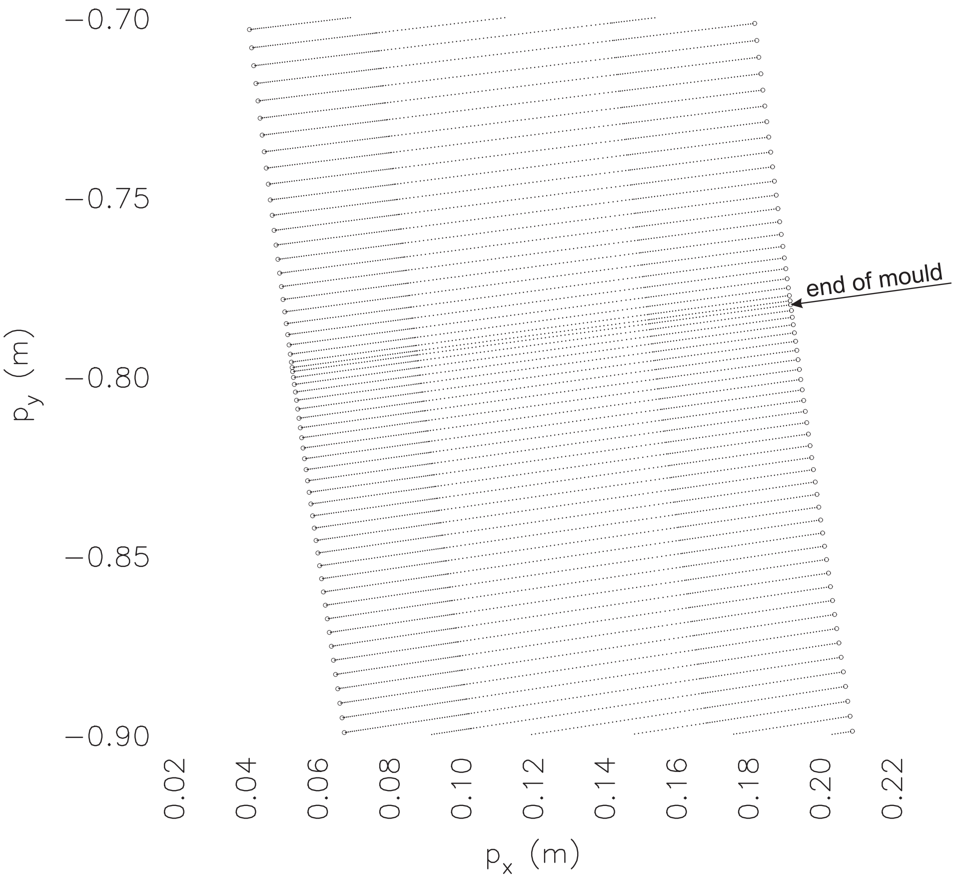

Figure 6.4: A detailed view of the node arrangement at the end of the mould.

6.3 JMatPro Thermo-Physical Properties

The thermo-physical properties of steel are calculated with the JMatPro. The following properties are included: thermal conductivity, specific heat, enthalpy and liquid fraction. They are imported by reading the export (.dat) file, which is generated by the export function in the JMatPro. For an example, the thermal conductivity, specific enthalpy, liquid fraction and specific heat for C45 steel grade (see composition in Table 6.3) are plotted in the Figures 6.5 to 6.8, respectively.

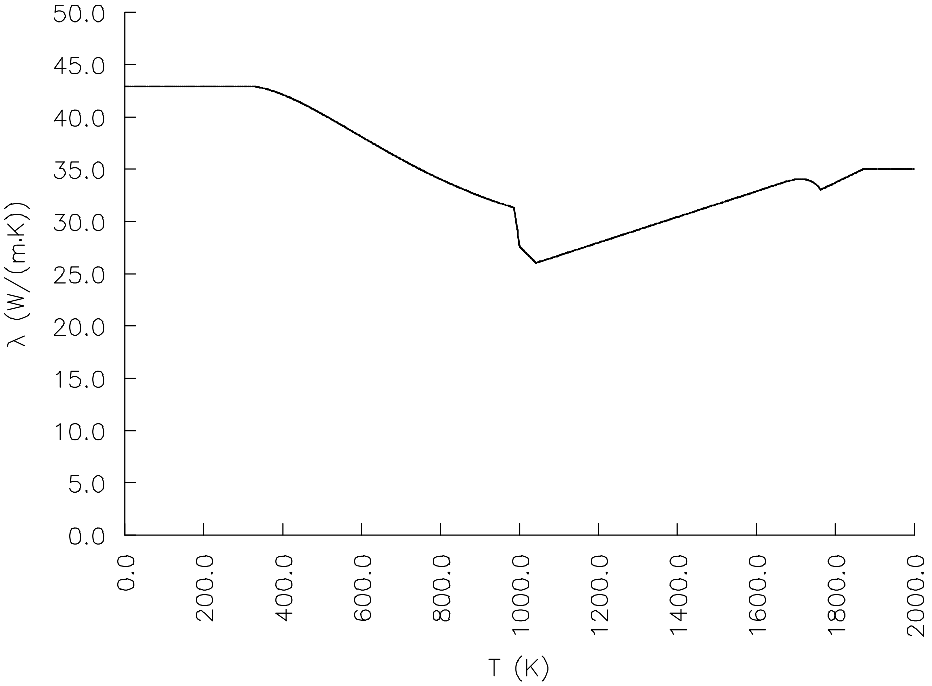

Figure 6.5: Thermal conductivity of the steel grade C45.

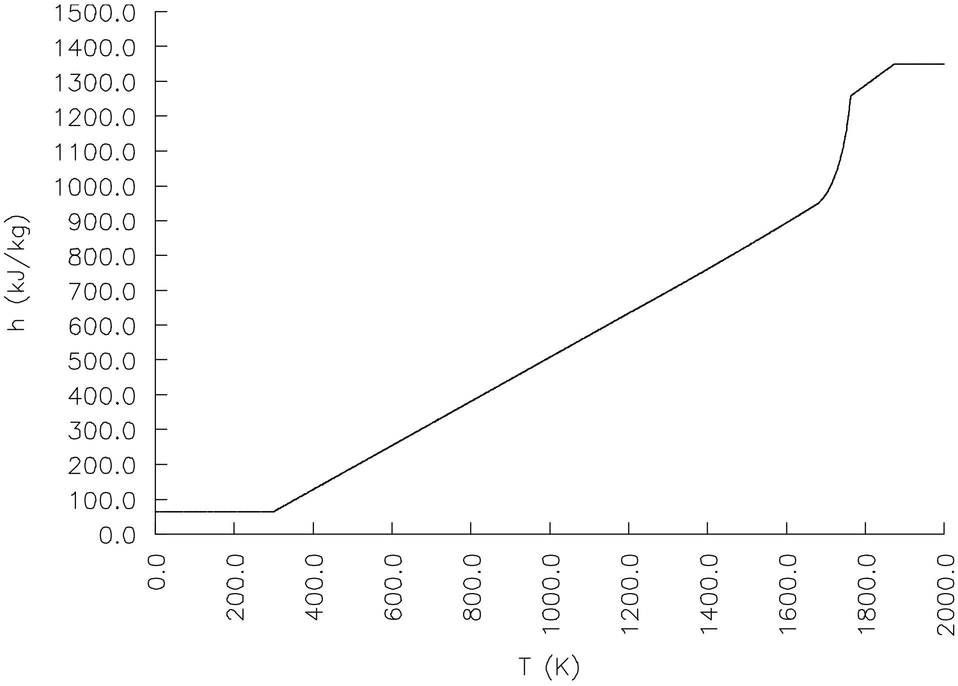

Figure 6.6: Enthalpy of the steel grade C45.

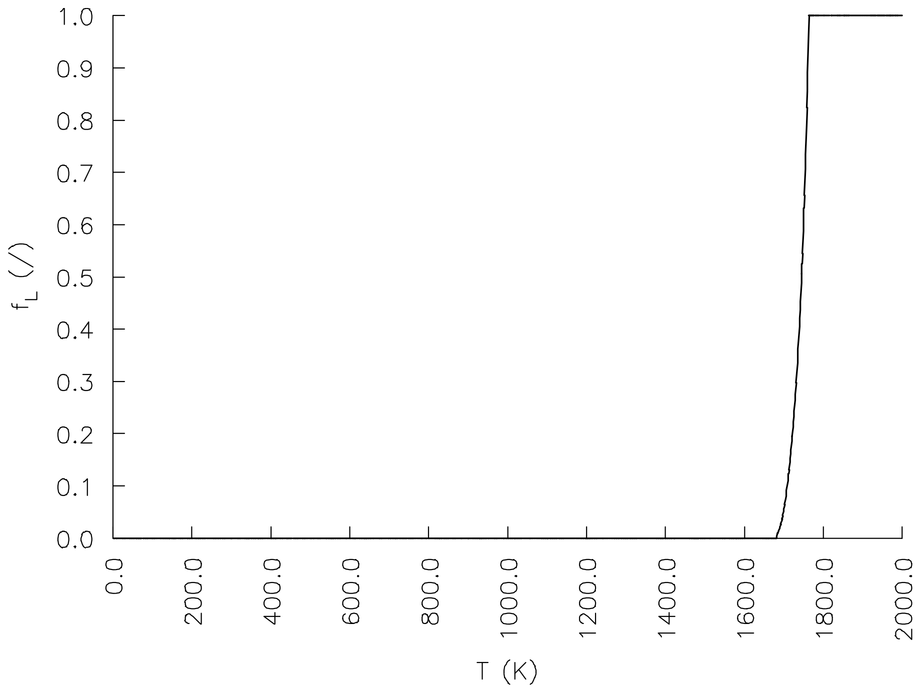

Figure 6.7: Liquid fraction of the steel grade C45.

It is found out that the specific heat needs to be modified before using it in the present numerical calculations. In the JMatPro calculations, where the solidification appears, the latent heat is also considered in the model for specific heat. The specific heat is then modified by re-calculating it in the interval between the solidus and liquidus temperature by using the linear function. The specific heat is also modified by removing the peaks (releasing heats) where the solid-solid transformations occur. Solid-solid transformations are bellow 1200 K. In that range, the values of the specific heat are calculated using the linear function between 299 K and 1200 K.

To demonstrate the modifications, the difference between the original and the modified specific heat for the steel grade C45 is presented. In Figure 6.8 the original one and in Figure 6.9 the modified one are plotted, respectively.

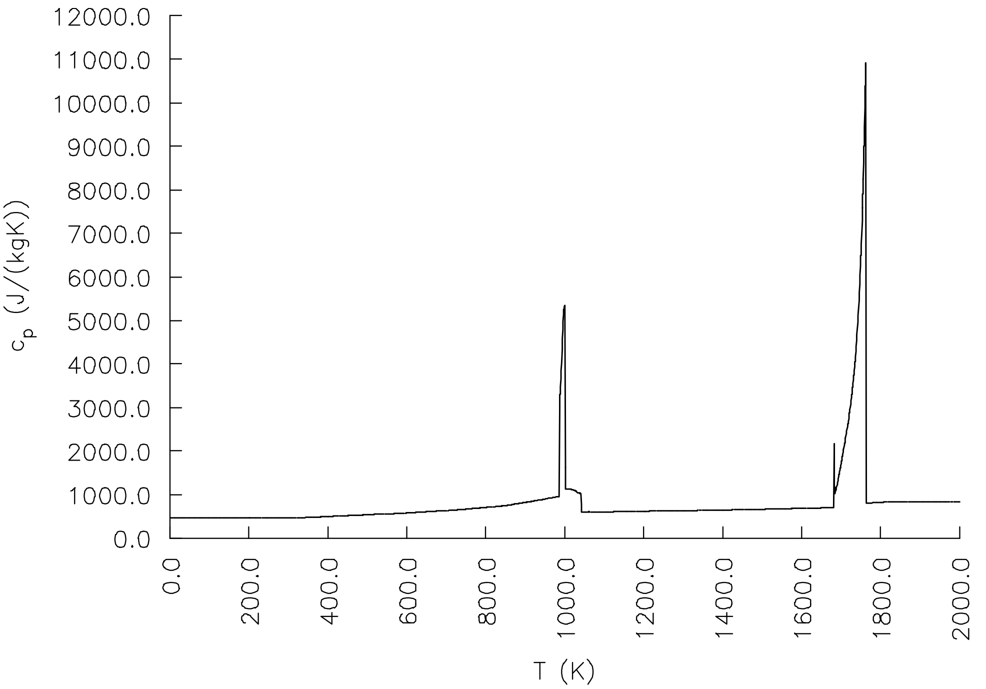

Figure 6.8: Specific heat of the steel grade C45 obtained by the JMatPro.

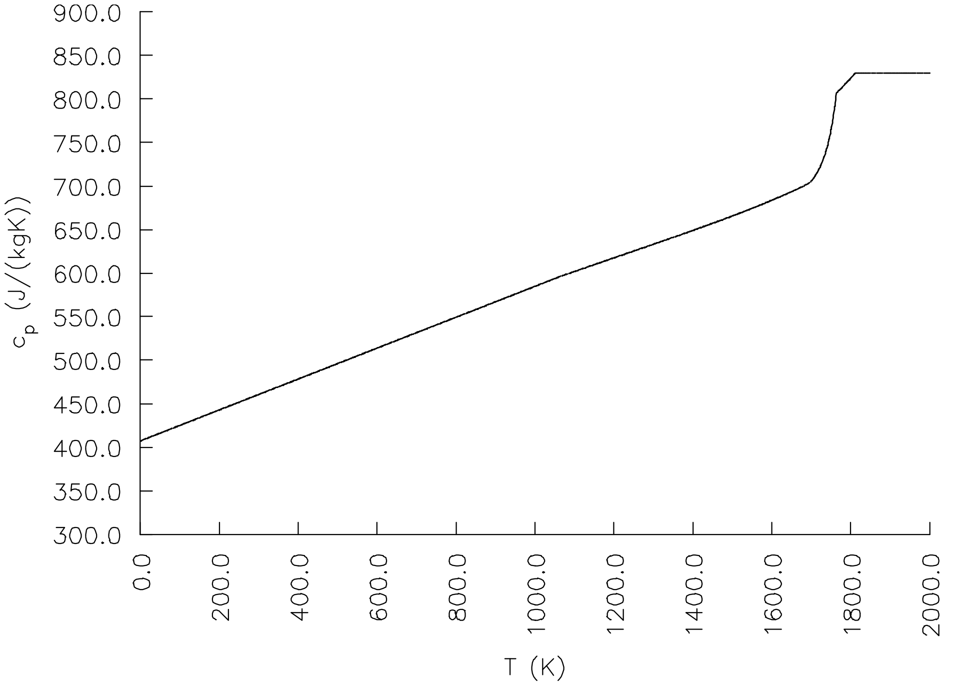

Figure 6.9: Modified specific heat of the steel grade C45 used in the simulations.

6.4 Initial Conditions

The initial condition for the velocity field is set in the same way as presented in the Section 2.7, i.e. by solving the potential field.

The initial temperature field is set to a constant value, equal to the casting temperature.

The uniform profiles for the turbulent kinetic energy and the dissipation rate are set, equal to $k_0 = 10^{-3}\,\mathrm{m}^2/\mathrm{s}^2$ and $\varepsilon_0 = 10^{-3}\,\mathrm{m}^2/\mathrm{s}^3$.

6.5 Boundary Conditions

The boundary conditions for the velocity components, the turbulent kinetic energy, the dissipation rate, and the temperature are defined in this section. For the temperature, the boundary conditions are taken from an already developed and validated simulation system in the Štore Steel company [Šarler *et al.*, 2005]. The simulation system was validated based on the temperature measurements on the billet surface by the pyrometer [Vertnik and Šarler, 2004c], installed on the continuous casting machine, and by the thermovision measurements with the high-speed thermograph camera FLIR ThermoVision SC6000HS [Gjerkeš *et al.*, 2009]. Figure 6.10 shows an example of the validation, where the comparison of the measured and simulated temperature in the middle of the cast steel billet surfaces is represented.

The boundary conditions for the velocity components and variables of the turbulence model are graphically represented in Figure 6.11. Their discussion is as follows:

I - Inlet

At the inlet, the profiles of the vertical velocity, the turbulent kinetic energy, and the dissipation rate are pre-calculated with a 2D channel flow solver (see Section 5.5.1). A 41×101 node arrangement with level refinement $b = 1.5$ is used. The time step is equal to $\Delta t = 7.5 \cdot 10^{-5}$ s. The inlet velocity is calculated from the mass balance with the following equation

$$u_0 = \frac{u_{cast} \cdot a_b}{d_2}, \tag{6.1}$$

where u_{cast}, a_b and d_2 are standing for the casting velocity, billet dimension and inlet diameter of the SEN, respectively. Here, we represent the results for the casting velocity 1.75 m/min and the billet dimension 0.140 m. The results are represented in Figures 6.13, 6.14 and 6.15 as the vertical velocity profile, the non-dimensional turbulent kinetic energy, and non-dimensional dissipation rate, respectively.

O - Outlet

At the outlet, the flow is assumed to be fully developed. The gradients in the normal direction of the velocity field, the turbulent kinetic energy, and the dissipation rate are zero.

SW - stationary wall

At the stationary wall, the no-slip boundary conditions are set. The velocity components, the turbulent kinetic energy, and the dissipation rate all set to zero.

MW - moving wall

The velocity is prescribed, equal to the withdrawal velocity in the casting direction. This velocity is changing as a function of radius. It is equal to the prescribed casting speed at the outer side (left wall), where the radius is 6 m. For other nodes, with radius ranging from $6 \div 5.86\,\mathrm{m}$, the withdrawal velocity u_w is calculated by the following equation

$$u_w = \omega_0 \cdot r\,, \tag{6.2}$$

where ω_0 is an angular velocity at the outer side and r is a radius, measured from the centre of a circle to the node. The circle centre is defined in the Section 6.2. An angular velocity at the outer side is calculated as

$$\omega_0 = \frac{u_{cast}}{r_0}\,;\; r_0 = 6\,\mathrm{m}\,. \tag{6.3}$$

FS - free surface

At a free surface (free-stream flow), the boundary conditions are the same as at the outlet, except for the vertical velocity component, which value is set to zero.

The boundary conditions for the temperature field (see Figure 6.12) are as follows:

D - Dirichlet

The temperature is prescribed and constant, equal to the casting temperature.

N - Neumann

The Neumann boundary conditions at the outer and inner side of the billet are prescribed with the heat fluxes in the mould and secondary cooling system. In the mould, the heat flux is calculated by the following equation [Šarler *et al.*, 2005]

$$hfl_m = \left(Q_0 - Q_1 \sqrt{\frac{L}{u_{cast}}} \right) \left[C_{mol,\min} + \left(C_{mol,\max} - C_{mol,\min} \right) \right], \tag{6.4}$$

where $Q_0 = 2.68 \cdot 10^6$ W/m^2, $Q_1 = 0.335 \cdot 10^6$ W/(m^{2}s$^{1/2}$), $C_{mol,\min} = 0.5$, $C_{mol,\max} = 1.5$. In equation (6.4), L is the billet length, measured from the top of the free surface. In the secondary cooling system, shown in Figure 6.16, the heat flux is calculated as

$$hfl_{sc} = h_{sc} \left(T - T_{sc} \right), \tag{6.5}$$

where h_{sc} and T_{sc} is the heat transfer coefficient and temperature of the cooling water, respectively. The heat transfer coefficient is calculated by the following equation [Hardin *et al.*, 2003; Šarler *et al.*, 2005]

$$h_{sc} = 1570 \dot{Q}_{sc}^{\ 0.55} \frac{[1 - 0.0075\theta_{sc}]}{3.25} \text{W/(m}^2\text{K)}, \tag{6.6}$$

where $\dot{Q}_{sc}$ and θ_{sc} are representing the spray cooling flux in l/(m^{2}s) and temperature of the cooling water in °C, respectively. A typical heat flux along the billet is plotted in Figure 6.17.

NO - Neumann at the outlet

At the outlet, the Neumann boundary condition is set. The gradient of the temperature in the normal direction is set to zero.

NFS - Neumann at the free surface

At the free surface, the boundary condition is the same as the Neumann boundary condition at the outlet.

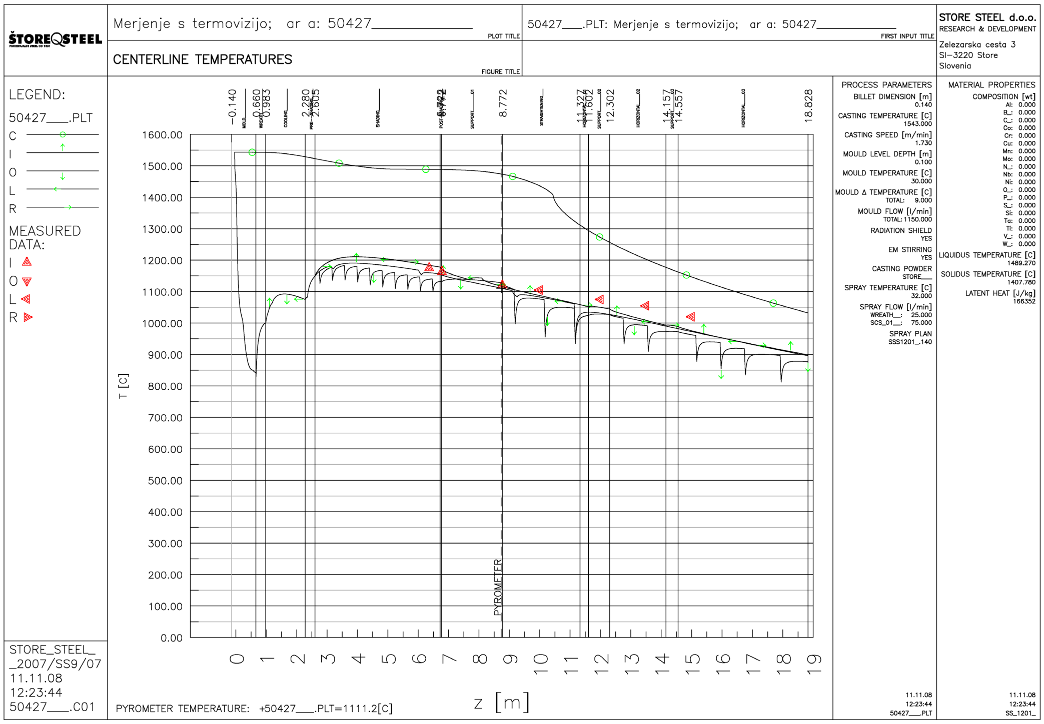

Figure 6.10: Comparison of the measured (triangles) and simulated (continuous line) temperature in the middle of the cast steel billet surfaces.

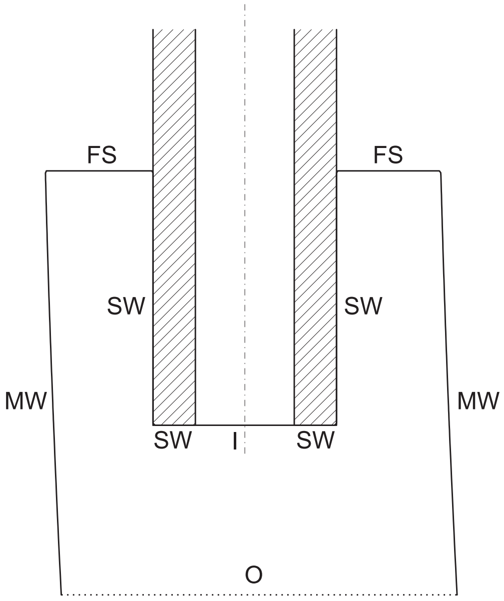

Figure 6.11: Boundary conditions for the velocity field. Characters represent: I-inlet, SW-stationary wall, FS-free surface, MW-moving wall and O-outlet.

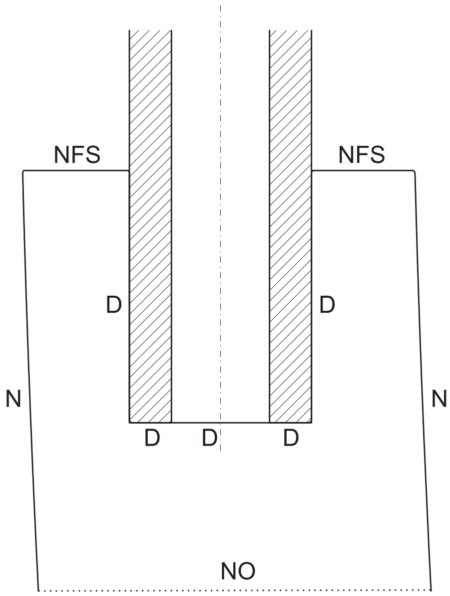

Figure 6.12: Boundary conditions for the temperature field. Characters represents: D-Dirichlet, N-Neumann, NFS-Neumann at the free surface and NO-Neumann at the outlet.

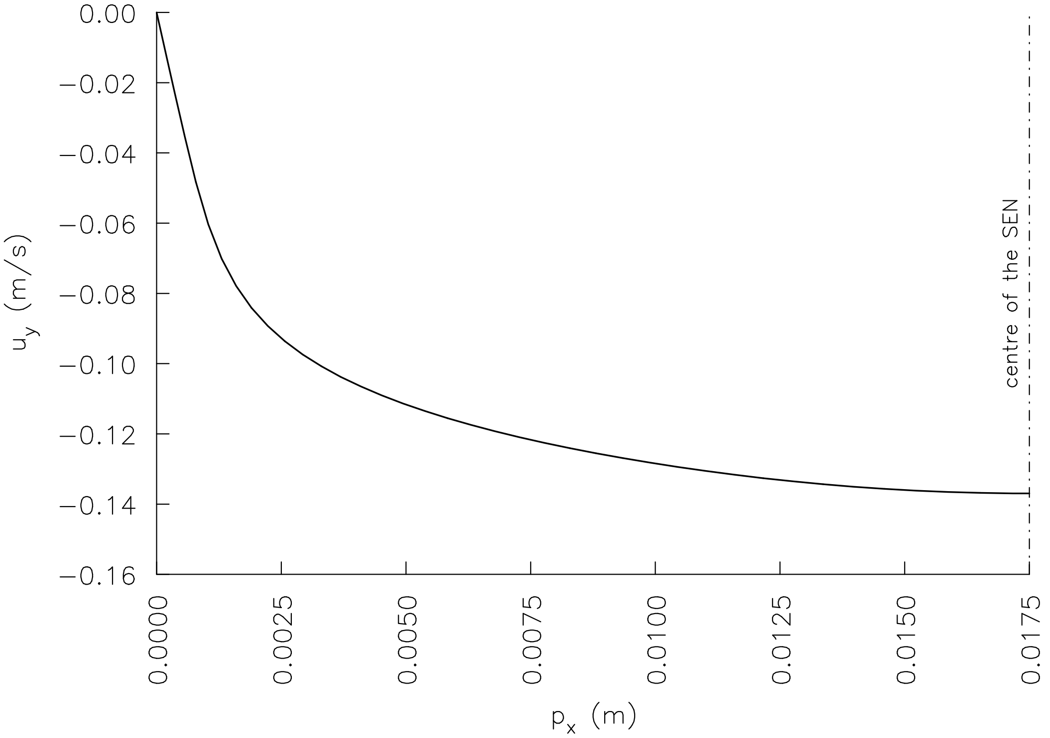

Figure 6.13: Velocity profile u_y at the SEN outlet.

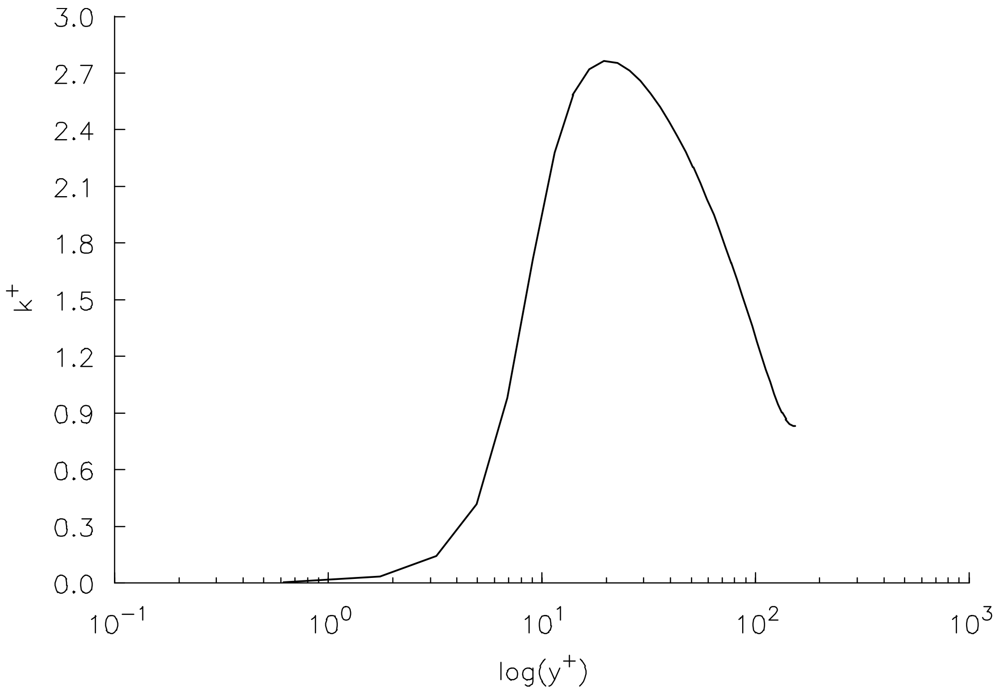

Figure 6.14: Non-dimensional turbulent kinetic energy at the SEN outlet.

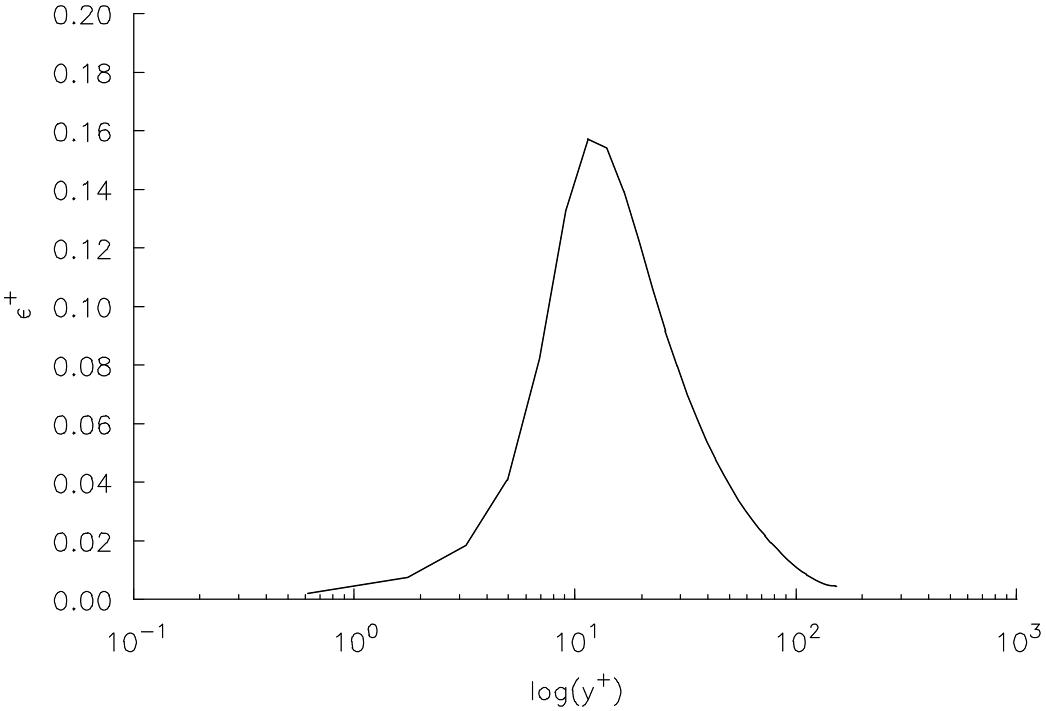

Figure 6.15: Non-dimensional dissipation rate at the SEN outlet.

Figure 6.16: Spray systems in the Štore Steel billet caster.

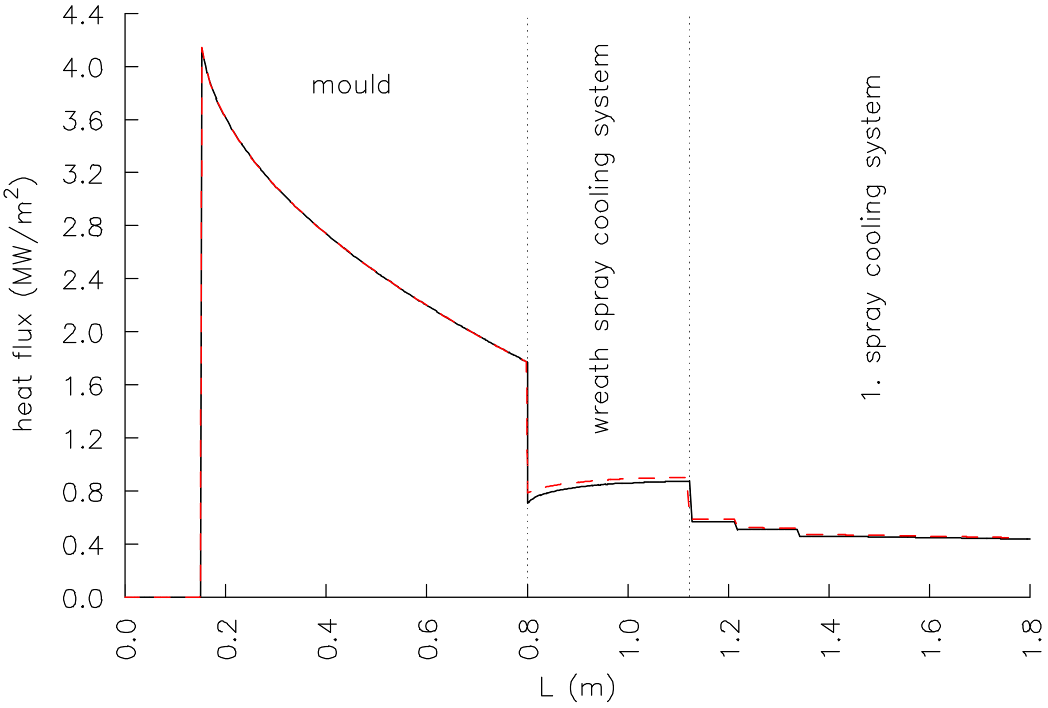

Figure 6.17: The heat flux at the surface. Solid black line: outer side. Red dashed line: inner side.

6.6 Numerical Examples

6.6.1 Simplified Model and Comparison with Fluent

The developed numerical model is verified by comparison with commercial software Fluent. Simplified boundary conditions and physical properties are used in order to reduce the unnecessary complexity of the verification process. The following simplifications are used in the geometry and boundary conditions:

- The steel level depth is set to $L_{level} = 0\,\mathrm{m}$. The SEN depth remains the same, i.e. $L_{depth} = 0.9\,\mathrm{m}$.
- The boundary conditions are simplified only at the outer and inner sides of the casting machine. They are changed to the Robin type, with the constant heat transfer coefficient in the mould $h_m = 2000\,\mathrm{W/(m^2K)}$ and in the secondary cooling system $h_s = 800\,\mathrm{W/(m^2K)}$.

The material properties are constant and equal for all phases. They are presented in Table 6.2. The casting speed and the casting temperature are equal to $u_{cast} = 1.75\,\mathrm{m/min}$ and $T_{cast} = 1800\,\mathrm{K}$, respectively. The inlet velocity of the molten steel in the SEN is $u_{y0} = -0.11667\,\mathrm{m/s}$, which corresponds to $\mathrm{Re} = 4900$ ($\Delta\ell = d_2$, see equation (5.10)). The node arrangement with 70861 nodes is generated in the same way as described in Section 6.2. The time step is set to $\Delta t = 2.5\cdot 10^{-4}\,\mathrm{s}$. The morphology constant in the Darcy's source terms is set to $C = 1.6\cdot 10^{8}\,\mathrm{m^{-2}}$. (in Fluent $10^6\,(\mathrm{N{\cdot}s{\cdot}m^{-4}})$ as the mushy zone constant).

Table 6.2: Simplified material properties.

property	value
ρ	$7200\,\mathrm{kg/m^3}$
λ	$30\,\mathrm{W/(m\,K)}$
c_p	$700\,\mathrm{J/(kg\,K)}$
T_S	$1680\,\mathrm{K}$
T_L	$1760\,\mathrm{K}$
h_m	$250000\,\mathrm{J/kg}$
μ_L	$0.006\,\mathrm{Pa{\cdot}s}$
β_T	$1\cdot 10^{-4}\,\mathrm{1/K}$

For Fluent solver, the mesh with 139200 quadrilateral cells is generated in Gambit software. The mesh is refined near the walls and around the SEN similar as in our numerical model. The generated mesh is represented in Figure 6.18, where the upper part of the mould with SEN is shown. The SIMPLE algorithm is chosen for the velocity-pressure coupling and the AKN turbulence model is set for the turbulence model. Fluent uses a simplified single-phase physical model to solve the fluid flow problems with the solidification. The involved equations have the same form as for the liquid phase, with additional Darcy's term in the momentum equations to account for the solidification effects. The momentum equations of the continuum mixture model are in the case of the constant density of all phases practically the same as in a single-phase model in Fluent. The only difference between our mixture model and a single-phase model in Fluent is found in the energy equation, where the convection term in the mixture formulation is a summation of the liquid and solid variables, multiplied by the liquid and solid fraction, respectively, i.e. $\nabla\cdot\left(\rho_S u_S h_S + \rho_L u_L h_L\right)$. While in Fluent, the convection term is a function of the single-phase variables, i.e. $\nabla\cdot\left(\rho u h\right)$. The time-averaging procedure of the convection term also brings differences in the resulting turbulent heat fluxes. Some differences of the heat transfer phenomena in the mushy zone are then anticipated, while in the pure liquid and pure solid zone, the equations of both formulations are the same.

The results are represented as profiles in the radial cross-section at different positions along the billet. The positions are measured as arc length from the top of the continuous casting machine. In Figures 6.19-6.22 the absolute velocity is represented, calculated with the present model and Fluent. The comparison shows very good agreement between both numerical models and methods. Of course, there are some differences, mainly because of using different turbulence models in each numerical model. We also represent the temperature profile in Figures 6.23-6.26 at the same locations as is presented for the absolute velocity. We arrive with the similar conclusions as for the absolute velocity, except at the regions near the wall, where large temperature gradients exist. Those differences are expected, since large heat fluxes are prescribed at the walls. However, we can get better agreement between both approaches by using a higher level of refinement near the walls. But on the other hand, finer arrangements require smaller time step, which can drastically increase the computational time. Another reason of observing these differences is found to be in the turbulent heat flux, which is different due to the differences in the formulations of the energy equation. In Figure 6.27 the temperatures at the surface along the billet are plotted, where the mentioned differences can be used to explain the mismatch of approximately 25 K between the results of the present method and Fluent. Additional differences in Figure 6.27 are found in the secondary cooling system, where much less meshless nodes are used as finite volumes in the Fluent. Definitely, better accuracy can be achieved in this region by using more nodes, but this leads to larger computational time to get the steady-state solution. With the present numerical method, the steady-state solution is achieved approximately in three days on platform HP xw9300 Workstation (see Section 5.1), starting from the initial conditions presented in Section 2.7. While in Fluent, the steady-state solution is obtained approximately in five days on the same platform. The computational time in Fluent can be reduced by finding an optimal value of the relaxation factors, or by using the standard k-ε turbulence model.

For a visual comparison, the absolute velocity and temperature fields are drawn. The absolute velocity is shown in Figure 6.29, where both results are drawn side-by-side. The shape of the liquid jet and the position of the re-circulating zones, obtained with the present method, are in a very good agreement with Fluent. In this figure, we also observe some anomaly at the end of the computational domain. The contours indicate that the length of the computational domain should be larger to satisfy the assumptions of the fully developed flow at the outlet. We repeated the simulation with a larger domain, i.e. $2.8\,\text{m}$, to justify the above claims. Figure 6.30 represents a comparison of the absolute velocity field between the simulations at different computational lengths. No differences are observed between both results, only at the outlet region, where the solution has no significance. The same conclusions are made for the temperatures at the surface along the billet, shown in Figure 6.28. To keep the computational time in the reasonable limits, the computational domain in all further simulations remains $1.8\,\text{m}$. The temperature field is shown in Figure 6.31, where the liquidus and solidus lines are plotted as well. We observe small instabilities of the temperature field around the jet, obtained by Fluent (centre picture in Figure 6.31). We tried to achieve better results by reducing the under-relaxation factors for the momentum equation and equations for the turbulent quantities, i.e. the turbulent kinetic energy and the dissipation rate. Latter on, we changed the discretization of the equations from the Second-Order upwind to Third-Order MUSCL. With the above tryouts, we did not get any improvements. However, with changing the turbulence model from LRN-AKN model to the standard k-ε, the instabilities disappear (right picture in Figure 6.31). But, with the standard k-ε model, the separation and reattachment positions are much different then in the case with LRN models. Despite the discussed instabilities, we perform the comparison with the results obtained with the AKN turbulence model, since the solution still converges to the steady-state.

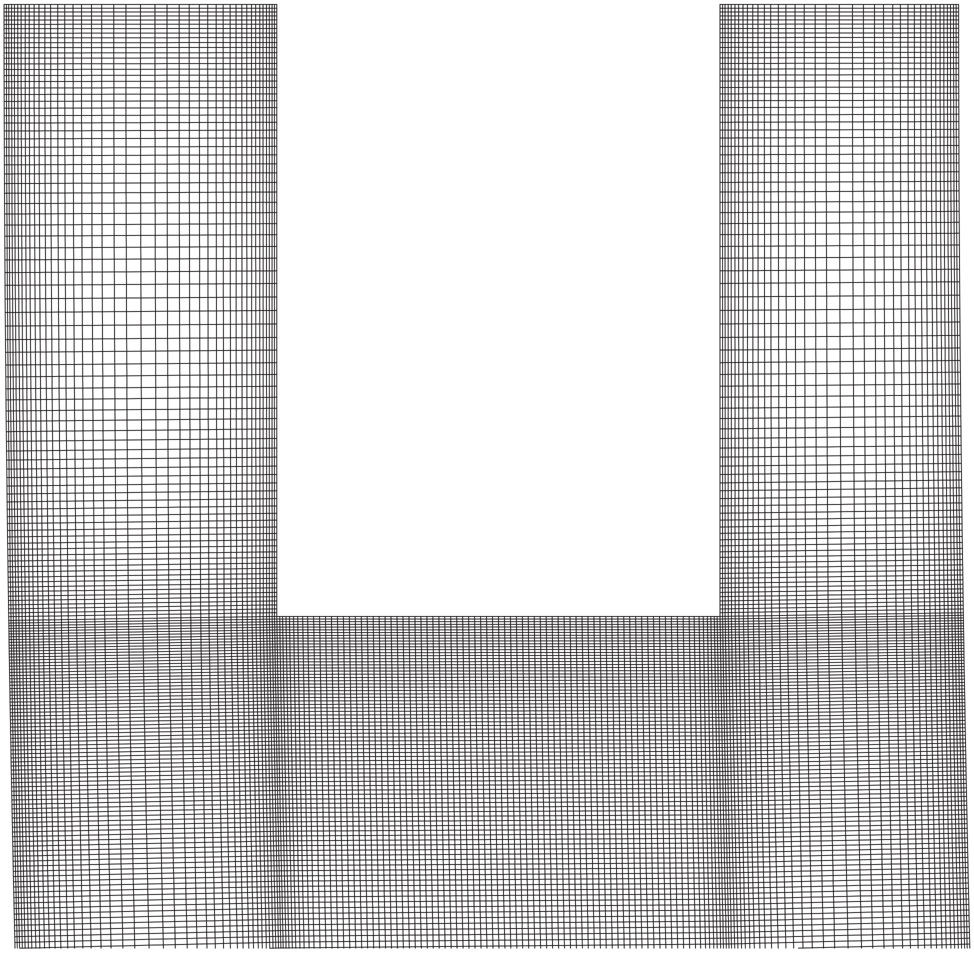

Figure 6.18: Mesh generated with the Gambit. A detail in the mould.

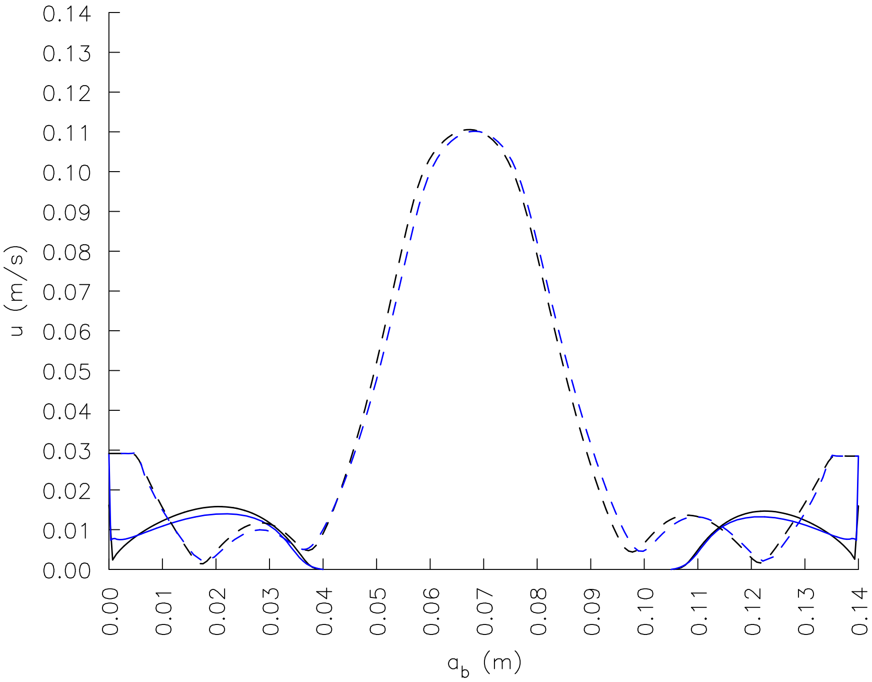

Figure 6.19: Solid lines: absolute velocity at the meniscus. Dashed lines: in the radial cross-section at the arc length 0.2 m. Black: present method. Blue: Fluent.

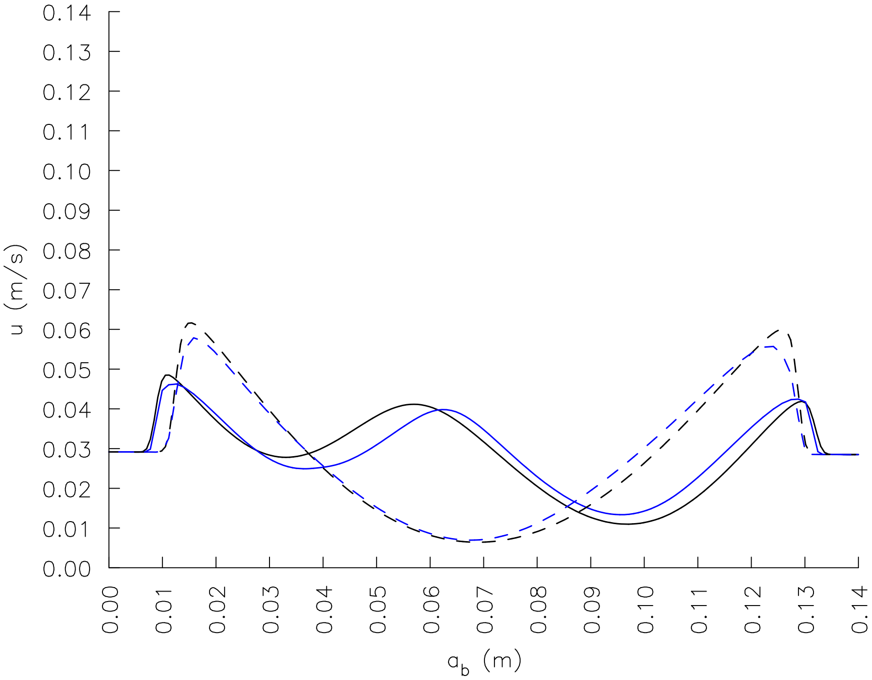

Figure 6.20: Solid lines: absolute velocity in the radial cross-section at the arc length 0.4 m. Dashed lines: at the arc length 0.6 m. Black: present method. Blue: Fluent.

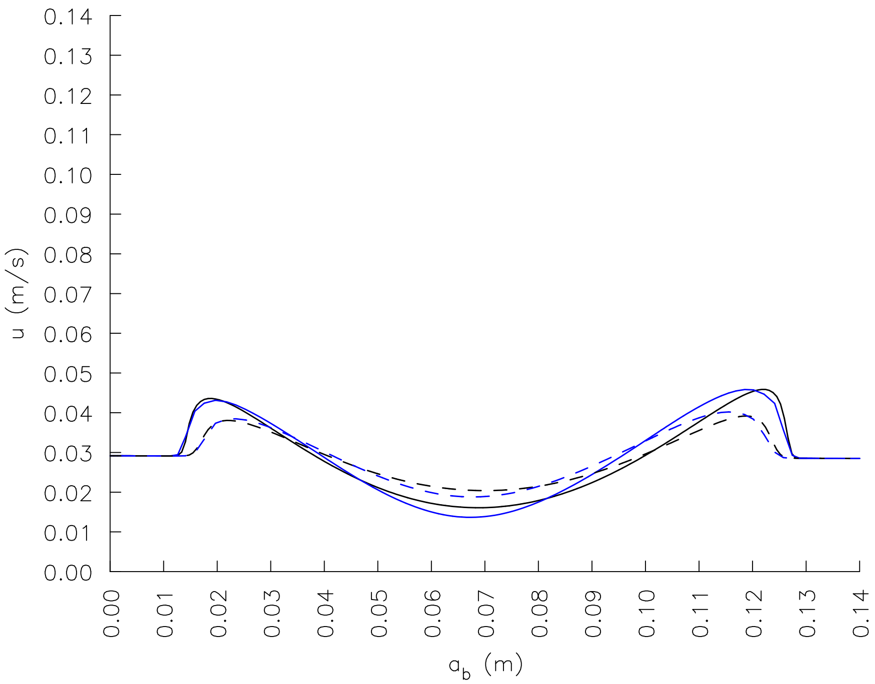

Figure 6.21: Solid lines: absolute velocity in the radial cross-section at the arc length 0.8 m. Dashed lines: at the arc length 1.0 m. Black: present method. Blue: Fluent.

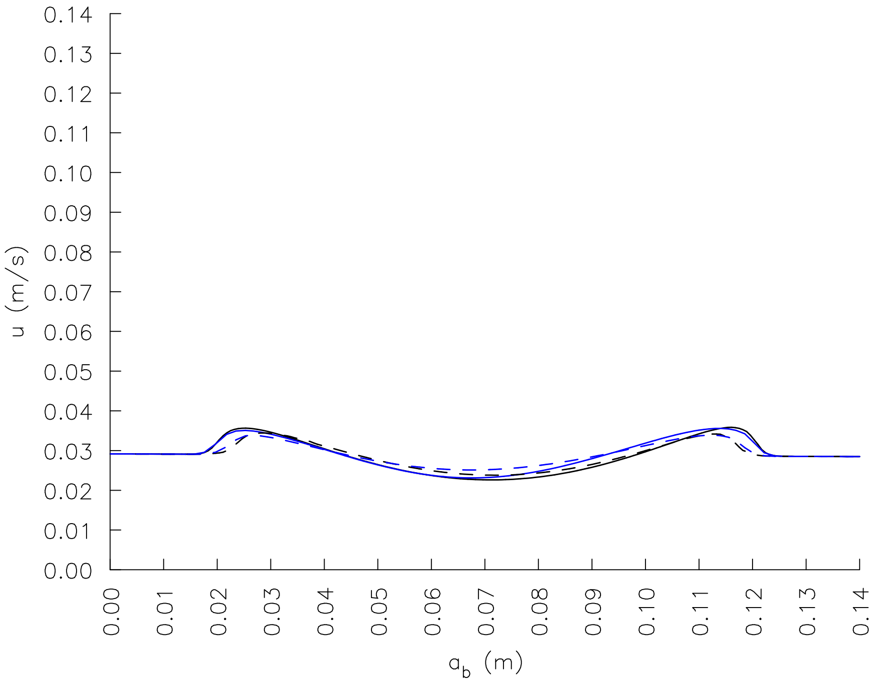

Figure 6.22: Solid lines: absolute velocity in the radial cross-section at the arc length 1.2 m. Dashed lines: at the arc length 1.4 m. Black: present method. Blue: Fluent.

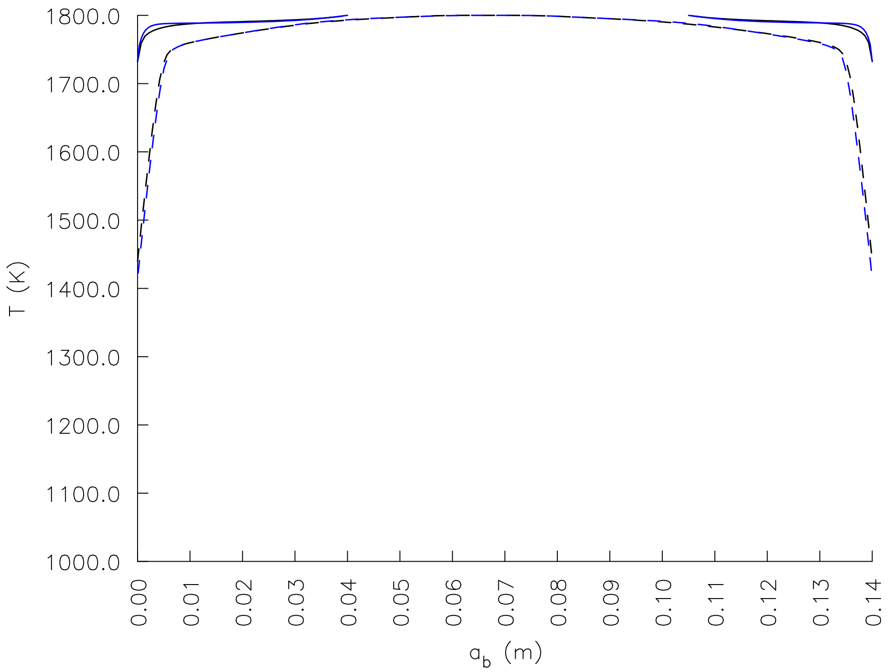

Figure 6.23: Solid lines: temperature profile at the meniscus. Dashed lines: in the radial cross-section at the arc length 0.2 m. Black: present method. Blue: Fluent.

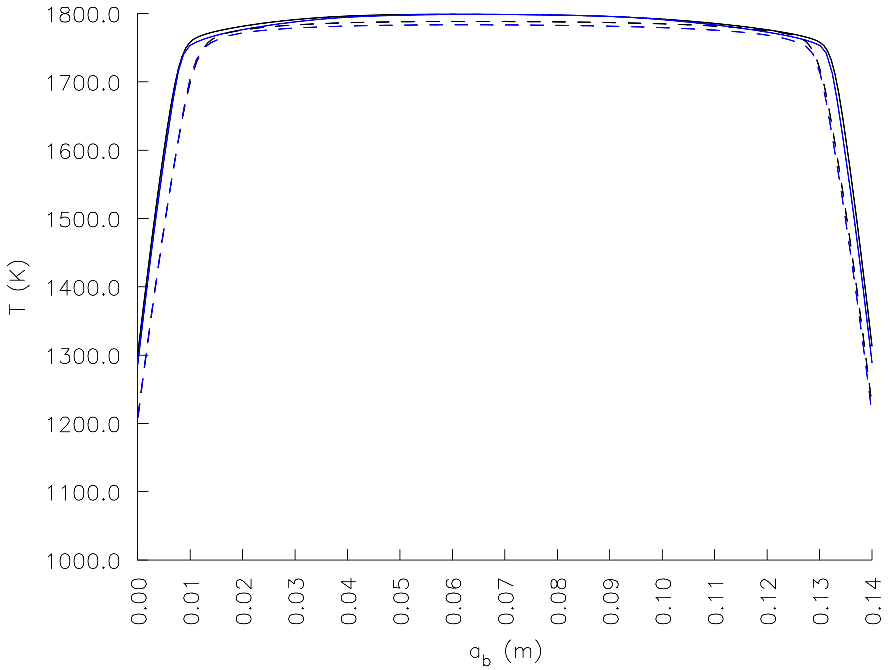

Figure 6.24: Solid lines: temperature profile in the radial cross-section at the arc length 0.4 m. Dashed lines: at the arc length 0.6 m. Black: present method. Blue: Fluent.

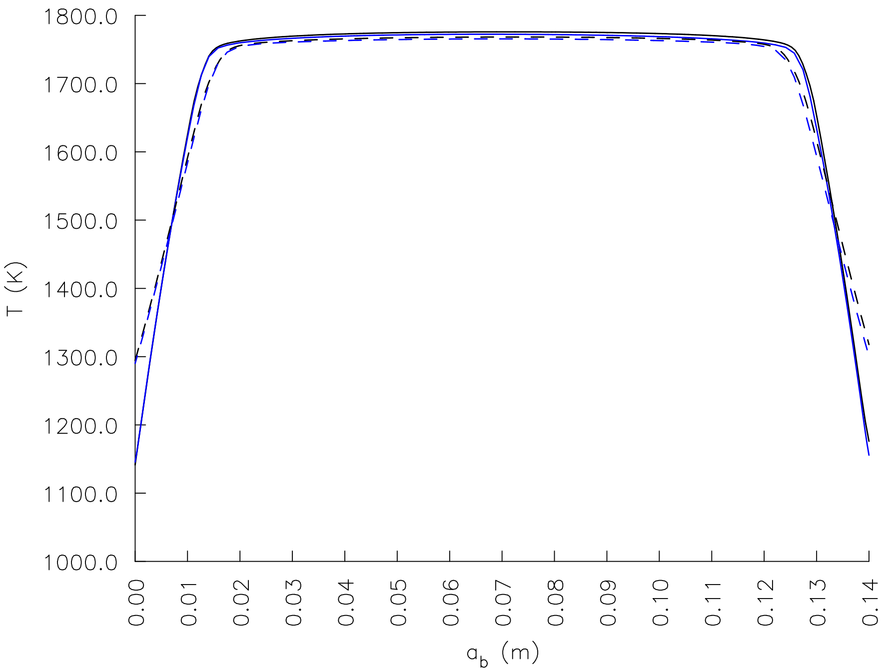

Figure 6.25: Solid lines: temperature profile in the radial cross-section at the arc length 0.8 m. Dashed lines: at the arc length 1.0 m. Black: present method. Blue: Fluent.

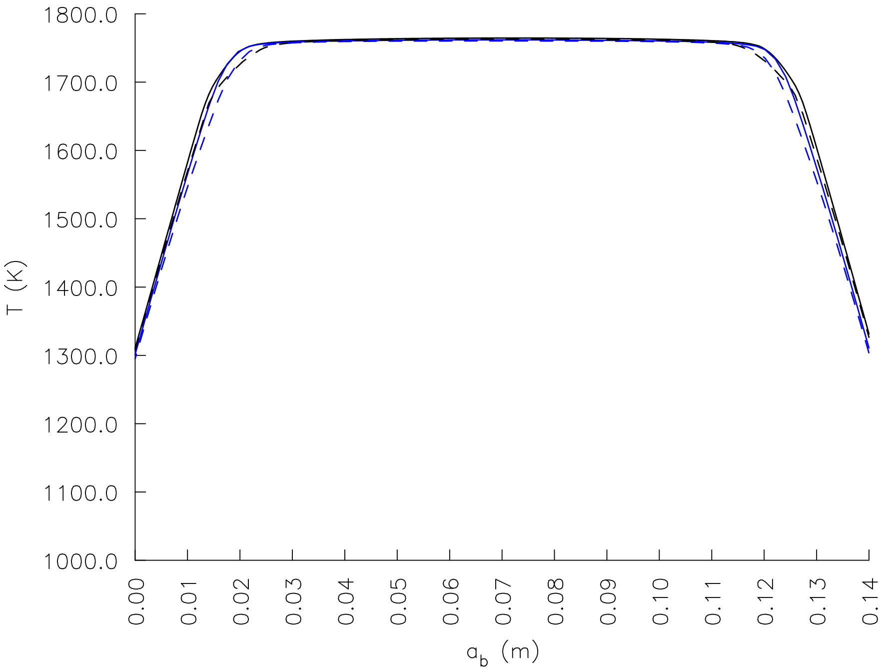

Figure 6.26: Solid lines: temperature profile in the radial cross-section at the arc length 1.2 m. Dashed lines: at the arc length 1.4 m. Black: present method. Blue: Fluent.

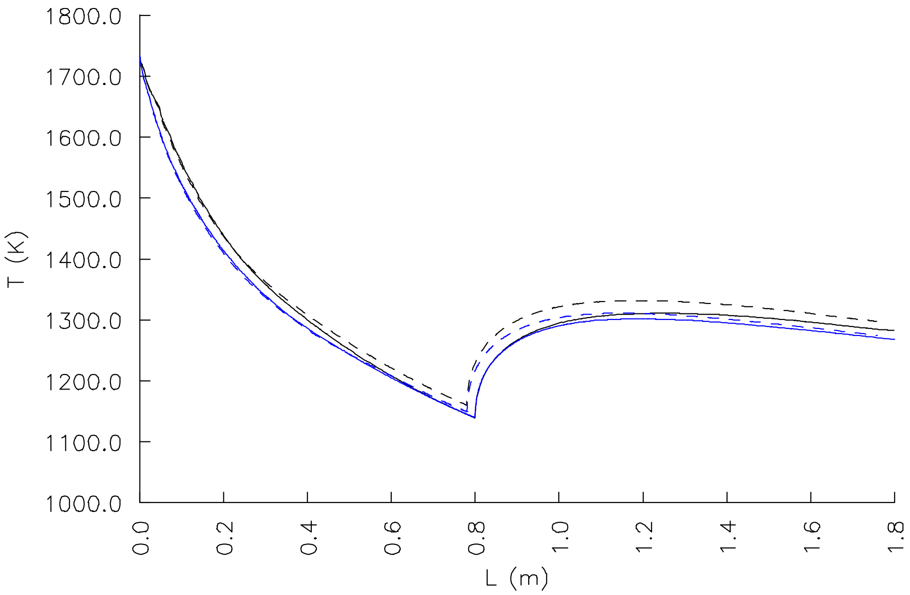

Figure 6.27: Temperature of the surface along the billet. Solid lines: outer side. Dashed lines: inner side. Black: present method. Blue: Fluent.

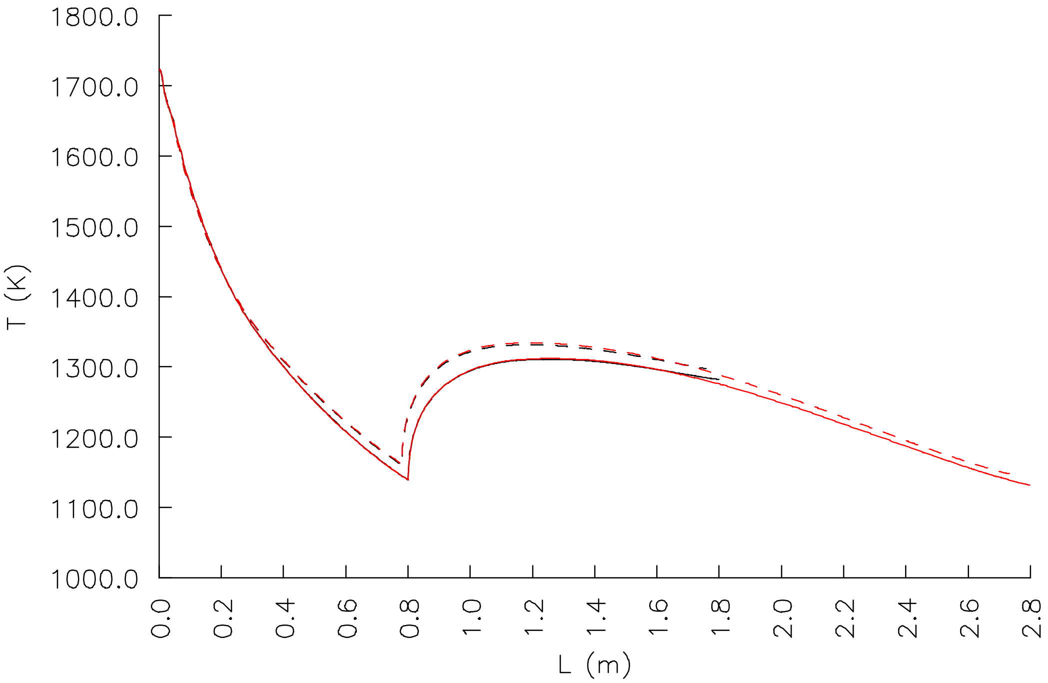

Figure 6.28: Temperature of the surface along the billet with the present method. Black lines: billet length $1.8\,\mathrm{m}$. Red lines: billet length $2.8\,\mathrm{m}$. Solid lines: outer side. Dashed lines: inner side.

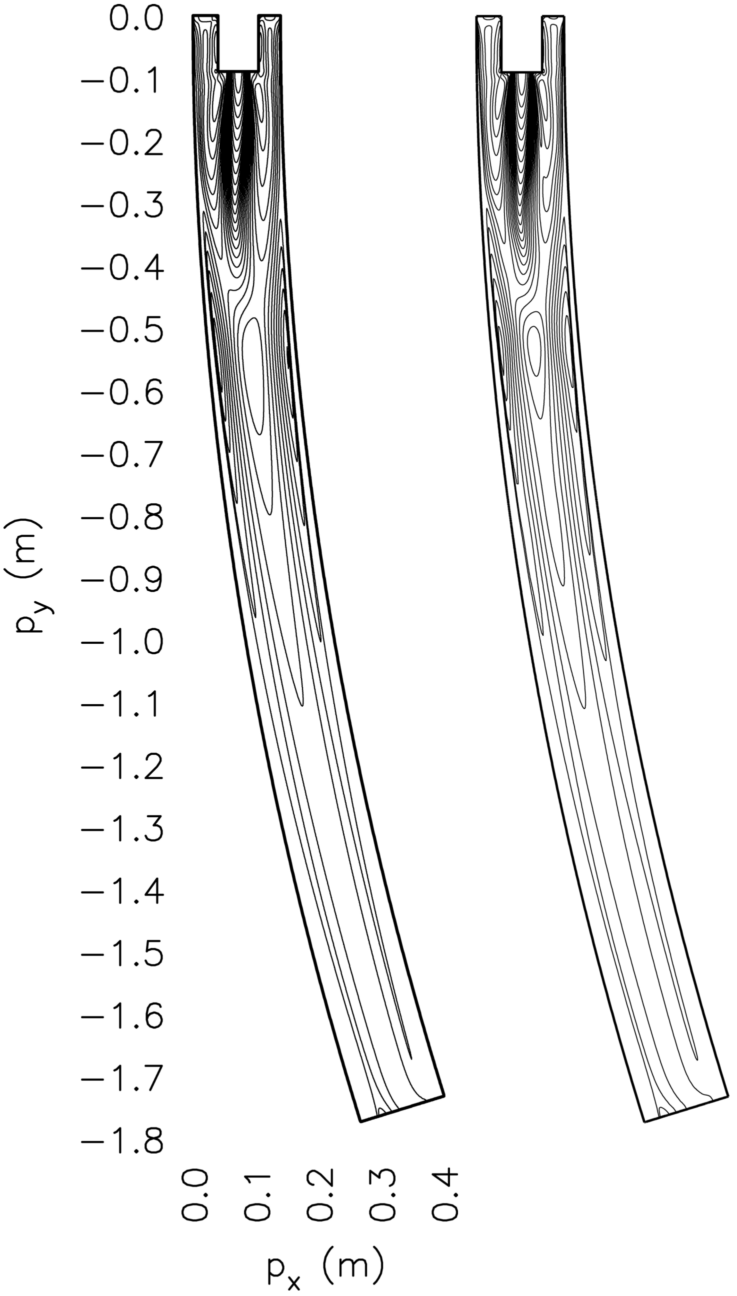

Figure 6.29: Absolute velocity field in the billet of length 1.8 m. Left: present model. Right: Fluent. Contours represent values between 0 m/s and 0.137 m/s with step 0.00685 m/s.

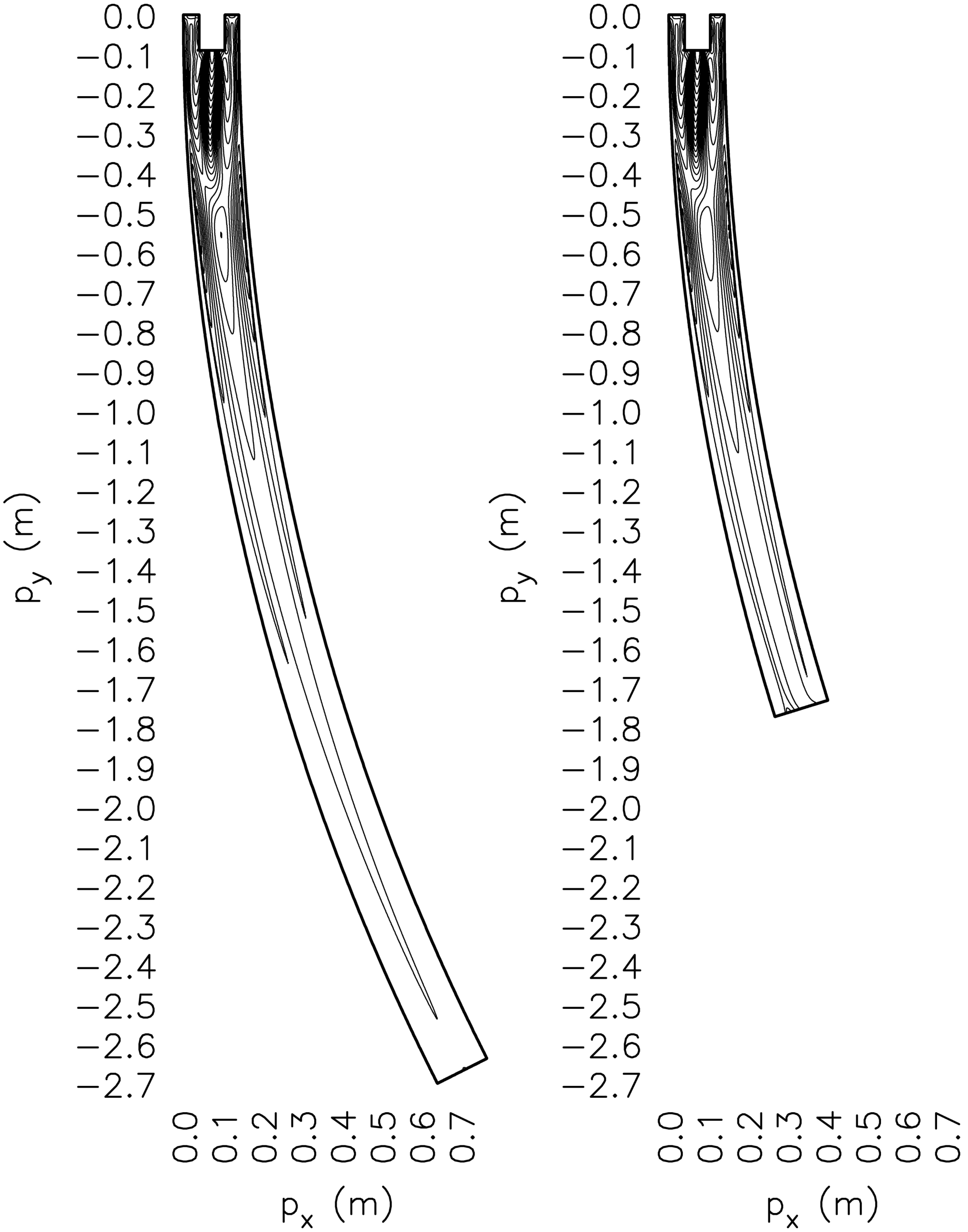

Figure 6.30: Absolute velocity field in the billet. Left: billet length 2.8 m. Right: billet length 1.8 m. Contours represent values between 0 m/s and 0.137 m/s with step 0.00685 m/s.

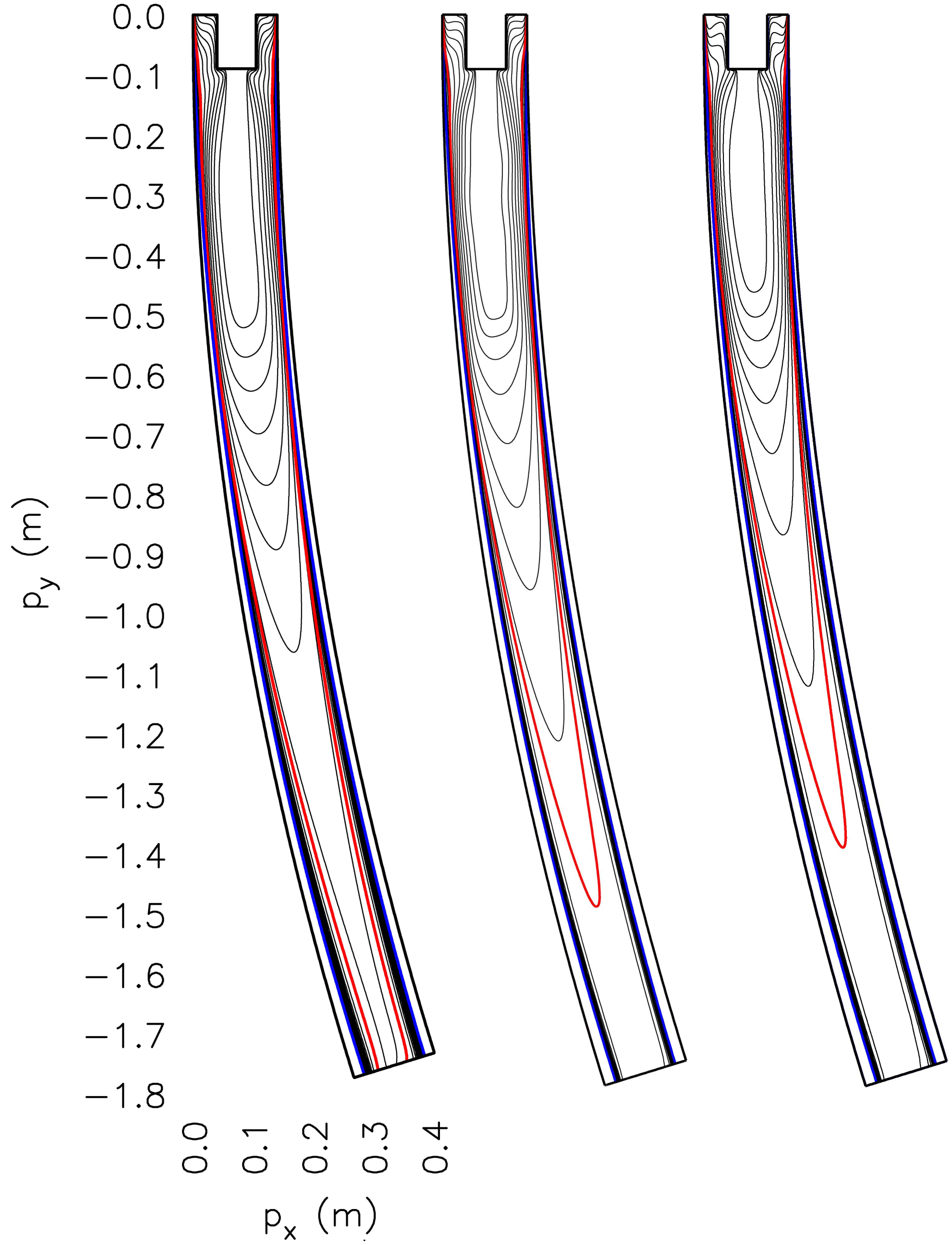

Figure 6.31: Temperature field in the billet. Left: present model. Center: Fluent-AKN. Right: Fluent-standard k-ε. Red line: liquidus temperature. Blue line: solidus temperature. Isotherms represent temperatures between 1680 K and 1800 K with step 5 K.

6.6.2 Simulation of the C45 Steel Grade

Simulations of the velocity and temperature fields in the billet of the C45 steel grade with the real process parameters, used in the Štore Steel continuous casting machine are presented. The material properties are taken from JMatPro, and they are graphically represented in Section 6.3. The chemical composition of the steel is represented in Table 6.3. The calculated material properties are exported into DAT format file, from which the properties are loaded into our numerical model. The thermal expansion β_T and dynamic viscosity μ are constant and taken from the previous test. The process parameters for the mentioned steel grade are taken directly from the Štore Steel technological program, which are believed to be the best known optimal process parameters of the casting process. The actual values are given in Table 6.4.

The procedure of the node arrangement generation is already presented in Section 6.2, where the generated node arrangement is shown in Figures 6.3 and 6.4. The morphology constant in the Darcy's source terms is set to $C = 1.6 \cdot 10^8\,\mathrm{m}^{-2}$. The absolute velocity field is shown in Figures 6.32 and 6.33. The molten steel flows from the SEN into the mould in a vertical direction. Just under the SEN, the liquid jet of the steel starts to obey the curved geometry of the casting machine. A flow separation occurs, which causes the molten steel to move upwards. The upward flow moves around the SEN to the meniscus, and then turns into downward direction. We can observe from Figure 6.33, that larger amount of the molten steel is flowing upward between the SEN and the inner side of the mould. The reason is in the position and the geometry of the SEN, which pour the molten steel onto the outer side of the mould and leaves more space for upward flow near the inner side of the mould. Under the mould, the flow direction of the liquid core almost completely obeys the curvature of the casting machine. The flow separation of the molten steel generates several re-circulating zones. Their size and position are shown in the Figure 6.34, where the streamlines are plotted. The streamlines with red colour represent the upward flow, and the streamlines with the blue colour the downward flow.

The temperature field is presented in Figures 6.35 and 6.36, where also the contours of the solidus and liquidus temperatures are plotted. The size of the mushy zone is very small, since the selected material C45 solidifies over a small temperature range, i.e. $\approx 80\,\mathrm{K}$. Also the liquid fraction, shown in Figure 6.7, indicates very rapid solidification. From Figures 6.35 and 6.36, higher temperatures near the inner side are observed. The reason is in the flow phenomena in the mould, where a larger amount of the molten steel flows upwards near the inner side. An actual temperature difference between the inner and the outer side of the billet is shown in Figure 6.37.

An important safety parameter for the engineers in the casting plant is the shell-thickness at the end of the mould. Its value can be obtained from the liquid fraction, plotted in Figure 6.38. Thickness at the outer side is equal $0.12\,\mathrm{m}$, and at the inner side $0.09\,\mathrm{m}$.

The results of this test are used further as the reference solution in analyzing the effects of various process parameters.

Table 6.3: Composition of the C45 steel grade.

	Al	Cr	Cu	Mn	Mo	Ni
wt %	0.0275	0.2000	0.1250	0.5500	0.0500	0.2000
	Si	V	C	P	S	
wt %	0.2750	0.0250	0.4600	0.0150	0.0125	

Table 6.4: Process parameters of the Štore Steel continuous casting machine.

property	description	value
u_{cast}	casting speed	$1.75\,\mathrm{m/min}$
T_{cast}	casting temperature	$1534\,^{\circ}\mathrm{C}$
$\dot{q}_w$	flow rate in wreath spray cooling system	$23\,\mathrm{l/min}$
$\dot{q}_s$	flow rate in first spray cooling system	$53\,\mathrm{l/min}$

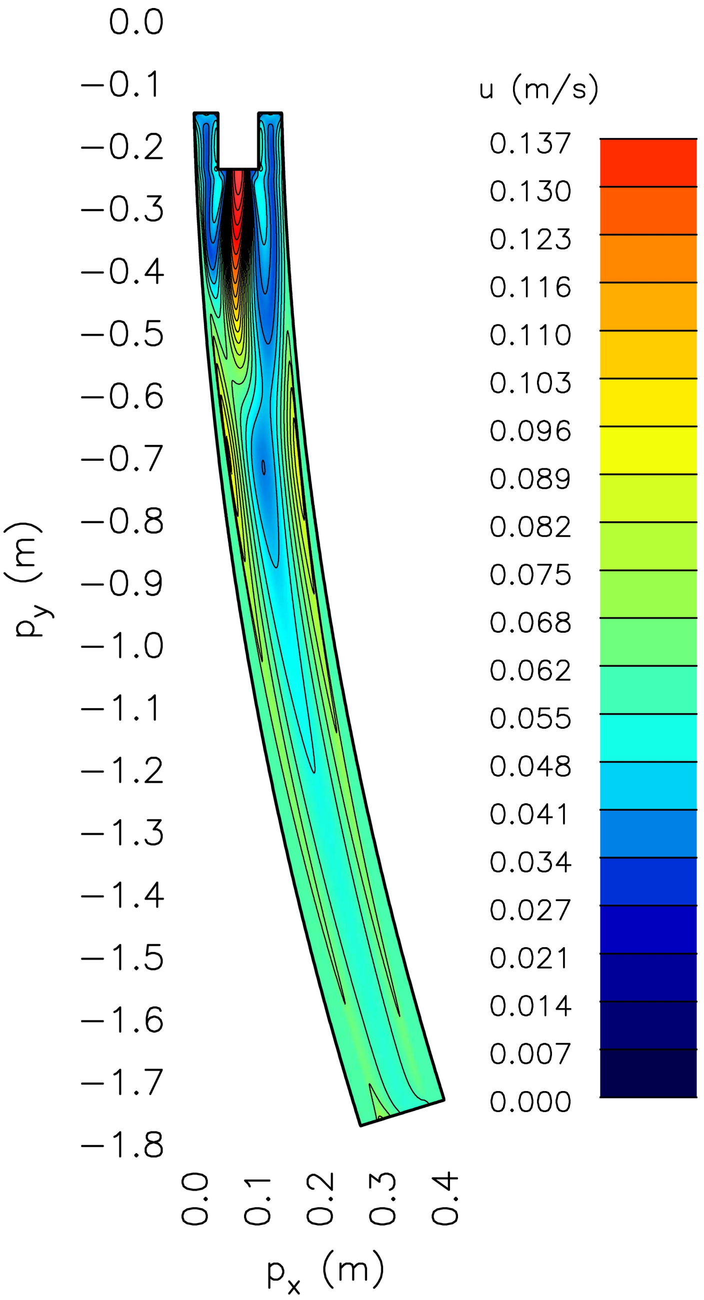

Figure 6.32: Absolute velocity field in the billet. Each line in the legend represents a contour level.

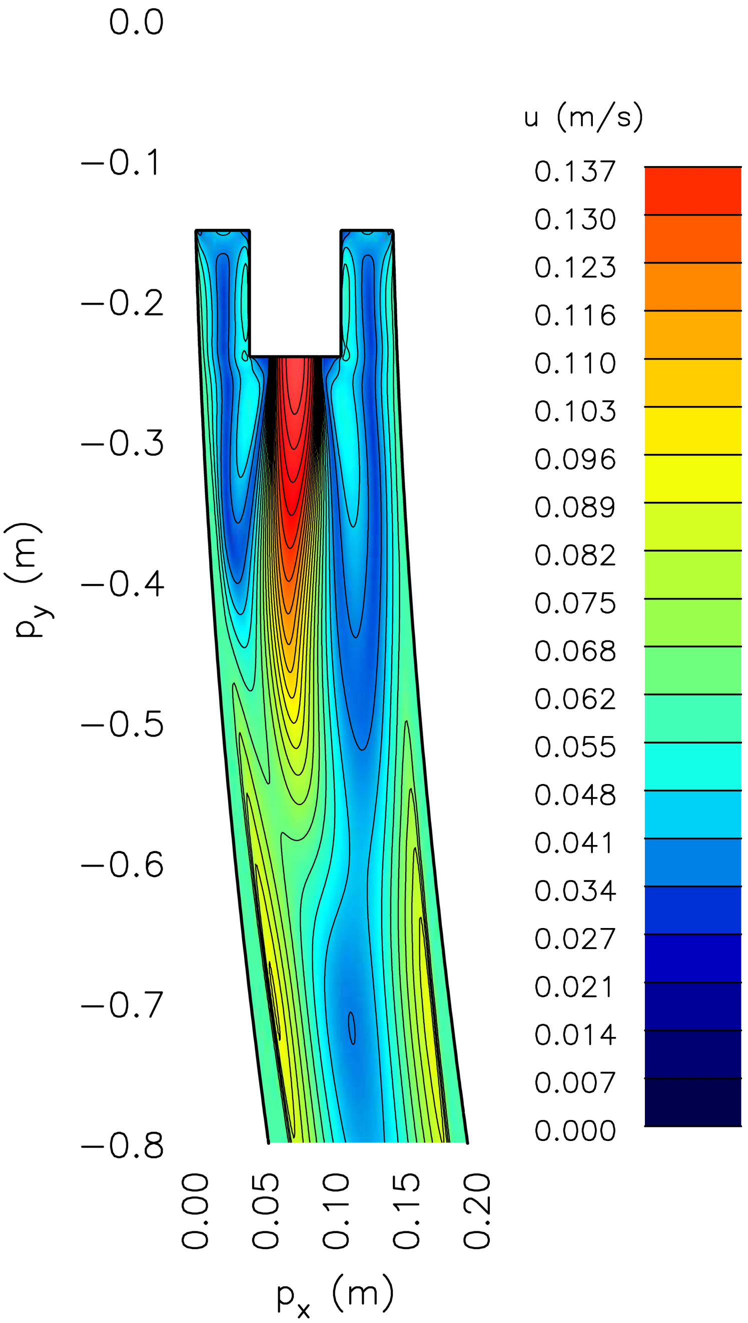

Figure 6.33: Absolute velocity field in the mould. Each line in the legend represents a contour level.

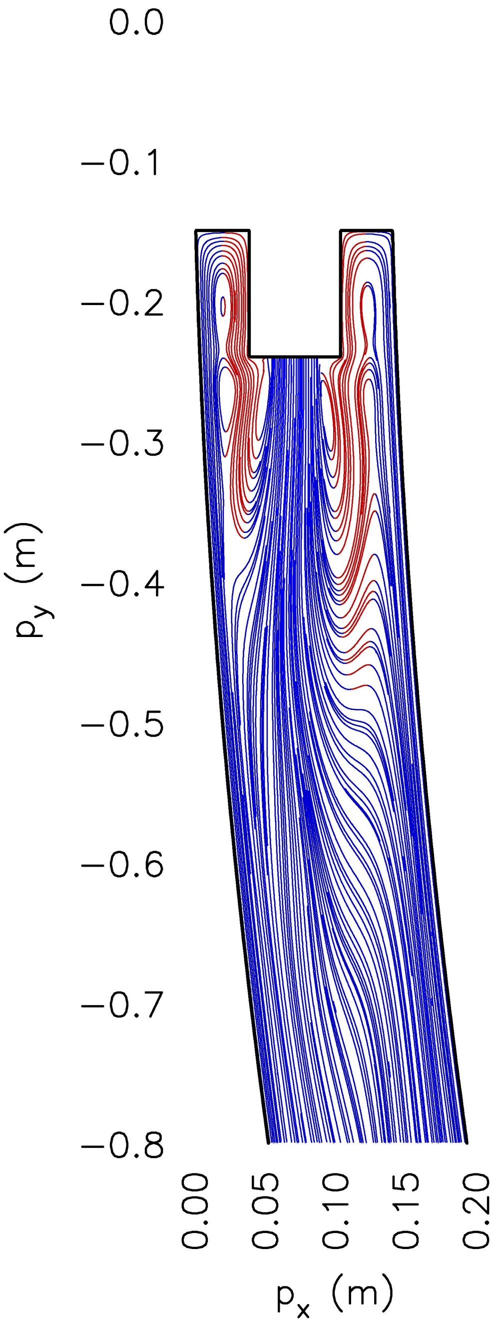

Figure 6.34: Streamlines in the mould. Blue lines: downward flow. Red lines: upward flow.

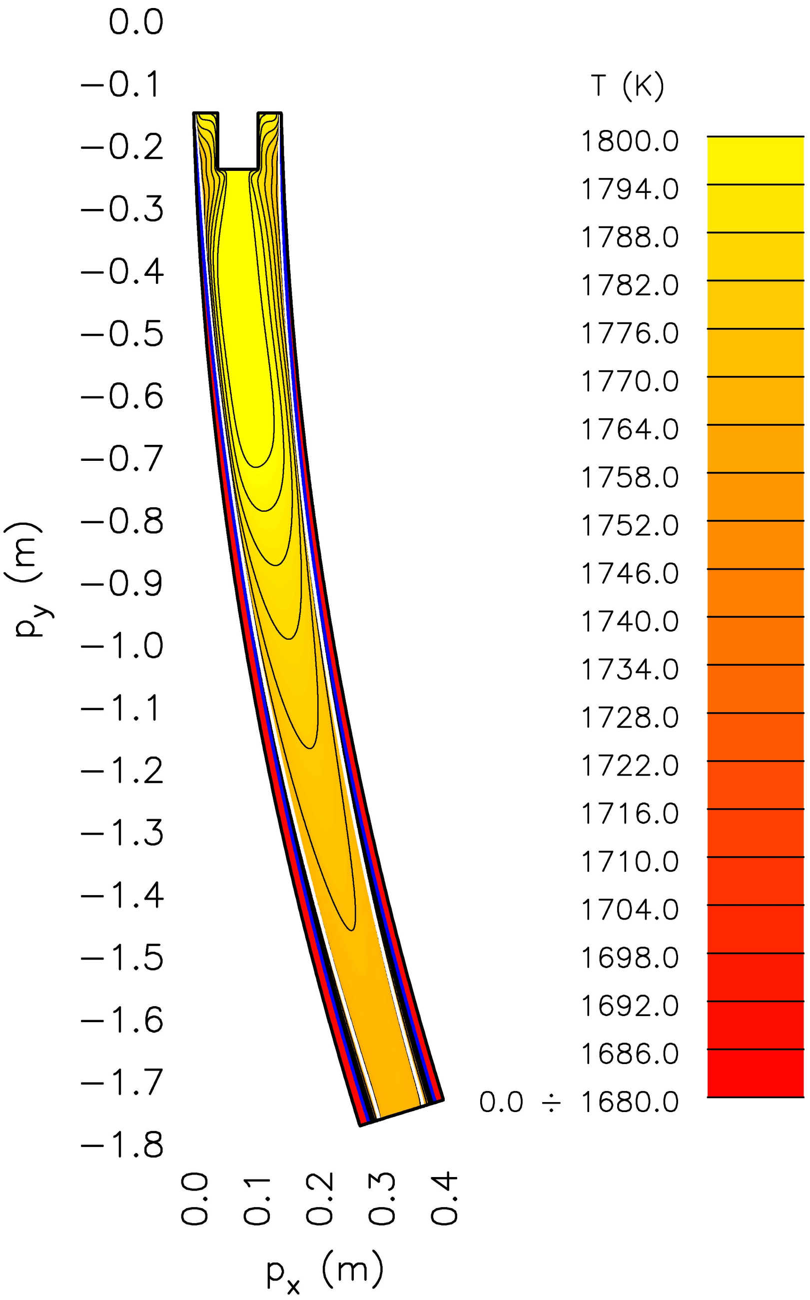

Figure 6.35: Temperature field in the billet. Each line in the legend represents a contour level. Blue contour line: solidus temperature. White contour line: liquidus temperature.

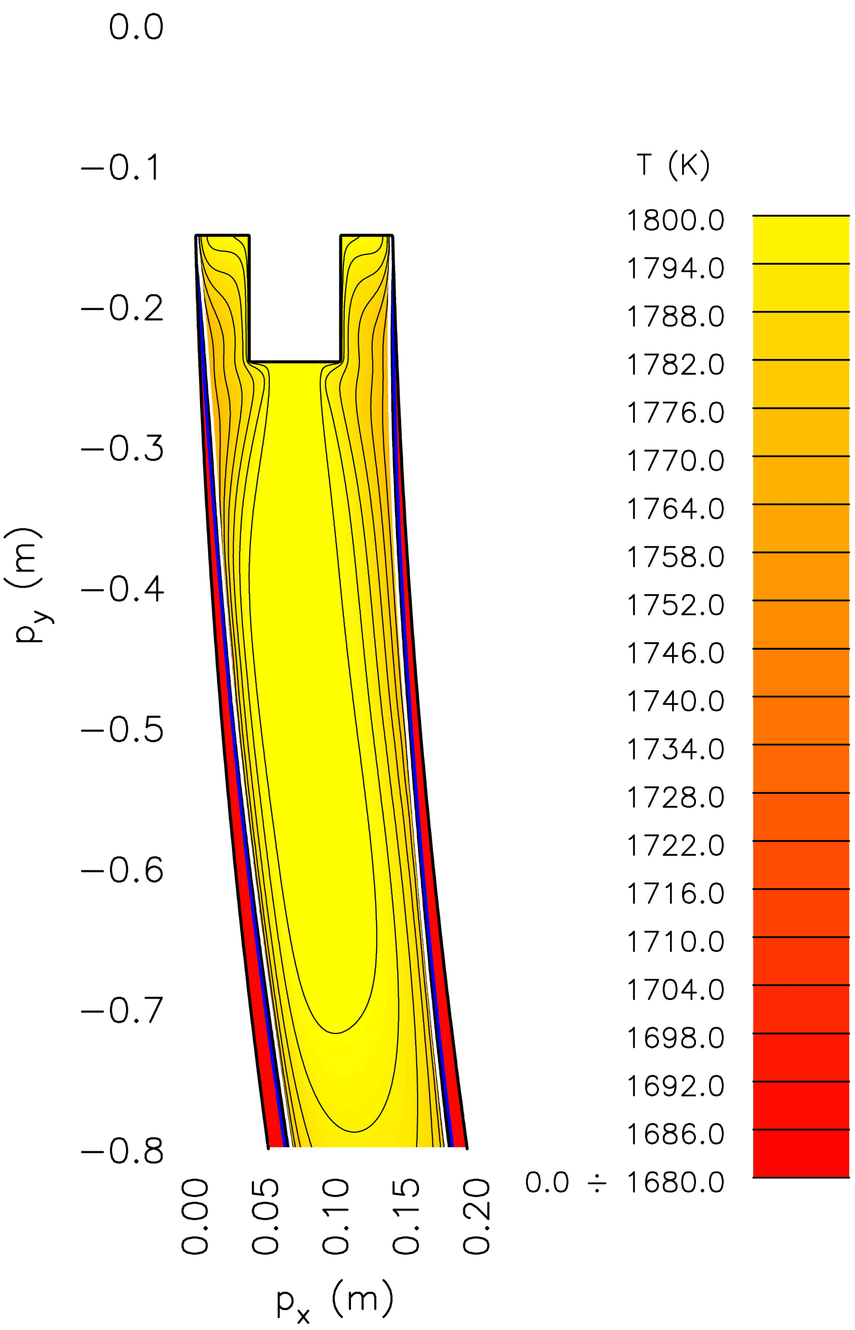

Figure 6.36: Temperature field in the mould. Each line in the legend represents a contour level. Blue contour line: solidus temperature. White contour line: liquidus temperature.

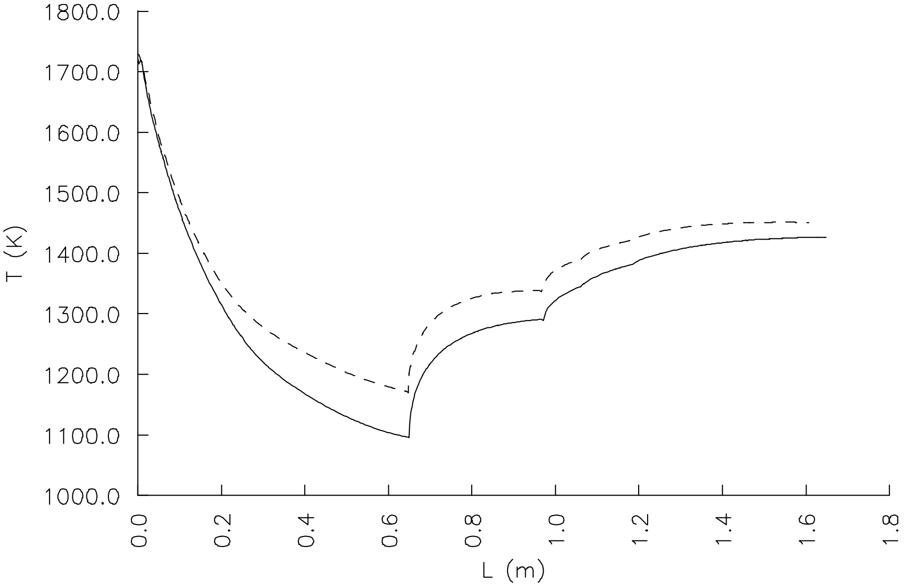

Figure 6.37: Temperature along the surface of the billet. Solid line: outer surface. Dashed line: inner surface.

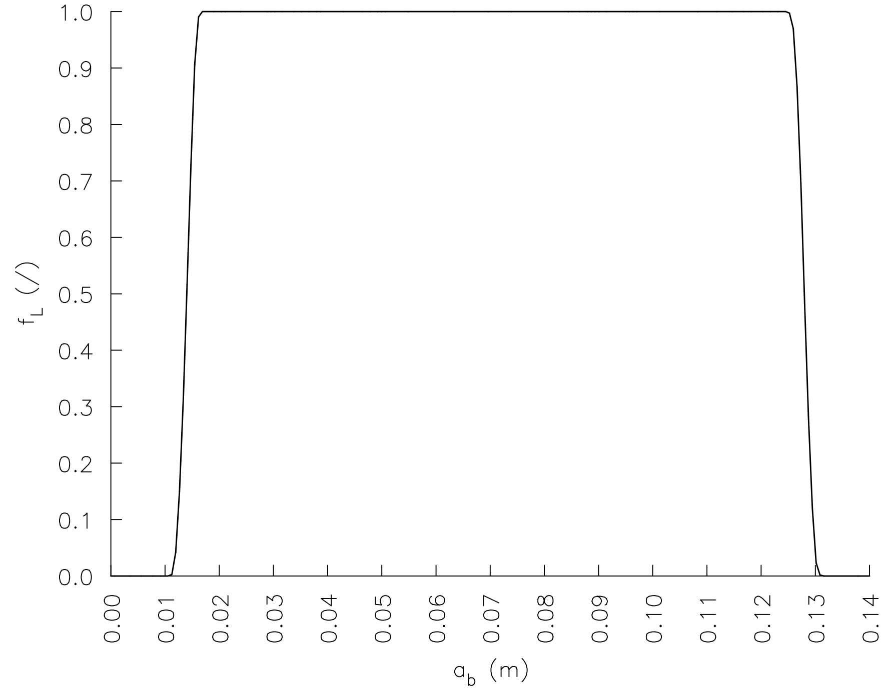

Figure 6.38: Liquid fraction profile in the radial cross-section at the end of the mould.

6.6.2.1 Sensitivity of the Darcy’s Constant

The morphology constant in the Darcy’s source terms greatly influences the final solution of the velocity and temperature fields. If the value of the constant is very large, the velocity in the mushy zone quickly becomes equal to the casting speed. This means that the pores of the permeable structure are very small and prevent the liquid material to move through the structure. The size of the pores is defined as the distance between the secondary dendrite arms.

In this test, the effect of the Darcy’s constant on the velocity and temperature field is analysed. The reference solution is solved with the $C = 1.6 \cdot 10^{8}\,\mathrm{m}^{-2}$. The related results are represented in the previous test. We repeated the same simulation with the Darcy’s constant $C = 1.6 \cdot 10^{9}\,\mathrm{m}^{-2}$ and $1.6 \cdot 10^{10}\,\mathrm{m}^{-2}$.

The Darcy’s term in the momentum equation prevents the fluid flow in the mushy zone to move in the upward or other directions and forces the liquid phase to move with the casting speed in the casting direction. The Darcy’s term becomes stronger or dominant if the Darcy’s constant is enhanced, and can prevail over other body forces in the momentum equation, such as buoyancy force. In Figure 6.39, the absolute velocity field at different Darcy’s constant is presented. The differences in the flow behaviour of the liquid jet can be observed, which is at $C = 1.6 \cdot 10^{10}\,\mathrm{m}^{-2}$ more oriented and extended in the casting direction as in the case with $C = 1.6 \cdot 10^{8}\,\mathrm{m}^{-2}$. Due to the extension of the liquid jet, the temperature field in the liquid core is higher, as shown in Figure 6.40. The opposite effects can be found for the surface temperature along the billet, as shown in Figure 6.41. The surface temperature is decreasing with the increased Darcy’s constant. The reason is in the mushy zone, where a larger amount of the material is moving in the casting direction with the casting speed.

However, because the mushy zone is relatively small, the effect of the Darcy’s constant is also very moderate. It is hard to say which value of the constant is more appropriate due to the lack of detailed knowledge of solidification phenomena in the mushy zone.

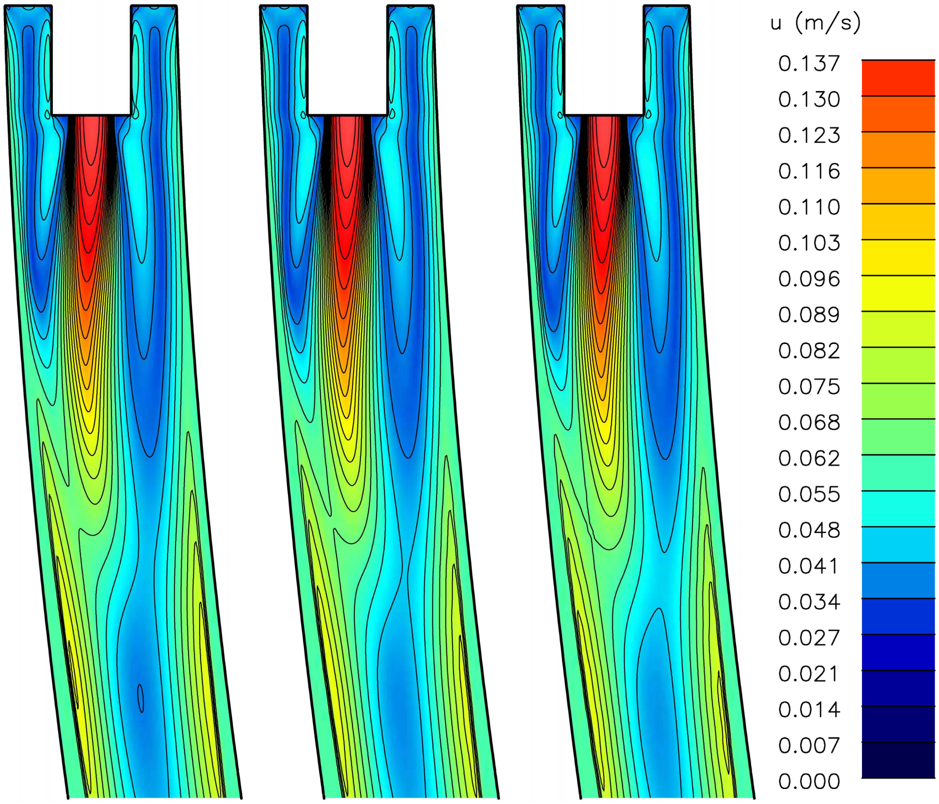

Figure 6.39: Absolute velocity field in the mould as a function of the Darcy's constant. Left: $C = 1.6 \cdot 10^8$ m^{-2}. Centre: $C = 1.6 \cdot 10^9$ m^{-2}. Right: $C = 1.6 \cdot 10^{10}$ m^{-2}.

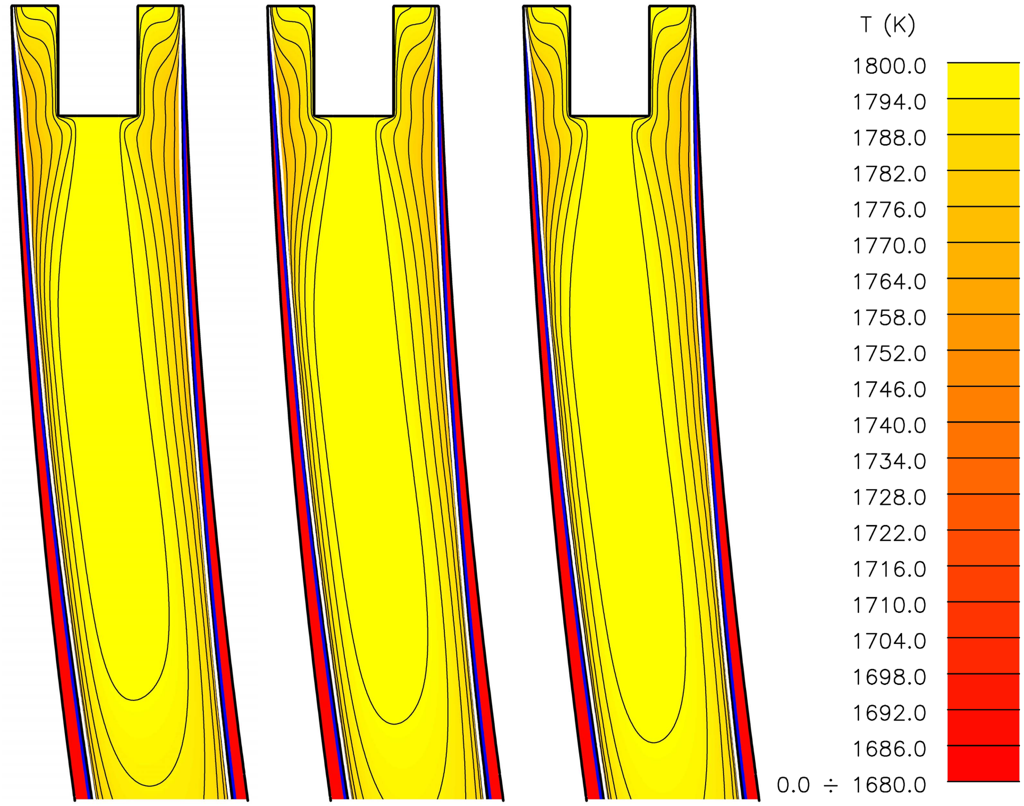

Figure 6.40: Temperature field in the mould as a function of the Darcy's constant. Left: $C = 1.6 \cdot 10^{8}\,\mathrm{m}^{-2}$. Centre: $C = 1.6 \cdot 10^{9}\,\mathrm{m}^{-2}$. Right: $C = 1.6 \cdot 10^{10}\,\mathrm{m}^{-2}$.

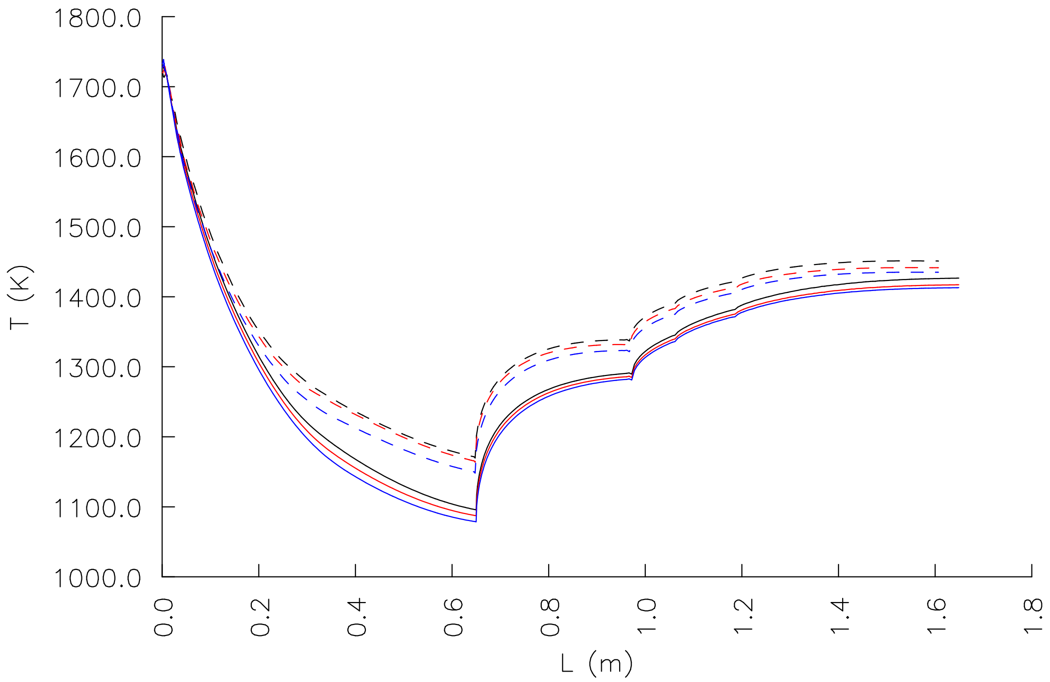

Figure 6.41: Surface temperature along the billet as a function of the Darcy's constant. Black: $C = 1.6 \cdot 10^{8}\,\mathrm{m}^{-2}$. Red: $C = 1.6 \cdot 10^{9}\,\mathrm{m}^{-2}$. Blue: $C = 1.6 \cdot 10^{10}\,\mathrm{m}^{-2}$. Solid lines: outer side. Dashed lines: inner side.

6.6.2.2 Simulation at Different Casting Speed

One of the most important process parameters in the continuous casting is the casting speed, which means the drawing speed of the strand through the casting machine. Among other process parameters, finding the optimal value of the casting speed is a crucial part for each steel grade. Its optimal value is usually a compromise between the highest production rate and the required quality of the casted billet. The engineers in the steel plant are trying to increase the production rate of the casting process, but they are limited by the desired quality of the steel. However, the casting speed is a process parameter, which can be controlled during the process, and can be used for regulation of the casting process. This means that, if one of the process parameters, which cannot be controlled during the process (such as the casting temperature of the molten steel), a compensation can be made by changing the casting speed. The effect of the casting speed with increasing and decreasing its value by $0.1\,\mathrm{m/min}$ is analysed.

In Figure 6.42, the absolute velocity field in the mould as a function of the casting speed is shown. With increasing of the casting speed, the liquid jet is extended in the casting direction. Because of the extension of the liquid jet, the velocity of the upward flow is higher. Also, the flow separation occurs at lower positions, and therefore larger re-circulating zones are obtained. Those effects can be seen in Figure 6.43, where the streamlines are plotted.

The variations in the casting speed have a strong effect on the temperature field in the billet, shown in Figure 6.44. With the increased casting speed, the smaller heat flux between the steel and the mould is presented, and therefore the temperature at the surface is higher. The surface temperatures along the billet are plotted in Figure 6.45. The opposite effect is observed for the shell thickness (see Figure 6.46), where a larger thickness is obtained at the lower casting speed.

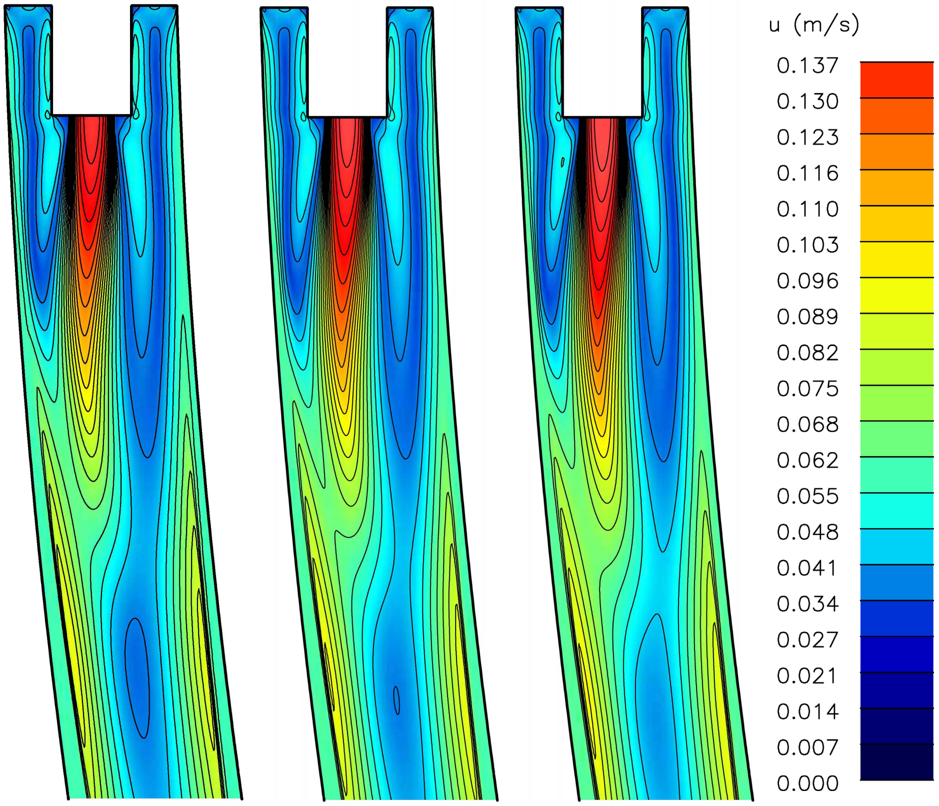

Figure 6.42: Absolute velocity field in the mould as a function of the casting speed. Left: $u_{cast} = 0.0275\,\mathrm{m/s}$ (1.65 m/min). Centre: $u_{cast} = 0.02916\,\mathrm{m/s}$ (1.75 m/min). Right: $u_{cast} = 0.03083\,\mathrm{m/s}$ (1.85 m/min).

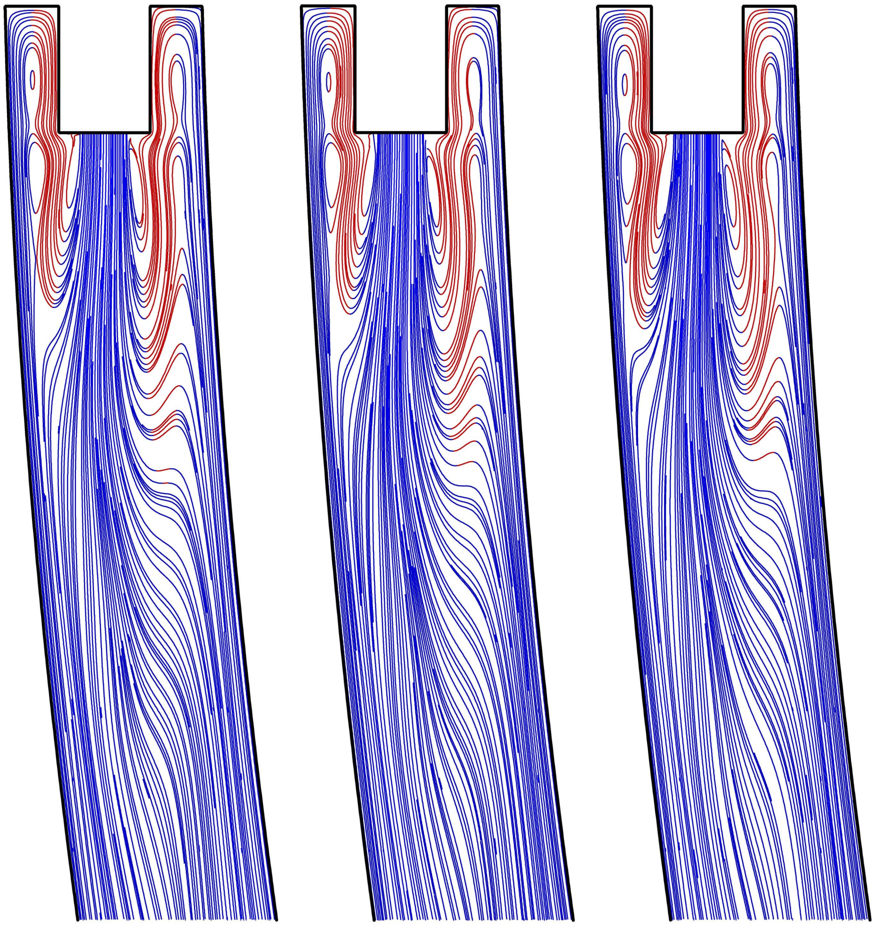

Figure 6.43: Streamlines in the mould as a function of the casting speed. Left: $u_{cast} = 0.0275$ m/s (1.65 m/min). Centre: $u_{cast} = 0.02916$ m/s (1.75 m/min). Right: $u_{cast} = 0.03083$ m/s (1.85 m/min).

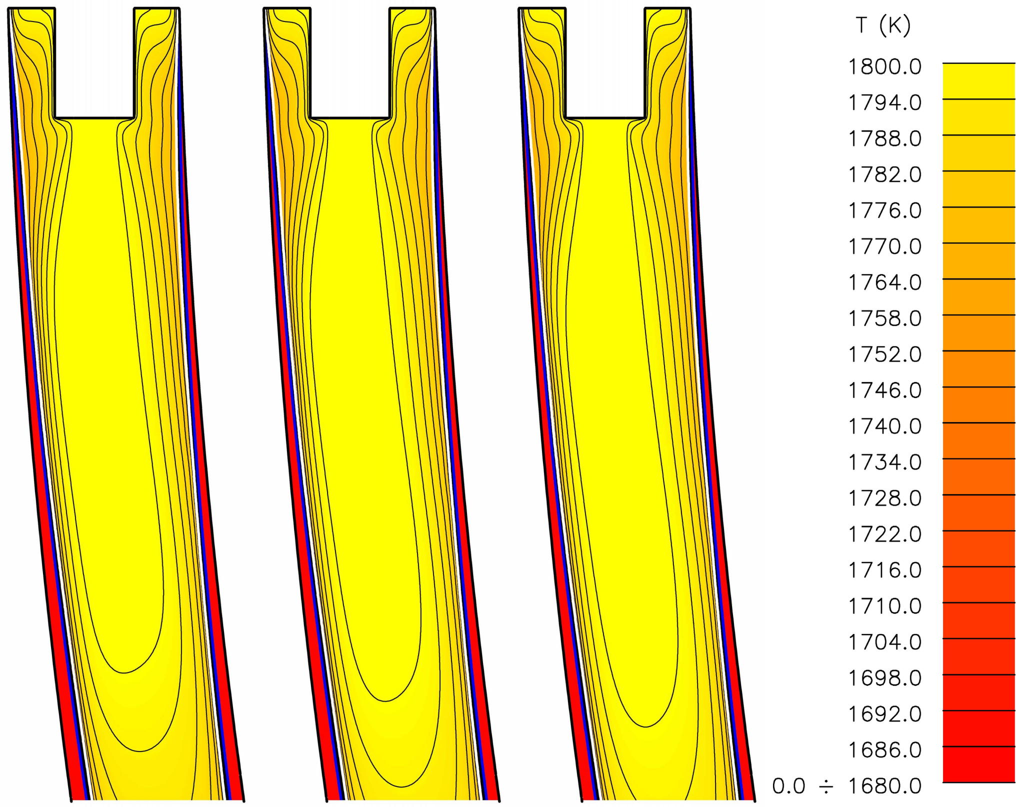

Figure 6.44: Temperature field in the mould as a function of the casting speed. Left: $u_{cast} = 0.0275\,\mathrm{m/s}$ $(1.65\,\mathrm{m/min})$. Centre: $u_{cast} = 0.02916\,\mathrm{m/s}$ $(1.75\,\mathrm{m/min})$. Right: $u_{cast} = 0.03083\,\mathrm{m/s}$ $(1.85\,\mathrm{m/min})$.

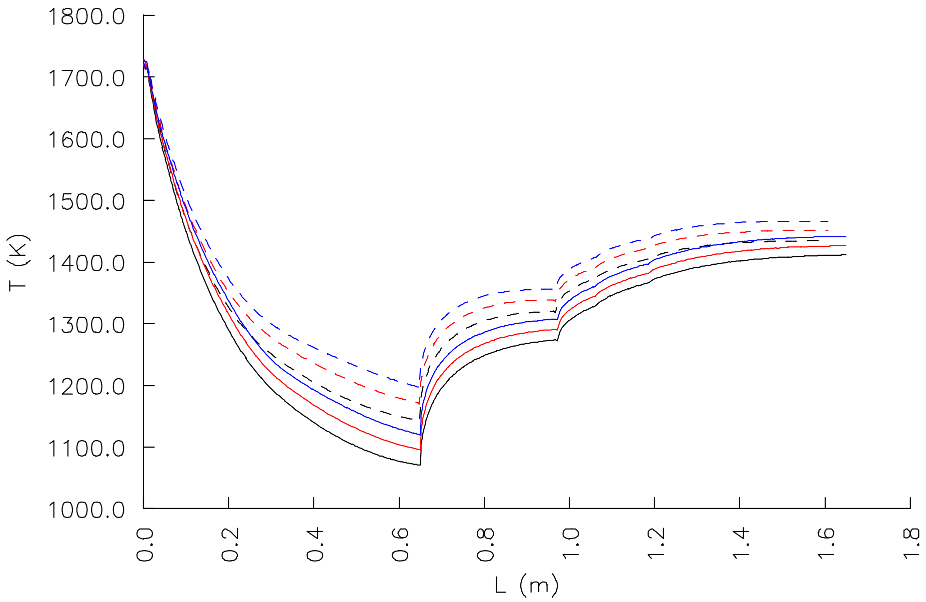

Figure 6.45: Surface temperature along the billet as a function of the casting speed. Black: $u_{cast} = 0.0275$ m/s (1.65 m/min). Red: $u_{cast} = 0.02916$ m/s (1.75 m/min). Blue: $u_{cast} = 0.03083$ m/s (1.85 m/min). Solid lines: outer side. Dashed lines: inner side.

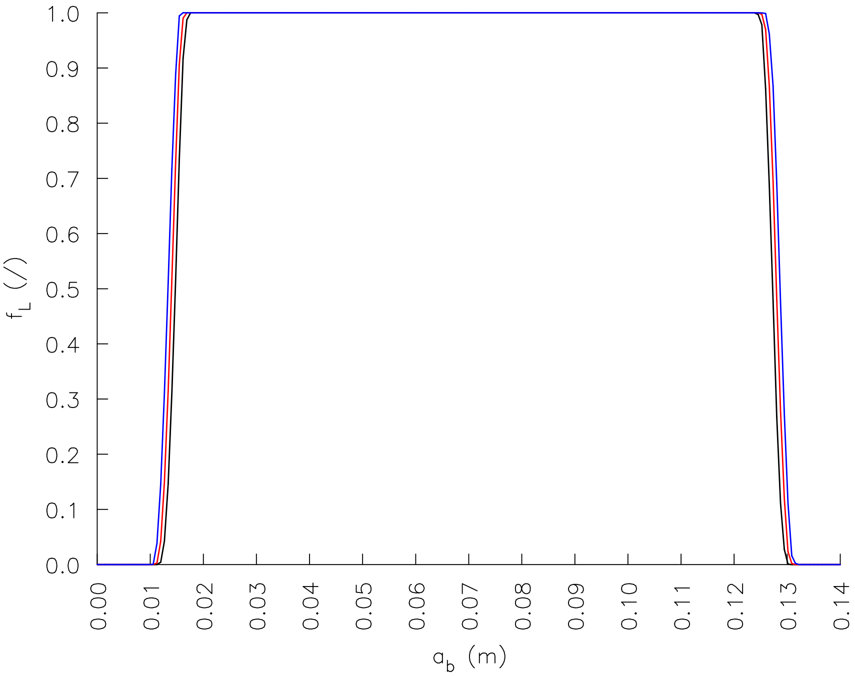

Figure 6.46: Liquid fraction profile in the radial cross-section at the end of the mould as a function of the casting speed. Black: $u_{cast} = 0.0275$ m/s (1.65 m/min). Red: $u_{cast} = 0.02916$ m/s (1.75 m/min). Blue: $u_{cast} = 0.03083$ m/s (1.85 m/min).

6.6.2.3 Simulation at Different Casting Temperature

The casting temperature, i.e. the temperature of the molten steel pouring from the SEN, is a process parameter, changing between the casting processes, and can very hardly be controlled and kept constant during the process. However, this parameter has a strong effect on the velocity and temperature fields in the mould. The results, obtained with the increased and decreased casting temperature by 10 K are presented.

In Figures 6.47 and 6.48, the absolute velocity field and streamlines in the mould are shown, respectively. We can observe that the casting temperature has influence on the velocity field in the mould. For example, if the casting temperature is raised, the solidification starts (when the temperature is equal to the liquidus temperature) later than in the case with the reference casting temperature (see Figures 6.49 and 6.51). This results in the expanded liquid core and lower velocity of the molten steel in the liquid core, compared to the reference test case. The expansion of the liquid core and its effect on the temperature field are very well visible in Figure 6.49. The surface temperatures are shown in Figure 6.50, where the temperatures are higher due to the expansion of the liquid core. The influence on the shell thickness at the end of the mould is presented in Figure 6.51.

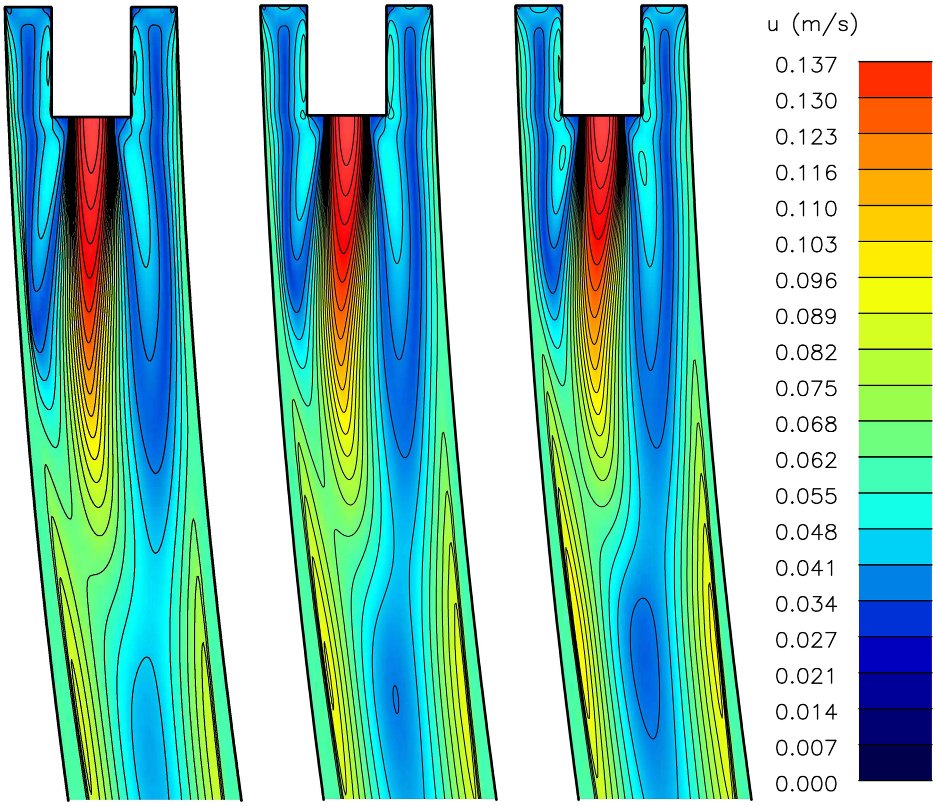

Figure 6.47: Absolute velocity field in the mould as a function of the casting temperature. Left: $T_{cast} = T_{cast0} - 10$ K. Centre: reference T_{cast}. Right: $T_{cast} = T_{cast0} + 10$ K.

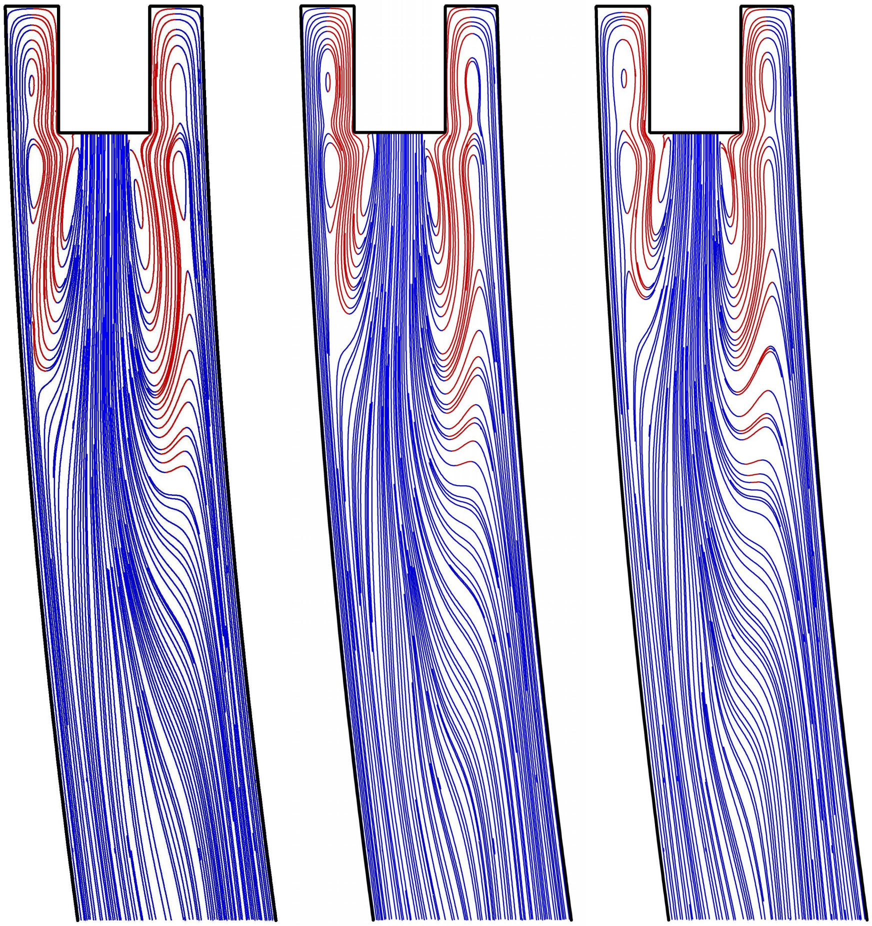

Figure 6.48: Streamlines in the mould as a function of the casting temperature. Left: $T_{cast} = T_{cast0} - 10$ K. Centre: reference T_{cast}. Right: $T_{cast} = T_{cast0} + 10$ K.

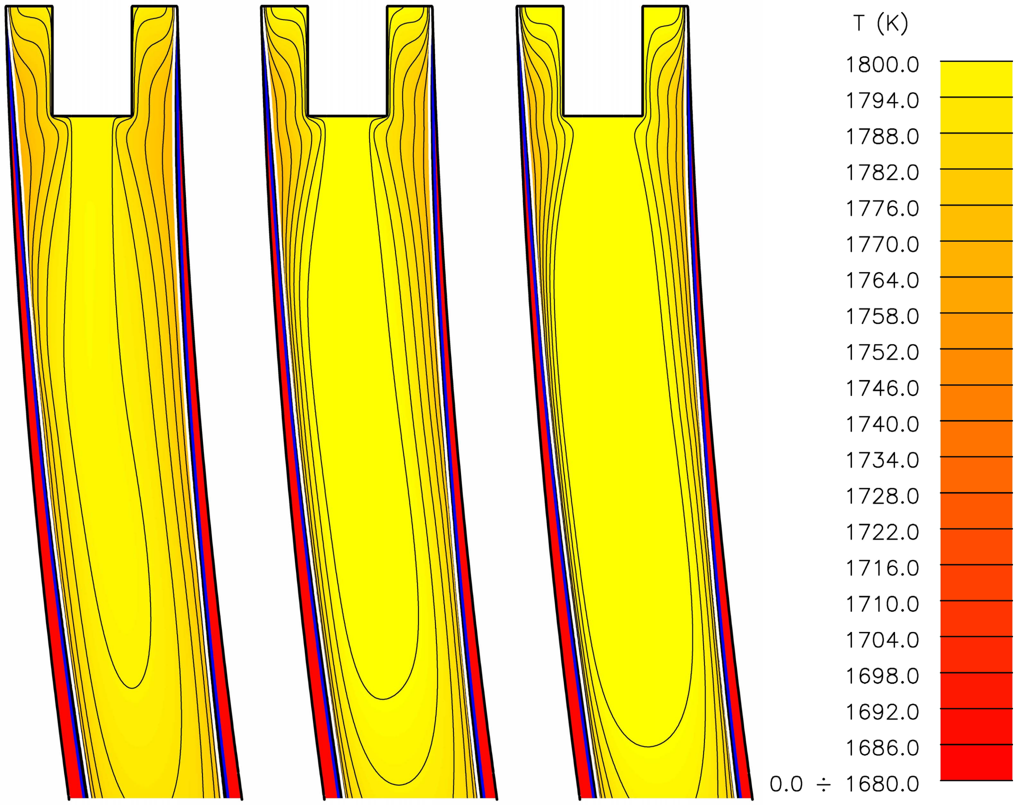

Figure 6.49: Temperature field in the mould as a function of the casting temperature. Left: $T_{cast} = T_{cast0} - 10$ K. Centre: reference T_{cast}. Right: $T_{cast} = T_{cast0} + 10$ K.

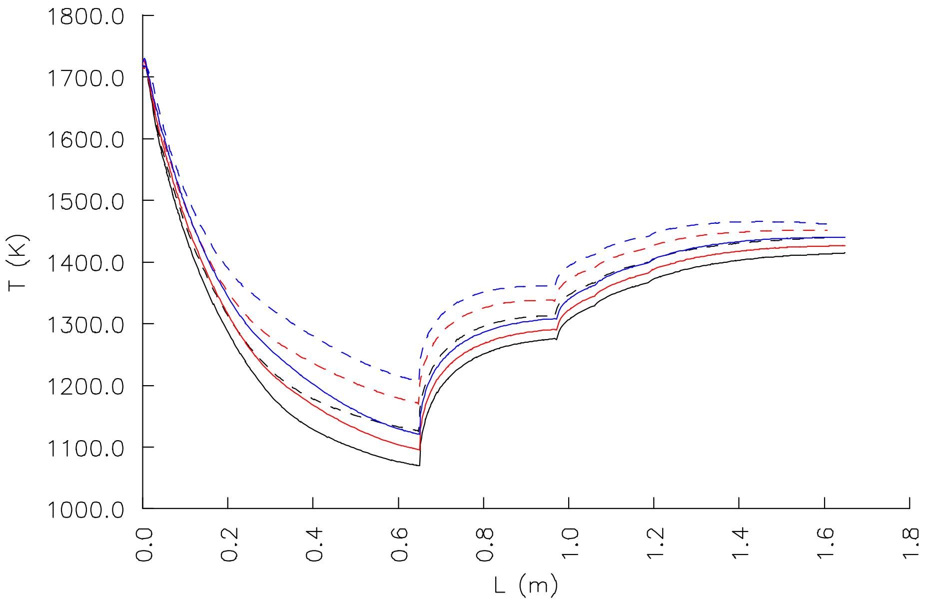

Figure 6.50: Surface temperature along the billet as a function of the casting temperature. Black: $T_{cast} = T_{cast0} - 10$ K. Red: reference T_{cast}. Blue: $T_{cast} = T_{cast0} + 10$ K. Solid line: outer side. Dashed line: inner side.

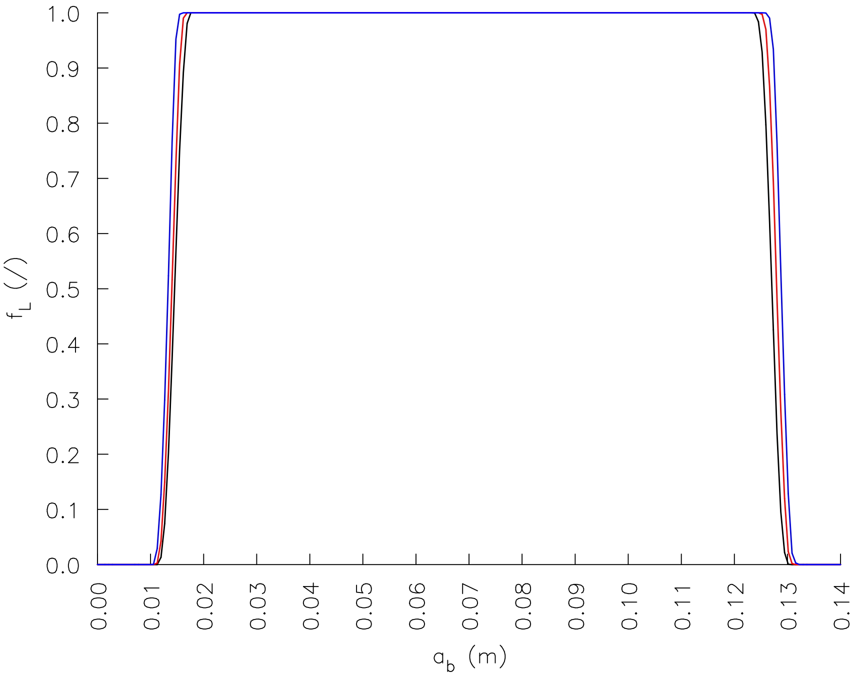

Figure 6.51: Liquid fraction profile in the radial cross-section at the end of the mould as a function of the casting temperature. Black: $T_{cast} = T_{cast0} - 10$ K. Red: reference T_{cast}. Blue: $T_{cast} = T_{cast0} + 10$ K.

6.6.2.4 Simulation at Different SEN Depth

The last simulation represents the influence of the SEN depth on the velocity and temperature fields in the mould. The depth of the SEN is changed for $0.02\,\mathrm{m}$ in the upward and downward directions. The absolute velocity field and the streamlines in the mould are shown in Figures 6.52 and 6.53, respectively. The whole velocity field remains almost unchanged, but repositioned in the vertical direction according to the SEN depth. The same behaviour is presented for the temperature field (see Figure 6.54). Therefore, in the case with increased SEN depth, the liquid steel is pouring more onto the outer side of the billet than in the case with the smallest SEN depth. This results in a larger temperature difference between the inner and the outer surface, shown in Figure 6.55. The shell thickness as a function of the SEN depth is plotted in Figure 6.56, where practically no differences are obtained.

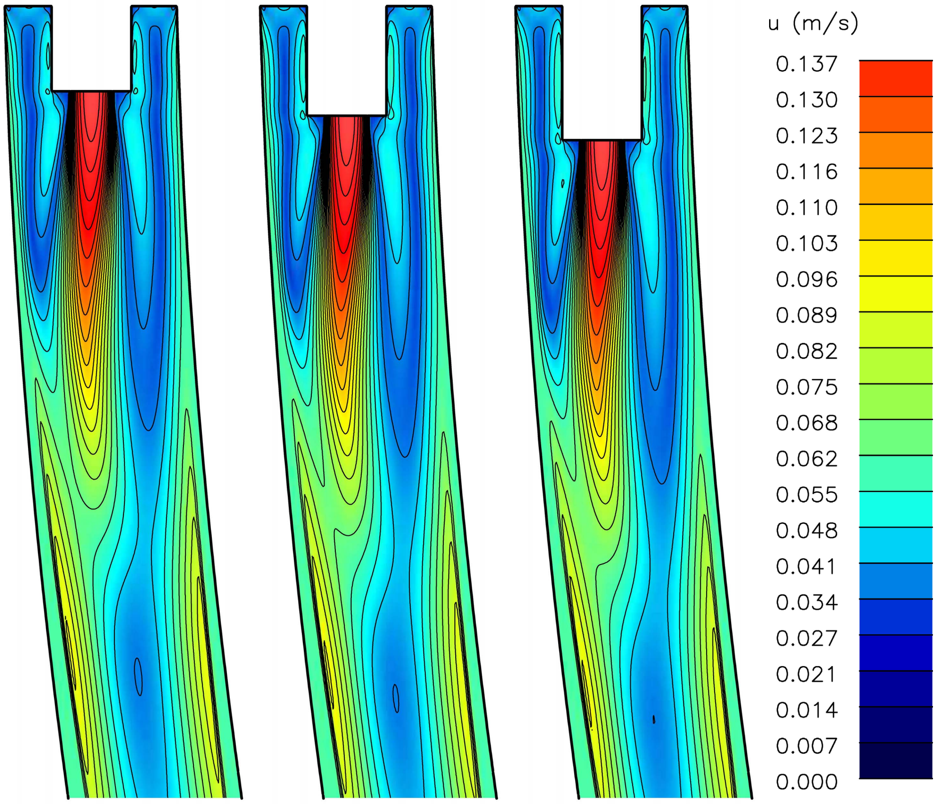

Figure 6.52: Absolute velocity field in the mould as a function of the SEN depth. Left: $L_{depth} = 0.07\,\mathrm{m}$. Centre: $L_{depth} = 0.09\,\mathrm{m}$. Right: $L_{depth} = 0.11\,\mathrm{m}$.

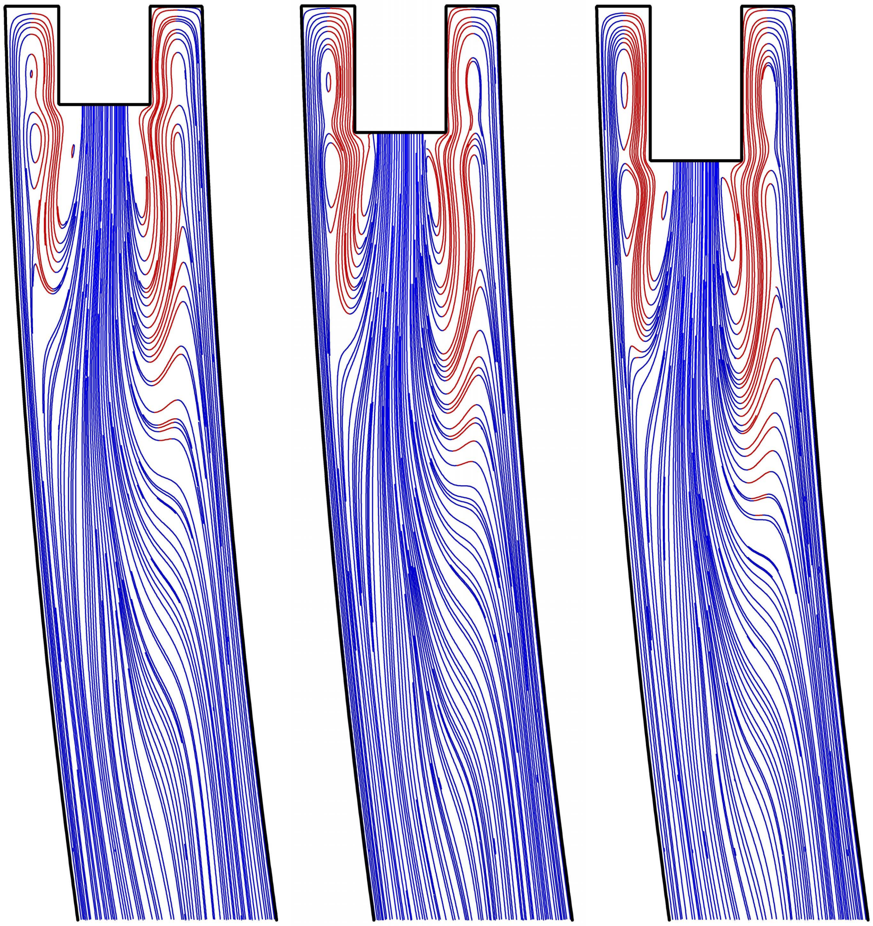

Figure 6.53: Streamlines in the mould as a function of the SEN depth. Left: $L_{depth} = 0.07\,\text{m}$. Centre: $L_{depth} = 0.09\,\text{m}$. Right: $L_{depth} = 0.11\,\text{m}$.

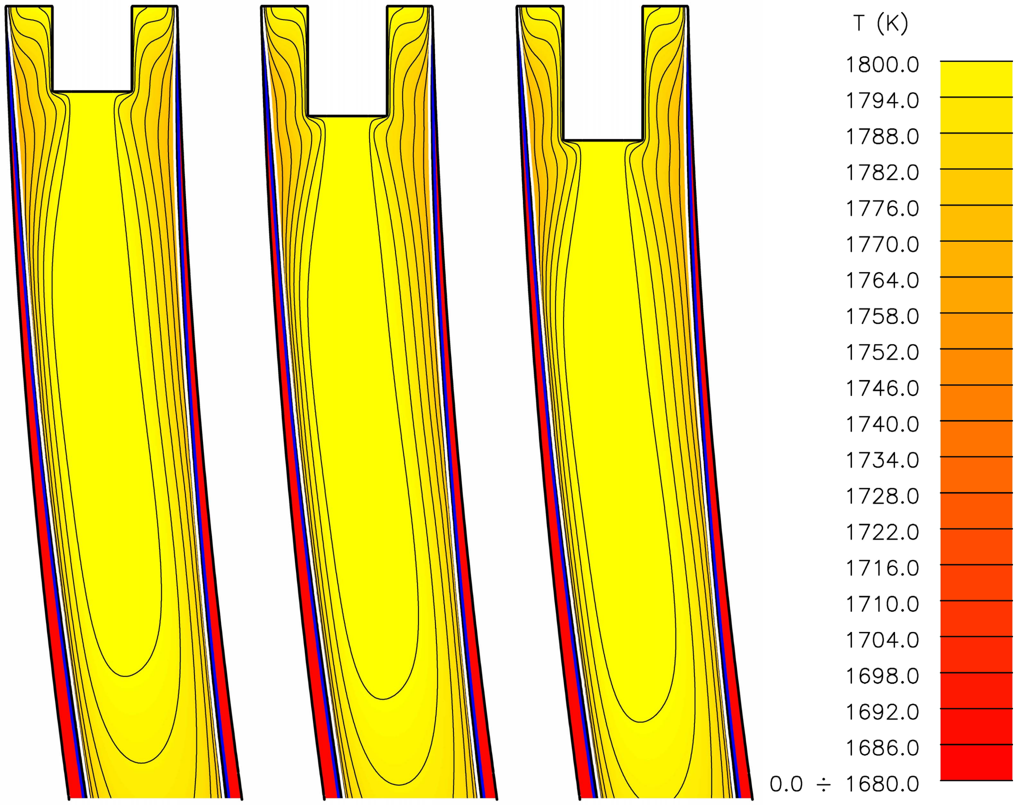

Figure 6.54: Temperature field in the mould as a function of the SEN depth. Left: $L_{depth} = 0.07\,\mathrm{m}$. Centre: $L_{depth} = 0.09\,\mathrm{m}$. Right: $L_{depth} = 0.11\,\mathrm{m}$.

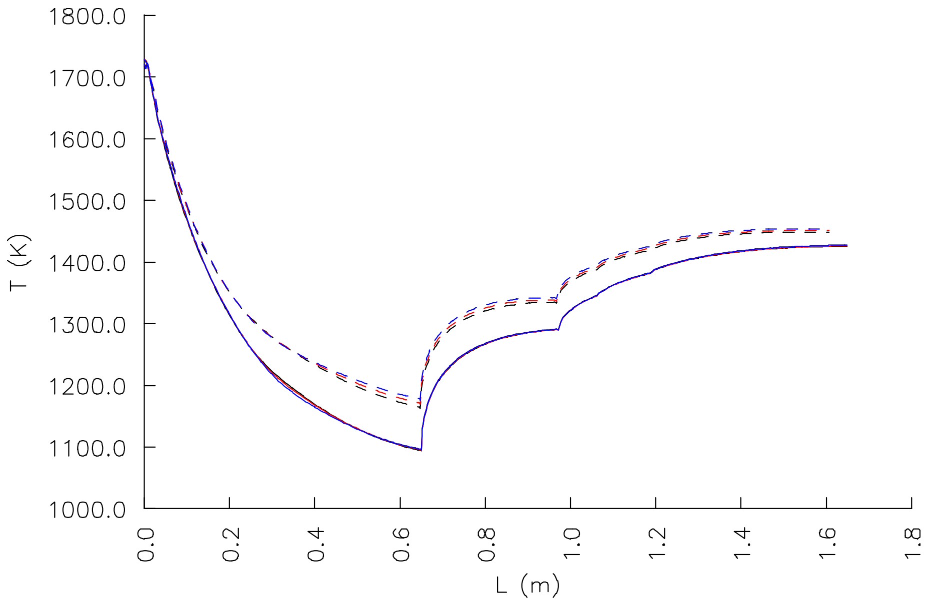

Figure 6.55: Surface temperature along the billet as a function of the casting temperature. Black: $L_{depth} = 0.07\,\mathrm{m}$. Red: $L_{depth} = 0.09\,\mathrm{m}$. Blue: $L_{depth} = 0.11\,\mathrm{m}$. Solid lines: outer side. Dashed lines: inner side.

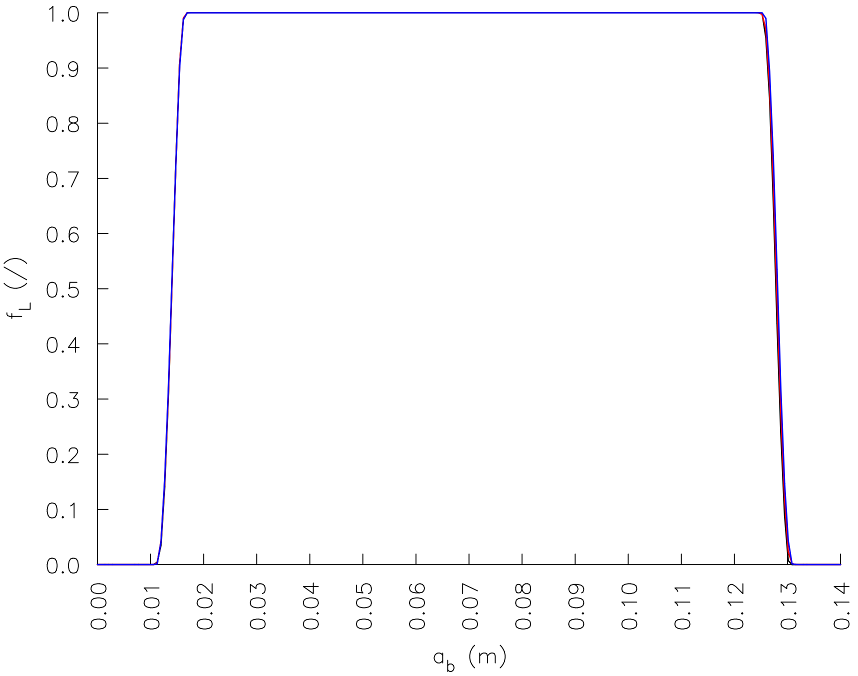

Figure 6.56: Liquid fraction profile in the radial cross-section at the end of the mould as a function of the casting temperature. Black: $L_{depth} = 0.07\,\mathrm{m}$. Red: $L_{depth} = 0.09\,\mathrm{m}$. Blue: $L_{depth} = 0.11\,\mathrm{m}$.

7 Summary and Conclusions

7.1 Summary of the Main Contributions

The numerical method based on the meshless LRBFCM is developed for solving the incompressible turbulent flow and the heat transfer inside a continuously cast steel billet. The solid-liquid phase-change phenomena are modelled by the single-domain mixture continuum model [Bennon and Incropera, 1987], where the mushy zone is treated as a porous media. The velocity-pressure coupling of the incompressible fluid is performed by the fractional step method, where the resulting pressure equation is solved globally through the direct sparse-matrix solver. The turbulent flow is considered by using the LRN k-ε turbulence model, which also includes additional terms due to the solidification effects in a mushy zone. The transport equations of the turbulence model are solved decoupled from the mass and momentum equations. The explicit time discretization is used in the involved mass, momentum, energy, k and ε equations.

The meshless method, i.e. LRBFCM, is based on the local collocation with the MQ-RBFs, where the free parameter is fixed and constant for each influence domain. The influence domain of the observed node is generated by searching the four optimal neighbour nodes, which are the closest one to the observed node and fulfils the criteria of calculating the derivatives in all directions of the selected coordinate system.

The present dissertation can be summarized by the following contributions:

- The presented meshless LRBFCM was already used in the previous works [Šarler and Vertnik, 2006; Vertnik and Šarler, 2006a; Vertnik *et al.*, 2006; Vertnik, 2007; Vertnik and Šarler, 2009a; Vertnik and Šarler, 2009b; Vertnik and Šarler, 2009c] for solving various transport problems. In the present dissertation, its applicability is extended to more complex physical problems. In order to keep its simplicity, locality, and explicitness, a lot of efforts have been used to select a proper velocity-pressure coupling algorithm for solving the incompressible turbulent flow problems in closed and open arrangements. A fractional step method is chosen, since it is found to be very robust for solving the above problems, and was already used by the conventional mesh and also meshless methods. The next stage is to solve a pressure Poisson equation, which solution is needed as a part of the fractional step method. The solution is obtained globally through the sparse-matrix formulation [Lee *et al.*, 2003]. This formulation is for the first time used in connection with the complex fluid flow problems and large node arrangements. The fractional step method is further extended to cope with the steady-state incompressible turbulent flows. Additional transport equations of the turbulence model are solved decoupled from the velocity and temperature field, without any inner iterations.

- The developed numerical method is tested on a two benchmark tests with the laminar incompressible flow, i.e. the natural convection in a square cavity and the flow through a backward-facing step. Both numerical examples are used to test the implementation of the fractional step method in different flow arrangements and the second one particularly for testing the inflow-outflow boundary conditions. The first test is also important due to the fully coupled problem between the heat and the fluid flow. The calculations are performed at various Ra numbers, ranging from moderate 10^6 to a very high value 10^8. The backward-facing step problem is a standard bench-mark test problem, which includes the flow separation and reattachment. It is performed in the present dissertation for various Re numbers, i.e. $300\text{-}800$, based on the step height. The results of both the tests are compared with other numerical results, obtained by the conventional mesh methods.
- The main focus of the present dissertation is in using the LRBFCM for numerical modelling of the turbulent flows. To verify the implementation of the selected EVMs, the following numerical examples are performed: a 2D channel flow, a 2D channel flow with heat transfer, combined forced and natural convection flow in a 2D vertical channel, and turbulent flow over a backward facing step. Three LRN turbulence models are implemented, i.e. JL, LS and AKN, while the main attention is given on the LS and AKN models. The first two examples are chosen in order to test the proper implementation of the mentioned LRN models, while the last two examples are very important in the connection with the continuous casting process. They both include similar physical phenomena as observed in the continuous casting process, i.e. combined forced and natural convection, a flow separation and reattachment. To verify the obtained numerical results, a comparison analysis is performed based on the available DNS data, experimental data, and the results obtained by the conventional mesh methods.

- The developed numerical model of the continuous casting of steel is described in detail. This involves the spatial discretization, the initial conditions, and the description of the boundary conditions for the velocity and temperature fields. Due to the lack of the benchmark tests for such a complex physical problem, the model is validated by comparison with the numerical results, obtained by the commercial software Fluent. The physical model is simplified by taking the constant thermo-physical properties, and simplified boundary conditions. A comparison analysis involves: the temperature and the velocity field inside a billet, and the temperature and the velocity profiles in the radial cross-section at various positions along the billet. After validation, the simulation is performed for C45 steel grade, with thermo-physical properties calculated with the commercial data base JMatPro. The boundary conditions are taken from the already developed simulation system of the Štore Steel casting machine. Real process parameters are considered, which are used in the Štore Steel company for C45 steel grade. The obtained results are further used as a reference solution for analyzing the effects of the numerical and process parameters on the velocity and temperature field inside the billet. The morphology constant of the porous media is considered as the numerical parameter, while the casting speed, the casting temperature, and the SEN depth as the process parameters. With the above analyses, the expected behaviour of the developed numerical model is approved.

7.2 Technological Relevance

The developed numerical model of the continuous casting of steel is found to be a very important tool for expanding the technologically relevant capabilities of the already developed simulation systems [Vertnik and Šarler, 2002; Vertnik and Šarler, 2004a; Vertnik and Šarler, 2004b; Vertnik and Šarler, 2006b; Vertnik and Šarler, 2006c; Vertnik and Šarler, 2006d] in the Štore Steel company and steel industry in general. The developed simulation system is based on the thermal numerical model, in which the velocity field is assumed to be constant and equal to the casting speed. These models are appropriate for optimizing the process parameters based on the calculated metallurgical length, shell thickness at the end of the mould, and surface temperature before the straightening. Despite the powerful futures of the already developed thermal model approved in practice, the developed thermo-fluid model with solidification can be used for simulation of the following additional technologically relevant problems:

- *Tracking the non-metalic inclusions inside a mould.*
  The inclusions can flow upward to the top surface of the molten steel, or can be trapped inside the mushy zone. What happens with the inclusions mainly depends on the size and position of the calculated re-circulating zones, and the resulting upward flow field. It is important to design the velocity field which moves the inclusions towards the top surface of the molten steel. If the inclusions are trapped in the mushy zone, they can later produce cracks in further processes, such as rolling, and reduce the quality of the final product.
- *Designing the optimal geometry of the SEN.*
  The velocity field in the mould greatly depends on the geometry of the SEN. Its optimal design can be obtained based on the water models, where the PIV or Laser Doppler Velocimetry (LDV) techniques are used to measure the velocity field. However, the experimental facility of the water model is expensive to construct, and the effects of the solidification phenomena on the convection can not be considered. The developed numerical model can greatly reduce the costs of the design procedure for finding the optimal geometry of the SEN. The main reasons are: the geometry modifications can easily be applied, and the solidification phenomena are considered.
- *Improving the macrosegregation pattern in the strand.*
  It is already discussed in Chapter 1, that the macrosegregation affects the final quality of the product. The segregation pattern of the particular solute element in the mould can be obtained by using additional transport equations for solute, which can be discretized in the same way as the transport equation for energy (see Section 4.4).

7.3 Conclusions and Future Work

The following conclusions can be summarized:

- The LRBFCM is capable of approximating all kinds of derivatives, such as first, second and mixed ones, needed for solving various PDEs. However, the obtained accuracy strongly depends on the number of neighbouring nodes in the influence domain and on the free parameter of the MQ-RBFs. Their effects on the accuracy were already discussed in our previous works [Šarler and Vertnik, 2006; Vertnik, 2007], and they are not repeated in the present dissertation. Therefore, the local collocation is made with five nodes in the influence domains (the observed node and four neighbours), and with the constant scaled free parameter, equal to 32 for each influence domain. We need to modify the searching procedure for finding the optimal neighbourhood nodes in the present dissertation. The most problematic node arrangements are those with very high levels of refinement near the walls. The solution of this problem is solved by searching the nodes not just the closest one, but also to find at least one node in each quadrant of the local coordinate system. The sparse matrix, used for solving the pressure field, is generated with the same influence domains as is used for local collocation. So, five nodes in each influence domain and using MQ-RBFs with constant scaled free parameter 32. We did not made any analysis about how the number of nodes in influence domains affects the solution accuracy of the sparse-matrix. This is left for future work. However, the comparison in the numerical example of the backward-facing step with the laminar fluid flow shows excellent accuracy of the calculated pressure field. It is worth to mention, that instead of the collocation, the WLS approximation can also be used to approximate the solution. The WLS method is very useful when approximating step-like functions, where the collocation some times does not produce good results. On the other hand, WLS method introduces several new difficulties: more nodes have to be used in the influence domains, corresponding weight function has additional free parameters, the matrices are larger and more complex to generate and solve. However, in the future, we should also try to implement the WLS method to see if we can get any improvements. The advantages of the LRBFCM are its simplicity, simple inclusion of different physics, accuracy, similar code for 2D and three-dimensional problems, no integrations are involved, and straightforward applicability in non-uniform node arrangements. Due to its locality and explicit time stepping, the method appears very suitable for parallelization.

- The developed numerical method is capable of solving various laminar incompressible fluid flow problems. Two numerical examples, which are representing the classical benchmark tests for verifying numerical methods. The comparison analyses show a very good agreement with other reference results. In the example of the backward-facing step, we demonstrated the solution on a non-uniform node arrangement with randomly repositioned nodes. The solution is obtained with the reasonable accuracy. Theoretically, the meshless methods should perform well on any kind of scattered node arrangements, but for physically complex problems, such kind of node arrangements should be avoided.

- The developed numerical method is capable of solving the incompressible turbulent flow problems. In the present dissertation, the LRN k-ε turbulence models are focused, which have advantages over the standard k-ε models. The LRN models involve damping functions, which are capable of reproducing the near wall behaviour of the boundary layer. But, in order to achieve this, a very fine node arrangement has to be used near the wall, i.e. $y^+ \leq 1$. Also, some of the LRN models, such as JL and LS, can become unstable due to the involved additional source terms. This source terms include the second and mixed derivatives of the velocity, which can produce numerical stiffness. Such problems are encountered in the backward-facing step example, where the large velocity gradients occur around the flow separation. Unstable skin friction and over-estimated reattachment length are the consequences. We believe that the LRBFCM is the main reason of the underlying instabilities. However, the results are greatly improved by increasing the number of the nodes in the step region. The commercial software package Fluent is using the modified LS model without those terms and different boundary conditions for ε to get rid of the numerical stiffness. But, this is not any more the original LS model, where the closure coefficients and damping functions are generated with involved additional source terms. The AKN model is far more stable and very appropriate for flow separations and reattachments, but its damping functions include the wall variable y^*, which depends on the normal distance to the nearest wall. If we are dealing with a pure liquid phase, than the wall distance is rather simple to calculate. However, when dealing with the solidification problems, this model is not so appropriate, since it is hard to define the nearest wall (which is somewhere in the mushy zone), and also the boundary conditions at the wall for ε are not zero. While on the other hand, the damping functions in the LS model depend only on the Re_t and the boundary condition for k and ε are of the Dirichlet type with zero value. Therefore, this model is a far more simple to implement for the solidification problem, since both k and ε become automatically zero in the mushy zone. For future needs, also other EVMs, such as k-ω [Bredberg, 2001] should be implemented.
- The numerical model of the continuous casting of steel is developed. The real curved geometry of the Štore Steel billet caster is considered, modelled in 2D. The LS turbulence model is used to calculate the turbulent flow inside the mould. The reason, why this model is chosen, is above discussed. A sensitivity study of turbulence models on the flow field is not made. However, it is well known [Lan *et al.*, 1997; Thomas *et*

al., 2001] that the choice of turbulence models influence the prediction of the flow field. In future, it is worth to include some other turbulence models (standard k-ε, AKN, k-ω, etc.). A 3D model implementation is foreseen in the future, since the billet is square and therefore the resulting fluid flow pattern depends also on the fluid flow behaviour near the corners of the mould. However, the discretization of the 3D geometry is far more complex than for the 2D, and the number of the nodes increases strongly. The verification of the developed numerical model is performed by comparison with the results obtained by Fluent. We do not expect an excellent agreement, since a simplified single-phase formulation is used in Fluent. Also, in Fluent, the AKN turbulence model is chosen. Despite those differences, the global picture of the obtained velocity and temperature fields are approximately and reasonably the same. Also, the comparison of the velocity and temperature profiles at various positions along the billet indicates a correct implementation of the numerical model. There is no doubt, that we have a great confidence in using the developed numerical model for further practical analysis. After verification, only one steel grade is simulated, i.e. C45, with the real process parameters, boundary conditions and realistic thermo-physical material properties. It is hard to say if the calculated velocity and temperature fields indicate the real situation in the casting process. The reason is in the lack of knowledge about fluid flow and solidification phenomena in the mould, since it is almost impossible at the present to measure the velocity and the temperature during the casting process. However, pretty much the same temperature profiles at the billet surface are obtained when compared with the already developed thermal numerical model in the Štore Steel company. This gives us additional courage for using the numerical model in further investigations. The obtained results of the C45 steel grade are used for analyzing the effects of the variable process parameters on the temperature and the velocity field in the billet. The main reason of the performed analysis is in testing the behaviour of the developed numerical model. In future, the model can be extended to cope with a 3D geometry. This requires the modification of the developed numerical model for running it on a computer network (i.e. cluster).

- The modelling of turbulence in the mushy zone is still an open question, since the turbulence models are developed and adjusted usually for problems with a pure liquid. Also the closure coefficients and damping functions, which close the turbulence model, are generated based on the experiments and DNS data for pure liquid. It is doubtful if these models are applicable for the solidification problems, such as continuous casting of steel, where the fluid flow in the mushy zone is also turbulent. The mushy zone is usually composed by a porous media and a slurry region. In the present dissertation, the slurry region is not considered, but the whole mushy region is treated as a porous media. In the literature, the turbulent flow in a porous media has not been studied extensively, even of its practical and theoretical importance. The most common model for macroscopic turbulence is the k-ε model, constructed in the same way as for the pure liquid flow [Antohe and Lage, 1996]. The model is constructed from the momentum equation for the porous media, where additional terms, such as Darcy, buoyancy, etc., produce also additional terms in the resulting k and ε equations. It is not known how these terms affect the closure coefficients and the damping functions of the turbulence models, which were developed only for the pure liquid problems. However, in the continuous casting process, the mushy region in the mould is usually very small compared to the pure liquid and the pure solid regions, and therefore the discussed uncertainties should not affect the velocity field in the pure liquid region. Definitely, there is a future need on experimental data with turbulent flow in a porous media, and the subsequent development of the turbulence models for such particular cases. In addition to this, there is also a need for the standard benchmark test on numerical modelling of turbulent flow in continuous casting. Such a benchmark has been recently proposed [Vertnik *et al.*, 2010].

Appendix A

A.1 Analytical Solution of the Convective-Diffusive Phase-Change Problem

The exact closed form solution for checking convective-diffusive solid-liquid phase-change problems appears to exist only for a relatively simple 1D steady-state class of problems with uniform velocity field. The solution used by Pardo and Weckman [Pardo and Weckman, 1986] for checking their one-domain FEM-based numerical method belongs to this class of problems. Pardo and Weckman's solution for equal and constant thermal properties of the phases has been generalized by [Šarler and Kuhn, 1998a] to cope with the generally different and constant thermal properties of the solid λ_{0S}, c_{0S} and liquid λ_{0L}, c_{0L} phase. The extended analytical solution is particularly useful because it allows one to check the proper response of the numerical method regarding the temperature dependence of the material properties. The respective test case is defined as follows: The domain Ω is described by the Cartesian coordinate $p_x^- < p_x < p_x^+$. The boundary conditions at p_x^- and at p_x^+ are of the Dirichlet type with uniform temperatures $T_\Gamma = T_\Gamma^-$ and $T_\Gamma = T_\Gamma^+$. The material moves with the constant uniform velocity $\mathbf{u} = \mathbf{u}_S = \mathbf{u}_L$ with components $\mathbf{u}_x = \mathbf{u}_0$. The boundary temperatures and the isothermal melting temperature are related by $T_{\Gamma^-} < T_M < T_{\Gamma^+}$. The liquid phase thus occupies the domain between p_x^- and the phase-change interface boundary at p_{Mx}, and the solid phase the domain between p_{Mx} and p_x^+. The corresponding exact temperature distribution in phase $\wp$ has been found [Šarler and Kuhn, 1998b] to be

$$T^{\wp}\left(p_x, p_y\right) = -\frac{\alpha_{\wp}}{v_x}\exp\left(\frac{u_x}{\alpha_{\wp}} p_x + A_P\right) + B_{\wp}; \tag{A.1}$$

$$\alpha_{\wp} = \frac{\lambda_{0\wp}}{\rho_0 c_{p0\wp}};\ \wp = S, L, \tag{A.2}$$

with $\alpha_{\wp}$ denoting the thermal diffusivity of the phase $\wp$; the four constants are

$$A_S = \log \frac{\dfrac{u_x}{\alpha_S}\left(T_M - T_{\Gamma^+}\right)}{\exp\left(\dfrac{u_x}{\alpha_S} p_x^+\right) - \exp\left(\dfrac{u_x}{\alpha_S} p_{Mx}\right)}, \tag{A.3}$$

$$A_L = \log \frac{\dfrac{u_x}{\alpha_L}\left(T_M - T_{\Gamma^-}\right)}{\exp\left(\dfrac{u_x}{\alpha_L} p_x^-\right) - \exp\left(\dfrac{u_x}{\alpha_L} p_{Mx}\right)}, \tag{A.4}$$

$$B_\wp = T_M + \frac{\alpha_\wp}{u_x} A_\wp \exp\left(\frac{u_x}{\alpha_\wp} p_{Mx}\right); \ \wp = S, L. \tag{A.5}$$

The position of the phase-change interface boundary is determined from the transcendental equation

$$-\rho_0 h_M u_x = -\lambda_L \frac{\partial}{\partial p_x} T^L\left(p_{Mx}, p_y\right) + \lambda_S \frac{\partial}{\partial p_x} T^S\left(p_{Mx}, p_y\right). \tag{A.6}$$

It is in the present dissertation solved by the simple bisection.

Bibliography

Abe, K., Kondoh, T. and Nagano, Y. (1994). A new turbulence model for predicting fluid flow and heat transfer in separating and reattaching flows-I. Flow field calculations. *International Journal of Heat and Mass Transfer*, 37:139-151.

Abe, K., Kondoh, T. and Nagano, Y. (1995). A new turbulence model for predicting fluid flow and heat transfer in separating and reattaching flows-II. Thermal field calculations. *International Journal of Heat and Mass Transfer*, 38:1467-1481.

Aboutalebi, M. R., Hasan, M. and Guthrie, R. I. L. (1995). Coupled turbulent flow, heat, and solute transport in continuous casting processes. *Metallurgical and Materials Transactios*, B26:731-743.

Adams, E. W. (1984). *Experiments on the Structure of Turbulent Reattaching Flow*. PhD Thesis, Stanford University, Department of Mechanical Engineering.

Ampofo, F. and Karayiannis, T. G. (2003). Experimental benchmark data for turbulent natural convection in an air filled square cavity. *International Journal of Heat an Mass Transfer*, 46:3551-3572.

Antohe, B. V. and Lage, J. L. (1996). A general two-equation macroscopic turbulence model for incompressible flow in porous media. *International Journal of Heat an Mass Transfer*, 40:3013-3024.

Armaly, B. F., Durst, F., Pereira, J. C. F. and Schonung, B. (1983). Experimental and theoretical investigation of backward-facing step flow. *Journal of Fluid Mechanics*, 127:473-496.

Atluri, S. N. and Shen, S. (2002). *The Meshless Local Petrov-Galerkin Method*. Tech Science Press, Forsyth.

Atluri, S. N. (2004). *The Meshless Method for Domain and BIE Discretisations*. Tech Science Press, Forsyth.

Barton, I. E. (1995). A numerical study of flow over a confined backward-facing step. *International Journal for Numerical Methods in Fluids*, 21:653-665.

Barton, I.E. and Kirby, R. (2000). Finite difference scheme for the solution of fluid flow problems on non-staggered grids. *International Journal for Numerical Methods in Fluids,* 33:939-959.

Batraeva, A. E., Ishmet, E. N., Andreev, S. M., Parsunkin, B. N., Salikhov, Z. G. and Svetlov, A. Yu. (2007). Dynamic control of the billet temperature in continuous-casting machines. *Steel in Translation*, 37:908-913.

Beckermann, C. and Viskanta, R. (1988). Double-diffusive convection during dendritic solidification of a binary mixture. *PhysicoChem Hydrodyn,* 10:195-213.

Beckermann, C. and Viskanta, R. (1993). Mathematical modeling of transport phenomena during alloy solidification. *Applied Mechanics Reviews,* 46:1-27.

Beckermann, C. (2000). Modeling of macrosegregation: applications and future needs. *International Matarials Reviews,* 47:243-261.

Bennon, W. D. and Incropera, F. P. (1987). A continuum model for momentum, heat and species transport in binary solid-liquid phase change systems - I. Model formulation. *International Journal of Heat and Mass Transfer*, 30:2161-2170.

Bennon, W. D. and Incropera, F. P. (1988). Numerical analysis of binary solid-liquid phase change using a continuum model. *Numerical Heat Transfer,* A13:277-296.

Billard, F., Uribe, J.C. and Laurence, D. (2008). A new formulation of the - model using elliptic blending and its application to heat transfer prediction, *Proceedings of 7th International Symposium on Engineering Turbulence Modelling and Measurements*, Limassol, Cyprus, June 4-6, 89-94.

Brandes, E. A. and Brook, G. B. (1992). *Smithells Metals Reference Book*. Seventh Edition, Butterwoth-Heinemenn, Oxford.

Bredberg, J. (1999), *Prediction of Flow and Heat Transfer Inside Turbine Blades Using EARSM, k-ε and k-ω Turbulence Models*, Thesis for the Degree of Licinetiate of Engineering, Department of Thermo and Fluid Dynamics, Chalmers University of Technology, Göteborg.

Bredberg, J. (2001). *On Two-Equation Eddy-Viscosity Models*. Internal Report 01/8, Department of Thermo and Fluid Dynamics, Chalmers University of Technology, Göteborg.

Bredberg, J. (2002), *Turbulence Modelling for Internal Cooling of Gas-Turbine Blades*, PhD thesis, Department of Thermo and Fluid Dynamics, Chalmers University of Technology, Göteborg.

Buhmann, M. D. (2003). *Radial Basis Function: Theory and Implementations*. Cambridge University Press, Cambridge.

Cameron, A. D., Casey, J. A. and Simpson, G. B. (1986). *Benchmark Tests for Thermal Analysis*. NAFEMS National Agency for Finite Element Methods & Standards, Department of Trade and Industry, National Engineering Laboratory, Glasgow.

Carr, J. C., Fright, W. R. and Beatson, R. K. (1997). Surface interpolation with radial basis functions for medical imaging. *IEEE Transactions on Medical Imaging*, 16: 96-107.

Car, J. C., Beatson, R. K., Cherrie, J. B., Mitchell, T. J. Fright, W. R., McCallum, B. C. and Evans, T. R. (2001). Reconstruction and representation of 3D objects with radial basis functions. *Proceedings of the 28th Annual Conference on Computer Graphics and Interactive Techniques,* ACM Press, New York, 67-76.

Car, J. C., Beatson, R. K., McCallum, B. C., Fright, W. R., McLennan, T. J. and Mitchell, T. J. (2003). Smooth surface reconstruction from noisy range data. *Proceedings of the 1st International Conference on Computer Graphics and Interactive Techniques in Australasia and South East Asia, February 11-14, 2003, Melbourne, Australia,* ACM Press, New York, 119-126.

Carlsaw, H. S. and Jaeger, J. C. (1995). *Conduction of Heat in Solids - Second Edition*. Clarendon Press, Oxford.

Cecil, T., Qian, J. and Osher, S. (2004). Numerical methods for high dimensional Hamilton-Jacobi equations using radial basis functions. *Journal of Computational Physics*, 196:327-347.

Chen, W. (2002). New RBF collocation schemes and kernel RBFs with applications. *Lecture Notes in Computational Science and Engineering,* 26:75-86.

Chen, C.S., Ganesh, M., Golberg, M.A. and Cheng, A.H.D. (2002). Multilevel compact radial basis functions based computational scheme for some elliptic problems. *Computers and Mathemathics with Applications*, 43:359-378.

Chen, Y. T., Nie, J. H., Armaly, B. F. and Hsieh, H. T. (2006). Turbulent separated convection flow adjacent to backward-facing step - effects of step height. *International Journal of Heat and Mass Transfer,* 49:3670-3680.

Chen, Y. T., Nie, J. H., Armaly, B. F., Hsieh, H. T. and Boehm, R. F. (2007). Developing turbulent forced convection in two-dimensional duct. *Journal of Heat Transfer*, 129:1295-1299.

Chiang, T.P., Sheu, T.W.H. and Fang, C.C. (1999). Numerical investigation of vertical evolution in a backward-facing step expansion flow. *Applied Mathematical Modelling*, 23:915-932.

Chien, K. -Y., (1982). Predictions of channel and boundary-layer flows with a low-Reynolds-number turbulence model. *American Institute of Aeronautics and Astronautics, Aerospace Sciences Meeting, 18th, Pasadena, Calif., Jan. 14-16,* 33-38.

Chorin, A.J. (1967). A numerical method for solving incompressible viscous flow problems. *Journal of Computational Physics*, 2:12-26.

Chorin, A.J. (1968). Numerical solution of the Navier-Stokes equations. *Mathematics of Computation*, 22:745-762.

Constales, D., Kačur, J. and Van Keer, R. (2002). On the optimal cooling strategy for variable-speed continuous casting. *International Journal for Numerical Methods in Engineering*, 53:539-565.

Crank, J. (1984). *Free and Moving Boundary Problems*. Oxford University Press, Oxford.

Dalhuijsen, A. J. and Segal, A. (1986). Comparison of finite element techniques for solidification problems. *International Journal of Numerical Methods in Engineering*, 29:1807-1829.

Dantzig, J. A. and Tucker III, C. L. (2001). *Modeling in Materials Processing*. Cambridge University Press, Cambridge.

Davidson, L. (2003). *In Introduction to Turbulence Models*, Report 97/2, Department of Thermo and Fluid Dynamics, Chalmers University of Technology Goteborg.

Davis, G. De Vahl (1983). Natural convection of air in a square cavity: a benchmark numerical solution, *International Journal of Numerical Methods in Fluids*, 3:249-264.

Divo, E. and Kassab, A.J. (2005). Modeling of convective and conjugate heat transfer by a third order localized RBF meshless collocation method. In Nowak, A.J., Białecki, R.A. and Weçel, G., editors, *Eurotherm 82: Numerical Heat Transfer, September 13-16, 2005, Gliwice-Krakow, Poland*, Zaklad Graficzny Politehniki Śląskiej, Gliwice, 357-366.

Divo, E. and Kassab, A. J. (2007). An efficient localized RBF meshless method for fluid flow and conjugate heat transfer. *ASME Journal of Heat Transfer*, 129:124-136.

Fasshauer, G. E. (1997). Solving partial differential equations by collocation with radial basis functions. In Mehaute, A.L., Rabut, C. and Schumaker, L.L., editors, *Surface Fitting and Multiresolution Methods*, 131-138.

Ferziger, J.H. and Perić, M. (2002). *Computational Methods for Fluid Dynamics, 3rd rev. ed.*, Springer-Verlag, Berlin.

Fic, A., Nowak, A. J. and Białecki, R. (2000). Heat transfer analysis of the continuous casting process by the front tracking BEM. *Engineering Analysis with Boundary Elements*, 24:215-23.

Fletcher, C.A.J. (1988). *Computational Techniques for Fluid Dynamics 2*, Springer-Verlag, Berlin.

Franke, R. (1982). Scattered data interpolation: Tests of some methods. *Mathematics of Computation*, 38: 181-200.
Gartling, D.K. (1990). A test problem for outflow boundary conditions-flow over a backward facing step. *International Journal for Numerical Methods in Fluids*, 11: 593-967.

Gresho, P.M., Gartling, D.K., Torczynski, J.R., Cliffe, K.A., Winters, K.H., Garratt, T.J., Spence, A. and Goodrich, J.W. (1993). Is the steady viscous incompressible two-dimensional flow over a backward-facing step at Re=800 stable?. *International Journal for Numerical Methods in Fluids*, 17:501-541.

Gonzalez, M., Goldschmit, M. B., Assanelli, A. P., Berdaguer, E. F. and Dvorkin, E. N. (2003). Modeling of the solidification process in a continuous casting installation for steel slabs. *Metallurgical and Materials Transactions*, B34:455-473.

Ghotbi, A. E., Manceau, R. and Boree, J. (2008). Revisiting URANS computations of the backward-facing step flow using second moment closures. Influence of the numerics. *Flow, Turbulence and Combustion*, 81:395-414.

Gjerkeš, H., Šarler, B. and Vertnik, R. (2009). In-plant thermography of the continuously cast billets. In: Ludwig, A., editor, *Proceedings of the 3rd Steelsim Conference*, *September 8-10, 2009, Leoben, Austria*, ASMET, CC10, CD-ROM.

Gu, Y. T. and Liu, G. R. (2006). Meshless technique for convection dominated problems. *Computational Mechanics*, 38:171-182.

Ha, M. Y., Lee, H. G. and Seong, S. H. (2003). Numerical simulation of three-dimensional flow, heat transfer, and solidification of steel in continuous casting mold with electromagnetic brake. *Journal of Materials Processing Technology*, 133:322-339.

Haq, S., ul-Islam, S. and Arshed, A. (2008). A numerical meshfree technique for the solution of the MEW equation, *CMES: Computer Modeling in Engineering & Sciences*, 38:1-24.

Hardin, R. A., Liu, K., Kapoor, A. and Beckermann, C. (2003). A transient simulation and dynamic spray cooling control model for continuous steel casting. *Metallurgical and Materials Transactions*, B34:297-306.

Hardy, R. L. (1971). Multiquadric equations of topography and other irregular surfaces. *Journal of Geophysical Research*, 76:1905-1915.
Heibi, Y., Man, Y. and Dacheng, F. (2006). 3-D inverse problem continuous model for thermal behaviour of mold process based on the temperature measurements in plant trial. *The Iron and Steel Institute of Japan International*, 46:539-545.

Henkes, R. A. W. M., Van der Vlugt, F. F. and Hoogendoorn, C. J. (1991). Natural-convection flow in a square cavity calculated with low-Reynolds-number turbulent models. *International Journals of Heat and Mass Transfer,* 34:377-388.

Hoffmann, K. A. and Chiang, S.T. (2000). *Computational Fluid Dynamics, Volume 3*. Engineering Education System, Wichita.

Hsieh, K. J. and Lien, F. S. (2004). Numerical modeling of buoyancy-driven trubulent flows in enclosures. *International Journal of Heat and Fluid Flow,* 25:659-670.

Hong, C. P. (2004). *Computer Modelling of Heat and Fluid Flow in Materials Processing*. Institute of Physics Publishing, London.

Irwing, W. R. (1993). *Continuous Casting of Steel*, The Institute of Materials, London.

Jones, W. P. and Launder, B. E. (1972). The prediction of laminarization with a two-equation model of turbulence. *International Journal of Heat and Mass Transfer,* 15:301-314.

Jović, S. and Driver, D. M. (1994). *Backward-Facing Step Measurements at Low Reynolds Number,* $Re_h=5000$. NASA Technical Report TM-108807.

Kansa, E. J. (1990a). Multiquadrics - a scattered data approximation scheme with applications to computational fluid dynamics - I. Surface approximation and partial derivative estimates. *Computers and Mathematics with Application,* 19:127-145.

Kansa, E. J. (1990b). Multiquadrics - a scattered data approximation scheme with applications to computational fluid dynamics - II. Solutions to parabolic, hyperbolic and elliptic partial differential equations. *Computers and Mathematics with Application* 19:147-161.

Kasagi, N., Tomita, Y. and Kuroda, A. (1992). Direct numerical simulation of passive scalar field in a turbulent channel flow. *Transactions of the ASME* 114:598-606.

Kasagi, N. and Nishimura, M. (1997). Direct numerical simulation of combined forced and natural turbulent convection in a vertical plane channel. *International Journal of Heat and Fluid Flow*, 18:88-99.

Keskar, J. and Lyn, D.A. (1999). Computations of a laminar backward-facing step flow at Re=800 with a spectral domain decomposition method. *International Journal for Numerical Methods in Fluids*, 29:411-427.

Kim, J., Moin, P. and Moser, R. (1987). Turbulence statistics in fully developed channel flow at low Reynolds number. *Journal of Fluid Mechanics*, 117:133-166.

Kim, D. S., Kim, W. S. and Cho, K. H. (2000). Numerical simulation of the coupled turbulent flow and macroscopic solidification in continuous casting with electromagnetic brake. *The Iron and Steel Institute of Japan International*, 40:670-676.

Kovačević, I., Poredoš, A. and Šarler, B. (2003). Solving the Stefan problem by the RBFCM. *Numeical Heat Transfer*, B44:1-24.

Kovačević, I. and Šarler, B. (2005). Solution of a phase-field model for dissolution of primary particles in binary aluminum alloys by an r-adaptive mesh-free method. *Materials Science and Engineering*, A413\414:423-428.

Kosec, G. and Šarler, B. (2008a). Solution of thermo-fluid problems by collocation with local pressure correction, *International Journal of Numerical Methods in Heat and Fluid Flow*, 18:868-882.

Kosec, G. and Šarler, B. (2008b). Local radial basis function collocation method for Darcy flow, *CMES: Computer Modeling in Engineering & Sciences*, 25:197-207.

Kunz, R.F. and Lakshminarayana, B. (1992). Stability of Explicit Navier-Stokes Procedures Using k - ε and k - ε Algebraic Reynolds Stress Turbulence Models. *Journal of Computational Physics*, 103:141-159.

Kubo, N., Ishii, T., Kubota, J. and Ikagawa, T. (2004). Numerical simulation of molten steel flow under a magnetic field with argon gas bubbling in a continuous casting mold. *The Iron and Steel Institute of Japan International*, 44:556-564.

Lam, C. K. G. and Bremhorst, K. (1981). A modified form of the k-ε model for predicting wall turbulence. *Transactions of the ASME*, 103:456-460.

Lan, X. K., Khodadadi, J. M. and Shen, F. (1997). Evaluation of six k-ε turbulence model predictions of flow in a continuous casting billet-mold water model using laser drop velocimetry measurements. *Metallurgical and Materials Transactions*, B28:321-332.

Lan, X. K. and Khodadadi, J. M. (2001). Fluid flow, heat transfer and solidification in the mold of continuous casters during ladle change. *International Journal of Heat and Mass Transfer*, 44:953-965.

Launder, B. E. and Sharma, B. I. (1974). Application of the energy-dissipation model of turbulence to the calculation of flow near a spinning disc. *Letters in Heat and Mass Transfer*, 1:131-138.

Laufer, J. (1948). *Investigation of Turbulent Flow in a Two-Dimensional Channel*. PhD Thesis, California Institute of Technology, California.

Libre, N.A., Emdadi, A., Kansa, E.J., Rahimian, M. and Shekarchi, M. (2008). A stabilised RBF collocation scheme for Neumann type boundary conditions. *CMES: Computer Modeling in Engineering & Sciences*, 24:61-80.

Le, H., Moin, P. and Kim, J. (1997). Direct numerical simulation of turbulent flow over a backward-facing step. *Journal of Fluid Mechanics*, 330:349-374.

Le, P., Mai-Duy, N., Tran-Cong, T. and Baker, G. (2008). A meshless modeling of dynamic strain localization in quasi-brittle materials using radial basic function networks, *CMES: Computer Modeling in Engineering & Sciences*, 25:43-66.

Lee, C. K., Liu, X. and Fan, S. C. (2003). Local muliquadric approximation for solving boundary value problems. *Computational Mechanics*, 30:395-409.

Lin, H. and Atluri, S. N. (2001). The Meshless Local Petrov-Galerkin (MLPG) method for solving incompressible Navier-Stokes equations, *CMES: Computer Modeling in Engineering & Sciences*, 2:117-142.

Liu, G. R. (2003). *Mesh Free Methods*. CRC Press, Boca Raton.

Liu, G. R. and Gu, Y. T. (2005). *An Introduction to Meshfree Methods and Their Programming*. Springer-Verlag, Berlin.

Louhenkilpi, S. (2003). Modeling of heat transfer in continuous casting. *Materials Science Forum*, 414/415:445-454.

Louhenkilpi, S., Miettinen, J. and Holoppa, L. (2006). Simulation of microstructure of as-cast steels in continuous casting. *The Iron and Steel Institute of Japan International*, 46:914-920.

Mai-Cao, L. and Tran-Cong, T. (2005). A meshless IRBFN-based method for transient problems, *CMES: Computer Modeling in Engineering & Sciences*, 7:149-171.

Mai-Cao, L. and Tran-Cong, T. (2008). A meshless approach to capturing moving interfaces in passive transport problems, *CMES: Computer Modeling in Engineering & Sciences*, 31:157-188.

Mai-Duy, N. and Tran-Cong, T. (2001). Numerical solution of Navier-Stokes equations using multiquadric radial basis function networks. *Neural Networks* 14:185-199.

Mai-Duy, N. and Tran-Cong, T. (2001). Numerical solution of differential equations using multiquadrics radial basis function networks. *International Journal for Numerical Methods in Engineering*, 23:1807-1829.

Mai-Duy, N. and Tran-Cong, T. (2002). Mesh-free radial basis function network methods with domain decomposition for approximation of functions and numerical solution of Poisson's equations. *Engineering Analysis with Boundary Elements*, 26:133-156.

Mai-Duy, N. and Tran-Cong, T. (2003). Indirect RBFN method with thin plate splines for numerical solution of differential equations. *CMES: Computer Modeling in Engineering & Sciences*, 4:85-102.

Mai-Duy, N., Khennane, A. and Tran-Cong, T. (2007a). Computation of laminated composite plates using integrated radial basis function networks, *CMC: Computers, Materials, & Continua*, 5:63-78.

Mai-Duy, N., Mai-Cao, L. and Tran-Cong, T. (2007b). Computation of transient viscous flows using indirect radial basic function networks, *CMES: Computer Modeling in Engineering & Sciences*, 18:59-77.

Markatos, N. C. and Pericleous, K. A. (1984). Laminar and turbulent natural convection in an enclosed cavity. *International Journal of Heat and Mass Transfer*, 27:755-772.

Minkowycz, W. J. and Sparrow, E. M. (1997). *Advances in Numerical Heat Transfer: Volume 1*. Taylor & Francis, Washington.

Nayroles, B., Touzot, G. and Villon, P. (1991). L'approximation diffuse. *Mecanique des Millieux Continus*, 2:293-296.

Ni, J. and Incropera, F. P. (1994). Extension of the continuum model for transport phenomena occurring during metal alloy solidification-II. Microscopic considerations. *International Journal of Heat and Mass Transfer*, 38:1285-1296.

Oñate, E., Sacco, C. and Idelsohn, S. (2000). A finite point method for incompressible flow problems. *Computing and Visualization in Science*, 3:67-75.

Özisik, M. N. (1994). *Finite Difference Methods in Heat Transfer*. CRC Press, Boca Raton.

Pardo, E. and Weckman, D. C. (1986). A fixed grid finite element technique for modelling phase change in steady-state conduction-advection problems. *International Journal for Numerical Methods in Engineering*, 23:1807-1829.

Patankar, S. V. (1980). *Numerical Heat Transfer and Fluid Flow*. Hemisphere Publishing, Washington.

Pfeiler, C. and Ludwig, A. (2005). Influence of argon gas bubbles and non-metallic inclusions on the flow behaviour in steel continuous casting. *Materials Science and Enginnering*, A413/414:115-120.

Pope, S. B. (2000). *Turbulent Flows*. Cambridge University Press, Cambridge, New York.

Power, H. and Barraco, W. A. (2002). Comparison analysis between unsymmetric and symmetric RBFCMs for the numerical solution of PDE's. *Computers and Mathematics with Applications*, 43:551-583.

Prescott, P. J., Incropera, F. P. and Bennon, W. D. (1991). Modeling of dendritic solidification systems: reassessment of the continuum momentum equation. *International Journal of Heat and Mass Transfer*, 34:2351-2359.

Prescott, P. J. and Incropera, F. P. (1995). The effect of turbulence on solidification of a binary metal alloy with electromagnetic stirring. *Journal of Heat Transfer*, 117:716-724.

Press, W. H., Teukolsky, S. A., Vetterling, W. T. and Flannery, B. P. (1992). *Numerical Recipes in FORTRAN, Second Eddition*. Cambridge University Press, Cambridge.

Ragone, D. V. (1995). *Thermodynamics of Materials*. John Wiley & Sons, New York.

Roache, P. J. (1998). *Verification and Validation in Computational Science and Engineering*. Hermosa, Albuquerque.

Sadat, H. and Couturier, S. (2000). Performance and accuracy of a meshless method for laminar natural convection. *Numerical Heat Transfer*, B37:455-467.

Sanyasiraju, Y.V.S.S. and Chandhini, G. (2008). Local radial basis function gridfree scheme for unsteady incompressible viscous flows. *Journal of Computational Physics*, 227:8922-8948.

Schaback, R. (1995). Error Estimates and Condition Numbers for Radial Basis Function Interpolation. *Advances in Computational Mathematics*, 3:251-264.

Schiestel, R. (2008). *Modeling and Simulation of Turbulent Flows*. ISTE Ltd, London.

Seo, E. R. (2001). *A Numerical Study of Buoyant Turbulent Flows Using Low-Reynolds Number k-e Model*. PhD Thesis, Texas Tech University, Department of Mechanical Engineering, Lubbock.

Seyedein, S. H. and Hasan, M. (1997). A three-dimensional simulation of coupled turbulent flow and macroscopic solidification heat transfer for continuous slab casters. *International Journal of Heat and Mass Transfer,* 40:4405-4423.

Shu, C., Ding, H. and Yeo, K. S. (2003). Local radial basis function-based differential quadrature method and its application to solve two-dimensional incompressible Navier-Stokes equations. *Computer Methods in Applied Mechanics and Engineering,* 192:941-954.

Shu, C., Ding, H. and Yeo, K. S. (2005). Computation of incompressible Navier-Stokes equations by local RBF-based differential quadrature method. *CMES: Computer Modeling in Engineering & Sciences,* 7:195-205.

Shyy, W., Pang, Y., Hunter, G. B., Wei, D. Y. and Chen, M. H. (1992). Modeling of turbulent transport and solidification during continuous ingot casting. *International Journal of Heat and Mass Transfer,* 35:1229-1245.

Šarler, B. (1995). Stefan’s work on solid-liquid phase changes. *Engineering Analysis with Boundary Elements,* 16:83-92.

Šarler, B. (1996). Numerical procedure for calculating temperature field in continuous casting of steel. *Materials and Technology,* 30:217-223.

Šarler, B. and Kuhn, G. (1998a). Dual reciprocity boundary element method for convective-diffusive solid-liquid phase change problems, Part 1. Formulation. *Engineering Analysis with Boundary Elements,* 21:53-63.

Šarler, B. and Kuhn, G. (1998b). Dual reciprocity boundary element method for convective-diffusive solid-liquid phase change problems, Part 2. Numerical examples. *Engineering Analysis with Boundary Elements*, 21:65-79.

Šarler, B. and Mencinger, J. (1999). Solution of temperature field in DC cast aluminium alloy billet by the dual reciprocity boundary element method. *International Journal of Numerical Methods in Heat and Fluid Flow*, 9:267-297.

Šarler, B., Gobin, D., Goyeau, B., Perko, J. and Power, H. (2000). Natural convection in porous media - dual reciprocity boundary element method solution of the Darcy model, *International Journal for Numerical Methods in Fluids*, 33:279-312.

Šarler, B. and Perko, J. (2001). DRBEM solution of temperatures and velocities in DC cast aluminium slabs. In Brebbia, C.A., Kassab, A.J., Chopra, M.B. and Divo, E., editors, *Boundary Element Technology XIV*, WIT Press, Southampton, 357-369.

Šarler, B., Perko, J., Chen, C.S. and Kuhn, G. (2001). A meshless approach to natural convection, In Atluri, S.N., editor, *International Conference on Computational Engineering and Sciences - 2001*, CD-ROM, 3-9.

Šarler, B., Perko, J., Gobin, D., Goyeau. B. and Power H. (2004a). Dual reciprocity boundary element method solution of natural convection in Darcy-Brinkman porous media. *Engineering Analysis with Boundary Elements*, 28:23-41.

Šarler, B., Perko, J. and Chen, C. S. (2004b). Radial basis function collocation method solution of natural convection in porous media. *International Journal of Numerical Methods for Heat & Fluid Flow*, 14:187-212.

Šarler, B. (2005). A radial basis function collocation approach in computational fluid dynamics. *CMES: Computer Modeling in Engineering & Sciences*, 7:185-193.

Šarler, B. and Vertnik, R. (2005). Solution of the transient direct chill casting problem with simultaneous material and interphase moving boundaries by the local radial basis function collocation technique. In: Chakrabarti, S. K., Hernández, S. and Brebbia, C. A., editors, *Fluid Structure Interaction and Moving Boundary Problems*, WIT Press, Southampton, 607-617.

Šarler, B., Vertnik, R., Šaletić, S., Manojlović, G. and Cesar J. (2005). Application of Continuous Casting Simulation at Štore Steel, *Berg- und Hüttenmännische Monatshefte,* 9:300-306.

Šarler, B. and Vertnik, R. (2006). Meshfree explicit radial basis function collocation method for diffusion problems. *Computers and Mathematics with Applications*, 51:1269-1282.

Šarler, B., Kovačević, I. and Chen, C. S. (2004). A mesh-free solution of temperature in direct-chill cast slabs and billets. In Mammoli, A.A. and Brebbia, C.A., editors, *Moving Boundaries VII*, WIT Press, Southampton, 271-280.

Šarler, B., Perko, J. and Chen, C. S. (2004). Radial basis function collocation method solution of natural convection in porous media. *International Journal of Numerical Methods for Heat & Fluid Flow*, 14:187-212.

Šarler, B., Vertnik, R. and Perko, J. (2005). Application of Diffuse Approximate Method in Convective-Diffusive Solidification Problems. *CMC: Computers, Materials, Continua*, 2:77-83.

Šarler, B., Vertnik, R., Gjerkeš, H., Lorbiecka, A., Manojlović, G., Cesar, J., Marčič, B. and Sabolič Mijovič, M. (2006). Multiscale integrated numerical simulation approach in Štore - Steel casthouse, *WSEAS Transactions on Systems and Control*, 2:294-299.

Šarler, B. (2009). *Chapter 7: Modelling of phase change processes*. In Nowak, A.J., editor, *Numerical Methods in Heat Transfer*, Institute of Thermal Technology, Silesian University of Technology, Gliwice, 165-190.

Šarler, B., Kosec, G., Lorbiecka, A. Z. and Vertnik, R. (2010). A meshless approach in solution of multiscale solidification modeling, *Materials Science Forum*, 649:211-216.

Thomas, B. G. and Storkman, W. R. (1988). Mathematical models of continuous slab casting. In: Giamei, A. F. and Abbaschian, G. J., editors, *Modeling and Control of Casting and Welding Processes - IV, April 17-22, Palm Cost, FL*, The Methallurgical Society, Warrendale, 287-297.

Thomas, B. G., Storkman, W. R. and Moitra, A. (1990). Optimizing taper in continuous slab casting molds. In: *Proceedings of the Sixth International Iron and Steel Congress, Nagoya, Japan*, Iron and Steel Institute of Japan, Tokyo, 348-355.

Thomas, B. G., Yuan, Q., Sivaramakrishnan, S., Shi, T., Vanka, S. P. and Assar, M. B. (2001). Comparison of four methods to evaluate fluid velocities in a continuous slab casting mold. *The Iron and Steel Institute of Japan International*, 41:1262-1271.

Tolstykh, A. I. and Shirobokov, D. A. (2003). On using radial basis functions in a "finite difference" mode with applications to elasticity problems. *Computational Mechanics,* 33:68-79.

Versteeg, H.K. and Malalasekera, W. (1995). *Computational Fluid Dynamics: The Finite Volume Method,* Prentice Hall.

Vertnik, R. and Šarler, B. (2002). *Graphical user interface of the simulation system for the continuous casting of billets in the Inexa-Štore d.o.o., version 2002/IS4/09,* University of Nova Gorica, Laboratory for Multiphase Processes, Nova Gorica, CD-ROM (in Slovenian).

Vertnik, R., Perko, J. and Šarler, B. (2004). Solution of temperature field in DC cast aluminium alloy billet by the Diffuse Approximate Method. *Materials and Technology,* 38:257-261.

Vertnik, R. and Šarler, B. (2004a). *Calculation and arrangement of the contraction data-base in the mould for various steel grades and formats of the Štore Steel casting machine: revision 0.*, University of Nova Gorica, Laboratory for Multiphase Processes, Nova Gorica, CD-ROM (in Slovenian).

Vertnik, R. and Šarler, B. (2004b). *Calculation of the regulation coefficients for the Štore Steel casting machine: revision 0.*, University of Nova Gorica, Laboratory for Multiphase Processes, Nova Gorica, CD-ROM (in Slovenian).

Vertnik, R. and Šarler, B. (2004c). *Validation of the Štore Steel simulation system: revision 0.,* University of Nova Gorica, Laboratory for Multiphase Processes, Nova Gorica, CD-ROM (in Slovenian).

Vertnik, R. and Šarler, B. (2005). Solution of the heat transfer model of the start-up phase of the direct chill casting process by a meshless numerical method. In: Nowak, A. J., Wecel, G. and Bialecki, R. A., editors, *Eurotherm Seminar 82 : numerical heat transfer 2005, September 13-16, Gliwice-Cracow, Poland*, Institute of Thermal Technology, Silesian University of Technology, Gliwice, 367-376.

Vertnik, R. and Šarler, B. (2006a). Meshless local radial basis function collocation method for convective-diffusive solid-liquid phase change problems. *International Journal of Numerical Methods for Heat & Fluid Flow*, 16:617-640.

Vertnik, R. and Šarler, B. (2006b). *Computer program for the time-depended calculation of the temperature field in the billet for the Štore Steel casting machine_2006/SS8/03*, University of Nova Gorica, Laboratory for Multiphase Processes, Nova Gorica, CD-ROM (in Slovenian).

Vertnik, R. and Šarler, B. (2006c). *Computer program for viewing and analyzing the technological state of the billet between the casting process for the Štore Steel casting machine_2006/SS8/03*, University of Nova Gorica, Laboratory for Multiphase Processes, Nova Gorica, CD-ROM (in Slovenian).

Vertnik, R. and Šarler, B. (2006d). *Computer program for viewing and analyzing the technological state of the billet after the casting process for the Štore Steel casting machine_2006/SS8/03*, University of Nova Gorica, Laboratory for Multiphase Processes, Nova Gorica, CD-ROM (in Slovenian).

Vertnik, R., Založnik, M. and Šarler, B. (2006). Solution of transient direct-chill aluminium billet casting problem with simultaneous material and interphase moving boundaries by a meshless method. *Engineering Analysis with Boundary Elements*, 30:847-855.

Vertnik, R. (2007). *Local Collocation Method for Phase-Change Problems,* Master Thesis, University of Nova Gorica, Nova Gorica, Slovenia.

Vertnik, R., Šarler, B., Buliński, Z. and Manojlović, G. (2007). Solution of transient temperature field in continuous casting of steel by a meshless method. In Ludwig, A., editor, *Proceedings of the ICASP2, June 17-20, 2007, Graz, Austria*, ASMET, 223-228.

Vertnik, R., Senčič, B. and Šarler, B. (2008). Solution of the incompressible turbulent flow by a meshless method. *ICCES MM'08, October 13-17, 2008, Suzhou, China,* Abstract.

Vertnik, R. and Šarler, B. (2009a). Solution of incompressible turbulent flow by a mesh-free method, *CMES: Computer Modeling in Engineering & Sciences,* 44:66-95.

Vertnik, R. and Šarler, B. (2009b). Simulation of continuous casting of steel by a meshless technique. *International Journal of Cast Metals Research*, 22:311-313.

Vertnik, R. and Šarler, B. (2009c). Simulation of turbulent flow and heat transfer in continuous casting of billets by a meshless method. In: Ludwig, A., editor, *Proceedings of the 3rd Steelsim Conference, September 8-10, 2009, Leoben, Austria*, ASMET, CC2, CD-ROM.

Vertnik, R. and Šarler, B. (2010). Local collocation approach for solving turbulent combined forced and natural convection problems. *Advanced in Applied Mathematics and Mechanics*, (in review).

Vertnik, R., Senčič, B. and Šarler, B. (2010). Continuous Casting of Steel: Solution of a Benchmark Test by a Meshless Method. *CMES: Computer Modeling in Engineering & Sciences,* (in review).

Viskanta, R. (1990). Mathematical modeling of transport processes during solidification of binary systems. *JSME International Journal,* Series II, 33:409-423.

Vogel, J. C. (1984). *Heat Transfer and Fluid Mechanics Measurements in the Turbulent Reattaching Flow Behind a Backward-Facing Step*. PhD Thesis, Stanford University, Department of Mechanical Engineering, Stanford.

Voller, V. R., Brent, A. D. and Prakash, C. (1989). The modelling of heat, mass and solute transport in solidification system. *International Journal of Heat and Mass Transfer*, 32:1719-1731.

Voller, V. R., Swaminathan, S. and Thomas, B. G. (1990). Fixed-grid techniques for phase change problems: a review. *International Journal for Numerical Methods in Engineering*, 30:875-898.

Wan, D.C., Patnaik, B.S.V. and Wei, G.W. (2001). A new benchmark quality solution for the buoyancy-driven cavity by discrete singular convolution, *Numerical Heat Transfer,* 40B:199-228.

Wang, H., Li, G., Lei, Y., Zhao, Y., Dai, Q. and Wang, J. (2005). Mathematical heat transfer model research for the improvement of continuous casting slab temperature. *The Iron and Steel Institute of Japan International,* 45:1291-1296.

Wang, J.G. and Liu, G.R. (2002). On the optimal shape parameter of radial basis functions used for 2D meshless method. *Computer Methods in Applied Mechanics and Engineering*, 26:2611-2630.

Wang, B.C., Yee, E., Yin, J. and Bergstrom, D.J. (2007). A general dynamic linear tensor-diffusivity subgrid-scale heat flux model for large-eddy simulation of turbulent thermal flows. *Numerical Heat Transfer*, B51:205-227.

Wang, Y. C., Li, D. Y., Peng, Y. H. and Zhu, L. G. (2007). Computational modelling and control system of continuous casting process. *The International Journal of Advanced Manufacturing Technology,* 33:1-6.

Wilcox, D. C. (1993). *Turbulence Modeling for CFD*, DCW Industries, Inc., California.

Williams, A.J., Croft, T.N. and Cross, M. (2003). Modelling of ingot development during start-up phase of direct chill casting. *Metallurgical and Materials Transactions,* B34:727-734.

Wiwatanapataphee, B., Wu, Y. H., Archapitak, J., Siew, P. F. and Unyong, B. (2004). A numerical study of the turbulent flow of molten steel in a domain with a phase-change boundary. *Journal of Computational and Applied Mathematics,* 166:307-319.

World Steel Committee on Economic Studies (2009). *Steel Statistical Yearbook 2008,* World Steel Association, Brussels.

Wrobel, L.C. (2001). *The Boundary Element Method - Volume 1: Applications in Thermofluids and Acoustics,* Willey, New York.

Založnik, M. (2006). *Modeling of Macrosegregation in Direct Chill Casting*, PhD thesis, University of Nova Gorica, Nova Gorica.

Zerroukat, M., Power, H. and Chen, C.S. (1998). A numerical method for heat transfer problems using collocation and radial basis functions, *International Journal for Numerical Methods in Engineering*, 42:1263-78.

Zhang, X., Song, K. Z., Lu, M. W. and Liu, X. (2000). Meshless methods based on collocation with radial basis functions. *Computational Mechanics*, 26:333-343.

Zhang, L., Rong, Y. M., Shen, H. F. and Huang, T. Y. (2007). Solidification modeling in continuous casting by finite point method. *Journal of Materials Processing Technology*, 192/193:511-517.

Zienkiewicz, O. C. and Taylor R. L. (2000). *The Finite Element Method, Fifth Edition, Volume 1, The Basics*. Butterworth-Heinemann, London.

Zienkiewicz, O. C. and Taylor, R. L. (2000), *The Finite Element Method, Fitfh Edition, Volume 3: Fluid Dynamics*, Butterworth-Heinemann, London.

Xie, Y., Yu, H., Ruan, X., Wang, B. and Ma, Y. (2008). Mathematical modeling of mould temperature field during continuous casting of steel. *Journal of Materials Processing Technology*, 199:49-55.

Yang, H., Zhao, L., Zhang, X., Deng,. K., Li, W. and Gan, Y. (1998). Mathematical simulation on coupled flow, heat, and solute transport in slab continuous casting process, *Metallurgical and Materials Transactions*, B29:1345 - 1356.

Yilmaz, T. and Fraser, S.M. (2007). Turbulent natural convection in a vertical parallel-plate channel with asymmetric heating, *International Journal of Heat and Mass Transfer*, 50:2612 - 2623.

Yin, J. and Bergstrom, D.J. (2004). LES of combined forced and natural turbulent convection in a vertical slot. *Computational Fluid Dynamics 2004*, Springer-Verlag, Berlin, 567 - 572.

Yoder, D.A. and Georgiadis, N.J. (1999), *Implementation and validation of the chien k-epsilon turbulence model in the WIND Navier-Stokes code*, NASA technical memorandum 209080.

Yuan, Q., Shi, T., Vanka, S. P. and Thomas, B. G. (2001). Simulation of fluid flow in the continuous casting of steel. In: Cross, Bailey, Evans, editors, *Proceedings: Computational Modeling of Materials, Minerals and Metals Processing*, The Materials, Minerals, and Metals Society, Warrendale, 491-500.

Yuan, Q., Sivaramakrishnan, S., Vanka, S. P. and Thomas, B. G. (2004). Computational and exeprimental sudy of turbulent flow in a 0.4-scale water model of a continuous steel caster. *Metallurgical and Materials Transactions,* B35:967-982.